IMPERIAL COLLEGE OF SCIENCE AND TECHNOLOGY

Petroleum Engineering Section,

Department of Mineral Resources Engineering.

The Role of Heterogeneities in Oil Recovery

by

MICHAEL RICHARD WHEAT

A thesis submitted for the degree of Doctor of Philosophy of the University of London, and the Diploma of Membership of the Imperial College.

November, 1984.

ABSTRACT

Reservoir heterogeneities cause early water breakthrough problems and are of much concern in miscible enhanced oil recovery (EOR) processes. Here the heterogeneities can cause the slugs of chemical to be rapidly dispersed and the recovery operation ruined. The objective of this research has been to identify and quantify the physical processes occuring in fluid flow and displacements within heterogeneous porous media using model fluid and pore structure systems. This understanding is needed not only for more efficient reservoir management but also to ensure that more realistic predictions are forthcoming from the reservoir simulation packages being developed for EOR processes.

The work has concentrated on studies of continuous and slug mode processes of relevance to oil recovery. Viscous and dispersive effects have been determined quantitatively for matched density miscible displacements within specially designed visual models having carefully controlled heterogeneity of layers and lenses. Variations in permeability, viscosity ratio and geometry have been used. Analytical models have been developed to predict the viscous crossflow effects, the optimum slug properties required to prevent disintegration by chase fluid by-passing, post breakthrough behaviour and the complex shapes of the fluid/fluid interfaces. Unit mobility ratio experiments in multi-layered systems have been used to determine the effects of transverse microscopic dispersion on chemical slug composition, over the range of dimensionless times of interest to the reservoir engineer. The long time approximations for modified longitudinal dispersion have been confirmed. The important influence of the coupling of dispersive mixing on the effective viscosity ratio and hence viscous crossflow has also been examined. Finally the

phenomena of imbibition and drainage, capillary pressure end effects and wetting phase trapping have been studied for immiscible displacements in hetergeneous media in order to distinguish the major differences between miscible and immiscible behaviour. The capillary forces have a profound effect especially at low flow rates. The experimental data have been matched by the analytical models and computer modelling and have been related to long core tests and scaled to the reservoir. It is clear that for heterogeneous reservoirs stringent mobility control and large slug volumes will be required for successful EOR.

CONTENTS

			Page No.
ABSTRACT			iv
CONTENTS			vi
ACKNOWLEDGEMENTS			xii
CHAPTER 1		INTRODUCTION	1
CHAPTER 2		FLOW THROUGH HOMOGENEOUS AND HETEROGENEOUS POROUS MEDIA - THE FUNDAMENTALS	4
	2.1	Laminar Flow and Darcy's Law	5
	2.2	Viscous Effects	9
	2.2.1	Mobility Effects	9
	2.2.2	Fluid Flow in Layered Media	12
	2.3	Diffusion and Dispersion	24
	2.3.1	Molecular Diffusion	25
	2.3.2	Microscopic Convective Dispersion	25
	2.3.3	Microscopic Longitudinal and Transverse Dispersion Coefficients	27
	2.3.4	Macroscopic Convective Dispersion	31
	2.3.5	Long Time Solution in Stratified Porous Media	32
	2.4	Capillary Forces	34
	2.4.1	Macroscopic Scale Effects	35
	2.5	Gravitational Forces	39
	2.6	Scaled Physical Models	40
	2.6.1	Scaling in Miscible Displacement	41
	2.6.2	Scaling in Immiscible Displacement	42
	2.7	Numerical Simulation - The Problems	43
	2.8	Enhanced Oil Recovery	45
CHAPTER 3		MODEL CONSTRUCTION AND EXPERIMENTAL PROCEDURES	48
	3.1	Model Design and Construction	48
	3.2	Fluid Systems	56
	3.2.1	Miscible Fluids	56
	3.2.2	Immiscible Fluids	61

	3.2.2	Dye Systems	61
	3.3	Experimental Procedure	63
	3.4	Effluent Measurement	64
	3.4.1	Ultra-Violet Absorption	64
	3.4.2	Colorimetry	64
	3.4.3	Refractive Index Measurement	65
	3.5	Model and Fluid Property Measurement	66
	3.5.1	Porosity	66
	3.5.2	Absolute Permeability	67
	3.5.3	Residual Saturations and Effective Permeabilities in Immiscible Displacement	67
	3.5.4	Capillary Pressure	67
CHAPTER 4		VISCOUS CROSSFLOW IN LAYERED SYSTEMS WITH MISCIBLE FLUIDS	69
	4.1	Equal Mobility Ratio Displacements	70
	4.2	Non-Unit Mobility Ratio Displacements	73
	4.2.1	Favourable Mobility Ratio Displacements	77
	4.2.2	Unfavourable Mobility Ratio Displacements	82
	4.3	Calculation of Fluid Crossflow	84
	4.4	Effluent Analysis and Fractional Flow Curves	95
	4.5	Correlation of Data and Discussion	97
CHAPTER 5		SLUG DEGRADATION DUE TO VISCOUS FORCES IN MISCIBLE LAYERED SYSTEMS	104
	5.1	Unit Mobility Ratio Case	104
	5.1.1	Experimental Results	106
	5.1.2	Slug Requirements	107
	5.2	Non-Unit Mobility Ratio Cases	109
	5.2.1	Experimental Observations	111
	5.2.2	Experimental Results	117
	5.2.3	Estimation of Slug Requirements	121
	5.2.4	Discussion	124
CHAPTER 6		THE EFFECT OF DISPERSION IN LAYRED SYSTEMS WITH FLUIDS OF EQUAL MOBILITY	127
	6.1	Dispersion in Stratified Media	128

	6.1.1	Continuous Injection Displacements	129
	6.1.2	Slug Mode Displacements	133
	6.2	Numerical Model	136
	6.3	Continuous Injection Results	139
	6.3.1	Numerical Calculations	139
	6.3.2	Experimental Results	140
	6.3.3	Discussion of Results	142
	6.4	Slug Mode Injection Results	143
	6.4.1	Numerical Calculations	143
	6.4.2	Experimental Results	144
	6.4.3	Discussion of Results	145
	6.5	Large Dimensionless Time Models	148
	6.5.1	Continuous Injection	148
	6.5.2	Slug Mode Injection	152
	6.6	Prediction of the Volume of the Reservoir Swept in Slug Mode Processes	155
CHAPTER 7		THE EFFECT OF DISPERSION IN MISCIBLE LAYERED SYSTEMS WITH FLUIDS OF UNEQUAL MOBILITY	162
	7.1	Previous Work	162
	7.2	Experimental Results	166
	7.2.1	Continuous Injection Results	166
	7.2.2	Slug Mode Injection Results	166
	7.3	Modelling Viscous and Dispersion Effects	167
	7.3.1	The Numerical Model	167
	7.3.2	Comparison with the Mixing Parameter Approach	170
	7.3.2	Numerical Results	171
	7.4	Discussion	175
CHAPTER 8		MISCIBLE FLUID FLOW IN A SYSTEM CONTAINING A LENS	178
	8.1	Unit Mobility Ratio Displacements	179
	8.2	Non-Unit Mobility Ratio Displacements	187
	8.3	Effluent Analysis and Fractional Flow Curves	196

CHAPTER 9 CAPILLARY PRESSURE EFFECTS IN IMMISCIBLE DISPLACEMENTS 198
9.1 Lensed Systems 199
9.1.1 Packing Number 20 199
9.1.2 Packing Number 21 202
9.1.3 Packing Number 22 204
9.1.4 Packing Number 24 207
9.2 Layered Systems 207
9.2.1 Waterflooding 208
9.2.2 Oilflooding 210
9.3 Comparison of Miscible and Immiscible Displacements 213
CHAPTER 10 SUMMARY AND CONCLUSIONS 215
10.1 Viscous Crossflow in Continuous Injection Processes in Layered Systems 215
10.1.1 Summary 215
10.1.2 Conclusions 216
10.2 Slug Degradation Due to Viscous Forces 217
10.2.1 Summary 217
10.2.2 Conclusions 218
10.3 The Effects of Dispersion in Layered Systems with Fluids of Equal Mobility 218
10.3.1 Summary 218
10.3.2 Conclusions 219
10.4 The Effects of Dispersion in Layered Systems with Fluids of Unequal Mobilities 220
10.4.1 Summary 220
10.4.2 Conclusions 221
10.5 Miscible Fluid Flow in a System Containing a Lens 221
10.5.1 Summary 221
10.5.2 Conclusions 222
10.6 Capillary Pressure Effects in Immiscible Displacements 222
10.6.1 Summary 222

10.6.2 Conclusions 223
10.7 Final Remarks 223
APPENDIX 1 224
A1.1 Air/Water Capillary Pressure Measurement 224
A1.2 Contact Angle Measurement 226
A1.3 Surface and Interfacial Tension Measurement 226
APPENDIX 2 DATA FOR STUDY OF VISCOUS CROSSFLOW IN LAYERED SYSTEMS 228
APPENDIX 3 DERIVATION OF EQUATIONS TO APPROXIMATE VISCOUS CROSSFLOW EFFECTS IN SYSTEMS WHERE A LAYER A IS WIDER THAN LAYER B 232
APPENDIX 4 DERIVATION OF AN APPROXIMATION FOR POST BREAKTHROUGH BEHAVIOUR 235
APPENDIX 5 EXPERIMENTAL DATA FOR STUDY OF SLUG DEGRADATION DUE TO VISCOUS FORCES 236
APPENDIX 6 CONTINUOUS INJECTION DATA FROM EQUIVISCOUS DISPERSION SENSITIVE EXPERIMENTS 248
APPENDIX 7 SLUG MODE DATA FROM EQUIVISCOUS DISPERSION SENSITIVE EXPERIMENTS 252
A7.1 Effluent Profiles 252
A7.2 Prediction of the Volume of the System Swept in Slug Mode Processes 258
APPENDIX 8 DATA FROM NON-UNIT MOBILITY RATIO DISPERSION SENSITIVE EXPERIMENTS 265
A8.1 Continuous Injection Data 265
A8.2 Slug Mode Injection Data 265
APPENDIX 9 DATA FROM DISPLACEMENTS IN LENS SYSTEMS 270
A9.1 Unit Mobility Ratio Displacements 270
A9.2 Non-Unit Mobility Ratio Disaplcements 270
APPENDIX 10 DERIVATIO'! OF EQUATIONS TO CALCULATE THE FINITE CROSSFLOW OF FLUID IN A LENSES SYSTEM DURING AN EQUIVISCOUS DISPLACEMENT 272

APPENDIX 11 DERIVATION OF EQUATION FOR NON-UNIT MOBILITY RATIO DISPLACEMENTS IN A NON-COMMUNICATING LENSED SYSTEM 277

NOMENCLATURE 279

REFERENCES 283

ACKNOWLEDGEMENTS

I would like to express my thanks to the following:

- My supervisor, Dr. R.A. Dawe, for his constant support and encouragement.
- Dr. R.J. Wright for his advice and guidance during the early stages of this project.
- Mr. M. Hughes for his invaluable technical assistance.
- Dr. M. Allmen for numerical consultation.
- My Colleagues, Mark Bilsland, Dave Jennings, Dave Shaw, Andy Lever, Ivor Ellul, Sezgin Daltaban, Eric Mahers, Prins Casinader, Rob Bond, Larissa Fradkin and Leo Coucoulas.
- The Science and Engineering Research Council and the Society of Petroleum Engineers for their financial support.
- The Oil Recovery Projects Division, AEE Winfrith for their interest, in particular Dr. K. Sorbie and Dr. C. Farmer.
- Finally to all those who quenched my thirst.

M.R. Wheat

CHAPTER ONE

INTRODUCTION

An inspection of any well log or core analysis report shows that the majority of rock properties vary from point to point down the well and from well to well over the reservoir. These heterogeneities will cause variations in oil distributions and hence give rise to uncertainties in oil in place calculations, as well as complicating displacement patterns and production profiles often, giving rise to premature water or gas breakthrough. However the Petroleum Engineer must be able to predict this reservoir performance so as to be able to manage the production to the best advantage under the prevailing political and economic constraints. As more complicated depletion practices involving large front end investment are introduced the description of the reservoir and the displacement processes must be more detailed and the assumption of homogeneous and isotropic properties for most hydrocarbon reservoir systems becomes totally unrealistic.

This thesis describes a study of displacements in heterogeneous systems. It has concentrated on the viscous and dispersive effects encountered during miscible displacements, and although the experiments have necessarily been on the laboratory scale, the results have been related to the reservoir situation when appropriate. The major objective has been to gain a fuller understanding of displacement processes, so that more realistic physical processes and reservoir parameters may be incorporated in the reservoir simulation models.

Heterogeneity within a porous medium implies that it has unlike quantities (eg. permeability or porosity) or differing characteristics (eg. pore size distribution or rock wettability) at different locations (ie. the quantities and characteristics are specifically location dependent). However in this thesis only those reservoir heterogeneities which actually interfere with the flow of fluids are considered.

Reservoir properties must be observed, correlated and predicted over a vast scale of length; from the pore scale (1-100μm) (through which the reservoir fluids must flow), through a core scale (0.01-1m) on which laboratory tests are carried out, a reservoir simulation grid block scale (1-10 m^3), up to the complete reservoir scale (1-100km) ie. a scale of the order of 10^{11}. These are summarised in figure 1.1.

The majority of the work reported in this thesis has concerned perfectly miscible displacements of relevance to chemical enhanced oil recovery (EOR) processes; but the differences between these and immiscible displacements are highlighted. A summary of the physics of flow through porous media relevant to this study is given in chapter two. The experimental model, and techniques are outlined in chapter three. Chapters four through seven and nine present experimental results for models packed with layered structures. More specifically in chapter four viscous crossflow effects are studied, chapters five and six examine slug disintegration and chapter seven investigates the combined effects of viscous and dispersive forces. Systems containing a lens structure are analysed in chapters eight and nine, for miscible and immiscible fluids respectively. The conclusions drawn from this work are given in chapter ten.

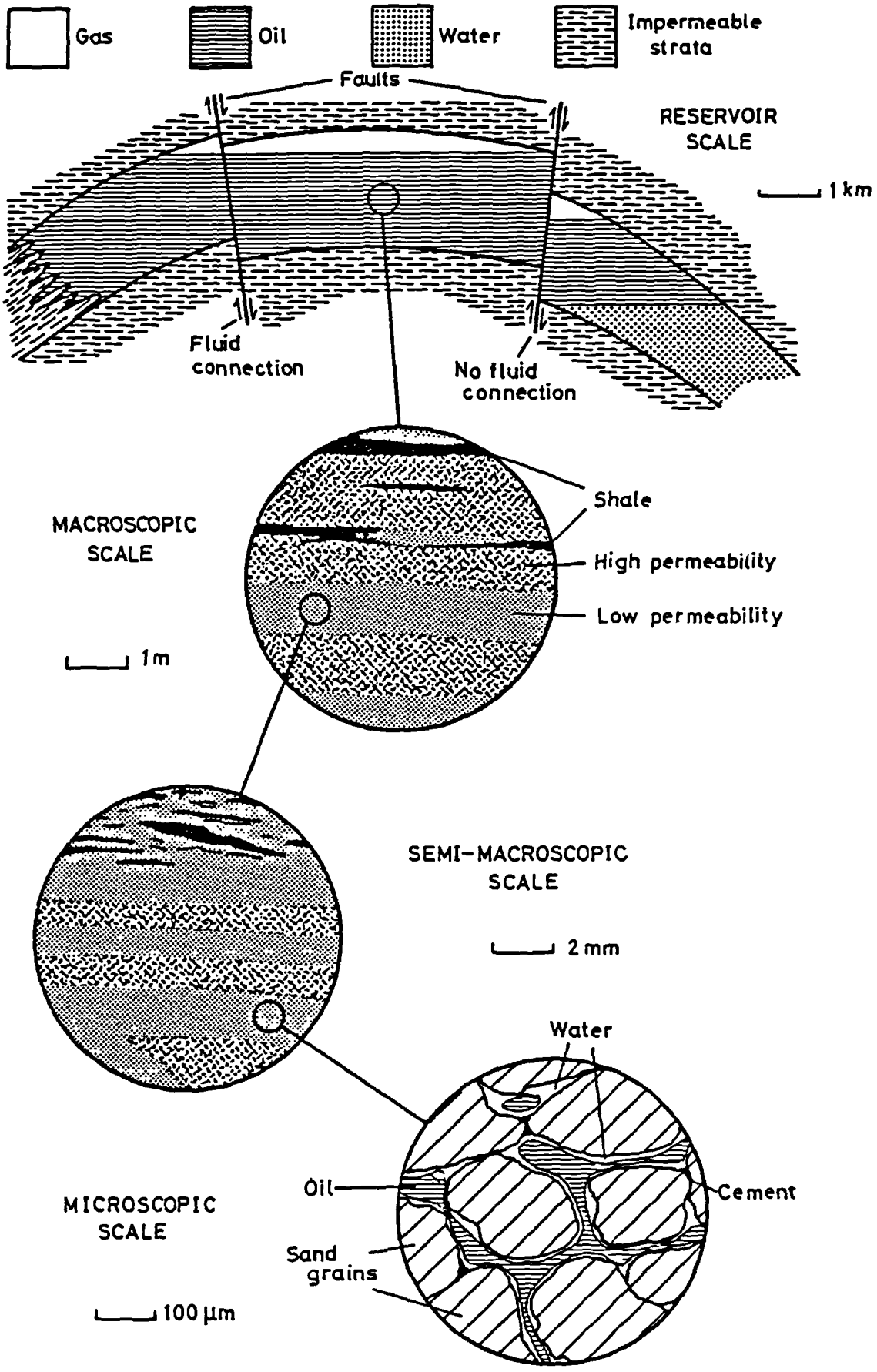

Figure 1.1 The scale of heterogeneity in a hydrocarbon reservoir (Ref. 1).

CHAPTER TWO

FLOW THROUGH HOMOGENEOUS AND HETEROGENEOUS POROUS MEDIA THE FUNDAMENTALS

Fluid movement within the porous matrix of a hydrocarbon reservoir is controlled by a balance between the viscous, capillary and gravitational forces. Also in ultra-low interfacial tension and miscible displacements the fluid compositions may be modified by diffusion and dynamic dispersion.

The interactions and dominance of any particular force depends on the scale. For instance at the pore scale, capillary forces, essentially the interfacial tension and wettability control the formation of residual oil[1], whereas at the reservoir scale capillary forces may only be significant at boundaries (e.g. reservoir layers) where the capillary pressure difference although small has a large gradient. Gravity effects are of major importance at the reservoir scale with underrunning of water or gas override[2,3], but may not be of great significance at the pore scale, although recent studies suggest that it may have a greater effect at this scale than previously thought[4]. The relative magnitude of the viscous forces to the other forces determine their importance at each scale. They increase with increasing flow rate and as the mobility ratio* diverges from unity. In ultra-low interfacial tension and miscible processes, fluid component mixing may modify the effects of viscous (chapter seven) and gravitational forces. At the pore scale molecular diffusion will be the dominant mixing mechanism, whereas fluid component mixing may not affect gross distributions when lengths are large or

* This term will be defined in the full text after this introduction.

times small (see transverse dimensionless time, chapter six).

This chapter reviews the basic concepts needed to discuss the flow of fluids through heterogeneous media. This necessarily begins with the homogeneous case.

2.1 Laminar Flow and Darcy's Law.

Although hydrocarbon reservoirs are vast bodies (typically for offshore commercial ventures of the order 15km by 5km) and the volumes of fluid injected and produced large by comparison with many other industrial processes (typically 1.5×10^4 m^3 per well per day offshore) the flow rates through all but a small fraction of the porous system close to the well bore, are such that laminar flow prevails. The transition between laminar and turbulent flow is given by a Reynolds number:

$$Re = \frac{V\rho d}{\mu} \qquad (2.1)$$

where d is some length dimension of the porous matrix (typically a grain diameter often of the order of 400μm). This dimensionless parameter is usually correlated against a friction factor (dimensionless presssure drop); a typical set of experimental data is shown in figure 2.1. In general the flow is laminar as long as the Reynolds number is less than 1.0. Under these conditions the fluids follow Darcy's law.

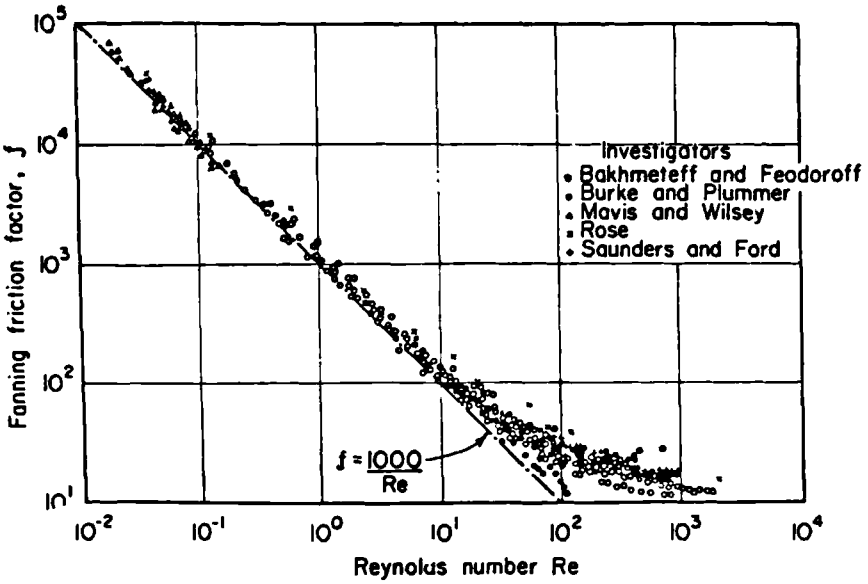

Figure 2.1 Correlation between Fanning's friction factor and Reynold's number for flow through porous media (after ref. 5).

For linear single phase flow Darcy's law is:

$$V = \frac{Q}{A} = -\frac{k}{\mu}\nabla\psi = -\frac{k\rho}{\mu}\nabla\Phi \qquad (2.2)$$

where ψ is the pressure potential:

$$\psi = p + \rho g z$$

and Φ is the fluid potential:

$$\Phi = \frac{p}{\rho} + gz \quad .$$

A most important parameter here is the absolute permeability (k) which has the dimensions of length squared and is a measure of the ability of the medium to transmit fluid. A full discussion of equation 2.2 and the deviations from it is given in many texts[5,6,7,8,9]. When considering the propagation of a fluid front through a system it is necessary to define the interstitial fluid velocity as:

$$U = \frac{V}{\phi} = \frac{Q}{A\phi} \quad . \qquad (2.3)$$

Comparison of equations 2.2 and 2.3 produces the factor k/ϕ which is defined as the conductance of the matrix, C.

Darcy's law has been generalised, without rigorous theoretical justification, to the multi-phase case by defining an effective permeability (k_i) for each fluid. Thus:

$$\frac{Q_i}{A} = - \frac{k_i}{\mu_i} \nabla \psi_i \quad . \tag{2.4}$$

This parameter is usually normalised as:

$$k_{ri} = \frac{k_i}{k}$$

where k_{ri} is termed the relative permeability of the i^{th} phase. The relative permeability is a function of wettability, saturation and saturation history[10]. As k_i is measured at the core scale under diffuse conditions*, averaging methods commonly termed pseudoisation are often needed in oil displacement calculations at larger scales to account for reservoir non-uniformily[9]. These modification procedures are a major source of uncertainty [9,11,12,13].

The recovery of petroleum fluids from a reservoir may be critically affected by one or a combination of the following:

(a) The displacement mechanism.
(b) The breakthrough vertical and areal sweep achieved by the displacing fluid.
(c) The increase in vertical and areal sweep achieved by the displacing fluid after breakthrough.
(d) The ratio of petroleum fluids to displacing fluid produced after breakthrough.

*Fluid saturations at any point along the length of the system are uniformly distributed with respect to thickness.

A useful definition of reservoir heterogeneity can therefore be obtained by identifying those features of the reservoir structure which affect items (a) through (d). Thus physical variations or lithologic changes that do not interfere with fluid flow are not considered important in this thesis.

It is necessary to identify the types of non-uniformities which will affect recovery at each scale. Inhomogeneities at the microscopic (pore) scale result from variations in particle geometry and uneven packing, complicated by diagenesis and compaction. The capillary forces in particular are affected by the effective pore size which in turn affects the magnitude of the saturation of residual oil. The core scale is important because laboratory parameter measurements are carried out on samples of this size (from 1" diameter plugs, 2" in length up to 4" diameter 36" long butted cores). Thus any heterogeneities which affect data obtained at this scale but which are ignored, may have a profound affect on subsequent predictive calculations at larger scales. Macroscopic (reservoir simulation grid block scale) heterogeneities on other hand occur on a much larger scale and relates to either distinct zoning of differing media or variation of properties within zones. Features which control fluid flow on the reservoir scale include reservoir geometry, faulting, folding and natural fracture systems.

Microscopic heterogeneity has been studied elsewhere[1], while characterisation of reservoir scale non-uniformities are provided by conventional structure contour and isopach maps of the pay interval. Consequently this work concentrates on the interaction between the fluids and non-uriform rock structure which might be expected at the reservoir simulation grid block scale.

2.2. Viscous Effects.

2.2.1 Mobility Effects.

The mobility (λ_i) of a fluid is defined as:

$$\lambda_i = \frac{k_i}{\mu_i} = \frac{k_{ri}.k}{\mu_i} \quad . \tag{2.5}$$

As the effective permeability appears in this relation the fluid mobility is a function of fluid saturation. The mobility ratio (M), which by convention is defined as the ratio of the displacing fluid mobility to that of the displaced fluid, is an important parameter in displacement processes.

It is necessary to decide on the values of relative permeabilities for use in equation 2.5. Taking a waterflood as an example; if the displacement is efficient and the oil behind the front is at residual saturation (figure 2.2a), the end point relative permeabilites* (k'_{roil},k'_{rw}) can be used, thus:

$$M = \frac{\lambda_W}{\lambda_{OIL}} = \frac{k'_W}{\mu_W}\frac{\mu_{OIL}}{k'_{OIL}} \quad \frac{k'_{rW}}{\mu_W}\frac{\mu_{OIL}}{k'_{rOIL}} \quad . \tag{2.6}$$

* Relative permeability of the media to a fluid at the irreducable saturation of the other fluid(s).

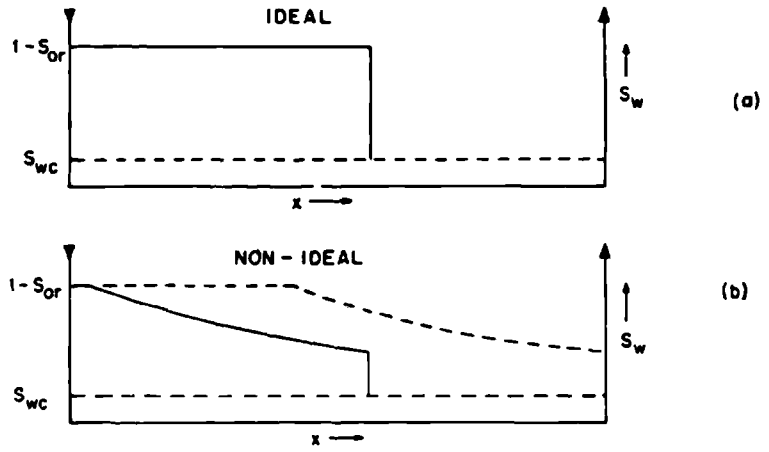

Figure 2.2 Waterflood saturation distributions for (a) an efficient (ideal) displacement and (b) a non-ideal displacement.

If a saturation gradient exists behind the displacement front (front 2.2b) then the displacing phase mobility at the average water saturation behind the flood front at breakthrough could be used[10].

In miscible displacements where two fluids mix instantaneously there are no residual phases in the system and the end point relative permeabilities equal unity. Thus the mobility ratio reduces to the ratio of the fluid viscosities:

$$M = \frac{\lambda_{DISPLACING}}{\lambda_{DISPLACED}} = \frac{\mu_{DISPLACED}}{\mu_{DISPLACING}} \quad . \qquad (2.7)$$

In a linear homogeneous system the fluid flow can be assumed one-dimensional and oil recovery can be predicted using the Buckley Leverett frontal advance theory[14,15]. Details and discussions of these methods may be found in many texts[7,9,10,16]. These techniques obtain insitu saturation profiles and recovery predictions which are in reasonable agreement with laboratory displacements[17], provided:

(a) For immiscible displacements the effect of capillary pressure at the displacement front is small[18].

(b) For miscible displacements the effect of fluid mixing processes is small (see next section).

(c) The fluid mobility ratio is less than or equal to unity.

When condition (c) is not fulfilled the displacing phase is more mobile than the displaced phase (M>1.0) and penetrates into the latter in the form of streamers, a phenomenon called viscous fingering (figure 2.3). This causes earlier breakthrough and poorer recovery than that predicted by the frontal advance theory.

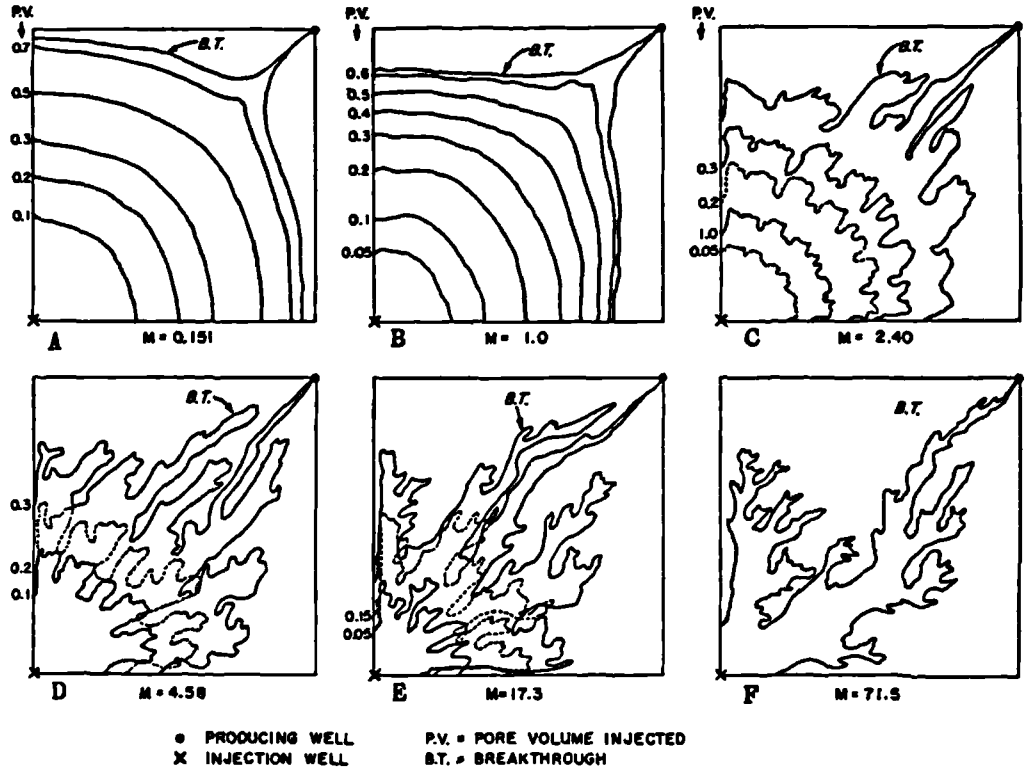

Figure 2.3 Displacement fronts illustrating viscous fingering (ref.19).

Viscous fingering in homogeneous systems has received considerable attention in the petroleum literature[19] through [31] particularly due to its influence on the fluid mixing that will occur in chemical or solvent injection processes. For heterogeneous reservoir media the effects of structural nonuniformities will dominate the displacement and a

macroscopically irregular front will occur on every scale. Thus for instance when simulating the reservoir scale, fluid flow will be dominated by the gross layering structures which are known to occur; this will be discussed in the next section and chapter four. Within these strata small scale inhomogeneities will dictate the detail of fluid flow patterns; this will be discussed in chapter eight.

2.2.2 Fluid Flow in Layered Media

Consider the linear system shown in figure 2.4, where fluid 1 is being displaced by fluid 2.

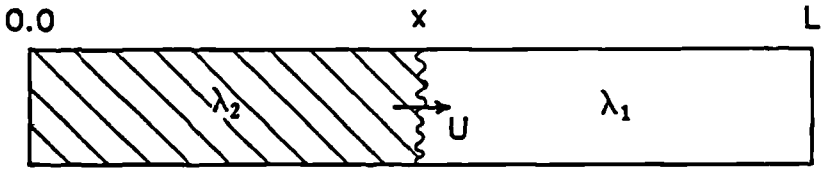

Figure 2.4 Schematic of a one layer linear system.

The advance of the displacement front in such a system is given by:

$$U = \frac{\lambda_2 \Delta p}{\phi(x(1-M)+ML)} \quad . \tag{2.8}$$

For a constant pressure drop the velocity of the front (U) will only be constant when both fluids have the same mobility (i.e. M=1.0). When the mobility ratio is greater than unity U will increase with time, because the viscous resistance within the system decreases as more of the lower mobility displacing phase enters. Conversely when the mobility ratio is less than unity, U will decrease with time.

Now consider a two layer system where the layers are separated by an impermeable barrier (figure 2.5). The relative frontal propagation is given by:

$$\frac{U_A}{U_B} = \frac{C_A}{C_B}\left[\frac{X_B(1-M)+M}{X_A(1-M)+M}\right] \tag{2.9}$$

where C is the conductance of a layer. Thus when the mobility ratio equals unity, the relative frontal positions (X_A/X_B) at any instant is given by the conductance contrast between the layers (C_A/C_B). The position of the front in the low conductance layer (X_B) when breakthrough occurs in the high conductance layer $(X_A=1.0)$, defined as X_B^* is obtained by integration of equation 2.9; thus:

$$X_B^* = \frac{M \pm \sqrt{M^2 + \dfrac{C_B(1-M^2)}{C_A}}}{(M-1)} \quad , \quad M \neq 1.0$$

$$X_B^* = \frac{C_B}{C_A} \quad , \quad M = 1.0 \quad . \tag{2.10}$$

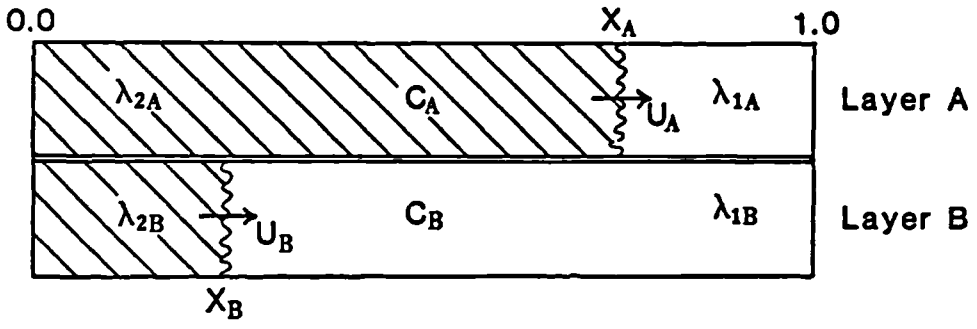

Figure 2.5 Schematic of a two layer linear system where the layers are separated by a no-flow barrier.

Figure 2.6 shows that when the mobility ratio is greater than one, less of the low conductance layer is swept at breakthrough than for the unit mobility ratio case, because the resistance to flow decreases quicker in the high

conductance layer as more high mobility fluid enters this layer than the low conductance layer. These are the unfavourable cases (M>1.0). Conversely, the favourable cases are when the mobility ratio is less than one. Here more of the low conductance layer is swept at breakthrough relative to the unit mobility ratio case, as the resistances to flow are equalised by more of the low mobility fluid going initially into the high conductance layer.

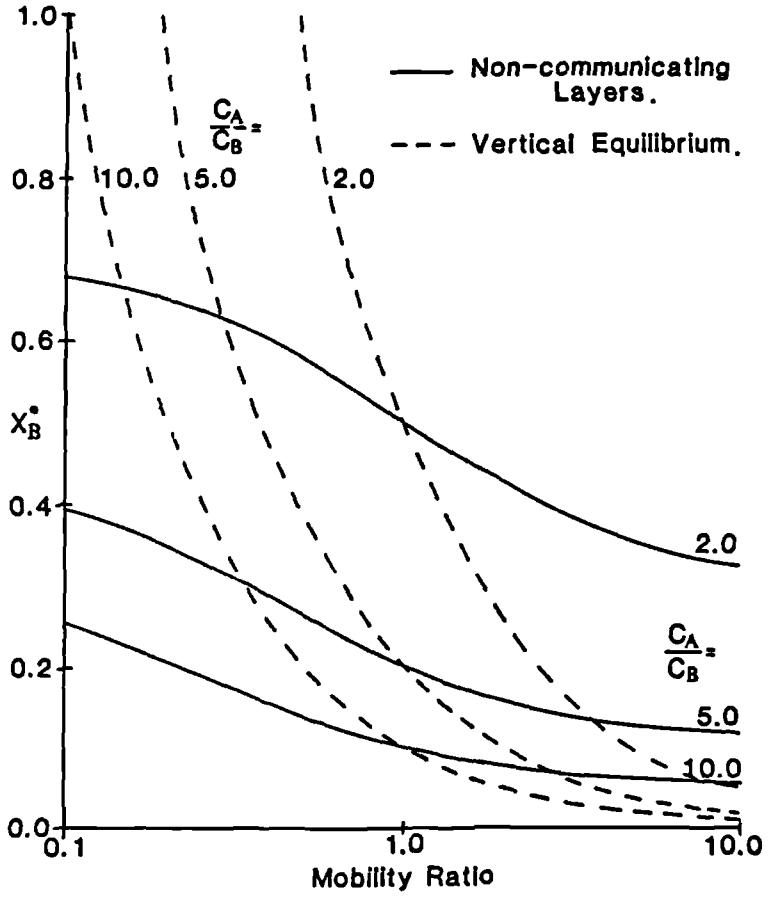

Figure 2.6 Variation of X_B^* with mobility ratio and conductance contrast for the assumptions of non-communicating layers and vertical equilibrium.

For this case, where it is assumed that there is no communication between the layers, figure 2.7 shows that for non-unit mobility ratio displacements there will be lateral pressure differences across the system; although as there is

no communication there is no lateral fluid flow. An alternate mathematical model is called the Vertical Equilibrium model (VE). Here infinite cross-conductivity is assumed between the layers, and so lateral fluid transfer occurs instantaneously and there are no lateral pressure differences across the system. Therefore the normalised pressure profiles are assumed to be the same as the unit mobility ratio case (figure 2.7a). Under these conditions the relative frontal propagation will be constant and,

$$X_B^* = \frac{C_B}{C_A M} \quad . \qquad (2.11)$$

The Vertical Equilibrium model is compared to the non-communicating layer model in figure 2.6. It can be seen that these cases only give the same result when the mobility ratio equals unity. As the mobility ratio departs from unity the difference between these two models increases.

The majority of the analytical methods used by Petroleum Engineers to calculate the volume of a layered system contacted by displacing fluid (sweep efficiency) are based on one of the above assumptions. Both the Stiles[32] and the Dykstra and Parsons[33] methods assume that fluid cannot flow between layers. Stiles also assumes that the mobility ratio is unity for vertical sweep (E_V) calculations. Thus the volume of fluid injected into a layer depends only on the permeability height product (kh) for that layer. For a series of N equal thickness layers with decreasing permeability, the vertical sweep (equation 2.12) is calculated when the displaced fluid breaks through in each layer (designated as I), thus:

$$E_V = \frac{I + \sum_{j=I+1}^{j=N} Z_j}{N} \qquad (2.12)$$

where $Z_j = \frac{k_j}{k_I}$.

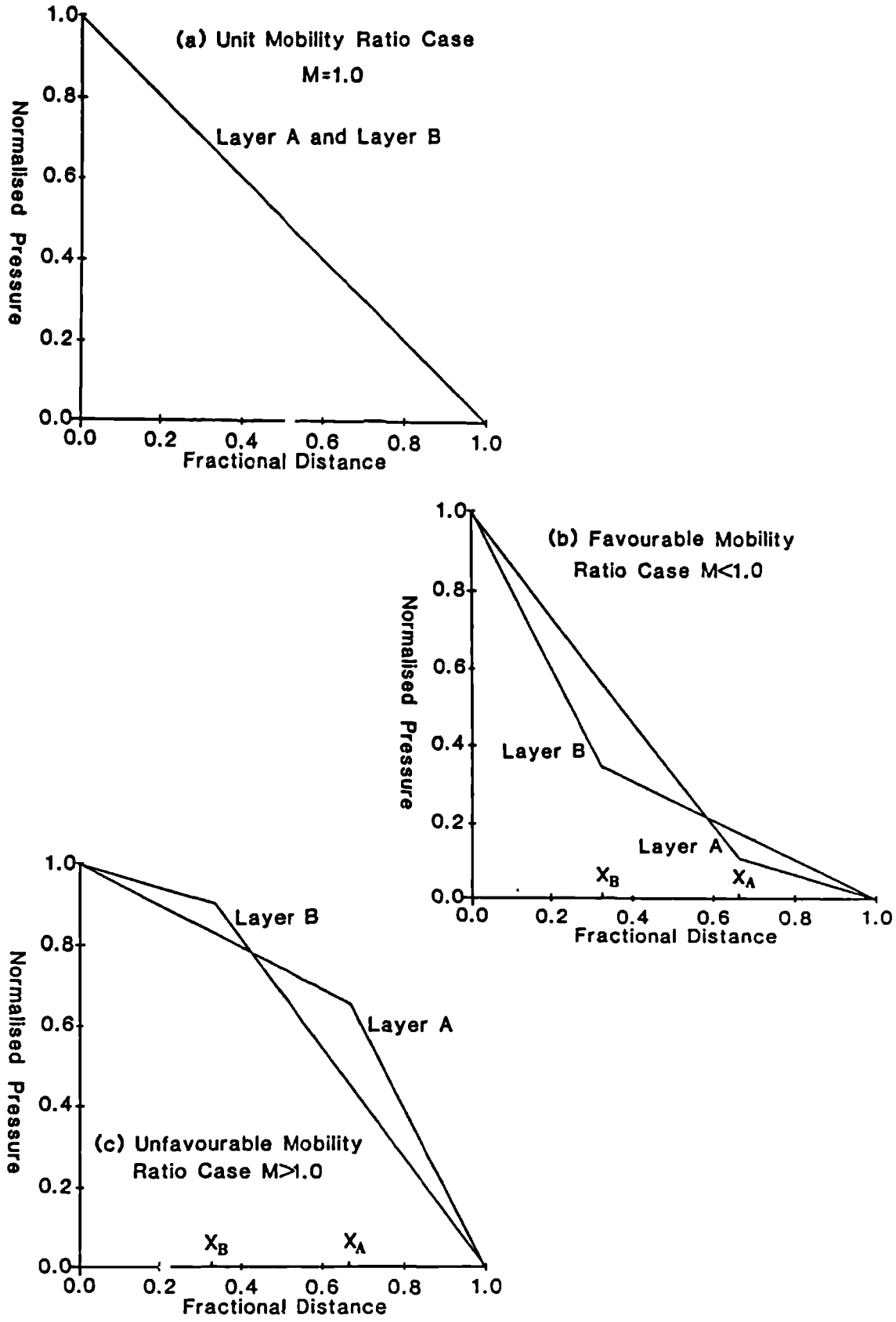

Figure 2.7 Instantaneous normalised pressure profiles for the non-communicating layer case.

Although the mobility ratio has been assumed equal to one for the vertical sweep calculation, Stiles uses the field value to calculate the producing water oil ratio (WOR):

$$WOR = M\left(\sum_{j=1}^{j=I} k_j \Big/ \sum_{j=I+1}^{j=N} k_j\right) \quad . \tag{2.13}$$

Therefore this method is inconsistent. Dykstra and Parsons used a similar model but included the mobility ratio, thus:

$$Z_j = \frac{M \pm \sqrt{M^2 + \frac{k_j}{k_I}(1-M^2)}}{(M-1)} \tag{2.14}$$

and

$$WOR = \frac{\sum_{j=1}^{j=I} k_i}{\sum_{j=I+1}^{j=N} \frac{k_j}{(M-Z_j(M-1))}} \quad . \tag{2.15}$$

They extended their analysis by assuming a continuous log normal permeability distribution and correlated the vertical sweep against the coefficient of variation (equation 2.16) for a range of mobility ratios:

$$V = \frac{\sigma}{\bar{X}} \tag{2.16}$$

(see figure 9 and 10 of reference 33).

Hiatt[34] used the Vertical Equilibrium (VE) assumption to predict E_v and WOR. This method is applicable to any mobility ratio, but is difficult to apply[10]. Warren and Cosgrave[35] extended Hiatt's technique to a system with log-normally distributed permeability. Recently Zapata and Lake[36] used VE to investigate the effect of viscous

crossflow*. They ignored gravitational and capillary pressure effects, but included relative permeability effects, so adding the complication of saturation dependent phenomena.

The no lateral communication model assumes that no fluid flows between adjacent layers (i.e. no viscous crossflow occurs). The Vertical Equilibrium assumption implies that fluid transfer between layers is instantaneous. Figure 2.8 compares characteristic curves (frontal position in layer A against that in layer B) for a laboratory displacement (see chapter four for details) with those predicted by these two models. It can be seen that the data from the experimental displacement, where there is finite communication between the layers, falls in between the predicted cases where either no or instantaneous communication is assumed. Therefore these models have improper assumptions and are inadequate for predicting actual displacement behaviour.

* The transfer of fluid between adjacent layers caused by transverse pressure differences (figures 2.7b and c) created by a displacing fluid mobility which differs from that of the displaced fluid (see chapter four for more detail).

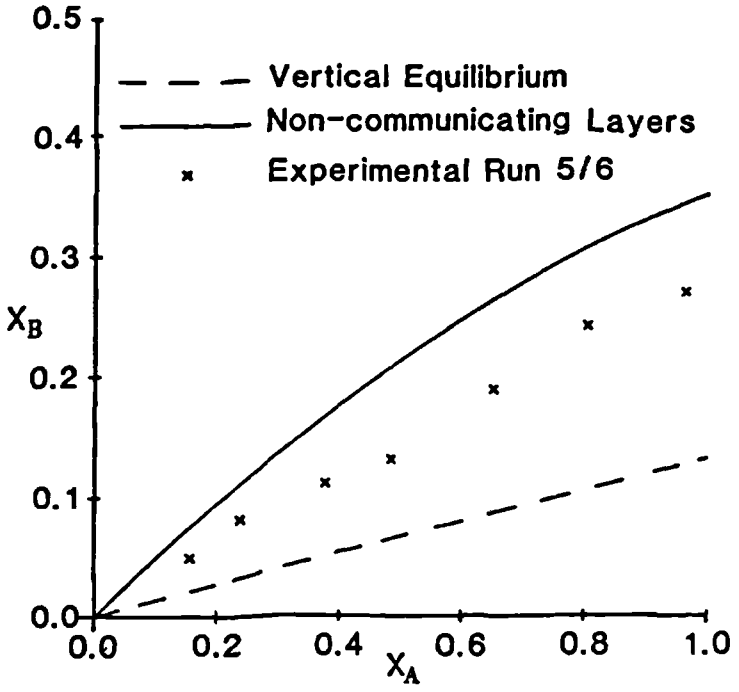

Figure 2.8 Characteristic curves from laboratory displacements compared to those predicted by vertical equilibrium and non-communicating layer models (C_A/C_B = 2.1, M=3.74).

The finite communication (i.e. finite amount of viscous crossflow) between adjacent layers has been included by Wright and Dawe[37]. They used a dual layer model, similar to figure 2.5, with a communicating boundary. The influence of fluid crossflow on the axial pressure profile within layer A can be calculated when layer B is wide relative to layer A. The flow rate within layer B can then be assumed constant and the pressure profile in layer B linear and unaffected by fluid crossflow. The intra-layer pressure profiles considered are illustrated in figure 2.9. These approximations are valid when the distance between the fronts (X_A - X_B) is large and fluid crossflow into layer B is small enough not to affect the pressure profile within that layer. A differential mass balance on an element of the system gives equation 2.17, which relates the axial pressure at any

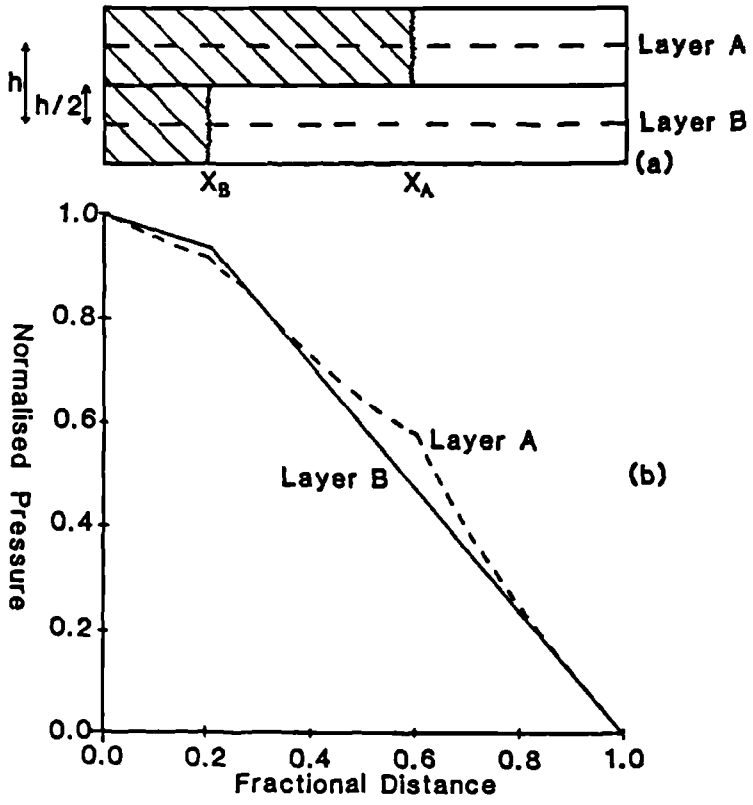

Figure 2.9 (a) Illustration of pressure axes (dashed) within the two layers.
(b) Axial pressure profiles, assumed for layer B and calculated for layer A.

point in layer A to the crossflow index (α):

$$\frac{d^2P_A}{dX^2} - \alpha P_A = \alpha(X-1) \qquad (2.17)$$

where

$$\alpha = \frac{4}{h_D^2\left(1 + \frac{C_A\mu_B}{C_B\mu_A}\right)} \quad .$$

Here $h_D = h/L$ and α accounts for the amount of communication between layers, and hence the quantity of fluid crossflowing. It can be modified for cases where interlayer communication is impaired (eg. due to non-continuous shale streaks etc.). Equation 2.17 is solved analytically both up and downstream of the front in layer A

to give a relation for P_A applying to any values of X_A and X_B (see equation A7 and A8, reference 37). Typical profiles are shown in figure 2.10 for a range of h_D values.

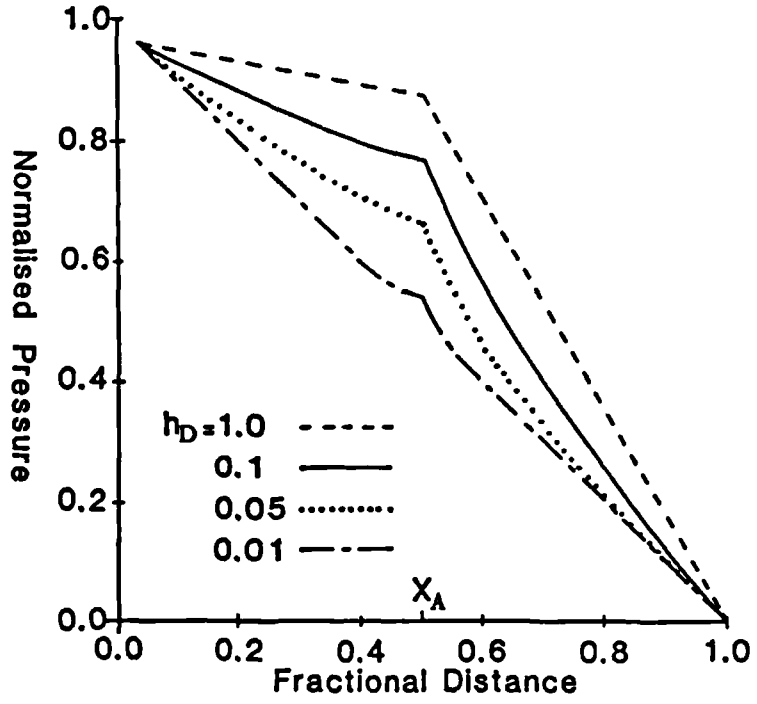

Figure 2.10 Calculated axial pressure profiles within layer A.

The relative velocity of the leading front (X_A) is given by the pressure gradient (dP_A/dx) on the downstream side, thus:

$$\frac{U_A}{U_B} = \frac{C_A}{C_B}\left[\frac{Z+1}{Z+(1/M)}\right] \qquad (2.18)$$

where

$$Z = \frac{\beta}{\gamma}\left[\frac{1+\exp(-2\beta(X_A-X_{CR}))}{1-\exp(-2\beta(X_A-X_{CR}))}\right]\left[\frac{1-\exp(-2\gamma(1-X_A))}{1+\exp(-2\gamma(1-X_A))}\right] .$$

β and γ are the crossflow indices applying to the up and downstream sides of X_A respectively and are given by:

$$\beta = \frac{2}{h_D\left(1 + \frac{MC_A}{C_B}\right)^{\frac{1}{2}}} \quad ; \quad \gamma = \frac{2}{h_D\left(1 + \frac{C_A}{C_B}\right)^{\frac{1}{2}}} \quad . \quad (2.19)$$

Equation 2.18 can be solved numerically to give characteristic curves (X_A versus X_B). Examples are shown in figure 2.11.

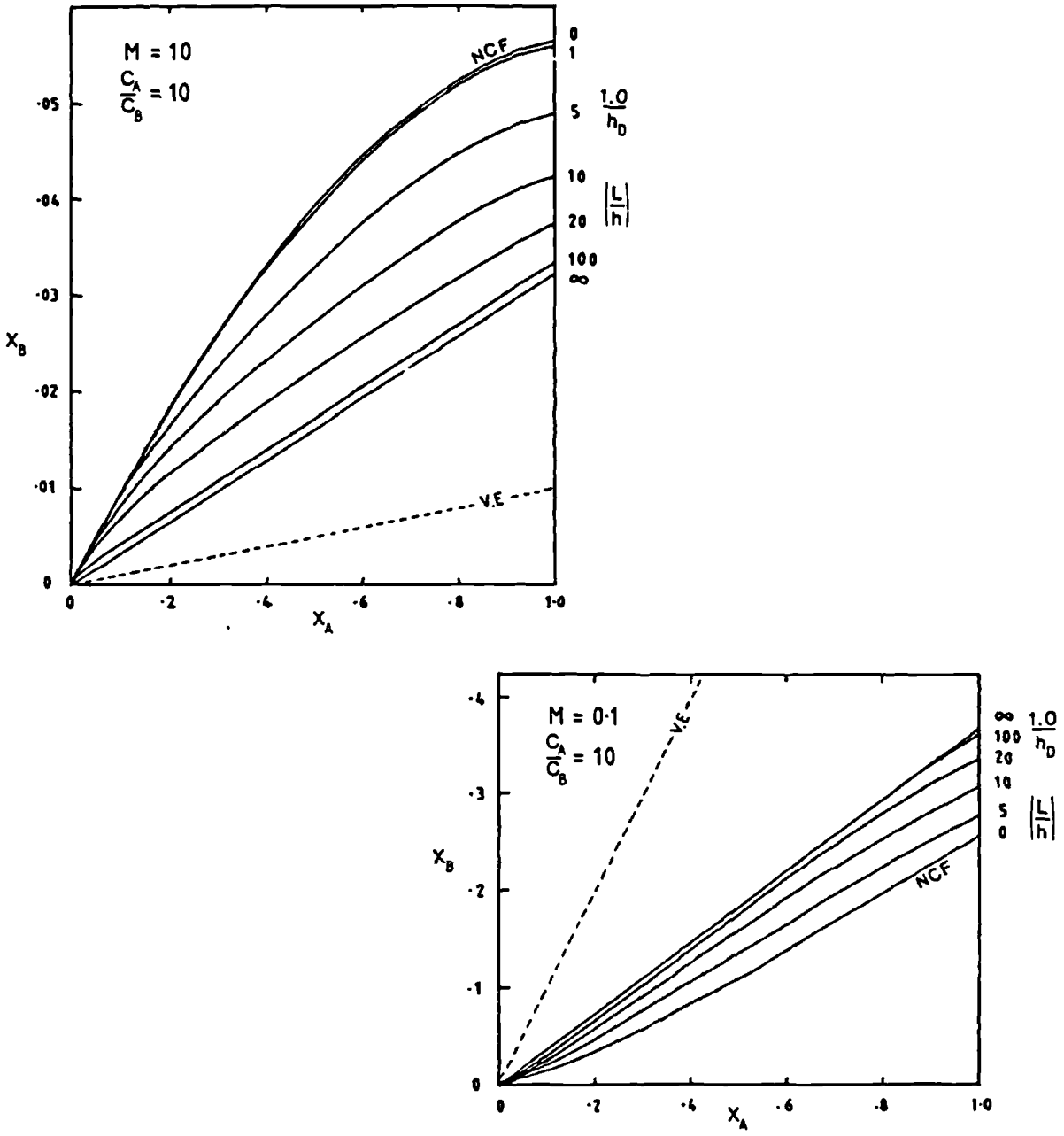

Figure 2.11 Characteristic curves calculated from equation 2.18 showing influence of the layer aspect ratio (h_D)[37].

When L/h tends to zero (i.e. very thick layers) the crossflowing fluid has little effect on the axial pressure profile within layer A, and the non-communicating layer case (NCF) is approached. But at the other extreme, L/h tending to infinity (maximum communication case; ie. very thin layers) the vertical equilibrium solution is not approached. This is because a finite amount of time is required for fluid to crossflow in the experiments. Thus Vertical Equilibrium is not, as has been assumed previously[34,35,36], a limiting condition for the calculation of viscous crossflow effects.

When L/h tends to infinity the characteristic curves (figure 2.11) tend to straight lines which implies a steady-state solution. It can be shown for this case that:

$$Z \simeq \left[\frac{1 + \frac{C_A}{C_B}}{1 + \frac{C_A M}{C_B}} \right]^{\frac{1}{2}} . \qquad (2.20)$$

Equation 2.20 is a useful approximation and will be referred to later.

This model has been tested experimentally in this work for h_D values between 0.025 and 0.5, mobility ratio's between 0.267 and 3.74 and conductance contrasts between 2.1 and 2.7. A number of extensions have been made which are discussed in chapter four.

2.3 Diffusion and Dispersion.

So far only the bulk movement of fluid between adjacent layers due to viscous crossflow has been discussed. Reservoir and displacement fluids contain a number of components, and in certain EOR processes chemicals are deliberately added to the injection water to alter the physical properties of the fluids, such as interfacial tensions, viscosities and wettabilities. These chemicals are expensive and the Engineer will wish to add only the minimum amounts for effectiveness in order to derive maxim m profit. During a displacement, the composition of miscible fluids may be altered by the transfer of the constituent components between fluids. Three mechanisms contribute to this mixing of miscible fluids: molecular diffusion, microscopic convective dispersion, and macroscopic convective dispersion. Molecular diffusion is due to random molecular motion. Microscopic convective dispersion results from the tortuous streamlines that fluid molecules must follow between pores, with the subsequent mixing of fluids by molecular diffusion within the pores. Macroscopic dispersion is due to heterogeneities which are large compared to laboratory core samples but are smaller than gross correlatable reservoir features such as strata.

This mixing of miscible fluids can either benefit or be detrimental to an EOR process. If the concentration of chemical falls below that needed to maintain miscibility or potency enhanced recovery of oil will be lost. Conversely these processes may act to moderate or damp out unfavourable viscous fingering/channelling processes (chapter seven). Also a finite amount of component transfer is required in some EOR processes on a microscopic scale for the chemical to be effective in mobilising residual oil[38].

2.3.1 Molecular Diffusion.

If two miscible fluids are in contact, initially with a shape interface, then as time passes they will diffuse into one another. This diffusion is caused by random molecular motion and is described by the Fick[7] diffusion equation:

$$\frac{dG}{dT} = - D_o A \frac{\partial c}{\partial x} \quad . \tag{2.21}$$

The value of the diffusion coefficient (D_o) is a function of the physical properties of the fluids and of the concentration, but for many reservoir problems an adequate description can be obtained by using an average value for a 50% mixture. Crank[39] discusses the use of a variable diffusion coefficient.

Equation 2.21 will apply to diffusion in porous media if the diffusion coefficient is modified to account for the tortuous path that the diffusing molecules must follow. Here an analogy with electrical conductivity is used, thus:

$$\frac{D}{D_o} = \frac{1}{F\phi} \tag{2.22}$$

where D is an effective diffusion coefficient.

2.3.2 Microscopic Convective Dispersion.

If there is gross fluid movement through the porous medium, further mixing occurs both in the direction of flow (axial) and perpendicular to it (transverse). This mixing is greater than would be expected by diffusion alone and has been explained by Blackwell et al[40] in terms of a "mixing cell" theory (figure 2.12).

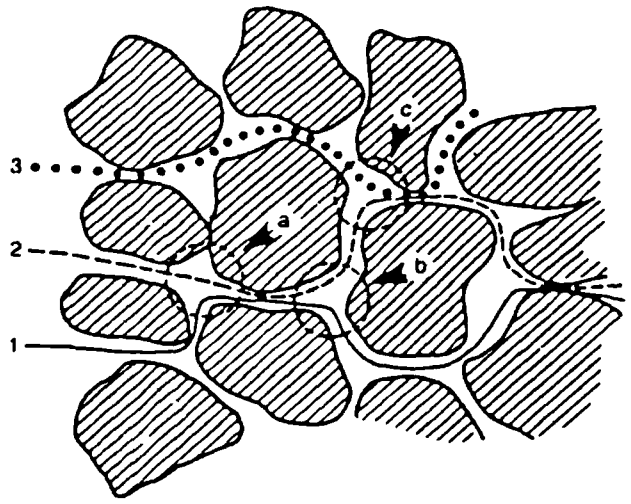

Figure 2.12 Pore network to illustrate the "mixing cell" theory of microscopic convective dispersion.

On average the streamlines are in the direction of bulkflow, but are forced to follow a tortuous path through the medium. Consider three streamlines (figure 2.12), which due to previous mixing, have different concentrations. Streamlines 1 and 2 enter pore A, where the concentration is homogenized by molecular diffusion, such that the composition of streamlines 1 and 2 leaving pore A are the same. Fluid molecules following streamline 2 then enter pore C where they are mixed by molecular diffusion with molecules from streamline 3. Thus fluid mixing occurs axially due to a combination of diffusion and mixing caused by the flow or convection.

Figure 2.12 can also be used to explain fluid mixing transverse to the direction of flow. Suppose streamlines 2 and 3 initially carry only oil molecules and streamline 1 only fluid molecules. Streamline 2 leaves pore A, where due to diffusion, some displacing fluid molecules were mixed with the oil molecules. In pore C, molecules from streamline 2 are mixed with pure oil molecules from streamline 3. So strealine 3 leaves pore C carrying some

displacing fluid molecules. Thus by this process, displacing fluid molecules become progressively dispersed normal to the direction of flow.

While longitudinal dispersion will be the most important fluid mixing mechanism in a stable displacement in homogeneous media, transverse dispersion becomes of increasing importance whenever the displacement front takes on a heterogeneous character (ie. due to viscous fingering, gravity tonguing and stratification). The effect of transverse dispersion in layered media will be discussed in chapters six and seven.

2.3.3 Microscopic Longitudinal and Transverse Dispersion Coefficients.

The diffusion-convection equation, which describes the concentration at any point and any time, can be written for constant flow in the x direction as:

$$K_L \frac{\partial^2 c}{\partial x^2} + K_t \left(\frac{\partial^2 c}{\partial y^2} + \frac{\partial^2 c}{\partial z^2} \right) - U \frac{\partial c}{\partial x} = \frac{\partial c}{\partial T} \qquad (2.23)$$

where the first term accounts for dispersion in the x direction (termed longitudinal dispersion), and the second and third terms account for dispersion in the y and z directions (termed transverse dispersion). If we assume for the purposes of illustration, dispersion in any one direction to be unaffected by dispersion in another direction, then the concentration profiles after a time T in a homogeneous media are given by:

$$\frac{c}{c_o} = \tfrac{1}{2} \left[1 - \operatorname{erf} \left(\frac{x - UT}{2\sqrt{K_L T}} \right) \right] \qquad (2.24)$$

in the x direction and,

$$\frac{c}{c_o} = \frac{1}{2}\left[1 \pm \text{erf}\left(\frac{W}{2\sqrt{K_t T}}\right)\right] \qquad (2.25)$$

in the y and z directions; where W is the distance from the initially sharp interface. The nature of these curves are shown in figure 2.13.

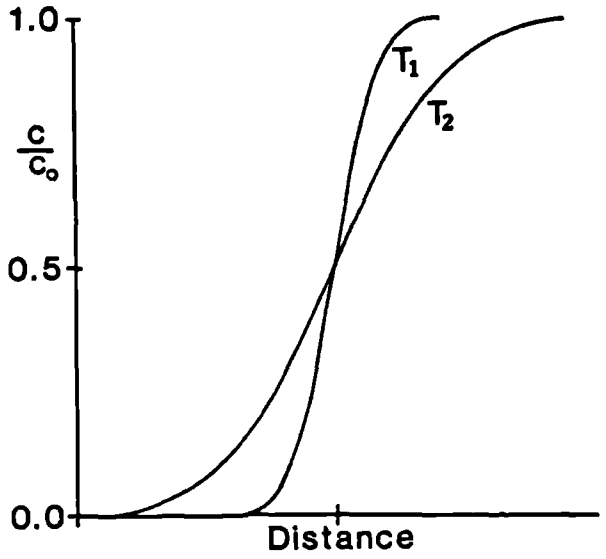

Figure 2.13 S-shaped concentration profiles at two different times ($T_2 > T_1$).

Many workers[40,41,42] have shown that the dispersion coefficients can be described by equations of the form:

$$K = D + E \qquad (2.26)$$

where E is a microscopic convective dispersion term. Perkins and Johnson[41] proposed the following equations for longitudinal and transverse dispersion coefficients:

$$\frac{K_L}{D_o} = \frac{1}{F\phi} + 0.5\,\frac{U\sigma d_p}{D_o} \quad , \quad \frac{U\sigma d_p}{D_o} < 50.0 \qquad (2.27)$$

$$\frac{K_t}{D_o} = \frac{1}{F\phi} + 0.0157\,\frac{U\sigma d_p}{D_o} \quad , \quad \frac{U\sigma d_p}{D_o} < 10^4 \qquad (2.28)$$

which are represented graphically in figure 2.14.

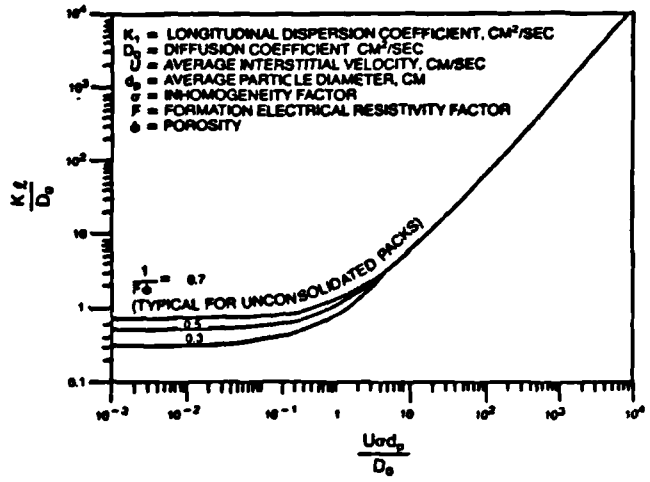

Figure 2.14a. Longitudinal microscopic dispersion coefficients (ref 41).

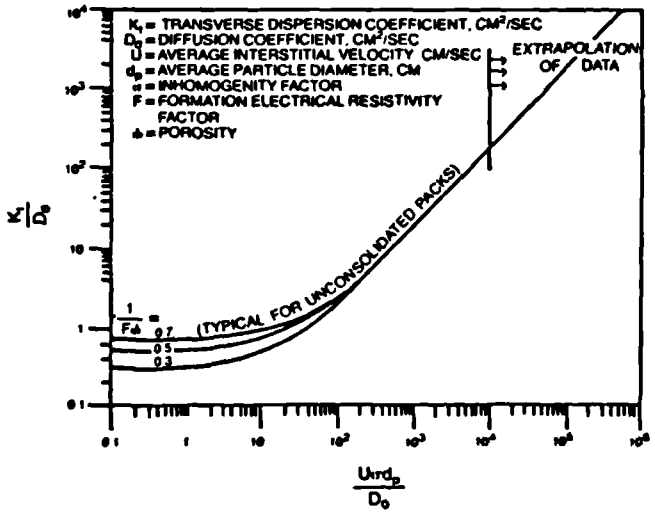

Figure 2.14b. Transverse microscopic dispersion coefficients (ref. 41).

At low flow rates ($U\sigma d_p D_o$ < 0.1 for longitudinal and < 50.0 for transverse dispersion) molecular dispersion dominates the process. For values of $U\sigma d_p/D_o$ between 4.0 and 50.0* for longitudinal and above 300.0 for transverse dispersion, convective dispersion dominates the mixing process. In between these two regions both mechanisms play an important role.

The inhomogeneity factor (σ) in equations 2.27 and 2.28 accounts for microscopic permeability heterogeneities. Perkins and Johnson[41] showed that σ increases with decreasing particle size (d_p) and from literature data suggested that an average value for the product σd_p to be 0.36cm. Using this value, a liquid diffusion coefficient of $2x10^{-5}$ cm^2/sec and a range of reservoir rates from 0.1 to 1.0 ft/D; values for the dimensionless group ($U\sigma d_p/D_o$) lie between 0.6 and 6. From figure 2.14a it can be seen that longitudinal dispersion in the reservoir is due to a combination of both diffusion and convective dispersion. Transverse dispersion (figure 2.14b) on the other hand is due solely to diffusion at reservoir rates, but convective dispersion may play an important role at laboratory rates which often tend to be higher.

In their excellent review of microscopic dispersion, Perkins and Johnson[41] show that other parameters, such as particle-size distribution, fluid saturations, mobility ratio, density ratio and particle shape, may affect the fluid mixing processes. Therefore it should be emphasized that equations 2.27 and 2.28 only give approximate values for the microscopic dispersion coefficients.

* Above 50 dispersion is greater than would be explained by the "mixing cell" theory and shows that diffsuion is no longer equalising the concentration within each pore.

For engineering purposes, equations 2.27 and 2.28 for the microscopic dispersion coefficients become:

$$K_L = \frac{D_o}{F\phi} + \alpha_L U \tag{2.29}$$

$$K_t = \frac{D_o}{F\phi} + \alpha_t U \tag{2.30}$$

where α_L and α_t are the longitudinal and transverse dispersivities respectively. Comparsion with the original equations shows the dispersivities to be functions of average particle size and local heterogeneity. We have seen that for laboratory displacements:

$$\alpha_L = 0.72 \text{ cm} \qquad \text{and} \qquad \alpha_t = \frac{\alpha_L}{30.0} \cdot \tag{2.31}$$

However recent field tests[43,44] have suggested dispersivity values of 3.66cm for a single well test and 2.5m for a multi-well test. These large values can be attributed to the larger scale heterogeneities present in field scale displacements. This increased fluid dispersion is termed macroscopic dispersion.

2.3.4 Macroscopic Convective Dispersion.

Two models, based on differing types of heterogeneity have been developed to account for macroscopic dispersion. Warren and Skiba[45] assumed that the porous media was made up of randomly placed heterogeneities. They used a Monte Carlo simulator to show that large dispersivities can be obtained due solely to random variations in permeability. Lake and Hirasaki[46] argued that due to the stratified nature of hydrocarbon reservoirs, conclusions based on heterogeneities randomly distributed were less satisfactory than ones based on layered heterogeneities. They proposed that an interaction between the differential velocities in adjacent layers and transverse dispersion (discussed in the next section) could account for macroscopic dispersion. Given the complex heterogeneous structure of the reservoir system,

it is likely that a combination of these two mechanisms is responsible.

2.3.5 Long Time Solution in Stratified Porous Media.

When a pulse of solute is injected into a stream of solvent flowing slowly through a capillary tube, the solute concentration is found to move as a symmetrical column of slowly increasing length. This observation is not that which might be expected. For a liquid in laminar flow through a tube, there is a parabolic distribution of velocities transverse to the axis of the tube, where the fluid in the centre of the tube flows at twice the velocity of the mean flow. Thus the solute concentration profile should be distorted by the flow into parabolic form. This apparent discrepancy has been explained by Taylor[47,48]. He recognised that there is not only mass transport by bulk flow but also by diffusion, and occurs both axially and transversely. Under the conditions studied the former is negligible in comparison to the bulk flow. Taylor showed that when the time to transport solute molecules axially by bulk flow (convection) is long compared to that required for diffusion to damp out lateral concentration variations, this phenomenon (known as "Taylor Dispersion") occurs. The condition for this is that:

$$\frac{L_c}{2\bar{U}} >> \frac{a}{3.8^2\, D_o} \quad . \tag{2.32}$$

In this case the concentration profile is given by:

$$\frac{c}{c_o} = \frac{1}{2}\left[1 \pm \operatorname{erf}\left(\frac{x - \bar{U}T}{2\sqrt{K_t T}}\right)\right] \tag{2.33}$$

the form of which is shown in figure 2.13. The length of the mixing zone (L_m) grows according to:

$$L_m = 3.625\sqrt{K_L' T} \tag{2.34}$$

where K_L' is the effective longitudinal dispersion coeficient in a capillary.

If condition 2.32 holds the solute zone travels with uniform lateral concentration through the capillary tube at the average velocity of the flow. However solvent molecules at the tube axis are travelling at twice the average velocity because of the parabolic velocity profile in the tube. Therefore these molecules are travelling faster than the solute zone and in fact travel through it. Aris[49] has shown that the effective longitudinal dispersion coefficient (K_L') is given by :

$$K_L' = D_o + \frac{a^2\bar{U}^2}{48D_o} \qquad (2.35)$$

Hence the longitudinal mixing zone is larger than would be expected from diffusion alone and is produced by a combination of the parabolic velocity distribution and lateral diffusion.

Lake and Hirasaki[46] and Marle et al[50] have shown that a dispersive phenomenon analogous to "Taylor dispersion" can occur in stratified porous media. In such a system a transverse velocity profile is produced by each layer having a different conductance. When the time required for convection to transport solute molecules parallel to the layers is large compared to that for transverse microscopic dispersion to damp out lateral concentration variations, a uniform lateral concentration profile is produced. The condition for this to occur is when the transverse dimensionless time (t) is greater than unity,

$$t = \frac{K_t L}{h^2 \bar{U}} \quad . \qquad (2.36)$$

This phenomena, as with its analogy in the capillary tube, produces a longitudinal mixing zone which is larger than

would be expected from microscopic longitudinal dispersion alone. As this will occur at large values of t (> 1.0), it will be refered to in this work as the Long Time Solution.

The effective longitudinal dispersion coefficient (k_{Leff}) which describes this phenomenon has been derived for continuous injection[46,50]. For a dual layer system this is:

$$K_{Leff} = \overline{K}_L + \frac{1}{12}\frac{L\overline{U}}{t}\left[\frac{\frac{C_A}{C_B} - 1}{\frac{C_A}{C_B} + 1}\right]^2 \qquad (2.37)$$

where $\overline{K}_L$ is the thickness-weighted average longitudinal dispersion coefficient. Note the similarity between equations 2.35 and 2.37.

2.4 Capillary Forces.

In the immisicible displacement of oil by water or gas capillary forces play an important role both on the microscopic and macroscopic scales. At the pore scale capillary forces control the distribution of the fluids (eg. residual oil), with the wetting phase adhering to the pore walls and in the crevices at particle contacts[1]. On the macroscopic scale capillary forces may be important at saturation discontinuities, boundaries between media and the outlet end of the system.

When two immiscible fluids co-exist in a porous matrix a discontinuity in pressure exists between the two fluids which depends on the curvature of the interface separating the fluids. This pressure difference is the capillary pressure and by convention defined by:

$$p_c = p_{nw} - p_w \quad . \qquad (2.38)$$

The interfacial curvature itself depends on the interfacial tension, pore geometries, pore sizes and their distribution, and rock wettability. Due to the complex geometry of the pore spaces a simple relationship to combine the pertinent variables which affect capillary pressure has not yet been developed, thus in practice empirical relations between capillary pressure and fluid saturation for the samples of reservoir rock are used. These experimental techniques and the resulting functions have been extensively reviewed in the literature[eg. 6,7,8,9,10,16].

A parameter to correlate the capillary pressure in different sands was suggested by Leverett[51]:

$$J(S) = \frac{p_c}{\gamma}\left(\frac{k}{\phi}\right)^{\frac{1}{2}} \qquad (2.39)$$

and is called the J function. It has been modified by other workers to include the analysis of rocks with different contact angles by the addition of the function, $f(\theta)$ to the denominator. This is sometimes written as Cos θ, but this form only strictly applies to cylindrical geometries and its application to the complex morphology of the porous matrix is questionable.

2.4.1 Macroscopic Scale Effects.

At the effluent end of the system there is a saturation (hence pressure) discontinuity across the outlet. Although the effect of capillary forces differs for the imbibition and drainage cases (wetting fluid saturation increasing and decreasing respectively) the result is the same, a build-up of wetting fluid at the effluent end of the system. This phenomenon is called the end or outlet boundary effect, and has been noted in the experiments reported in chapter nine. The magnitude of this acccumulation decreases with increasing flow rate, reflecting the balance between capillary and viscous forces on this scale.

Another rate dependent capillary pressure effect occurs at the fluid/fluid displacement front, where there is discontinuity in the saturation profile. Douglas et al[52], using a numerical approach, showed that for an imbibition process the steepness of the saturation profile increases with increasing rate (figure 2.15).

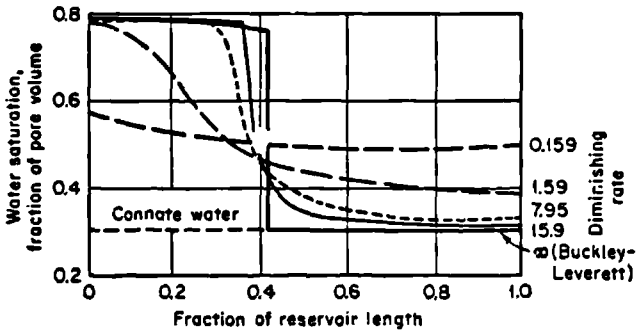

Figure 2.15 Saturation profiles at four different rates showing the effect of capillary pressure[52].

In the limit at infinite rate, when capillary forces can be neglected in comparison to the viscous forces, the Buckley Leverett solution (section 2.1.1) is obtained.

In heterogeneous systems capillary forces can be important at the boundaries between two media (figure 2.16a), if their capillary pressure functions are different (figure 2.16b).

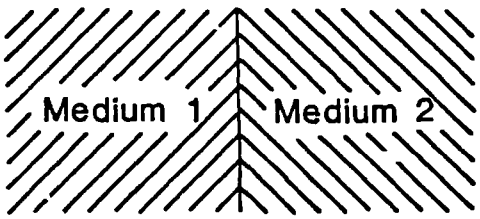

Figure 2.16a Two media in hydrostatic contact.

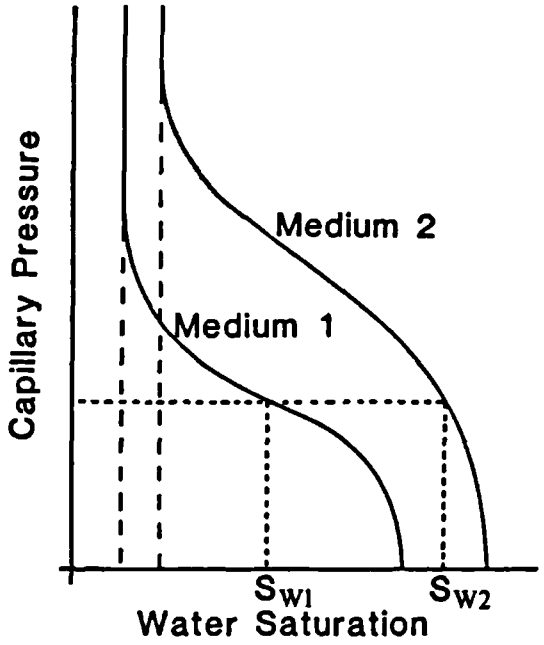

Figure 2.16b Capillary pressure functions for media 1 and 2.

At equilibrium, the wetting fluid saturations within the media differ but are not independent, since by hydraulic continuity they are connected by:

$$p_{c1}(S_{W1}) = p_{c2}(S_{W2}) \quad . \qquad (2.40)$$

If this equilibrium is disturbed (ie. due to flow), the capillary forces will cause a counterflow of fluid between the media to restore equilibrium. Richardson and Perkins[53] observed this effect in a two layered sandpack model during a waterflood. They found that although water tended to advance more rapidly in the more permeable sand, the separation between the fronts in each layer decreased with decreasing flow rate (figure 2.17).

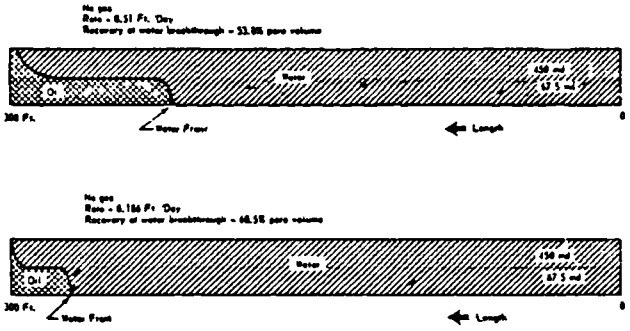

Figure 2.17 The effect of flooding rate in a stratified sandpack during waterflood (ref. 53).

The phase and capillary pressures in each layer for this situation are illustrated in figure 2.18.

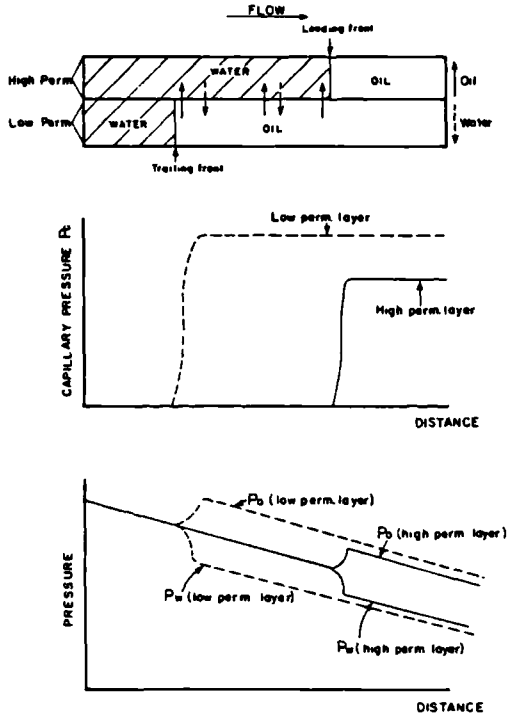

Figure 2.18 Phase and capillary pressure profiles for a dual layer system during waterflood (ref 54).

It can be seen that as the capillary equilibrium has been disturbed there are pressure differences across the system and hence a tendency for fluid to flow counter currently in

such a direction to restore this equilibrium. The rate dependent results obtained by Richardson and Perkins are explained because at a slower rate there is more time for this counter current fluid flow (capillary crossflow) to occur, thus the fronts are brought closer together. Similar experiments in layered and lensed systems will be reported in chapter nine for comparison with the miscible displacement work (chapters four through eight).

Yokoyama and Lake[54] studied this capillary crossflow effect numerically. They defined a transverse capillary number :

$$N_{CT} = \left[\frac{\gamma \cos \theta}{\mu_{eff}} \frac{\bar{k}_H}{(\bar{k}_L \bar{\phi})^{\frac{1}{2}}} \right] \frac{L}{h^2 U} \qquad (2.41)$$

to scale these effects (note similarity to equation 2.36). They found that when N_{CT} was small (value depends on shape of capillary pressure function) capillary crossflow has no effect. However when N_{CT} is large an analogous phenomena to the long time solution for dispersion (section 2.3.5) occurs. Although for the capillary crossflow case the iso-concentration lines are not continuous at the inter layer boundary due to the discontinuity in the capillary pressure.

2.5 Gravitational Forces.

For the work presented in this thesis gravity effects have either been eliminated by the use of matched density fluids (miscible experiments) or minimised by the use of the thin models flooded horizontally (immiscible experiments). But as these effects are important in the reservoir they will be discussed briefly for completeness.

The proportion of the vertical cross-section of the reservoir system that is swept by displacing fluid is influenced primarily by gravity and permeability

stratification. Solvents (miscible gases) are usually lighter than reservoir oils which are in turn less dense than brines and chemical displacing fluids. These density differences can cause fluid segregation with the lighter phase tending to rise to the top of the system and the heavier phase tending to fall to the bottom. Crane et al[55] and Craig et al[56] have both studied homogeneous systems with a small dip. They have shown that when the viscous to gravity force ratio:

$$R_{V/G} = \frac{\Delta p_H}{\Delta p_V} = \frac{VL\mu_{OIL}}{k} \frac{1}{g\Delta\rho H} \qquad (2.42)$$

is small there is severe gravity segregation (gravity tonguing) which leads to early displacing fluid breakthrough. As $R_{V/G}$ increases the magnitude of gravity tonguing decreases, until when $R_{V/G}$ is large the displacement is dominated by viscous forces. For a heterogeneous reservoir with low dip the influence of the gravity forces will be determined totally by the arrangement of the non-uniformities and the displacement rate.

In reservoirs with large dip gravity forces can be used to advantage to stabilize a displacement against gravity tonguing and/or fingering/channelling phenomena, by injecting the displacing fluid updip (if lighter then the resident fluid) and downdip (if heavier then the resident fluid). The necessary conditions for a stable displacement in homogeneous systems have been proposed[23,57] but no such guidelines are currently available for heterogeneous systems.

2.6 Scaled Physical Models.

Laboratory models are very useful for conducting fundamental investigations, studying complex phenomena and verifying numerical techniques. In order to interpret the results from these laboratory models for field or core scale

applications it is necessary that the physical forces under investigation are adequately scaled between the model and prototype. Scaling is achieved through a series of dimensionless parameters, the numerical value of which must be the same for both model and prototype.

There are two basic approaches to formulating scaling parameters. In the first, dimensional analysis, all relevant variables must be recognized and combined into a set of independent dimensionless groups. In the second, inspectional analysis, the mathematical equations describing flow are reduced to dimensionless form, and the coefficients in these equations are used as the scaling parameters. Dimensional analysis often produces groups that do not have a large physical significance for the problem under consideration. While inspectional analysis produces groups whose physical meaning can be apparent, it is based on a mathematical description which must by necessity have simplifying assumptions and therefore may lead to relevant groups being missed. Thus most investigators have proposed to use a combination of these methods.

2.6.1 Scaling in Miscible Displacement.

The appropriate dimensionless groups for miscible displacement have been derived by Pozzi and Blackwell[58] and Geertsma et al[59]. These basic scaling laws may be classified, for convenience, as follows:

1. Groups describing the geometry of the reservoir or large scale heterogeneities (ie. L/H, L/W and the angle of dip θ).
2. A group relating viscous and gravitational forces (i.e. equation 2.42).
3. Some groups describing boundary and initial conditions.

4. Groups relating fluid properties (i.e dimensionless viscosity, density and diffusion coefficient ratios).

5. Some groups to scale the effects of mixing or microscopic dispersion, ie.:

$$\frac{K_L}{UL} \quad , \quad \frac{K_t L}{UH^2} \quad , \quad \frac{K_t L}{UW^2} \quad . \tag{2.43}$$

In practice it is not always possible to scale all these groups simultaneously, as in most cases impractically large models would be required. But for some problems it is permissible to scale only those groups which are believed to significantly affect the process. For example in a gravity stabilized displacement transverse dispersion may be left unscaled, while in displacements dominated by gravity or viscous fingering/channelling (eg. experiments reported in chapters six and seven) the scaling of longitudinal dispersion may be neglected.

2.6.2 Scaling in Immiscible Displacements.

Scaling laws for immiscible displacements have been derived by many authors[eg. 59 through 63]. These include classifications 1 to 4 for miscible scaling plus two additional ones reflecting the immiscible nature of these processes. The extra requirements are:

(a) A group relating capillary and viscous forces, i.e.:

$$R_{C/V} = \frac{(k\phi)^{\frac{1}{2}}\gamma f(\theta)}{VL\mu_{OIL}} \quad . \tag{2.44}$$

(b) The same relative permeability and capillary pressure versus saturation functions.

Bentsen[61], and Perkins and Collins[62] have discussed how relative permeability and capillary pressure functions may be redefined so that requirement (b) may be relaxed.

Carpenter et al[64] used two four layered models of different sizes to show that these scaling laws can be extended to stratified media. Due to the requirement of geometrical similarity both model and prototype must have the same distribution of permeabilities and the scaling laws must be fulfilled between corresponding layers.

2.7 Numerical Simulation - The Problems.

The transport of fluids through a porous medium can be represented mathematically by a set of non-linear second order partial differential equations. As analytical solutions are only available for the simplest cases, it is necessary to use numerical solution methods for reservoir applications. The most commonly used method is the finite difference approximation. Here the reservoir is sub-divided into a mesh (called the grid system), and the partial differential equation is solved numerically for each grid point.

As this method is an approximation to the true solution it suffers from a number of sources of error. The first concerns the definition of grid block properties. The rock properties assigned to each grid block are necessarily assumed either homogeneous and isotropic, or some simple anisotropy may be provided for. In view of the complex geological system involved this idealisation of properties is unrealistic.

Theoretically, the finer the grid mesh, the better the numerical approximation to the exact solution. But since the minimum grid size is limited by computer storage, workers have been compelled to modify some of the rock and fluid properties so that coarser meshes may be used. For this reason several authors[11,12,13] have proposed to reduce the number of grid blocks required by using modified

saturation dependent functions, commonly called pseudo functions. These are derived from fine grid simulations of a small volume of the reservoir. The solution which they produce is limited by how well the physical system can be defined and accuracy of the fine grid simulation.

Numerical dispersion in finite difference simulators results in the profile of the parameter being solved for being more dispersed then the true solution[65,66]. This artificial dispersion is caused by the use of a truncated Taylor series in finite difference approximations. This incurs truncation errors which produce inaccuracies of the same order as the first term neglected from the series[67]. The reduction of numerical dispersion to manageable levels by increasing the number of grid blocks is generally impractical due to the large computer storage and larger run times needed.

There is also a grid orientation effect which causes convergence of the solution to two different answers, depending on whether the grid is oriented parallel or diagonal to the line connecting the injecting and the producing wells. This is due to the five point finite difference formulation (figure 2.19) which dictates that diagonal flow cannot be represented. It is found that the magnitude of this effect increases as the mobility ratio becomes more adverse. One way to overcome this problem is to use a nine point scheme[66], but this is more complex to program and does not extend easily to three dimensions.

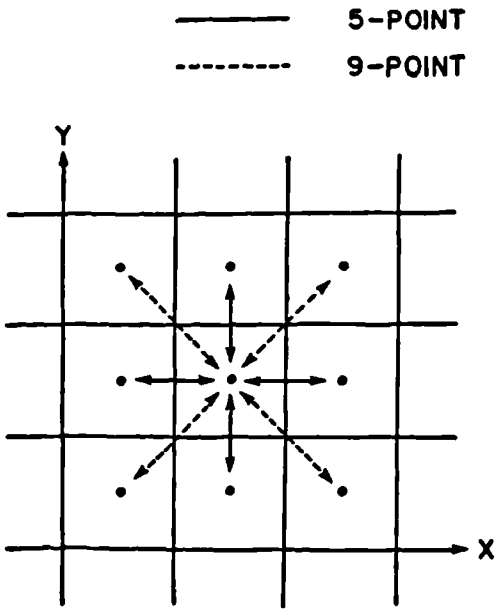

Figure 2.19 Comparison of five and nine point difference schemes.

2.8 Enhanced Oil Recovery.

One of the major disadvantages of using water, and under certain conditions gas, to displace oil from a hydrocarbon reservoir is that these fluids are immiscible leaving even in the swept regions a residual saturation of oil trapped in the pore spaces by capillary forces. The magnitude of this residual saturation can be correlated, as a function of capillary number N_c as shown in figure 2.20.

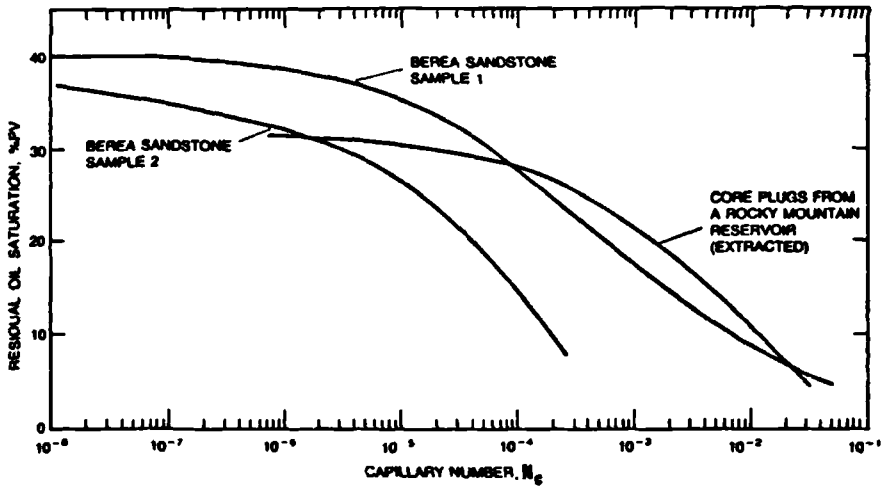

Figure 2.20 Dependence of residual oil saturation on capillary number (after ref. 68).

N_c quantifies the relative importance of viscous and capillary forces on the pore scale. Over the ranges of velocity, oil viscosity and interfacial tension found in conventional water or gas flooding processes the residual oil saturation is insensitive to capillary number. As the displacement velocity and oil viscosity cannot be varied enough to alter the capillary number, to reduce the residual oil saturation to any great extent it is necessary to reduce the interfacial tension by several orders of magnitude. This can only be achieved if the displacing phase is either miscible with the reservor oil or the inherent interfacial tension is very low. Figure 2.20 shows that the relationship between capillary number and residual oil saturation is not an exact function, being highly dependent on the rock system.

When combined with the areal and cross-sectional sweep efficiencies, the low pore scale displacement efficiency means that only in the order of thirty per cent of the original oil in place is produced. The other seventy per cent is the target for Enhanced Oil Recovery processes. Most processes currently proposed do not attempt to alter substantially the sweep and therefore it is the microscopic oil drops that are to be recovered. These processes can be divided into three types: Miscible flooding, Chemical flooding and Thermal recovery (which is out of the range of this thesis). Miscible flooding processes involve the injection of gas which, for the reservoir pressure and temperature, is either first contact or multicontact miscible with insitu fluids. First contact miscible fluids are instantaneously miscible in all proportions, while multi-contact miscible fluids require the mass transfer of components between them to achieve miscibility. Chemical flooding displacing phases are aqueous solutions of either surfactant or polymer or both. Surfactant molecules are intended to reduce the interfacial tension between the oil

and displacing water to an ultra-low level, while polymer molecules increase the displacing phase viscosity and thus improve the areal and cross-sectional sweep efficiencies.

As in all spheres of oil production, economics plays a very important role in Enhanced Oil Recovery. The miscible solvent or chemical to be used will invariably be relatively expensive and to be economically viable a process may have to operate in slug mode. This means that a limited volume of solvent or chemical will be injected which is then displaced either miscibly or immiscibly towards the production wells. If it is displaced immiscibly, the volume in the slug will decrease with time due to a residual saturation being left behind. In a homogeneous system, slug mode processes may be efficient, but as we will discuss in chapters five and seven heterogeneities can severely disrupt the process and lead to low oil recoveries. Due to the high cost of solvent/chemical and extra equipment that might be required, Enhanced Oil Recovery processes require heavy front end investment. This together with the fact that recovered oil is produced late in the project life has meant that the economics of these processes are unfavourable and has led to relatively few being attempted. Infill drilling for some fields could be useful if the non-swept or poorly swept areas can be delineated.

However it is the aspects of fluid flow in heterogeneous porous media that are of interest in this thesis. Various experimental and theoretical models have been used to predict the effects on process performance that might occur during the life of some of these EOR schemes. In particular the mobility ratio and dispersive effects in layered or lensed systems have been considered, mainly in miscible displacements but a detailed but qualitative comparison with the immiscible displacement process is given in chapter 9.

CHAPTER THREE

MODEL CONSTRUCTION AND EXPERIMENTAL PROCEDURE

In this work two-dimensional visual models have been used to study fluid flow in heterogeneous media. Well defined models and fluid systems have been systematically varied to highlight the viscous and dispersive effects which occur. This chapter gives the details of the experimental apparatus and procedures.

3.1 Model Design and Construction.

The flow studies have been performed on glass bead packs bound in a sealed perspex box (figure 3.1). The box consists of two 1.3 cm thick sheets of perspex (the model walls), two end pieces (the shortest edges) and two side pieces (the longest edges). The order of construction is to glue (made by dissolving perspex in chloroform) the two end pieces and one side piece onto one of the model walls and then the other wall is glued on top. The second side piece is removable to allow the model to be packed. This side is sealed with a rubber gasket which is held in place by the removable side piece, a securing strip and a series of screws. The bead pack thickness in all models was approximately 0.6cm and three different plan areas were used (table 3.1). The fluid enters and leaves the model through holes in the end pieces which are separated from the packing by fine mesh gauzes (nylon or brass).

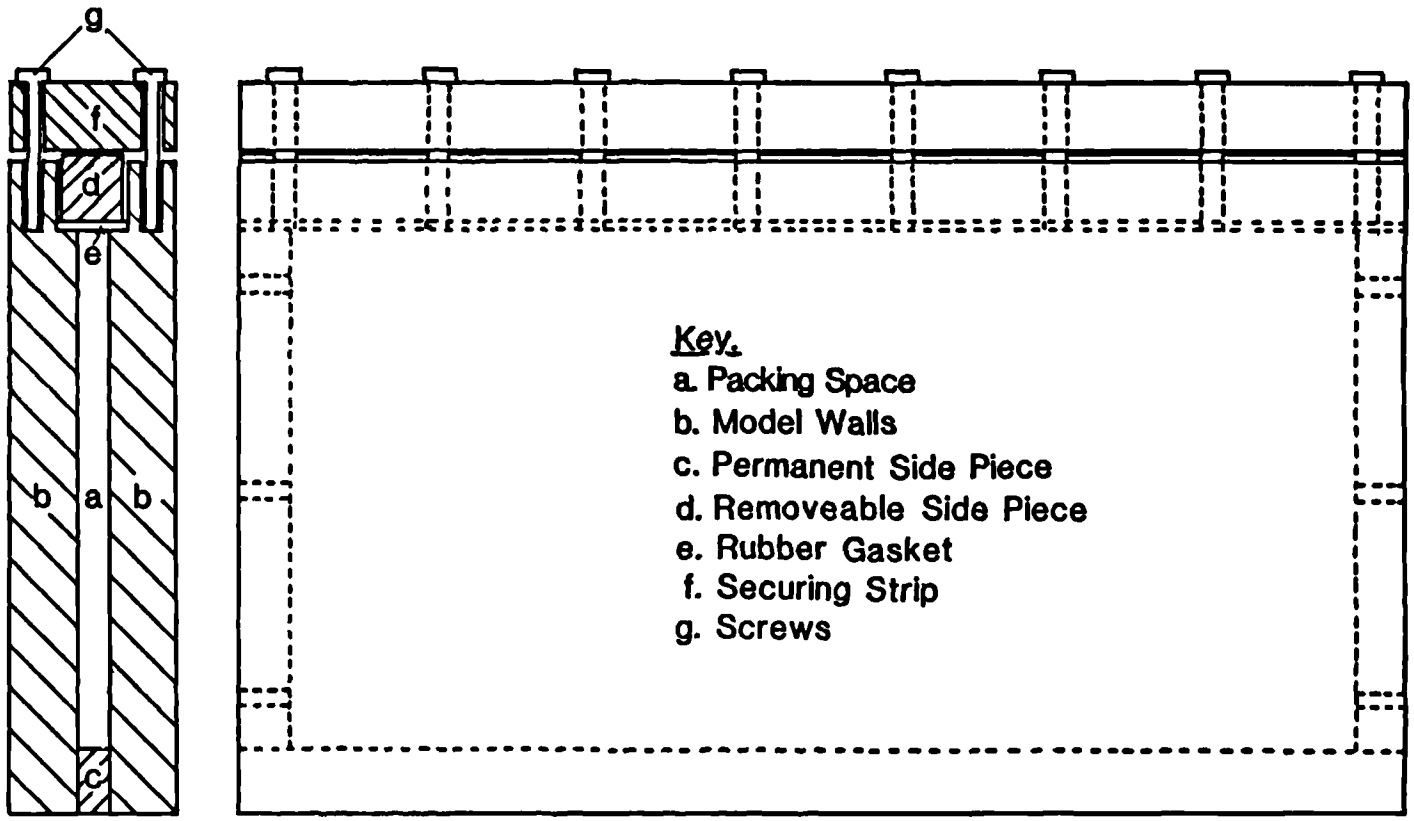

Figure 3.1 Front and cross-sectional end elevation of model type α.

Model type	Dimensions of Packed Volumes (cm)			Model Used in Chapters	Inlet and Outlet Grooves
	Length	Width	Thickness		
α	20.0	10.0	0.6	4,5,8	YES
β	58.0	10.0	0.6	9	NO
γ	57.4	10.0	0.6	6,7	YES

Table 3.1 Model types and dimension.

The models were packed with Ballotini glass beads and the heterogeneous structures (figure 3.2) were produced using beads of different diameters (table 3.2). As the characteristics of the displacements changed slightly each time the model was repacked, every packing has been given a number. In the following text each experimental run will be identified by two numbers separated by a slash (eg. 3/7), where the first number denotes the packing and the second the run. The type of heterogeneity and the experiments carried out on each packing are summarised in table 3.3.

GRADE	SIZE (μm)	
	MINIMUM	MAXIMUM
6	640	750
9	310	425
11	165	255
14	80	105

Table 3.2 Ballotini glass bead sizes.

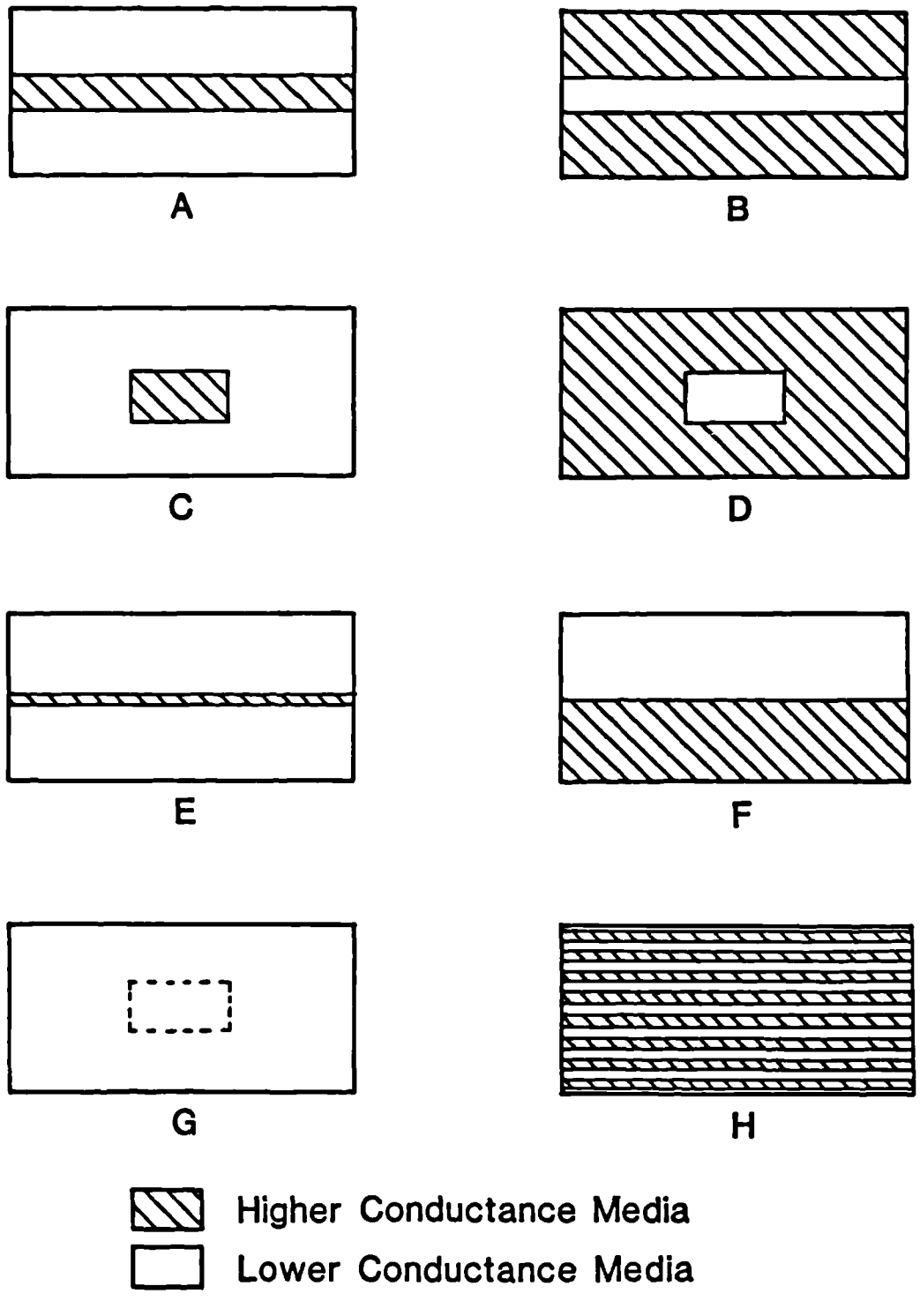

Figure 3.2 Packing patterns used.

PACKING NUMBER	NUMBER OF RUNS	MODEL TYPE	PACKING PATTERN	GRADE OF BEADS USED	CONDUCTANCE CONTRAST	DATA IN CHAPTERS	SIZE OF HETEROGENEITY
1	11	α	A	6 and 9	2.45	4,5	2cm WIDE
2	5	α	C	6 and 9	2.50	8	3cm WIDE 6.67cm LONG
3	11	α	A	6 and 9	2.50	4,5	As 1
5	8	α	E	6 and 9	2.10	4,5	0.5cm WIDE
6	8	α	B	6 and 9	0.385	4,5	As 1
10	9	α	F	6 and 9	2.33	4,5	
11	7	α	A	6 and 9	2.50	4,5	As 1
12	5	α	A	6 and 9	2.70	4,5	As 1
15	7	α	A	6 and 9	2.55	4,5	As 1
16	9	α	D	6 and 9	0.40	8	As 2
20	5	β	C	6 and 9	2.50	9	3cm WIDE 10cm LONG
21	4	β	D	6 and 9	2.50	9	As 20
22	5	β	D	6 and 9	2.50	9	As 21 *
24	9	β	G	9	2.50	9	As 22
25	35	γ	H	11 and 14	3.30	6,7	**
26	6	β	A	6 and 9	2.55	9	As 1
27	5	β	A	6 and 9	2.55	9	As 1

* Lens Beads treated with a water repellent chemical.

** Middle layers 0.6cm wide - layers at edge of packing 0.3cm wide.

Table 3.3 Summary of experiments.

The models were packed in the vertical position with the open side upper-most. The glass beads were carefully dropped into the box and horizontal interfaces created by filling to above the required level and removing excess beads with a suction tube. Care was taken not to disturb the remaining beads. Vertical interfaces (eg. packing patterns C, D and G) were formed by inserting removable baffles. The packing order was then as figure 3.3. The beads used for packing pattern H were smaller than those used for other packings because it was used to investigate the effects of microscopic dispersion. Here in order to scale the results to field conditions it was necessary to minimise axial microscopic dispersion (i.e. in the direction of bulk fluid flow); such dispersion increases with increasing particle size.

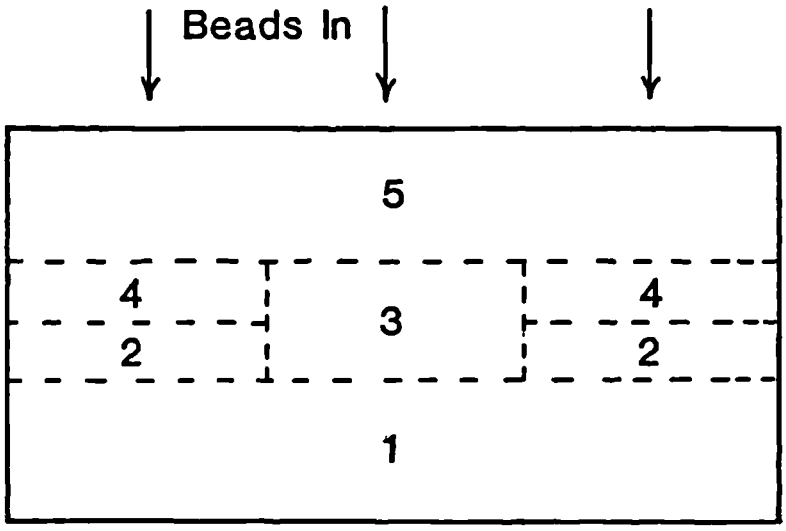

Packing Order:

(i) Pack section 1 and level with suction tube.

(ii) Insert baffles and pack sections 2.

(iii) Pack section 3 and level with suction tube. Also remove 'stray' beads from sections 2.

(iv) Pack sections 4 and level sections 3 and 4 with suction tube.

(v) Carefully remove baffles and pack section 5.

Figure 3.3 Packing order for lensed models.

Two arrangements for the injection and production of fluid have been used. Model types α and γ were used for miscible displacement experiments and contain 3mm thick grooves in each end piece. The packing was constrained 3mm away from the end pieces, producing inlet and outlet ports (figure 3.4).

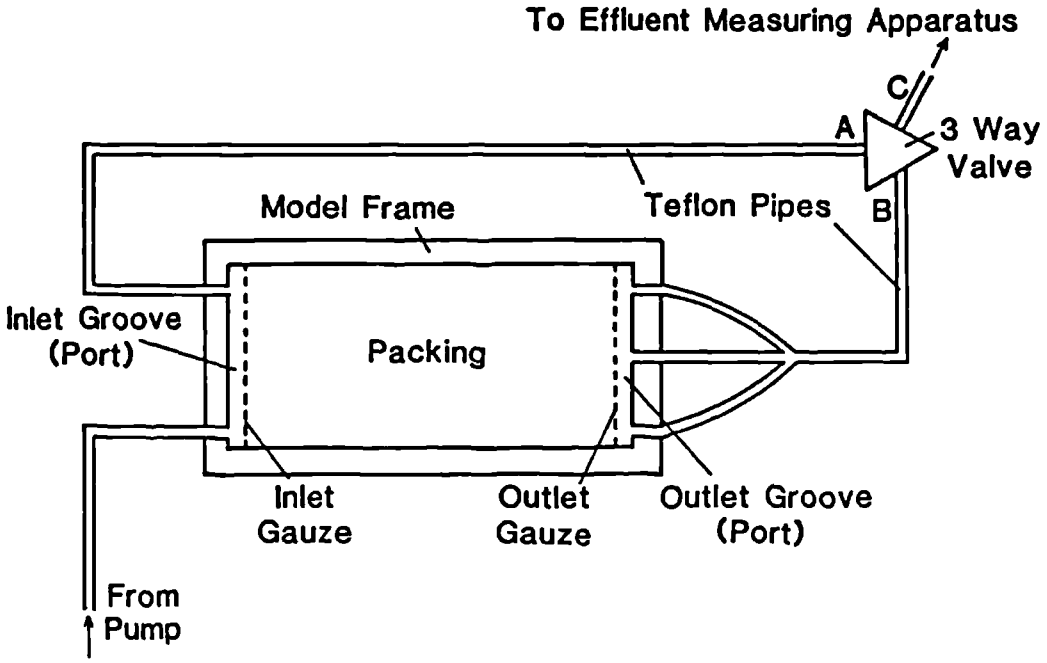

Figure 3.4 Experimental arrangement for miscible displacements.

These allow fluid to be displaced linearly through the model from the inlet to the outlet. The fluids were delivered by a constant rate Altex pump (between 0.05 and 4.0 ml/min) through Teflon tubing (0.5mm id). A three way valve allowed the model to be operated in either of the modes. In

bypass mode (tubes A and C connected, B closed), fluids flowed through the inlet port and bypassed the model. This allowed the inlet port to be filled with displacing fluid. By switching to displacement mode (tubes B and C connected, A closed), fluid was forced to flow through the model and an instantaneous step function change in displacing fluid was introduced. An injection of a slug of fluid was achieved by changing back to by-pass mode after the required slug volume had been injected, changing the fluid in the inlet port and then switching back to displacement mode.

For immiscible displacements (model type β) a modified injection scheme (figure 3.5) was used to overcome the capillary end effect at the boundary between the inlet gauze and the packing.

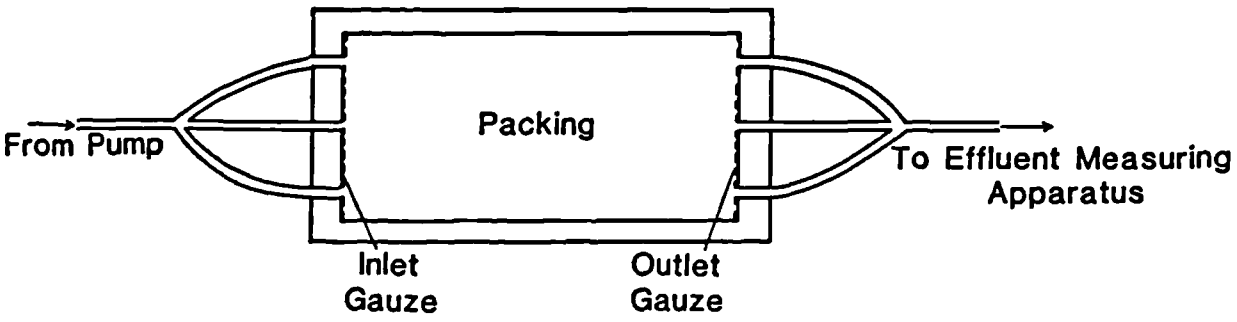

Figure 3.5 Experimental arrangement for immiscible displacements.

In these cases the models had no inlet or outlet ports and fluid was injected directly into the packing. Here the gauzes were fixed along the ends of the model adjacent to the fluid injection holes. In packings 22 and 24 (table 3.3) the wettability of the lenses was altered to oil-wet by treatment with dimethyldichlorosilance.

3.2 Fluid Systems.

The physical properties of the fluid systems used in this project and the reasons for their choice are discussed in this section. All the fluids used in the models were chemically inert with respect to perspex.

3.2.1 Miscible Fluids.

Gravity forces were eliminated in the miscible displacement experiments by matching the densities of displacing and displaced fluids to within 10^{-4} g/cm^3. Glycerol/water mixtures (figure 3.6) were used for the higher viscosity fluids and sodium chloride solutions

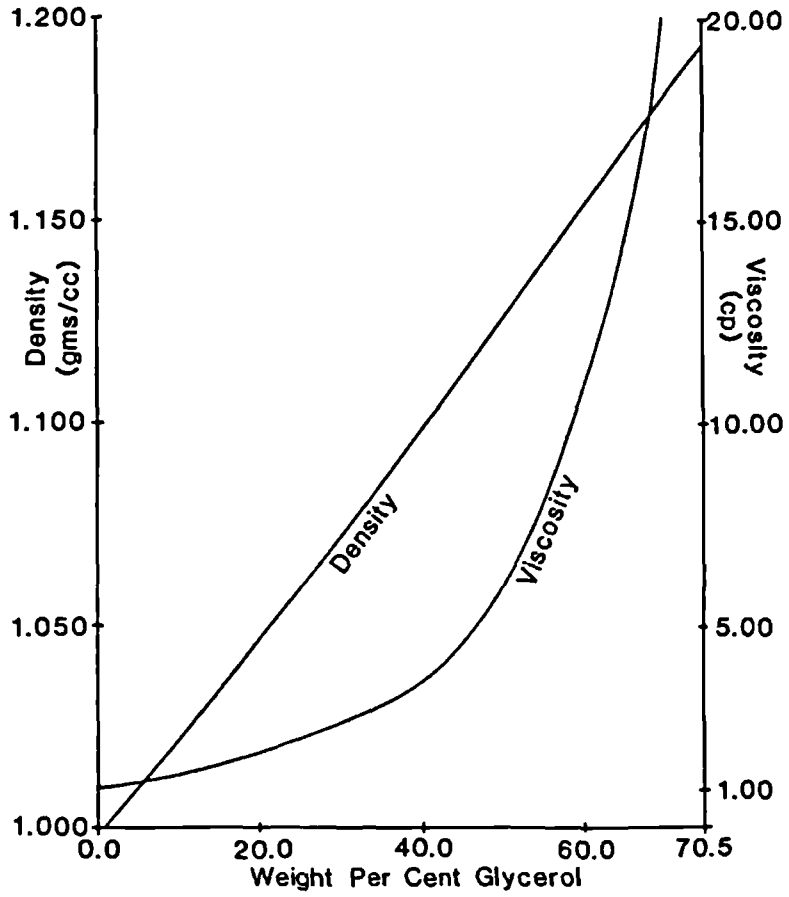

Figure 3.6 Viscosity and density data for glycerol/water mixtures at 20°C.

(figure 3.7) of the same density were paired with them (table 3.4) to provide the lower viscosity fluids.

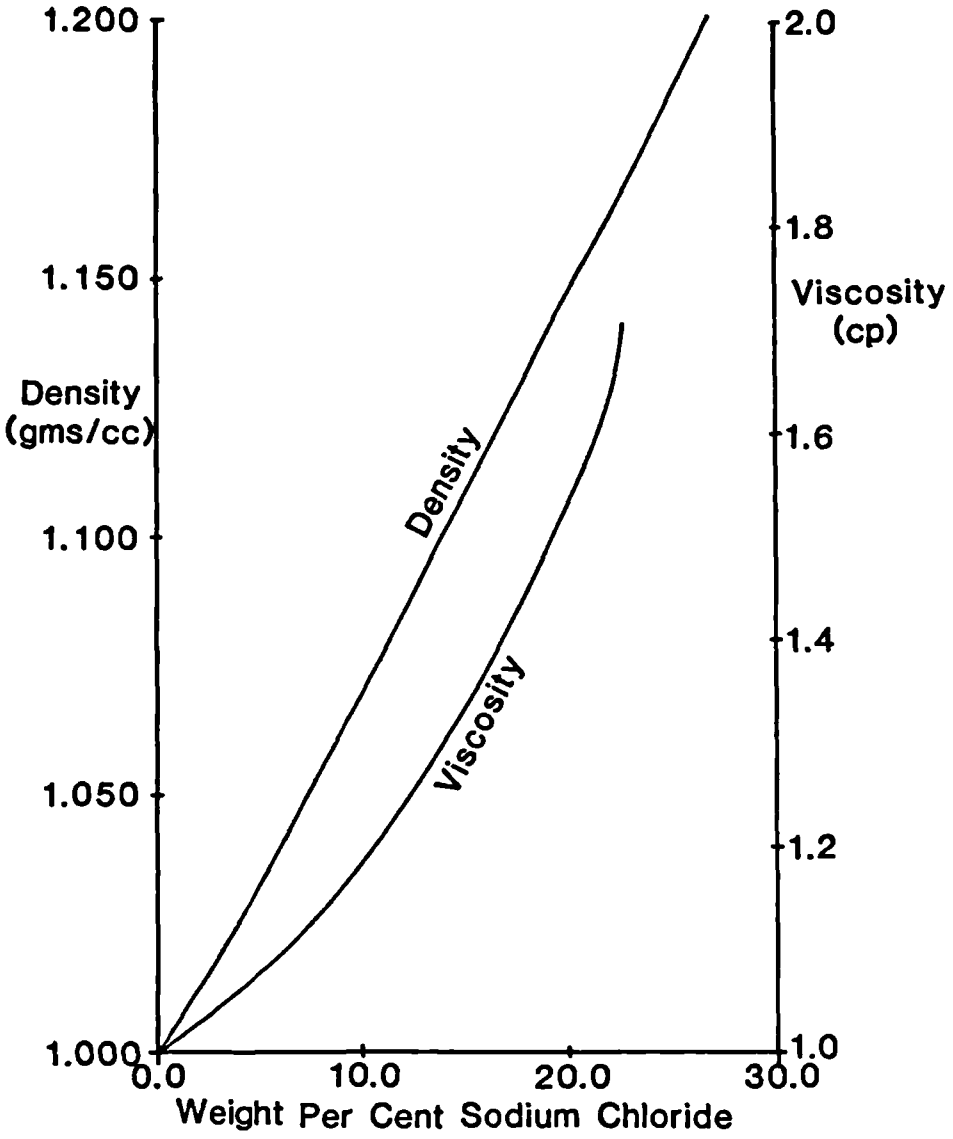

Figure 3.7 Viscosity and density data for sodium chloride solutions at 20°C.

The dispersion studies used sodium sulphate solutions (figure 3 8) for the least viscous fluid because it has a similar diffusion coefficient in water (0.77±0.03 cm^2/sec at 1.0M) as glycerol (0.77±0.03cm^2/sec at 1.0M) and the ultra-violet absorption tracer 2-Nitrophenol (Phenol - 0.84 cm^2/sec at <0.2M). These experiments are summarised in table 3.5.

PACKING NO	RATIO OF VISCOSITY OF GLYCEROL SOLUTION TO VISCOSITY OF BRINE					SLUG MODE EXPERIMENTS
	1.0	1.14	1.70	2.50	3.74	
1	1,2,3	-	-	-	5,6,7 8,9,10 11,12	3,7,9,10,12
2	3,6	-	-	-	4,7,8	3
3			5,6,7 8,9,10 11,12		2,4,1	4,7,8,9,10
5	1,2	7,8	3,4		5,6	2
6	3,4		5,6,7,8		9,10	4,6,8
10	1,2,9				3,4,5 6,7,8	1,4,6,7,8
11	2,6				3,4,5 7,8	3,4,5
12	1		2,3,4,5			2,3,4,5
15	1			2,3,4 5,6,7		ALL RUNS
16	1,2,9			3,4,5 6,7,8		1,2,3,7,8

Table 3.4 Summary of experiments using glycerol and sodium chloride additives.

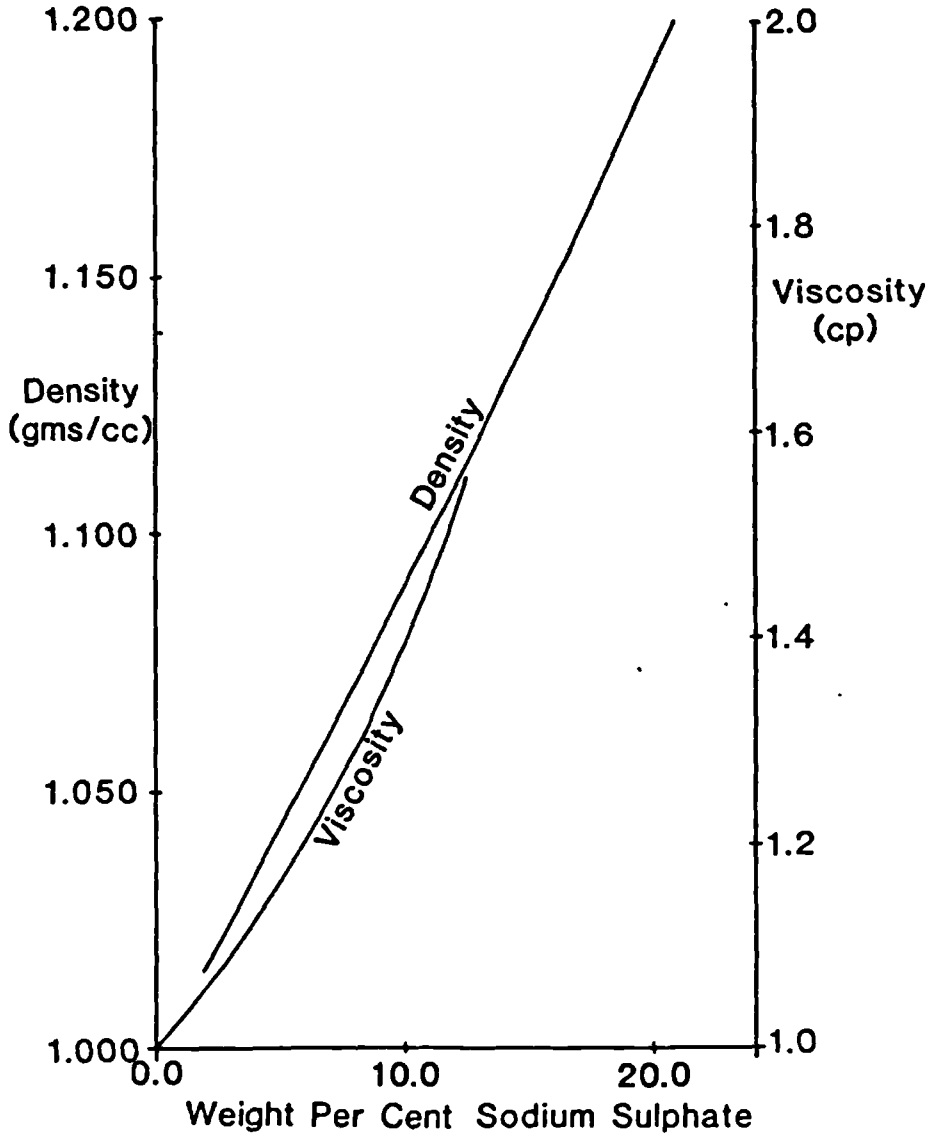

Figure 3.8 Viscosity and density data for sodium sulphate solutions at 20°C.

RUN NO.	RATE (ml/min)	AVERAGE DISPLACEMENT VELOCITY (cm/sec)	INJECTION MODE			MOBILITY RATIO				
			CONT-INUOUS	20% SLUG	40% SLUG	0.5	0.735	1.0	1.36	2
7	3.818	$2.65x10^{-2}$	o					o		
8	0.168	$1.17x10^{-3}$	o					o		
9	0.0833	$5.78x10^{-4}$	o					o		
10	3.297	$2.29x10^{-2}$			o			o		
11	0.172	$1.19x10^{-3}$			o			o		
12	0.0516	$3.59x10^{-4}$			o			o		
13	0.163	$1.13x10^{-3}$		o				o		
14	3.810	$2.65x10^{-2}$		o				o		
15	0.518	$3.60x10^{-4}$		o				o		
16	3.790	$2.63x10^{-2}$	o						o	
17a	3.854	$2.67x10^{-2}$	o				o			
17b	0.0502	$3.48x10^{-4}$	o						o	
18	3.815	$2.65x10^{-2}$	o							o
19	3.864	$2.68x10^{-2}$	o			o				
20	0.171	$1.18x10^{-3}$	o							o
21	0.121	$8.38x10^{-4}$	o			o				
22	0.983	$6.83x10^{-3}$	o					o		
23	0.411	$2.85x10^{-3}$	o					o		
24	0.157	$1.09x10^{-3}$	o			o				
25	0.0519	$3.60x10^{-4}$	o							o
26	0.0555	$3.85x10^{-4}$			o	1				2
27	0.0379	$2.63x10^{-4}$	o			o				
28	3.357	$2.33x10^{-2}$			o	2				1
29	3.700	$2.57x10^{-2}$	o							o
30	3.621	$2.51x10^{-2}$			o	1				2
31	0.173	$1.20x10^{-3}$			o	2				1
32	0.0552	$3.83x10^{-4}$			o	2				1
33	0.0932	$6.47x10^{-3}$	o							o
34	0.172	$1.20x10^{-3}$			o	1				2
35	0.0934	$6.48x10^{-3}$	o			o				

1 - Leading front

2 - Trailing front

Table 3.5 Summary of dispersion sensitive experiments.

3.2.2 Immiscible Fluids.

In the immiscible displacement experiments a refined oil soltrol (density = 0.760 g/cm^3, viscosity = 1.565 cp at 20^{o}C) was used as the oil phase. As the density of the oil and water phases differed, these experiments (table 3.6) were conducted horizontally to minimize the influence of gravity forces.

3.2.3 Dye Systems.

At least one fluid in each experiment contained a dye to allow the displacement front(s) to be followed photographically. Preliminary tests showed that there were problems with the water soluble dyes adsorbing onto the surfaces of the glass beads. Two levels of adsorption were encountered. Permanent adsorption which left the model with discoloured beads after it had been washed out with clear fluids, and temporary adsorption which caused the dye front to lag behind the fluid/fluid displacement front. These phenomena were affected by the pH of the aqueous fluids, which after contact with the packed bed was alkaline (pH $\simeq$ 10). Washing the model with 0.1M hydrochloric acid followed by distilled water reduced the adsorption tendency. Trails with Methylene Blue and Carbolan Green G125 showed that they temporarily adsorbed even after this treatment, but Lissamine Scarlet 3B 100 (also called Kenacid Red) was suitable for the aqueous solutions at a concentration of 0.02g per 100g of fluid. Unfortunately this dye salted out in sodium chloride solutions, so it was only possible to dye the higher viscosity glycerol solutions.

PACKING NUMBER	RUN NUMBER	WATER(W) OR OILFLOOD(O)	RESIDUAL SATURATION	END POINT MOBILITY RATIO	RATE (10^{-2} cc/sec)
20	1	O	Yes	0.769	6.67
	2	W	Yes	1.300	1.0
	3	W	No	1.080	6.67
	4	O	Yes	0.769	6.67
	5	W	Yes	1.300	6.67
	6	O	No	0.530	6.67
21	1	O	No	0.530	6.67
	2	W	Yes	1.300	6.67
	3	O	Yes	0.769	6.67
	4	W	No	1.080	6.67
22	1	O	No	0.530	6.67
	2	W	Yes	1.300	6.67
	3	O	Yes	0.769	6.67
	4	W	No	1.080	6.67
24	2	O	No	0.530	6.67
	3	W	Yes	1.300	6.67
	5	W	No	1.080	6.67
	6	W	No	1.080	6.67
	7	O	Yes	0.769	6.67
	8	O	Yes	0.769	6.67
26	2	O	No	0.530	1.67
	3	W	Yes	1.300	1.67
	4	O	Yes	0.769	1.67
	5	W	Yes	1.300	6.67
	7	W	No	1.080	1.67
27	1	O	No	0.530	6.67
	2	W	Yes	1.300	6.67
	3	O	Yes	0.769	6.67
	4	W	Yes	1.300	0.5
	5	O	Yes	0.769	0.5

Table 3.6 Summary of immiscible displacement experiments.

In the immiscible experiments there were no problems with oil soluble dyes adsorbing. Waxoline Red O and Waxoline Blue AP-FW dyes were used at a concentration of 0.02g and 0.01g per 100g of fluid respectively.

3.3 Experimental Procedure.

After packing, the model was filled with water. To stop air entrapment,carbon dioxide gas was first passed at low pressure through the packed bed to displace the air. In order not to over pressurize the model a head of water (~20cm) was placed in the line between the gas cylinder and the model. Degassed water was then passed into the bed, which displaced and absorbed the carbon dioxide (all aqueous fluids were degassed by boiling or vacuum before use). During water injection the exit end of the model was raised to above the inlet level, thus, enabling gravity segregation to achieve a uniform saturation. Before an experiment was attempted the glass beads in the model were treated with 0.1M hydrochloric acid followed by distilled water to reduce the dye adsorption tendency; as discussed in the previous section.

The movement of the displacement fronts were followed photographically. Model type α was used in the vertical position; the camera photographed light transmitted through the model from a rear tungsten light (positioned behind). The majority of these experiments were recorded on tungsten film (ASA 160) to avoid colour distortion, but in the earlier experiments daylight film (ASA 200) was used which produced a yellow tint. Model types β and γ were used horizontally, suspended over a white light lightbox. The camera was held by a tripod above the model and daylight film was used. In all the experiments the area surrounding the model was blacked out. The time was recorded on each photograph by positioning a stop watch near the model and

illuminating it with a thin light beam from behind the camera.

It was necessary to determine the conductance contrast for each packing because of the small random packing variations. For the layered packings this was calculated from the relative frontal propagation in an equiviscous displacement (table 3.3). In lensed packings this was not possible due to the extra streamline distortion that occurred at the lens boundaries (as discussed in chapter eight). For these packings the conductance contrast was taken to be that calculated from the porosities (section 3.5.1) and absolute permeabilities (section 3.5.2); which gave a conductance contrast of 2.5.

3.4 Effluent Measurement.

Three methods of effluent concentration monitoring have been used during this project.

3.4.1 Ultra-Violet Absorption.

In the dispersion sensitive experiments (chapters six and seven) the concentration of the effluent stream was monitored continuously with an ultra-violet absorption meter. A 0.3×10^{-3} M solution of 2-nitrophenol was used as a tracer in one of the fluids and the absorption was measured at a wavelength of 400nm. As 2-nitrophenol absorbs best in alkaline solution, fluids were set to pH 12. A linear relationship was found between absorption and tracer concentration.

3.4.2 Colorimetry.

Non-continuous concentration data was obtained by analysing 0.5 ml effluent samples with a colorimeter. In

experiments 11/6,7,8 and 16/5,6,7 lissamine scarlet dye (0.005g per 100g of fluid) was used as a tracer with a green filter (number 540). Two calibration curves (figure 3.9) were necessary; one for when the dye was dissolved in pure water and one when dissolved in glycerol solution.

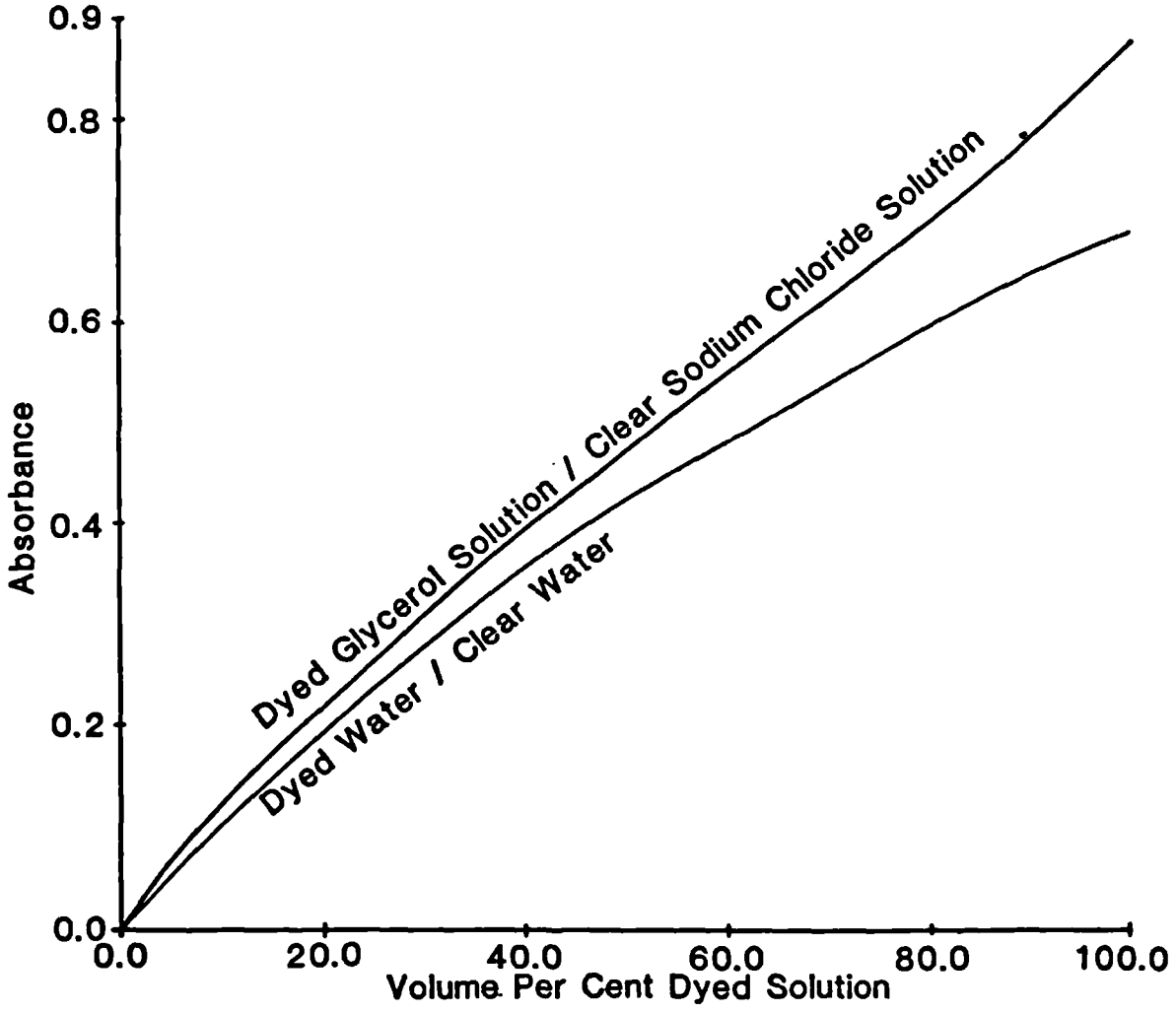

Figure 3.9 Colourimetric calibration curves for lissamine scarlet dye and a green filter (number 540).

3.4.3 Refractive Index Measurement.

Experiments 11/7,8 and 16/5,6 were non-unit viscosity ratio displacements. The effluent stream in these runs was additionally monitored for refractive index variations. The

calibration curve is given in figure 3.10. Effluent stream samples were taken at regular intervals during the displacements.

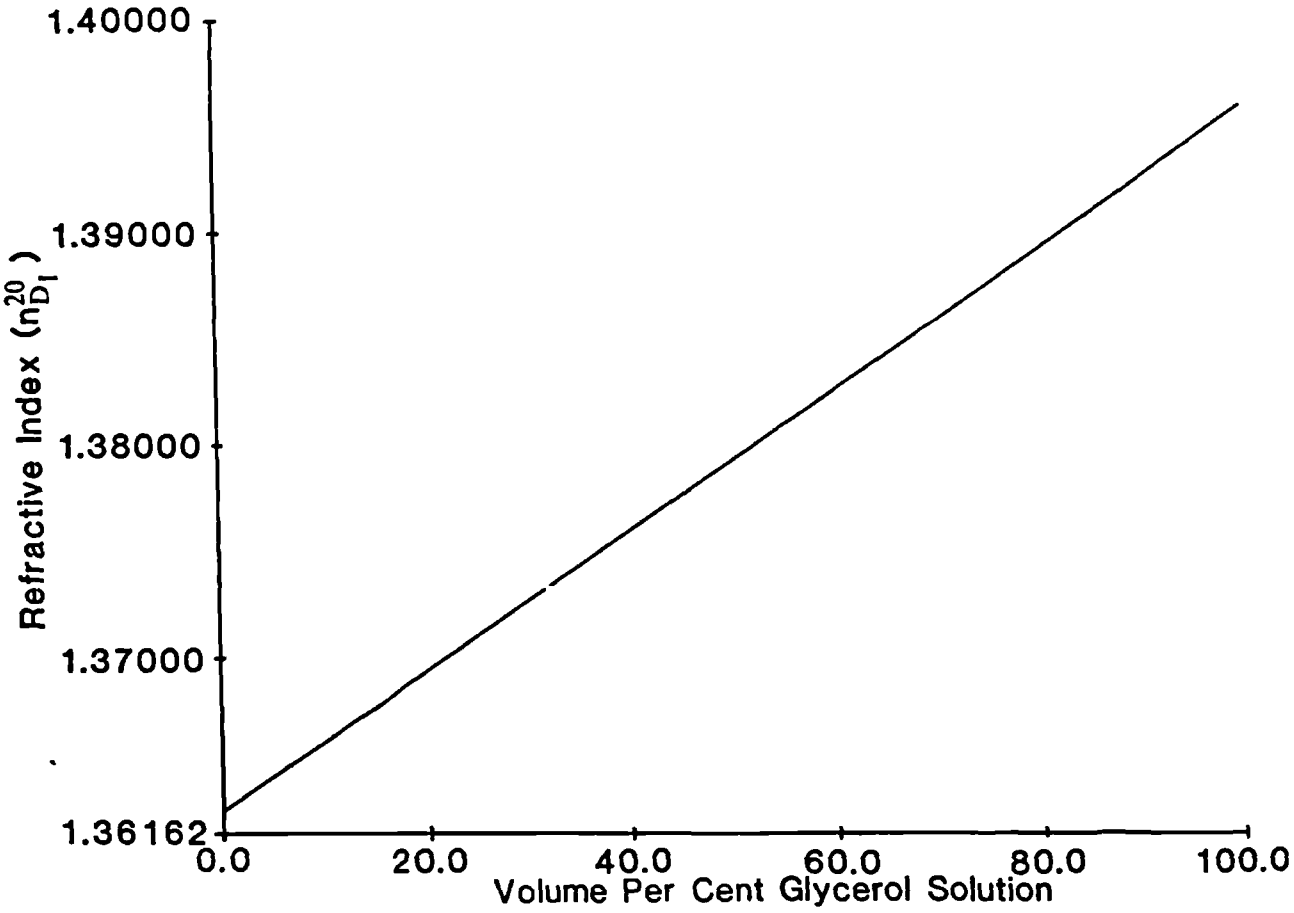

Figure 3.10 Calibration curve for refractive index measurement.

3.5 Model and Fluid Property Measurement.

3.5.1 Porosity.

The pore volume and porosity of the packed models was obtained by weighing the model before and after packing and during water filling. A value of 40% ± 2% was obtained for the porosity of all the grades of beads used.

3.5.2 Absolute Permeability.

The absolute permeabilities of glass bead grades 6 and 9 were determined by filling model type β separately with a single grade of bead. The pressure drop was then determined with a strain gauge transducer for various flow rates. The absolute permeability was then calculated from the slope of the flow rate versus pressure drop by Darcy's law:

k (Ballotini grade 9) = 144 D

k (Ballotini grade 6) = 360 D

3.5.3 Residual Saturations and Effective Permeabilities in Immiscible Displacements.

The residual saturations to both soltrol and water were obtained from a material balance over the system when displaced fluid was no longer produced. Once residual saturation was obtained, the end point effective permeability was determined by measuring the pressure drop at various flow rates and the end point relative permeability obtained. The residual saturation and relative permeability values obtained were, within experimental accuracy, the same for both grades of bead and were:

Residual saturation to soltrol = 0.11 ± 0.01 PV.

to water = 0.07 ± 0.01 PV.

End point relative permeability for soltrol = 0.83 ± 0.03

for water = 0.69 ± 0.03

3.5.4 Capillary Pressure.

The drainage and imbibition curves for the water-wet glass beads (grades 6 and 9) were measured for the water/soltrol system (figure 3.11), by the method detailed in appendix one. These measurements were converted to soltrol/water values by:

$$\left[\frac{p_c}{\gamma \cos \theta}\right]_{AIR/WATER} = \left[\frac{p_c}{\gamma \cos \theta}\right]_{SOLTROL/WATER} \qquad (3.1)$$

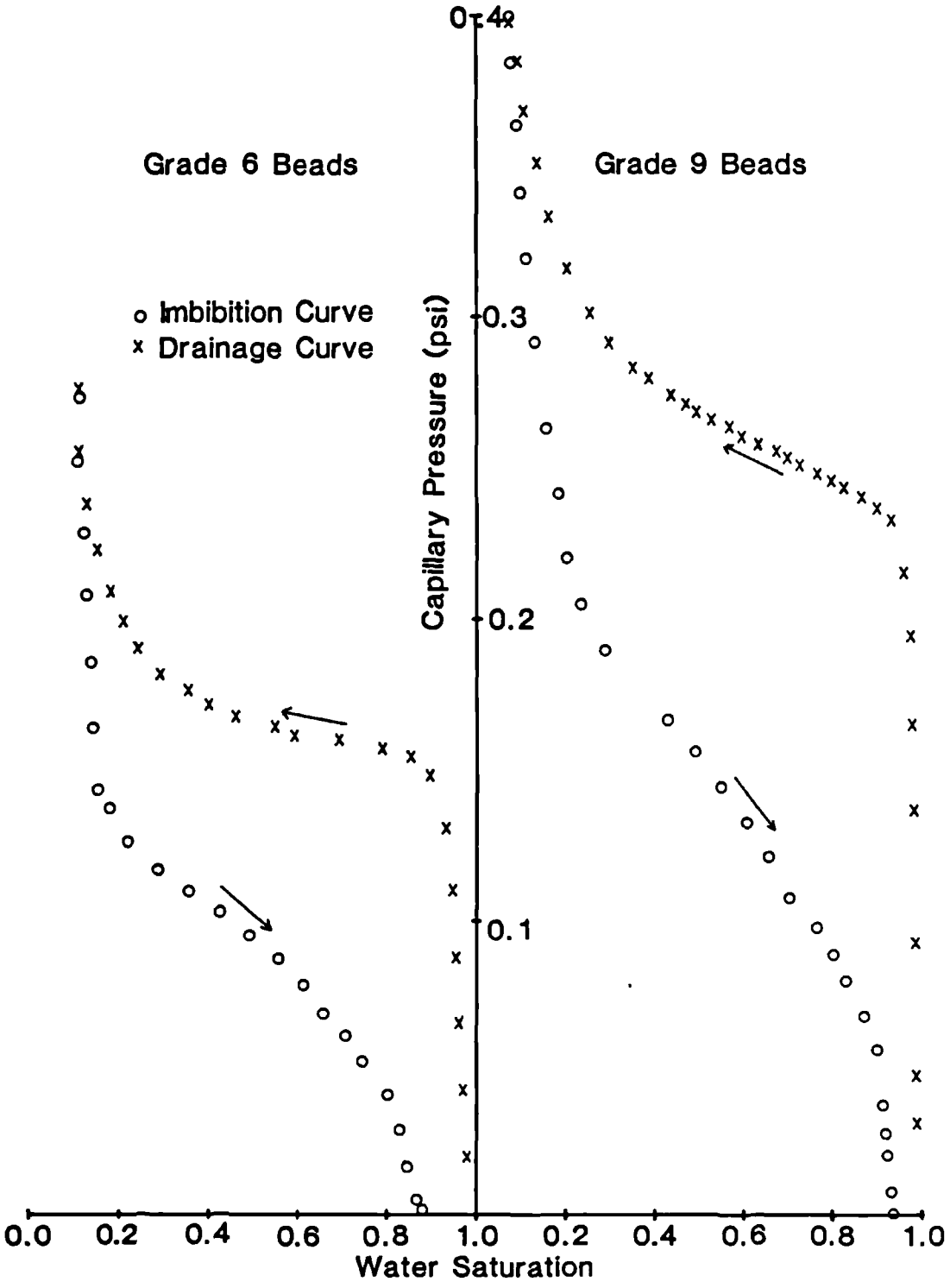

Figure 3.11 Water/soltrol capillary pressure curves for Ballotini glass bead grades 6 and 9.

where γ and θ values have been obtained by the methods detailed in appendix one.

CHAPTER FOUR

VISCOUS CROSSFLOW IN LAYERED SYSTEMS WITH MISCIBLE FLUIDS

In chapter two we discussed the fluid/matrix and fluid/fluid interactions which influence sweep efficiency in heterogeneous systems. In miscible processes gross fluid movement is governed by the gravitational and viscous forces and dispersion phenomena. This chapter investigates stratified systems, with negligible gravitational forces.

In section 2.2.2 the frontal propagation rate in each layer was shown to depend on fluid mobility ratio, conductance contrast between the layers and lateral pressure communication across the interlayer boundary. When the layers are separated by an impermeable barrier (hence no pressure communication) the frontal propagation rates are given by equation 2.9. A number of reservoir performance prediction methods use this approximation[32,33], however these rates must be modified when finite communication exists and fluid can transfer between the layers. Here characteristic frontal geometries are generated by viscous crossflow. In this chapter the results from laboratory experiments for systems with a wide range of layer widths and mobility ratios are presented to improve the understanding of this mechanism. They are used to test methods for predicting relative frontal propagation given in section 2.2.2 for continuous injection processes. Modifications to the method given by Wright and Dawe[37] allows the determination of post breakthrough behaviour and the quantitative prediction of the complex fluid/fluid interfacial shapes.

4.1 Equal Mobility Ratio Displacements.

When both the displacing and displaced fluids have the same mobility (eg. orange water displacing green water) the fronts propagate in proportion to the conductance contrast between the layers (figure 4.1). Here the fluid/fluid interfacial geometry is rectangular and conforms to the inter-layer boundary. Under certain conditions, which will be discussed in chapters six and seven, the fronts can be modified by microscopic dispersion.

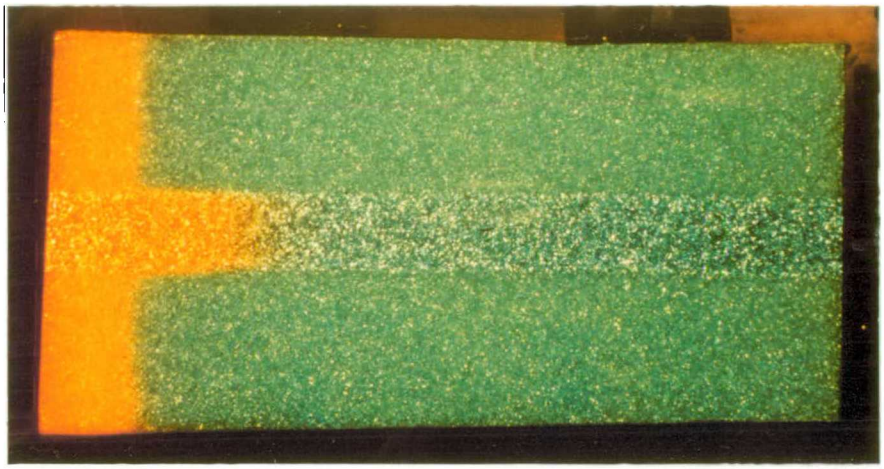

Figure 4.1 Photograph of equiviscous displacement (run 1/3).

The proportion of a dual layer system swept when fluid breakthrough occurs in the high conductance layer is given by:

$$E_{BT} = b + \frac{(1-b)C_B}{C_A} \qquad (4.1)$$

where b denotes the fraction of the model that is high conductance medium. Figure 4.2 shows that when the conductance contrast gets large, very little of the low conductance layer is swept at breakthrough, and E_{BT} tends towards the volume of the high conductance layer. The total amount of injection fluid required to sweep the whole system

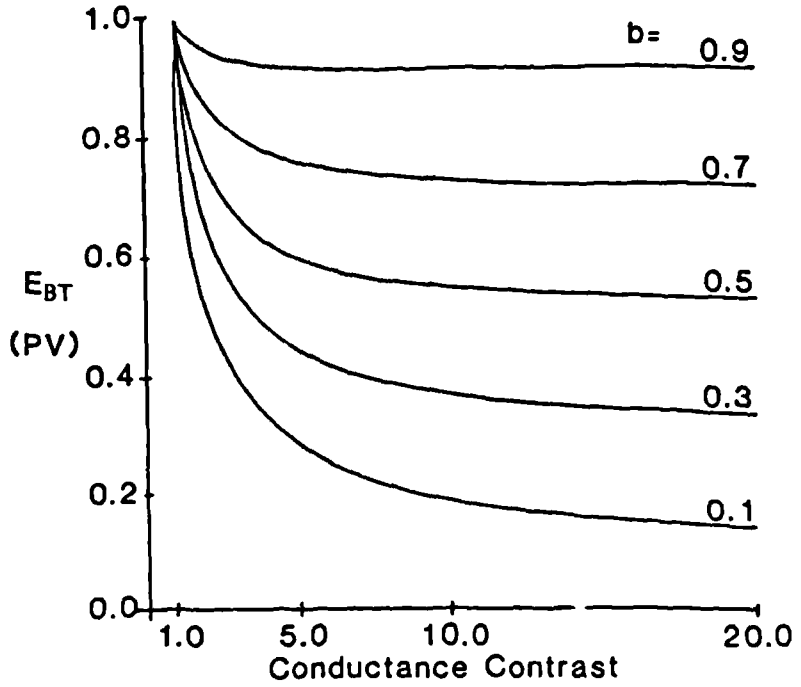

Figure 4.2 Graphical representation of equation 4.1 (M=1.0).

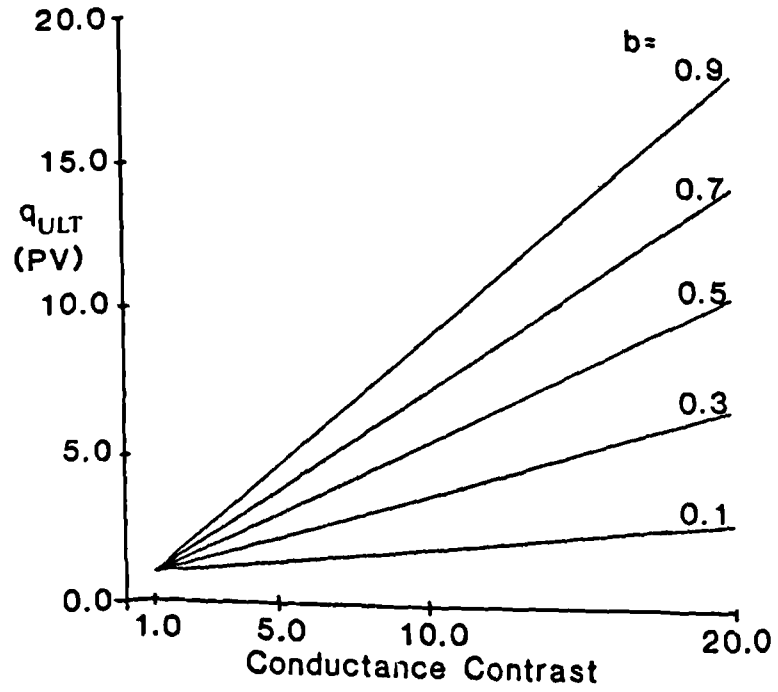

Figure 4.3 Graphical representation of equation 4.2 (M=1.0).

(q_{ULT}) is given by:

$$q_{ULT} = (1-b) + \frac{bC_A}{C_B} \qquad (4.2)$$

Figure 4.3 shows that even for a moderate degree of heterogeneity (eg. $C_A/C_B \sim 5.0$) large volumes of fluid are needed.

Although it is theoretically possible to sweep the whole system with di placing fluid, practically there will be an upper limit on the proportion of displacing fluid in the effluent stream (F_D), above which the process will become uneconomic. For a dual layer system:

$$F_D = \frac{b}{b + \frac{C_B(1-b)}{C_A}} \qquad (4.3)$$

Figure 4.4 shows that unless the high conductance media is only a small fraction of the total system width, F_D will be greater than 0.85.

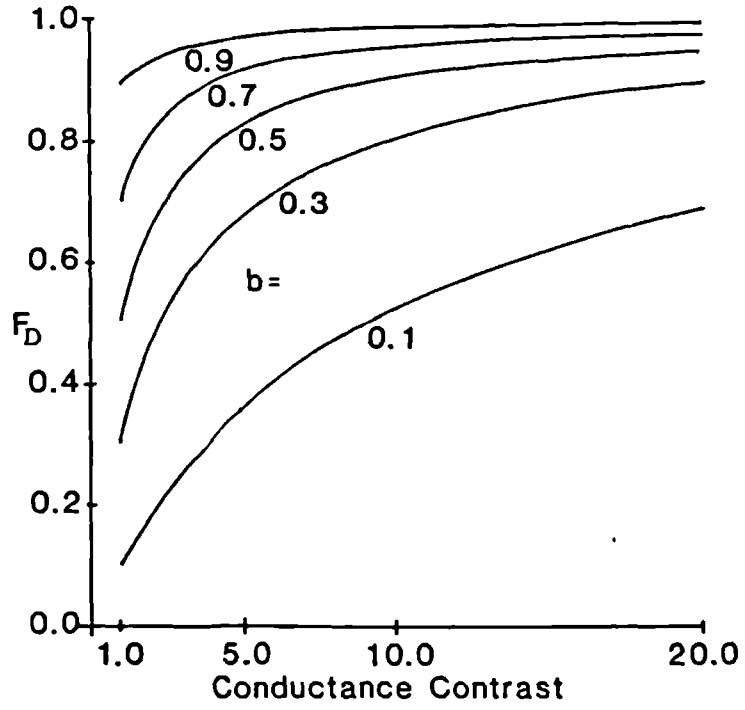

Figure 4.4 Graphical representation of equation 4.3 (M=1.0).

4.2 Non-Unit Mobility Ratio Displacements.

Chemical and miscible Enhanced Oil Recovery (EOR) processes are unlikely to have unit mobility ratios. For instance surfactant floods will often have unfavourable mobility ratios, particularly when initiated at the tertiary stage. This is due in part to the higher relative permeability of the rock to the surfactant behind the oil displacement front than that at the secondary stage. The addition of polymer to the chemical solution reduces this mobility by increasing its viscosity, but for economic reasons only a small slug of polymer thickened solution can be used. This must finally be displaced by a cheap fluid, usually water, which has a high mobility. Unfavourable mobility ratios are also likely to occur in miscible displacements due to the low viscosity of the solvents (eg. LPG).

Consider two layers separated by a no-flow boundary (figure 2.5). If the mobility of the displacing fluid differs from that of the displaced fluid the axial pressure profiles in the two layers will be different (figure 2.7a and b). This causes the relative frontal advance for the favourable case to be less than the unit mobility ratio case, and for the unfavourable case to be greater (figure 4.5).

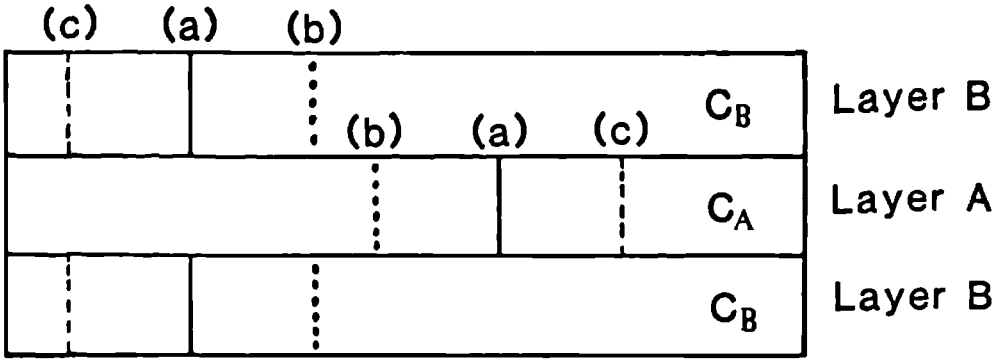

Figure 4.5 Stratified system ($C_A > C_B$) showing the effect of mobility ratio on the relative frontal advance.

(a) M=1, equal mobility case.

(b) M<1, favourable mobility ratio case.

(c) M>1, unfavourable mobility ratio case.

There will be lateral pressure differences between the layers due to the unequal axial pressure gradients (figure 2.7a and b). Therefore if the no-flow barrier is removed there is a tendency for fluid to transfer between the layers. The direction of this transfer is illustrated in figure 4.6. Due to the intra-layer instabilities (fingering) that occur in unfavourable displacements, the fluid which crossflows at the fronts in this case is a mixture of displaced and displacing fluids.

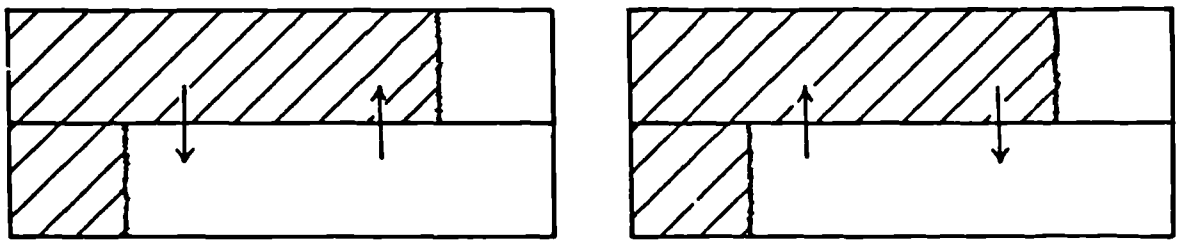

(a) Favourable case. (b) Unfavourable case.

Figure 4.6 Direction of viscous crossflow.

This transfer of fluid between layers alters the relative frontal separation compared to the no crossflow case and modifies the fluid/fluid interfacial geometry (figure 4.7) compared to the unit mobility case (figure 4.1). The pointed nature of the favourable displacement front and the 'bulbous' nature of the unfavourable displacement front have been shown in the experiments reported here to be characteristic of these cases.

Figure 4.7b shows that for the unfavourable case relatively little of the low conductance layers have been swept compared to the high conductance layer even though there are only moderate conductance (2.45) and mobility (3.74) contrasts. This is because although fluid initially enters both layers in proportion to the conductance contrast, the transverse pressure field causes fluid to crossflow out of the low conductance layer. Therefore for a large conductance contrast and an unfavourable mobility ratio, very little of the low conductance layer would be flooded. Conversely for a favourable displacement (figure 4.7a) crossflow acts to bring the fronts in the layers closer together. Thus favourable viscous crossflow could be used to stabilize a displacement front against the effects of heterogeneity in a layered system.

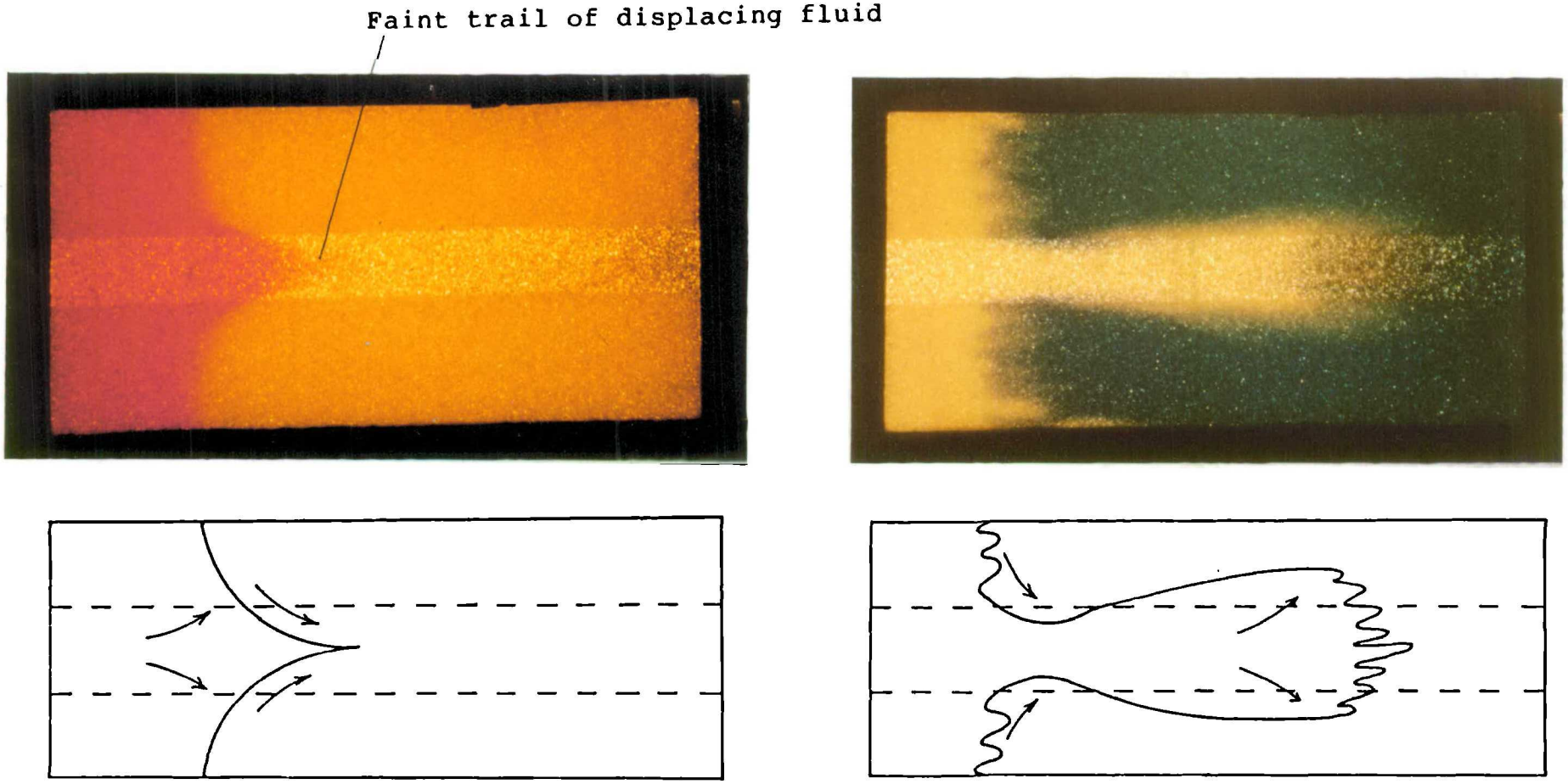

(a) Favourable mobility ratio displacement (run 1/8).

(b) Unfavourable mobility ratio displacement (run 1/6).

Figure 4.7 Experimental photographs and schematic diagrams of non-unit mobility ratio displacements.

4.2.1 Favourable Mobility Ratio Displacements.

Three values of the layer width (h) to system length (L) ratio (h_D=0.025, 0.1 and 0.5) have been used to study viscous crossflow. The experiments are summarised in table 4.1.

Packing number	$\frac{C_A}{C_B}$	h_D	Experimental run Mobility ratio								
			0.267	0.4	0.588	0.877	1.0	1.14	1.7	2.5	3.74
1.	2.45	0.1	8,12				1,2,3				5,6,11
3.	2.5	0.1		12	5,7				9,6	11	1,2,4
5.	2.1	0.025	5		3	8	1,2	7	4		6
6.*	2.6	0.1	9		5		3,4		7		10
10.	2.33	0.5	3,7				1,2,9				5,8
11.	2.5	0.1	8				2,6				7

* This model differs from the other in that it has a central low conductance layer.

Table 4.1 Summary of experiments used to investigate unit and non-unit mobility ratio displacements.

The effect of varying h_D on the characteristics curves of the favourable displacements are illustrated in figure 4.8. As the layer width decreases relative to the system length (ie. h_D decreases) the effect of viscous crossflow becomes more favourable (ie. the frontal separation (X_A - X_B) decreases). As the majority of hydrocarbon reservoirs are relatively long compared to their thickness, practical values of h_D will lie below 0.1. Larger values may characterize systems where the lateral pressure communication is impaired (eg. due to non-continuous shale streaks).

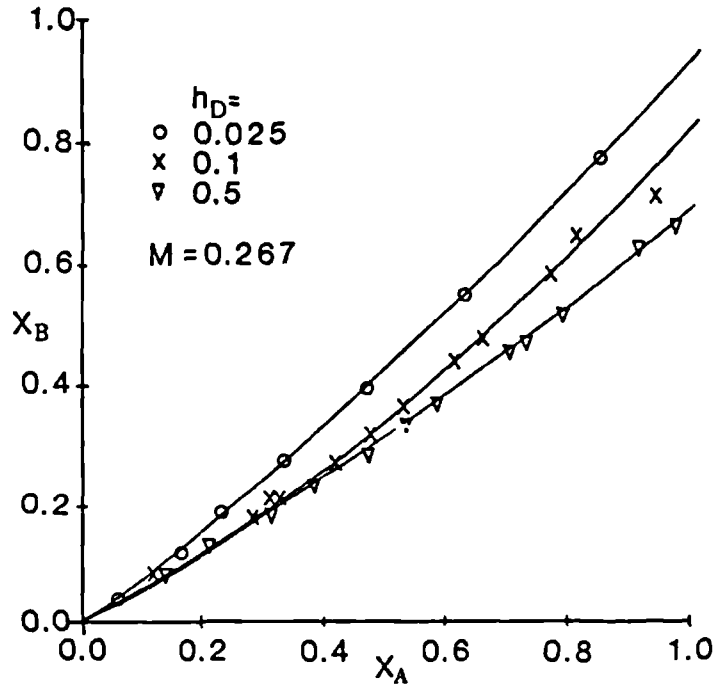

Figure 4.8 Effect of h_D on the characteristic curves for a favourable displacement (M < 1.0).

The experimental characteristic curves for the favourable mobility ratio displacements are presented in appendix two. In all cases it can be seen that the frontal separation is less than the unit mobility ratio case for the entire displacement. Comparison with curves predicted for finite crossflow[37], discussed in section 2.2.2, shows quantitative agreement to be good for the early stages of the displacement, but that predicted values of the frontal separation are too small during the later stages. This discrepancy is because the mathematical model was developed for the cases involving large frontal separation and does not take into account the interaction by the crossflow forces of two adjacent displacement fronts. Nevertheless it still gives much closer agreement with our experimental results than either the no-crossflow or vertical equilibrium models.

In the previous section it was postulated that favourable viscous crossflow could be used to stabilize a displacement front against the effects of heterogeneity. None of our experiments produced a 'shock front' across all layers, but rather a 'cusp' of more viscous fluid protruding into the less viscous fluid (figure 4.7a). This is to be expected as some penetration of displacing fluid into the higher conductance layer is required before the transverse pressure fields causing favourable viscous crossflow can be set-up. An analysis of the experimental photographs (figure 4.9) shows that only in the case where the conditions (lowest values of h_D (0.025) and M (0.267)) produce the strongest favourable viscous crossflow, did the frontal separation become constant (run 5/5).

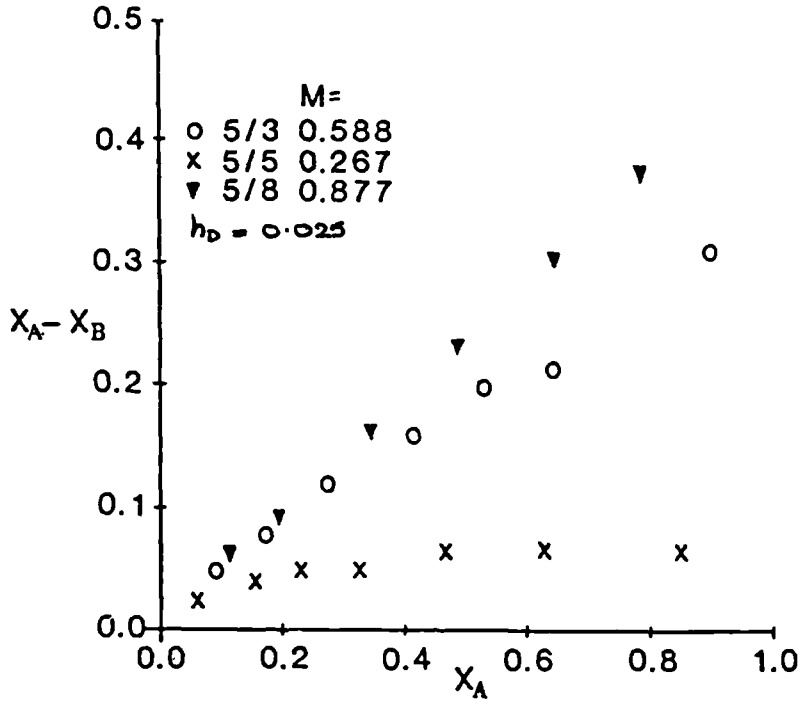

Figure 4.9 Frontal separation versus frontal position in layer A.

In all the other experiments the frontal separation increased with time. Therefore, although favourable viscous crossflow will under certain conditions stabilize the displacement front against the effect of conductance variations, in most favourable mobility ratio displacements channelling along the most permeable layer will still occur, but this will be less than for the unit mobility ratio case.

Packing number six differed from the other packings in that it contained a central low conductance layer (figure 4.10a).

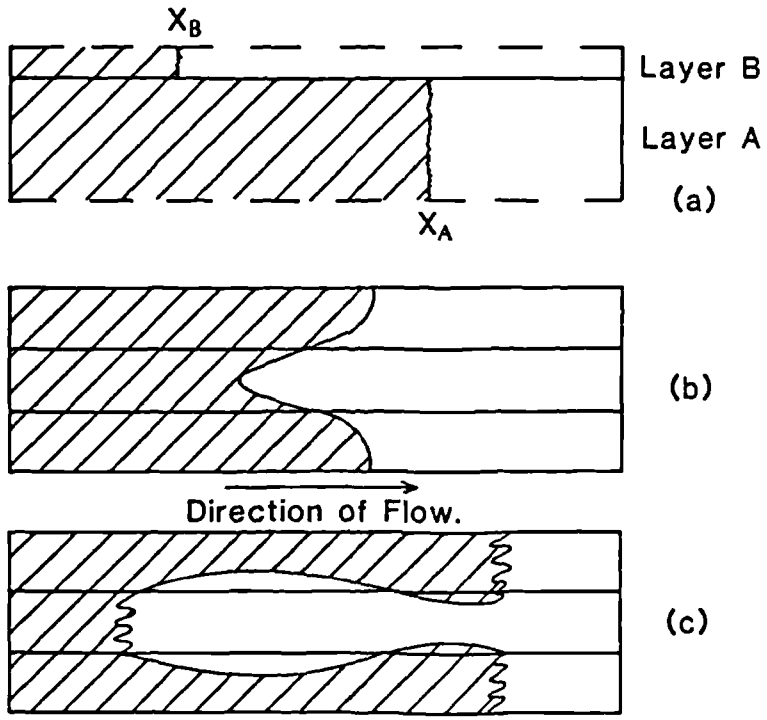

Figure 4.10 Schematic of packing number six with (a) unit, (b) favourable and (c) unfavourable mobility ratio cases.

Here layer A the high conductance layer, is wide relative to layer B. Therefore to model this case it is necessary to assume steady-state flow in layer A and calculate the

propagation of the front in layer B. The equations for this case are derived in appendix three and the predicted characteristic curves are compared to the experimental in appendix two. Qualitative agreement with the higher mobility ratio case (M=0.588) is reasonable and X_B values for a mobility ratio of 0.267 differ by some 30%. Figure 4.10b illustrates the favourable displacement pattern in packing six. Comparison with figure 4.7a shows that this is the reverse configuration of the favourable displacement in a system with a central high conductance layer.

A number of the photographs of the displacements produced in this investigation have been modelled numerically by AEE Winfrith[70] *. A 40x20x1 finite difference grid with four layers in the high conductance channel and 16 in the low conductance channel was used to simulate half of the experimental model. Figure 4.11 illustrates the numerical results which correspond to a similar stage in the displacement as figure 4.7a. Although the gross frontal shapes agree well, the numerical results contain a more dispersed front than is apparent from the experimental data. This is due to numerical dispersion which has been discussed in Section 2.7.

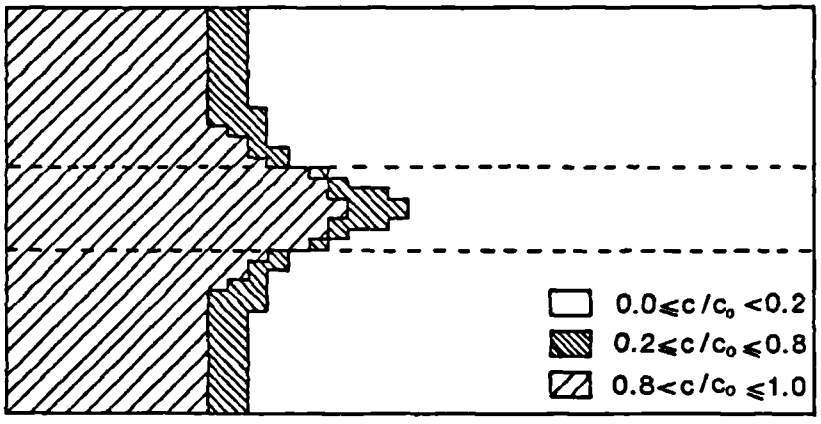

Figure 4.11 Result of numerical simulation[70] of experimental run 1/8.

* Dr. K. Sorbie is thanked for these results.

4.2.2 Unfavourable Mobility Ratio Displacement.

The experimental characteristic curves for the unfavourable displacement cases are presented in appendix two. All the experimental results show frontal separations which are greater than those for the unit mobility ratio case. Quantitative agreement between experimental and predicted values is good in all cases.

Figure 4.12 shows that as h_D decreases the frontal separation in an unfavourable mobility ratio displacement increases.

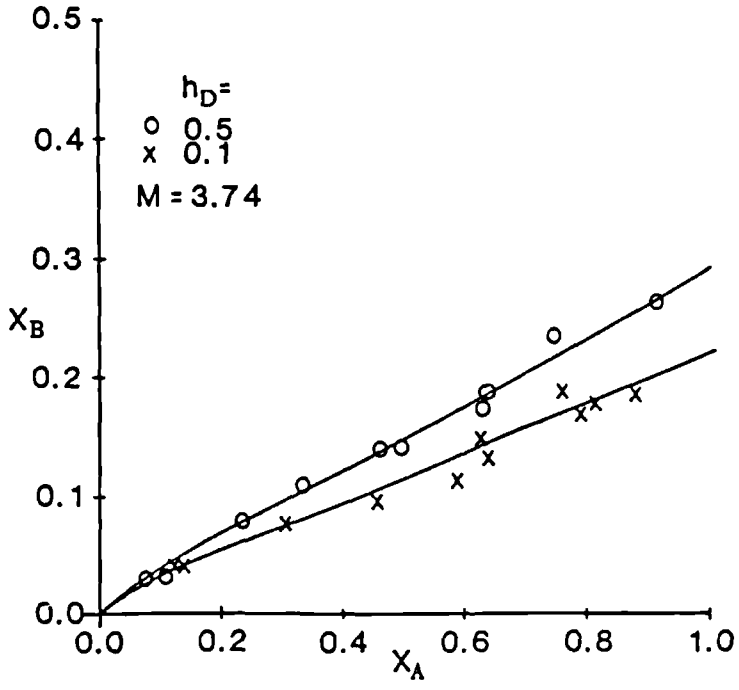

Figure 4.12 Effect of h_D on the characteristic curves for an unfavourable displacement (M > 1.0).

Tne increased scatter of the data points presented for the unfavourable displacements compared to that for the favourable displacements is due to the difficulty in determining the frontal positions with the relatively large intra-layer instabilities (fingers).

Figure 4.10c illustrates the unfavourable displacement pattern in packing six. Comparison with figure 4.7b shows that, as with the favourable case, this is 'back to front' compared to the displacement in a system with a central high conductance layer. In appendix two the experimental data for two unfavourable displacements in packing six are compared to values predicted by the method outlined in the previous section. The quantitative agreement between the experimental and predicted data with the lower mobility ratio (M=1.7) case is good, but differs in the order of 20% for a mobility ratio of 3.74.

The numerical simulation results[70] corresponding to a similar stage in the displacement (run 1/5) as figure 4.7b is shown in figure 4.13.

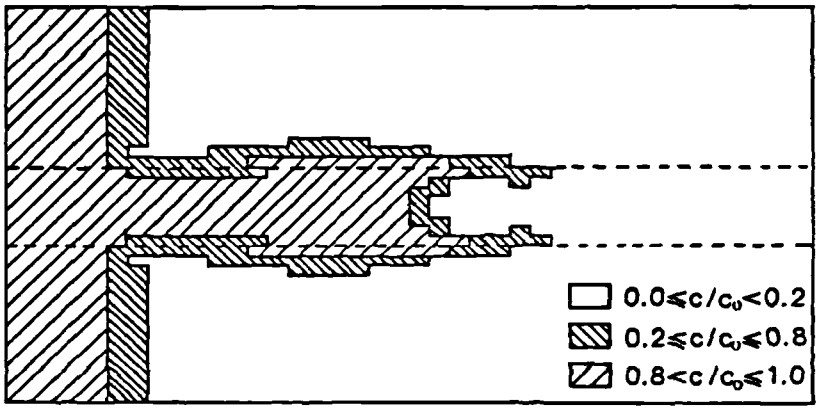

Figure 4.13 Result of numerical simulation[70] of experimental run 1/5.

There is a tendency for channels of displacing fluid to occur along the inter-layer boundaries presumably because of an instability in the pressure fields in this region. This effect should perhaps receive further attention.

4.3 Calculation of Fluid Crossflow.

In order to test the proposed mechanism for viscous crossflow, a method has been formulated to calculate the geometry of the fluid/fluid interfaces.

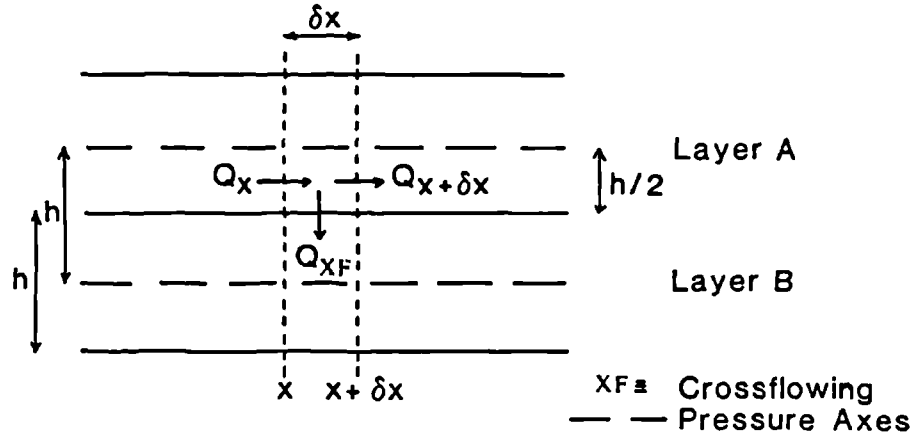

Figure 4.14 Small element of dual layer system.

Consider a differential element of a dual layer system (figure 4.14). A material balance gives:

$$Q_x = Q_{x+\delta x} + Q_{XF} \qquad (4.4)$$

where Q_{XF} denotes the component of the flow that is crossflowing across the inter-layer boundary. Expanding equation 4.4 gives:

$$Q_x = Q_x + \frac{dQ}{dx}\delta x + Q_{XF} \qquad (4.5)$$

which reduced to:

$$Q_{XF} = -\frac{dQ}{dx}\delta x \quad . \qquad (4.6)$$

As the fluid flow between the pressure axes in the centre of the layers are of interest, only flow in half of layer A and half of layer B need be considered. Thus Darcy's law for flow in half of layer A is:

$$Q_A = - \frac{hWk_A}{2\mu_A} \frac{dp_A}{dx} \qquad (4.7)$$

Combining equation 4.6 and 4.7 gives:

$$Q_{XF}\Big|_{dx,dT} = \frac{hWk_A}{2\mu_A} \frac{d^2p_A}{dx^2} \delta x \quad . \qquad (4.8)$$

Therefore the rate of axial flow within a layer is proportional to the first differential of the pressure gradient within that layer (equation 4.7), and the rate of fluid crossflow is proportional to the second differential of the pressure gradient (equation 4.8).

The pressure distribution within layer A as calculated by the finite crossflow method[37] was shown in figure 2.10 for a range of h_D values. Figures 4.15 illustrates the first and second differentials of this distribution. When the layer width is large compared to the system length (h_D=1.0), the no-crossflow case, the pressure distribution consists of two straight lines. The pressure gradients (figure 4.15a) are constant on either side of the front, implying constant axial flow (equation 4.7), and the rate of change of the pressure gradient (figure 4.15b) is zero, implying that no fluid crossflow (equation 4.8) to layer B occurs. The discontinuity in the curves in figures 4.15a and 4.15b is due to the different viscosities in the two regions. For lower values of h_D ($\sim$ 0.1), the pressure gradient and hence the axial flow rate tends to decrease with increasing distance along the layer. Here the second differential of the pressure distribution and hence the rate of fluid crossflow increases as the frontal position is approached from each side. This can be seen to be the case for all h_D values (figure 4.15b); therefore although fluid may crossflow across the entire length of the inter-layer boundary, the maximum crossflow occurs at the front. When the layer is thin compared to its length (h_D=0.01) the pressure gradient (dP/dX) is unity along most of the layer's axis and only varies around the frontal region. Here fluid crossflows only in this region (figure 4.15b).

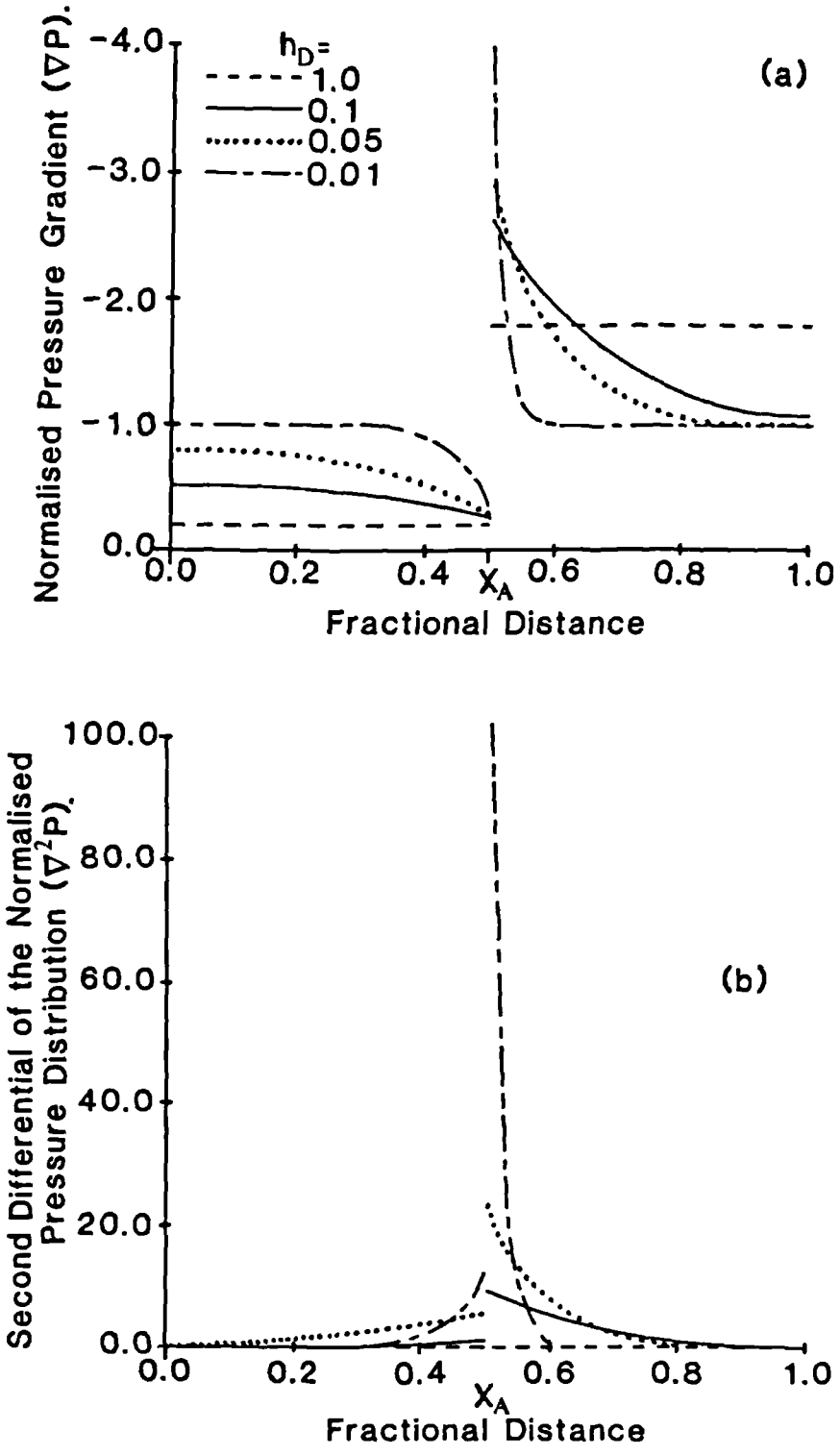

Figure 4.15 The (a) first and (b) second differentials of the pressure distributions in figure 2.10 (C_A/C_B=10.0, M=10.0 and X_A=0.5).

While the transfer of fluid from one layer to the other is influenced by the shapes of the axial pressure profiles, the complex fluid/fluid interfacial geometries are determined by the interaction between the pressure fields in adjacent layers. Typical profiles are shown in figure 4.16. In both cases the curves cross in between the fronts at a point X_{CR} (the no crossflow point). Here there is no pressure difference between the layers and therefore no tendency for fluid to crossflow. Clearly X_{CR} divides the curves into two sections, with fluid crossflow from layer A to layer B in one section and in the opposite direction in the other section. Although fluid may crossflow along the entire length of the system, it is that which occurs in between the fronts that affects the interfacial geometries. Therefore the position of X_{CR} relative to the frontal positions is very important as it dictates the proportion of the layer over which fluid crossflows in each direction.

For the limiting case of the non-communicating layers:

$$X_{CR} = X_B\left[\frac{M(1-X_A)+X_A}{M(1-X_A)+X_B}\right] \qquad (4.9)$$

Figure 4.17 shows X_{CR} values calculated from equation 4.9 for frontal positions predicted by the finite crossflow method, compared to experimental values. Crossflow does not appear to affect the X_{CR} values. In the unfavourable displacements there is an overlap (discussed later) of fluid/fluid interfaces around the no-crossflow point, and therefore points plotted in figure 4.17 are approximate values. This figure shows that for favourable displacements X_{CR} stays close to the front in layers A for the entire displacement, while for an unfavourable displacement X_A and X_{CR} are only close at the beginning and end of the displacement.

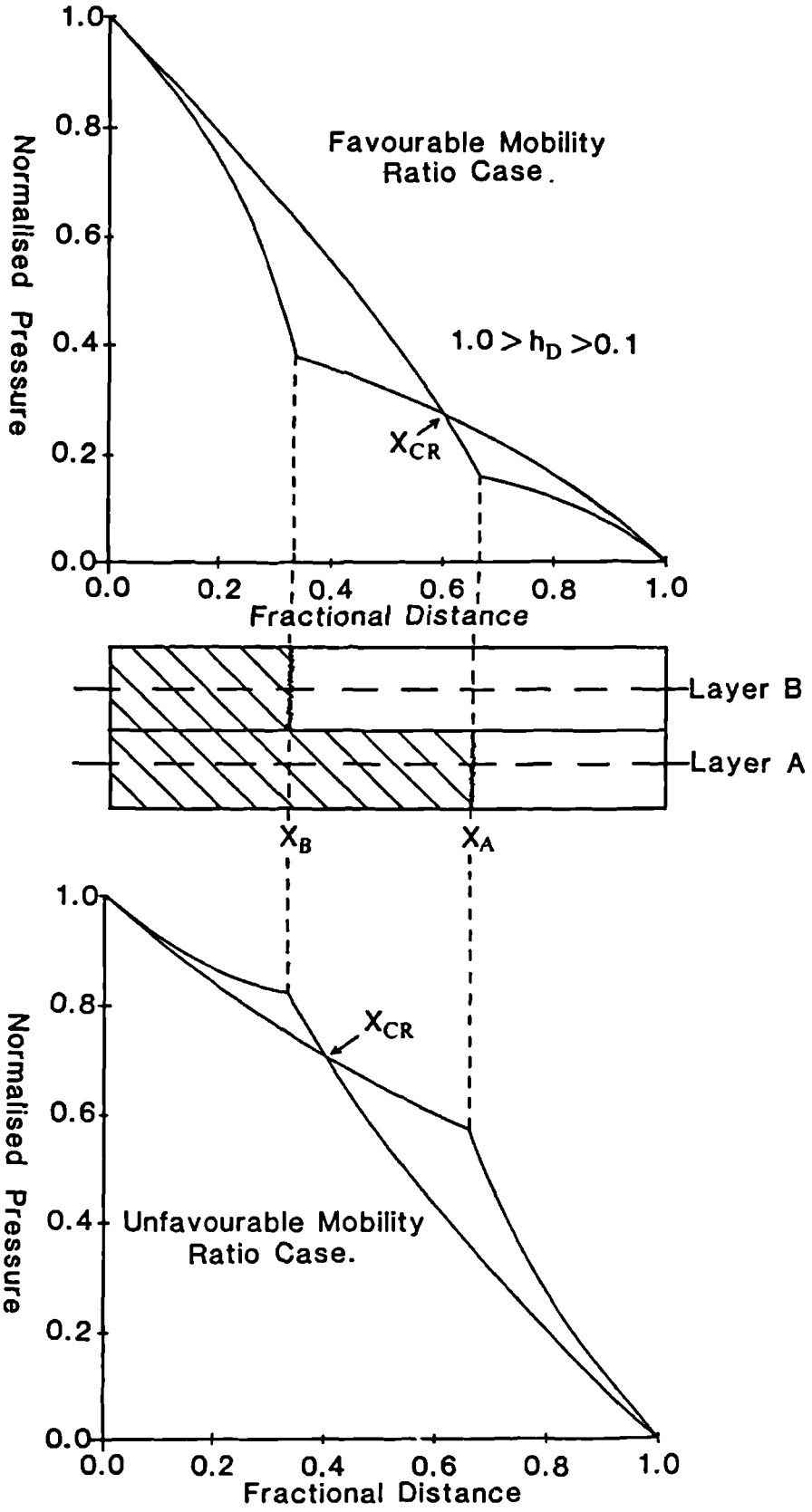

Figure 4.16 Typical axial pressure profiles for (a) favourable and (b) unfavourable displacements.

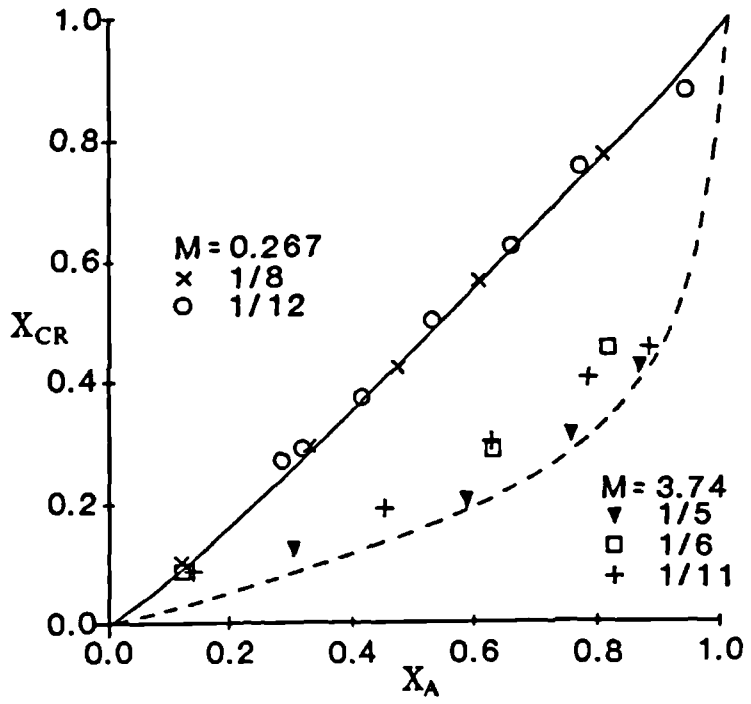

Figure 4.17 Comparison of predicted (curves) and observed (points) no crossflow points.

The volume of fluid crossflowing per length increment and per time step is given by:

$$VOL_{XF}\Big|_{dx,dT} = Q_{XF}\Big|_{dx,dT} dT \quad . \tag{4.10}$$

To be consistent with the finite crossflow method we assume constant flow rate in layer B:

$$dT = \frac{dx_B}{U_B} \quad . \tag{4.11}$$

Combining equations 4.8, 4.10 and 4.11 yields:

$$VOL_{XF}\Big|_{dx,dT} = \frac{hW}{2} \frac{k_A}{\mu_A} \left(\frac{d^2 p_A}{dx^2} \right) \delta x \ \frac{dx_B}{U_B} \quad . \tag{4.12}$$

If it is assumed that the volume of layer B into which fluid crossflows has a lateral dimension x_L, then:

$$VOL_{XF}\Big|_{dx,dT} = x_L W \delta x \phi_B \quad . \tag{4.13}$$

Equating equations 4.12 and 4.13 gives:

$$\frac{x_L}{h}\Big|_{dx,dT} = \frac{k_A}{\mu_A} \frac{dx_B}{2} \frac{1}{\phi_B U_B} \left(\frac{d^2 p_A}{dx^2} \right) \quad . \tag{4.14}$$

As the second differential of the pressure distribution as

calculated from the finite crossflow method[37] is dimensionless, it is necessary to reintroduce dimensions by multiplying the right hand side of equation 4.14 by:

$$\frac{\nabla p_{TOTAL}}{L^2} = \frac{Q_B}{W(h/2)} \left[\frac{X_B(\mu_2-\mu_1)+\mu_1}{k_B} \right] \quad . \qquad (4.15)$$

Thus:

$$\left.\frac{x_L}{h}\right|_{dx,dT} = \frac{k_A}{k_B} \frac{dx_B}{2L} \left(\frac{d^2P_A}{dX^2}\right) \left[\frac{X_B(\mu_2-\mu_1)+\mu_1}{\mu_A} \right] \qquad (4.16)$$

as $Q_B = U_B(h/2)W\phi_B$.

If we assume constant porosity, note that between X_{CR} and X_A $\mu_A = \mu_2$ and remembering that, $M = \mu_1/\mu_2$, then equation 4.16 becomes:

$$\left.\frac{x_L}{h}\right|_{dx,dT} = \frac{C_A}{C_B} \frac{dX_B}{2} \left(\frac{d^2P_A}{dX^2}\right) [X_B(1-M)+M] \quad , \quad X_{CR} \leq X \leq X_A \quad . \qquad (4.17)$$

Similarly for crossflows between X_B and X_{CR} :

$$\left.\frac{x_L}{h}\right|_{dx,dT} = \frac{C_B}{C_A} \frac{dX_A}{2} \left(\frac{d^2P_B}{dX^2}\right) \left[\frac{X_A(1-M)+M}{M} \right] \quad , \quad X_B \leq X \leq X_{CR} \quad . \qquad (4.18)$$

Figure 4.18 shows a simplfied representation of viscous crossflow in a two layer system. Once fluid has crossflowed to an adjacent layer, its axial velocity will be different to what it was in the previous layer. Preliminary studies suggest that these 'new' velocities may be approximated by two values in each case (figure 4.18). The relative magnitude of these velocities are such that crossflowed fluid in the favourable displacement case tends to flow away from X_{CR} (figure 4.18a) and in the unfavourable displacement case tends to flow towards X_{CR} (figure 4.18b).

Equations 4.17 and 4.18 have been solved numerically to predict the movement of fluid 'parcels' at the interfacial boundaries. To be consistent with the arqument of the last paragraph, these tracers were initiated from the no crossflow point in the favourable mobility ratio case and from the two fronts in the unfavourable mobility ratio case.

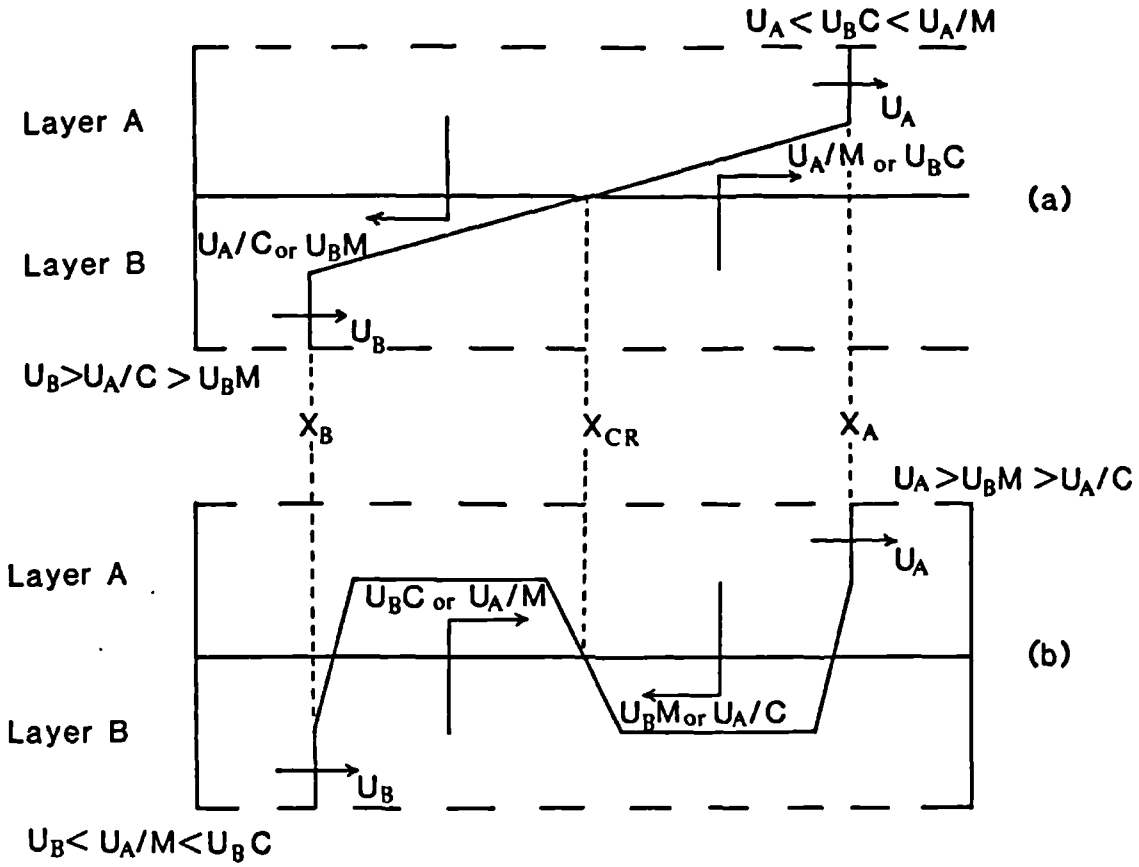

Figure 4.18 Schematic view of viscous crossflow (a) favourable case and (b) unfavourable case.

Preliminary results showed that the velocity of the crossflowed fluid was best represented by either $U_B C$ or U_A/C (figure 4.18) depending on the direction of crossflow. Fluid/fluid interfacial geometries predicted by the above method are compared to experimental data in figure 4.19. In both cases agreement is very good when the simplicity of the theoretical approach is considered.

The effect of X_{CR} remaining close to X_A (figure 4.17) for the duration of a favourable displacement is clearly shown in figure 4.19a.

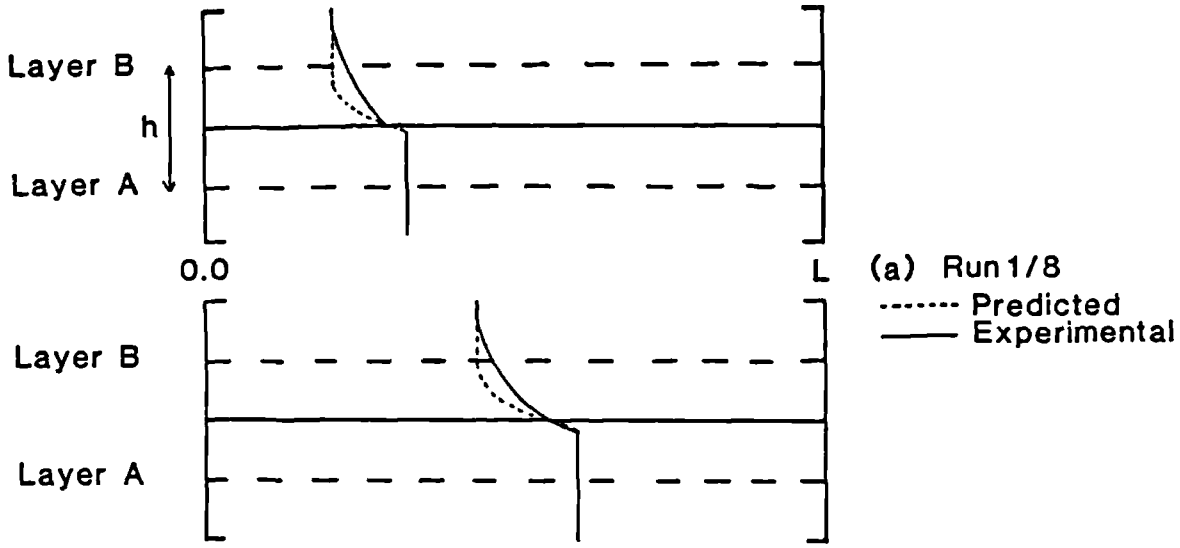

(a) Favourable mobility ratio case.

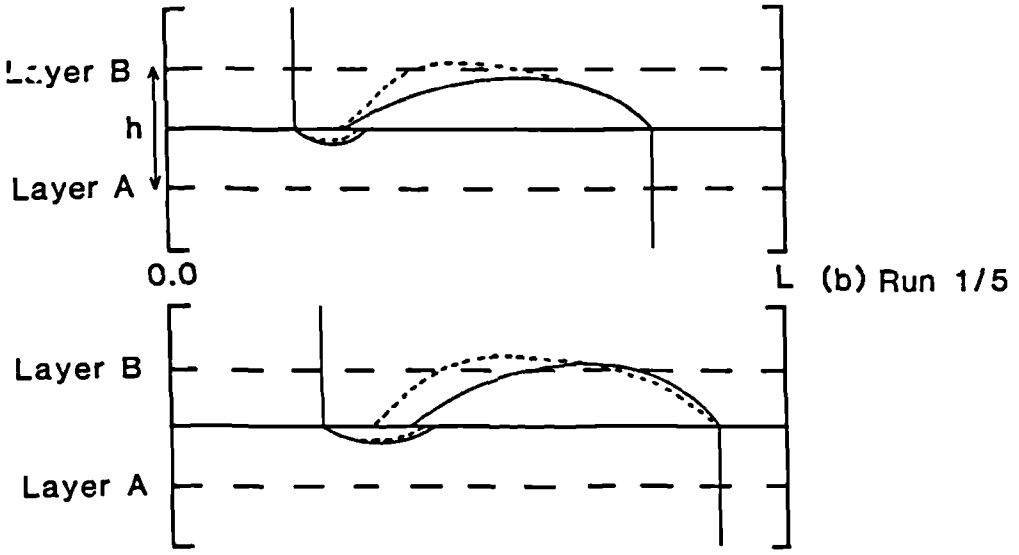

(b) Unfavourable mobility ratio case.

Figure 4.19 Comparison of predicted and experimental fluid/fluid interfacial geometries.

Here the majority of the crossflow occurs behind X_{CR} in the low conductance layer. As illustrated in figure 4.18a fluid that has crossflowed flows past the fluid fronts (X_A and X_B) in a favourable displacement. This explains the faint trail of displacing fluid which can often be seen in the high conductance layer ahead of the front (figure 4.7a). In the unfavourable case both the predicted and experimental geometries (figure 4.19b) show an overlapping of crossflowed fluid where the profiles in the high and low conductance

layers meet. This is a consequence of the crossflow being strongest around the fronts and relatively weak elsewhere. Thus once fluid has crossflowed to the adjacent layer under the influence of the pressure field around one front, it will only crossflow back to its original layer if it comes under the influence of the pressure field around the other front. Figure 4.19 shows that in both the favourable and unfavourable cases, due to the position of X_{CR} compared to the frontal positions (X_A and X_B), the majority of the crossflowing fluid flows from the high conductance layer into the low conductance layer.

All the theoretical methods considered so far have accounted for fluid flow within and out of each layer, but have not considered how fluid entering a particular layer affects the pressure distribution within that layer. A more complex analysis would be needed if this interaction was to be included. It is necessary to solve:

$$\frac{\partial^2 P_A}{\partial X^2} = \alpha(P_A - P_B)$$

and

$$\frac{\partial^2 P_B}{\partial X^2} = \alpha'(P_B - P_A) \qquad (4.19)$$

simultaneously. This gives equations for the pressure distribution in each layer of the form:

$$P_A = C_{I1}\exp(C_{J1}X) + C_{I2}\exp(C_{J2}X) + C_{I3}\exp(C_{J3}X) + C_{I4}\exp(C_{J4}X)$$

$$P_B = C_{I5}\exp(C_{J5}X) + C_{I6}\exp(C_{J6}X) + C_{I7}\exp(C_{J7}X) + C_{I8}\exp(C_{J8}X) \qquad (4.20)$$

The constants (C_I's and C_J's) could be evaluated directly since six boundary conditions exist for the system,

$$P = 1.0 \quad \text{and} \quad X = 0.0 \ ,$$

$$\left.\begin{aligned} M\left(\frac{dP_A}{dX}\right)_{UPSTREAM} &= \left(\frac{dP_A}{dX}\right)_{DOWNSTREAM} \\ (P_A)_{UPSTREAM} &= (P_A)_{DOWNSTREAM} \end{aligned}\right\} X = X_A \ ,$$

$$\left.\begin{aligned} M\left(\frac{dP_B}{dX}\right)_{UPSTREAM} &= \left(\frac{dP_B}{dX}\right)_{DOWNSTREAM} \\ (P_B)_{UPSTREAM} &= (P_B)_{DOWNSTREAM} \end{aligned}\right\} X = X_B \ ,$$

$$P = 0.0 \quad \text{when} \quad X = 1.0 \ .$$

The method of solution would be similar to that in appendices three and four. This will be studied in a future project[76].

4.4 Effluent Analysis and Fractional Flow Curves.

The compositions of the effluent from the models can give some information on heterogeneities. From the effluent data (figure 4.20a) for continuous injection experiments with mobility ratios of 3.74, 1.0 and 0.267, fractional flow curves were obtained by the Jones and Rozelle method[71] (figure 4.20b). This method uses a modified version of the Welge[15] technique to calculate the fractional flow functions at the effluent end of the model, and thus attempts to convert the two dimensional system to a one dimensional representation.

The unit mobility ratio effluent history shows the characteristic broadening of the residence time distribution due to the stratified nature of the media (figure 4.1). By comparison this broadening is exaggerated for the unfavourable case by viscous crossflow which is also responsible for the 'hump' and subsequent 'trough' in the effluent history (figure 4.20a) brought about by the 'bulbous' nature of the leading front and the 'pinch-in' between the fronts (figure 4.7b). By contrast the favourable effluent history shows the profile of homogeneous media. Here favourable viscous crossflow has stabilised the displacement front against the effect of stratification (figure 4.7a).

In a two layered system with no microscopic fluid dispersion the fractional flow graph will consist of two straight lines joined at a fluid saturation equal to that contained in the first layer to breakthrough at the effluent end of the system. The effect of fluid dispersion in the system is to bend the straight lines.

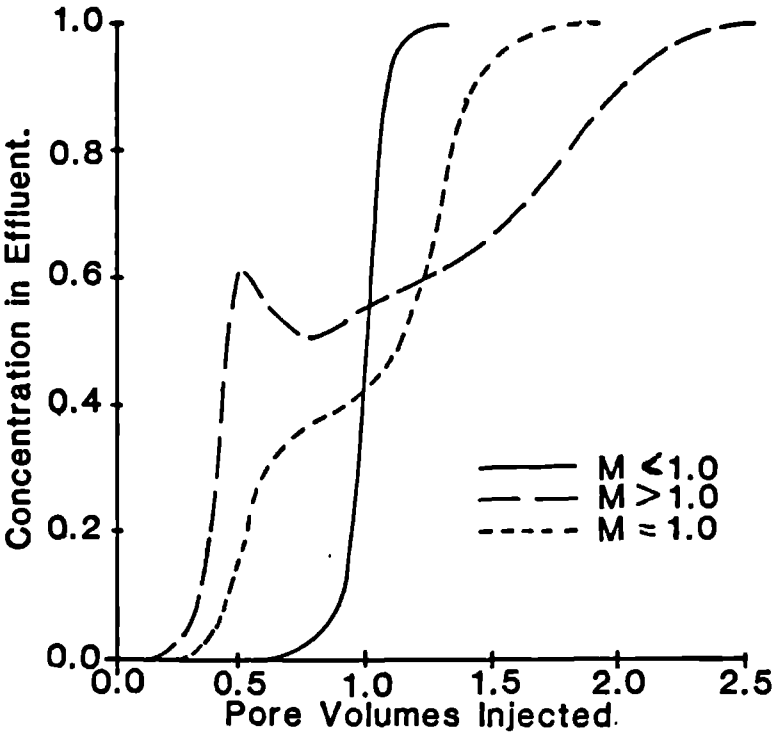

Figure 4.20a Experimentally obtained effluent data.

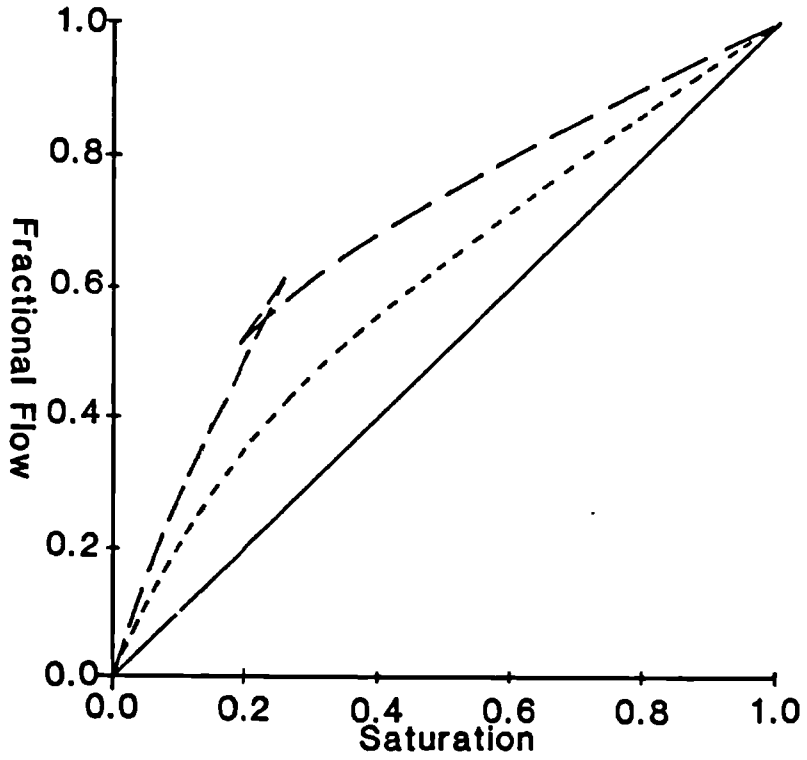

Figure 4.20b Calculated fractional flow curves.

The loop in the unfavourable mobility ratio fractional flow curve can be explained because the two dimensional 'bulbous' front cannot be accommodated by the one-dimensional representation. The favourable cases shows the characteristic shock front nature. Pseudo-fractional flow curves obtained from effluent data may be used to calculate the saturation profile at breakthrough from a one dimensional calculation method (i.e. Buckely-Leverett[14]), but they cannot be used to describe the flow of fluid through a grid block in a numerical experiment as they are specific to the effluent end of the experimental system.

4.5 Correlation of Data and Discussion.

Experimental and predicted[37] values of the fraction of the low conductance layer swept at breakthrough in the high conductance layer (X_B^*) are compared in figure 4.21.

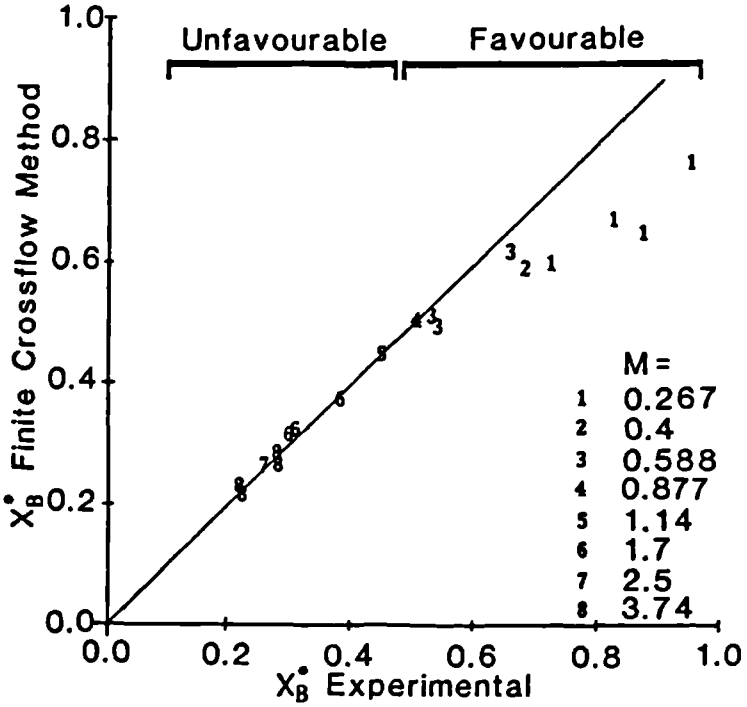

Figure 4.21 Comparison of experimental X_B^* values with those calculated by the finite crossflow method.

Agreement is very good for the unfavourable mobility ratio displacements, but all the favourable mobility ratio displacements have experimental values higher than the theoretical data. This discrepancy increases as the mobility ratio and hence frontal separation decreases.

In chapter two it was shown that when the layers are relatively thin ($h_D \rightarrow 0.0$), the characteristic curves (X_A versus X_B) become linear, which implies a steady-state solution. Equations 2.18 and 2.20 can now be used to calculate the ratio of the frontal velocities in a two layer model. Figure 4.22 correlates theoretical X_B^* (U_B/U_A at breakthrough) values against experimental data.

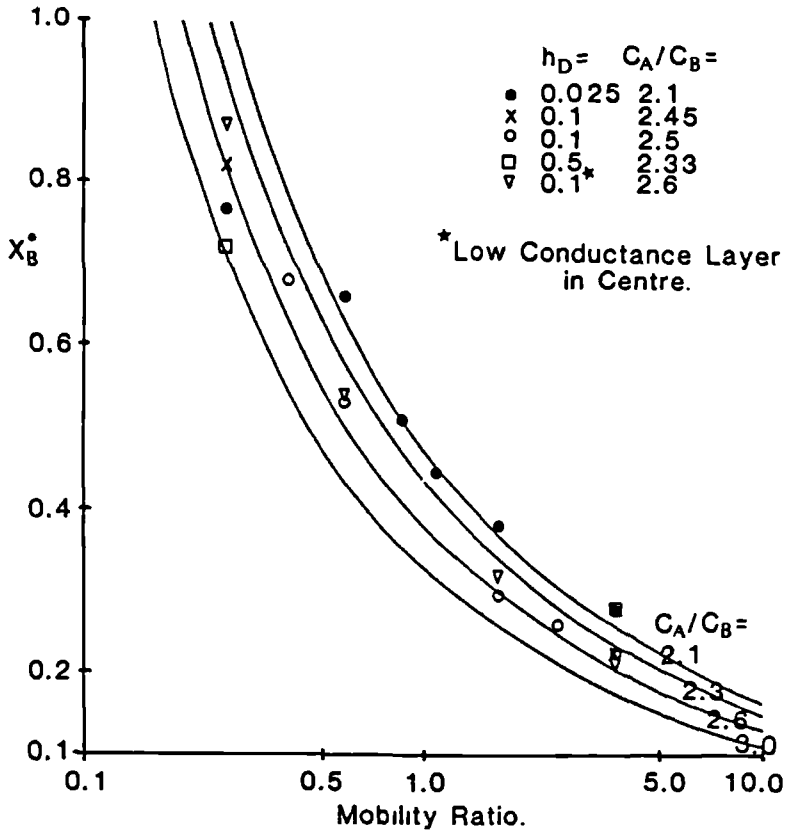

Figure 4.22 Correlation of experimental and predicted X_B^* values.

Although the experimental data contains a range of layer aspect ratios ($0.025 \leq h_D \leq 0.5$) agreement with the theoretical curves is generally good. Exceptions occur when h_D is large (0.5) or when the mobility ratio is very favourable (0.267).

As oil reservoir geometry is such that practical h_D values will be less than 0.1, the steady-state approximation can be used to estimate the volume swept by injection fluid at breakthrough in the high conductance layer. Thus for a dual layer system:

$$E_{BT} = b + \frac{(1-b)U_B}{U_A} \qquad (4.21)$$

where b is the fraction of the system that is high conductance media and U_B/U_A is calculated from equations 2.18 and 2.20. In figure 4.23 E_{BT} is plotted against conductance contrast for a range of mobility ratios and b values of 0.2 and 0.5. As this figure contains both mobility ratio and conductance contrast values outside the range validated by the experimental data, and the calculations are based on rectangular fluid/fluid interfaces which are clearly (figures 4.7a and b) approximations, these predictions can only be considered estimates. Figure 4.23 shows that E_{BT} decreases as the mobility ratio and conductance contrast increase, which corresponds to increased channelling in the high conductance layer. Thus even at moderate conductance contrasts, (ie. C_A/C_B=10.0) and unfavourable mobility ratios, very little of the low conductance layer has been swept at breakthrough.

The number of pore volumes needed to sweep the entire system (E_{ULT}) can be estimated if the propagation rate of the front in the low conductance layer (X_B) after breakthrough, can be calculated. Equations for this

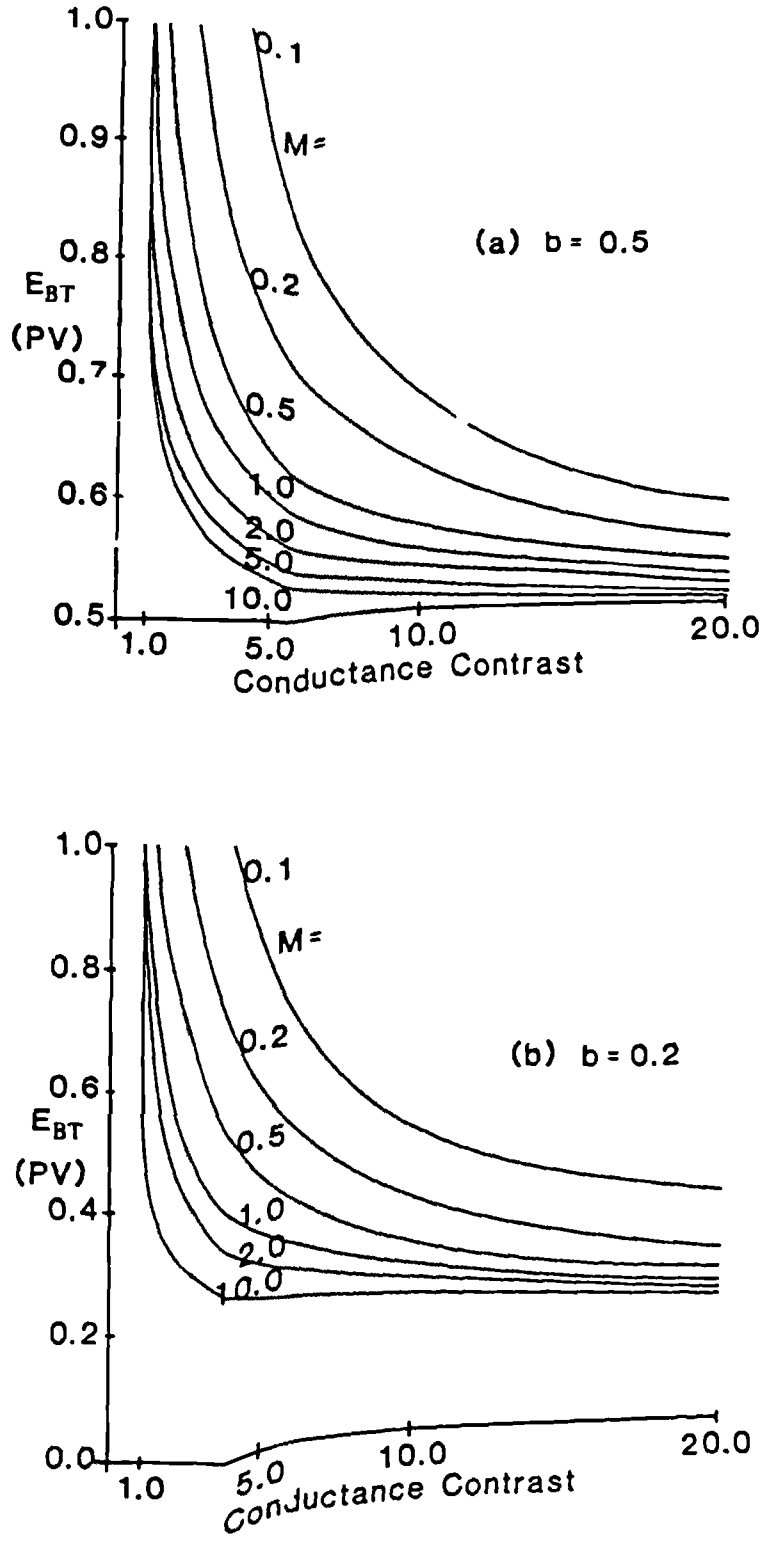

Figure 4.23 Correlation of breakthrough sweep efficiency calculated from equation 4.21.

situation are derived in appendix four, where it is shown that:

$$\left(\frac{U_B}{U_A}\right)^* = \frac{C_B}{C_A M}\left[\frac{1.0+Z^*}{(1/M)+Z^*}\right] \quad . \tag{4.22}$$

As h_D tends to zero (ie. thin layers) Z^* is given by:

$$Z^* = \left(\frac{C_A/C_B + 1/M}{C_A/C_B + 1.0}\right)^{\frac{1}{2}} \quad . \tag{4.23}$$

Here * denotes post breakthrough behaviour. Thus the number of pore volumes required to completely sweep a dual layer model is given by :

$$q_{ULT} = 1.0 + b\left\{1.0 - \left(\frac{U_B}{U_A}\right)\right\}\left(\frac{U_A}{U_B}\right)^* \quad . \tag{4.24}$$

This relationship is plotted for b values of 0.2 and 0.5 in figure 4.24. When the conductance contrast and mobility ratio are both large, channelling in the high conductance layer means that large volumes of displacing fluid (>10PV) need to be injected before the system is completely swept (cf. the unit mobility ratio case figure 4.3).

As with the unit mobility ratio case an important consideration is the proportion of displacing fluid in the production stream after breakthrough (F_D). For a dual layer model this is given by:

$$F_D = \frac{b}{b + \left(\frac{U_B}{U_A}\right)^* (1-b)} \tag{4.25}$$

which is plotted for b values of 0.2 and 0.5 in figure 4.25.

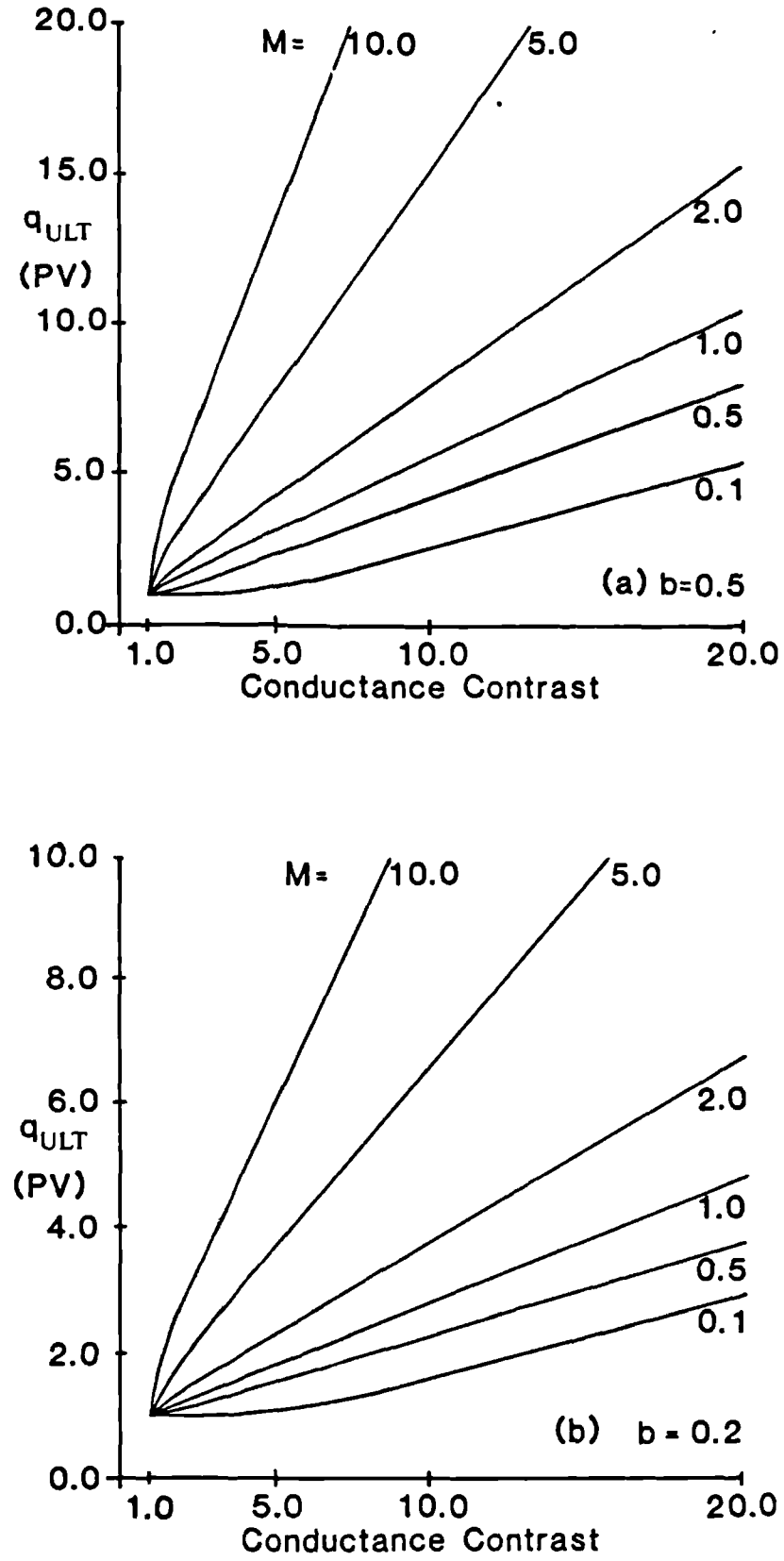

Figure 4.24 Correlation of ultimate sweep efficiency calculated from equation 4.24.

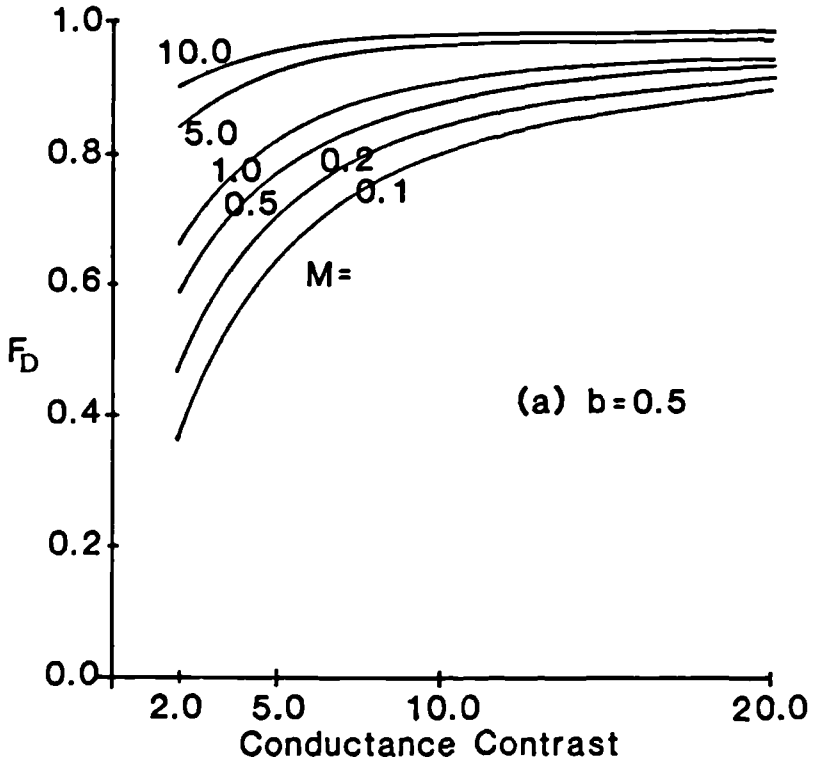

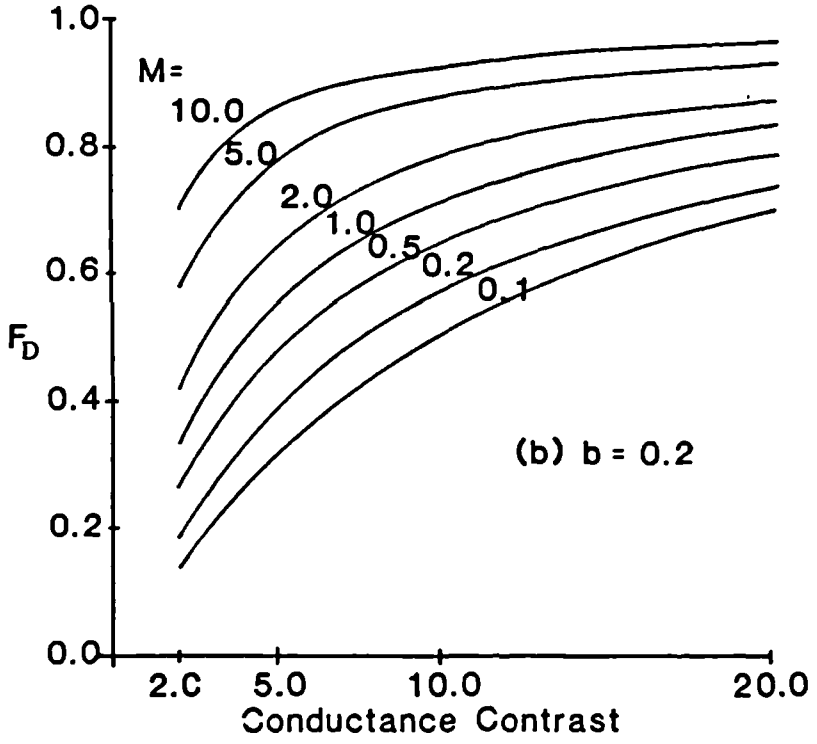

Figure 4.25 Graphical representation of equation 4.26

CHAPTER FIVE

SLUG DEGRADATION DUE TO VISCOUS FORCES IN MISCIBLE LAYERED SYSTEMS

In chemical EOR processes the quantity of chemical used must be kept as low as possible in order to keep costs down. Thus many schemes propose a small volume or 'slug' which is then displaced through the reservoir by a cheap chase fluid, normally water. The slug must withstand the physical degradation processes that occur in the reservoir. This chapter concentrates on the effect viscous forces have on the efficiency of miscible slug mode processes. Subsequent chapters will discuss how the concentration of the chemical may be affected by the transverse dispersion of components across axial fluid/fluid boundaries. Adsorption, gravity and other degrading mechanisms are outside the scope of this thesis.

5.1 Unit Mobility Ratio Case.

Chapters two and four have discussed in detail the layered case of continuous injection miscible displacement. For a unit mobility ratio displacement the fluid/fluid interfacial geometries will be rectangular and the fronts will travel at velocities proportional to the conductance of the layers. These velocity differences give rise to axial fluid/fluid interfaces at the layer boundaries (figure 4.1). If the composition of the fluids differ, component transfer across these interfaces (figure 5.1a) will occur in front of the slower moving front (X_B) due to microscopic transverse dispersion. Even so as seen in section 4.1 the whole system can be swept so long as sufficient volumes are passed through the system.

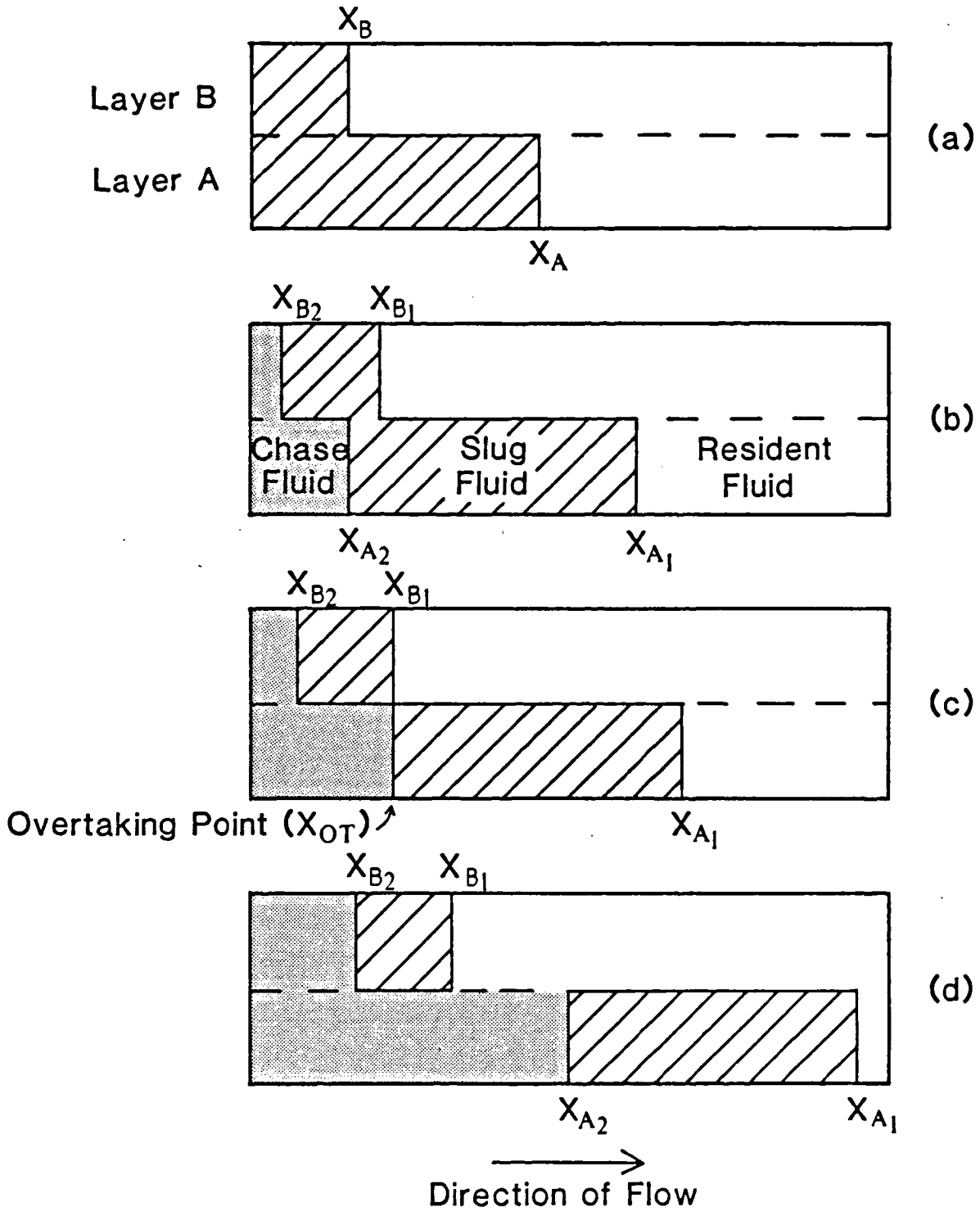

Figure 5.1 Degradation of a slug in a layered system with negligible fluid mixing.

In slug mode fluid mixing will also occur in the trailing portion of the displacement (figure 5.1b). Here there will only be a continuous band of injection concentration chemical across the system before the overtaking point (X_{OT}) occurs (figure 5.1c). This is defined as when

the trailing front in the high conductance layer (X_{A2}) has travelled the same distance as the leading front in the low conductance layer (X_{B1}). After this occurs the slug is divided into two independent portions and the maximum interfacial area is available for microscopic dispersion (figure 5.1d). The details of microscopic dispersion effects in slug mode miscible displacements are described in chapter six. Here the viscous effects are considered.

5.1.1 Experimental Results.

The packings were characterised and base case overtaking points were determined by slug mode unit mobility ratio displacements. The high conductance layer to model width ratios, b, for these packings ranged from 0.05 to 0.5. A typical experimental displacement pattern is shown in figure 5.2. For each of these experiments the positions

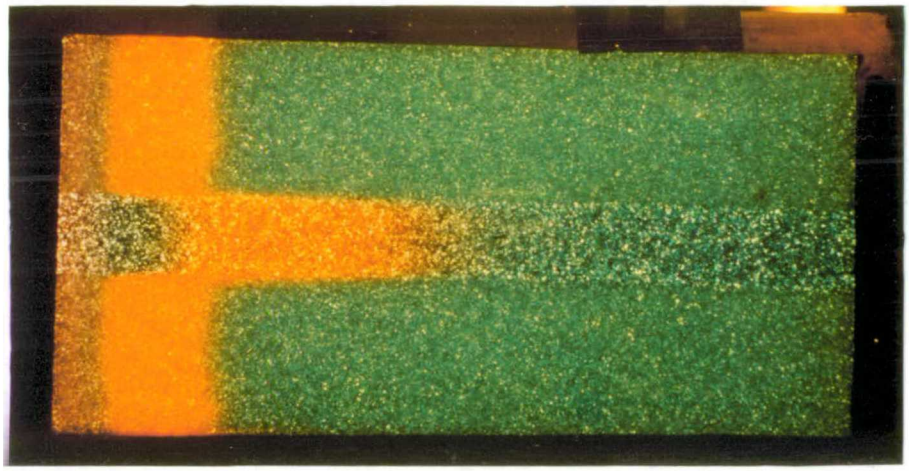

Figure 5.2 Photograph of experiment 1/3 close to the overtaking point.

of the trailing front in the high conductance layer (X_{A2}) have been plotted against those of the leading front in the low conductance layer (X_{B1}). The overtaking points have been determined from these graphs to be where $X_{A2} = X_{B1}$. These

experiments are summarised in table 5.1, and their characteristic curves and X_{A2} versus X_{B1} graphs are presented in appendix five.

Model No	C_A / C_B	Run No	b	Slug Volume	X_{OT} Measured	X_{OT} Predicted	S_{OPT} Predicted
1	2.45	3	0.2	16.0	0.22	0.21	76.3
5	2.1	2	0.05	20.0	0.35	0.36	55.3
6	2.6	4	0.8	34.7	0.27	0.25	140.3
10	2.33	1	0.5	62.3	0.685	0.66	95.0
15	2.55	1	0.2	26.1	0.36	0.33	79.6

Table 5.1 Summary of unit mobility ratio slug mode displacements.

5.1.2 Slug Requirements.

For unit mobility ratio displacements in dual layer systems (figure 5.1), the relative frontal advance is given by the conductance contrast (C_A /C_B) between the layers:

$$\frac{U_A}{U_B} = \frac{C_A}{C_B} \quad . \tag{5.1}$$

As this is a steady-state process:

$$\frac{X_{A1}}{X_{B1}} = \frac{X_{A2}}{X_{B2}} = \frac{C_A}{C_B} \quad . \tag{5.2}$$

At the overtaking point (figure 5.1c), the volume of slug fluid (pore volumes) injected into layer A is:

$$I_A = X_{OT}(C_A/C_B - 1)b \tag{5.3}$$

and the volume of slug fluid (pore volumes) injected into layer B is:

$$I_B = (1-b)X_{OT}(1-C_B/C_A) \quad . \tag{5.4}$$

The total slug volume in the system in pore volumes is:

$$S = I_A + I_B \qquad (5.5)$$

and the overtaking point can be generalised as:

$$X_{OT} = \frac{S}{b(C_A/C_B-1) + (1-b)(1-C_B/C_A)} \quad . \qquad (5.6)$$

The optimum slug volume (S_{OPT}) is defined as that when $X_{OT}=1.0$. In this case the overtaking point is not therefore within the system. Thus:

$$S_{OPT} = b(C_A/C_B-1) + (1-b)(1-C_B/C_A) \quad . \qquad (5.7)$$

The experimental and predicted (equation 5.6) overtaking points are compared in table 5.1; these all agree to within experimental precision. The optimum slug volume (equation 5.7) has been plotted against conductance

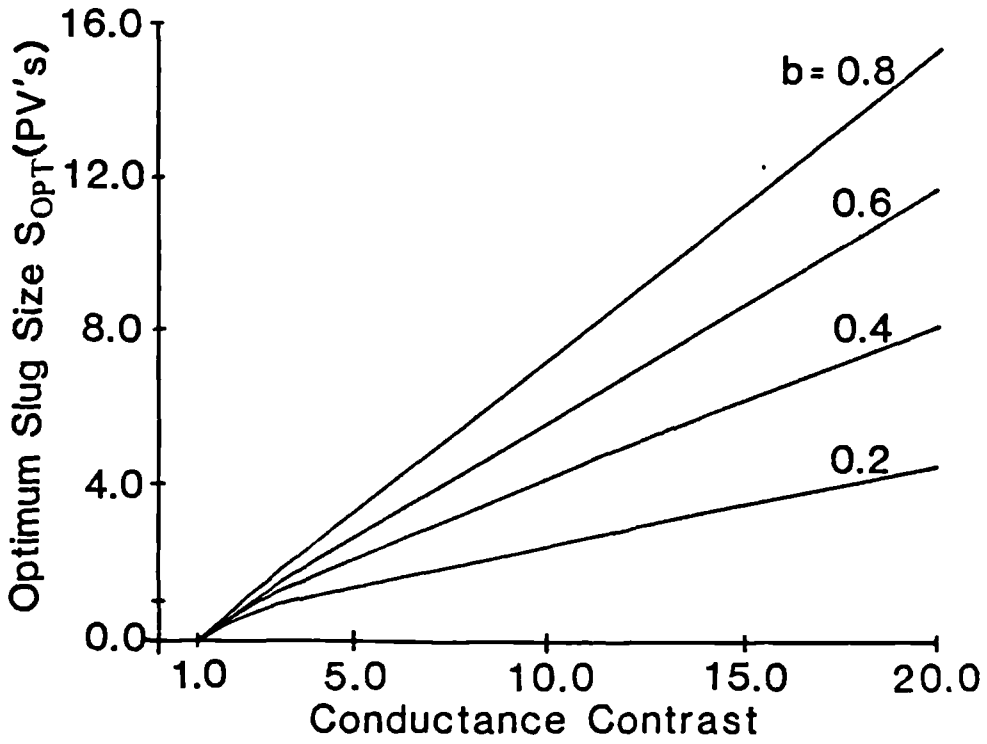

Figure 5.3 Calculated relationship between the optimum slug size and conductance contrast for unit mobility ratio displacements.

contrast for a range of high conductance layer to model width, b, values in figure 5.3. It must be emphasised that this point does not correspond to that where the slug chemical becomes suddenly ineffective at remobilising residual oil, but rather where the portions of the slug in adjacent layers separate and after which the transverse microscopic dispersion may reduce the chemical concentration to below its effective value. This will be discussed in chapter six.

5.2 Non-Unit Mobility Ratio Cases.

A typical chemical EOR process in slug mode is illustrated in figure 5.4. Each 'slug section' will

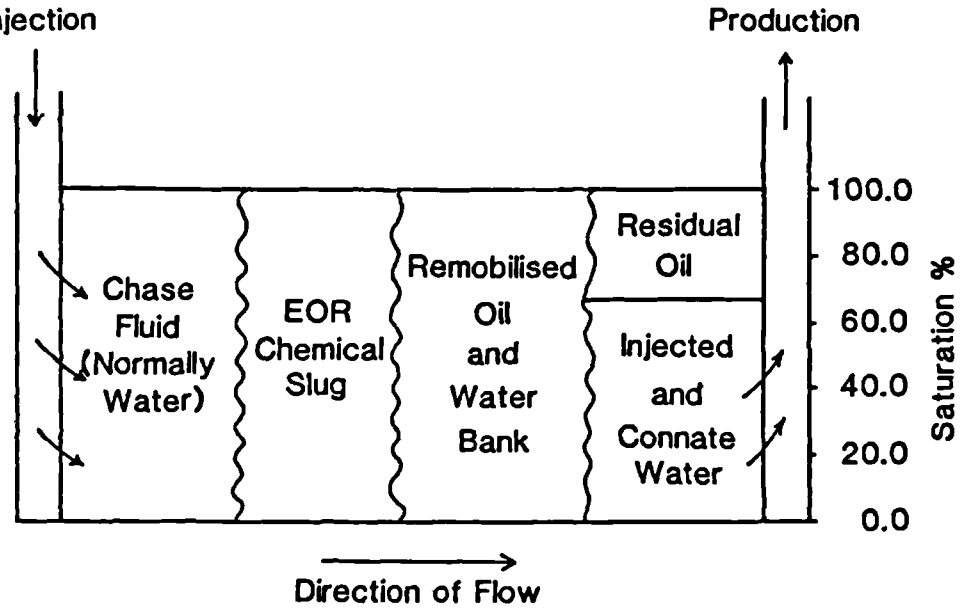

Figure 5.4 Schematic diagram of a typical slug mode chemical EOR process.

probably have a different mobility, therefore the interfacial geometries in practical processes (ie. heterogeneous strata) will be affected by the complexities of viscous crossflow (chapter four) unlike the unit mobility ratio case. For the three fluid system (resident, slug and chase fluids) which will be discussed in this chapter (figure 5.1) there are nine possible displacement patterns (figure 5.5).

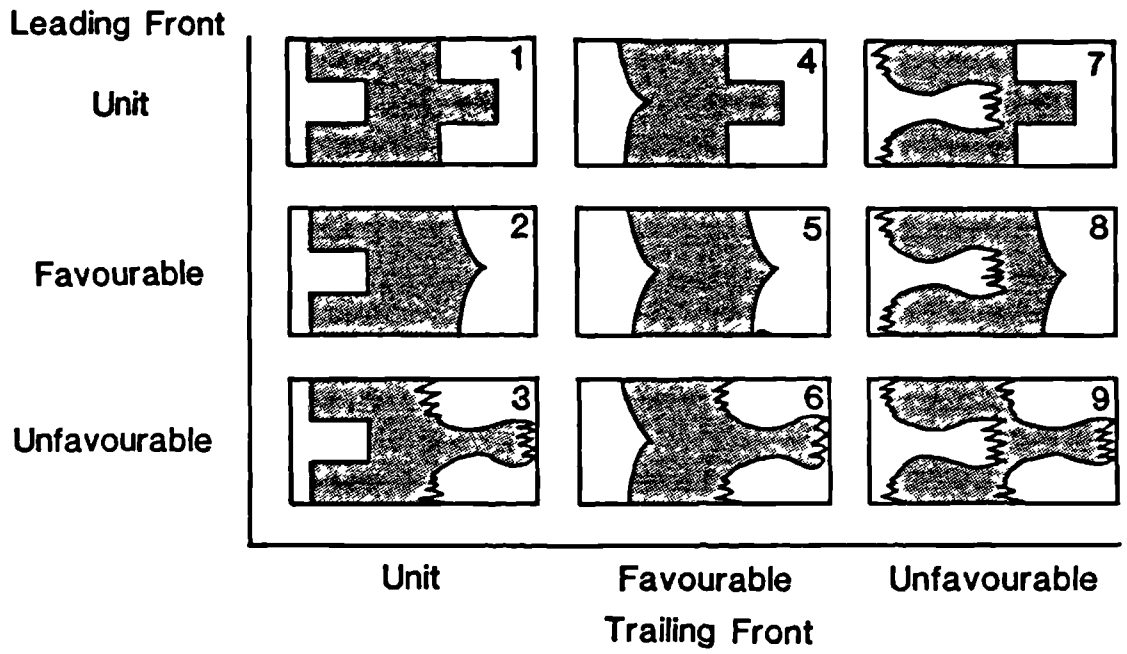

Figure 5.5 The various possible displacement patterns caused by frontal modifications due to viscous crossflow for the different combinations of fluid mobility.

Pattern one (the unit mobility ratio case) has been discussed in the previous section. Displacement patterns five and nine, which represent the most and least favourable cases respectively, will be discussed next, followed later by patterns two, six and eight which are generalisations of the experiments to be reported later in this chapter.

Displacement pattern five (M_{CS} and $M_{SR} < 1.0$).

In this, the ideal case, the chase fluid has a lower mobility than that of the slug fluid which is lower than that of the residual fluid. Here the favourable viscous crossflow of fluid stabilizes the process and a relatively small slug volume could be used to sweep the entire reservoir. Unfortunately the large volume of viscosifying agent (polymer) which would need to be added to the slug and chase fluids would make the process uneconomic, and the well injectivities may be impractically low due to the high chase fluid viscosities. Therefore less advantageous displacement patterns must be considered.

Displacement pattern nine (M_{CS} and $M_{SR} > 1.0$).

This case represents the least attractive possibility. Here severe channelling and viscous fingering occur, and the overtaking point would occur early in the displacement unless a substantial slug volume ($\gg$ one pore volume) was used. Large quantities of chase and slug fluid would be produced before the low conductance layers were swept. Additional mixing due to the intra-layer instabilities (ie. fingering) may cause the slug chemical concentration to be reduced more rapidly than by microscopic dispersion alone (chapter seven).

5.2.1 Experimental Observations.

From the experiments undertaken to investigate slug mode processes it is evident that the transverse pressure fields created around each non-unit mobility ratio front interfere with each other. This causes a modification to both frontal geometries and relative frontal propagation rates (U_A / U_B) compared to those expected in a continuous injection displacement. This is illustrated in figure 5.6 where the characteristic curves are compared for continuous injection and slug mode processes. It is possible to show that this modifying effect decreases with increasing distance from the front (figure 5.7) by injecting one of the slugs as smaller parcels but each dyed a different colour (see frontispiece of this thesis).

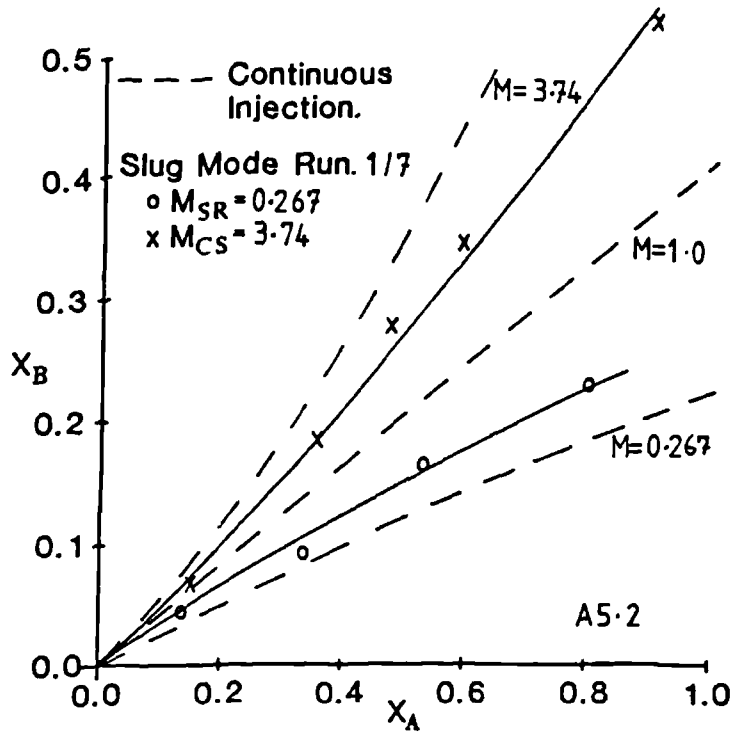

Figure 5.6 Comparison of characteristic curves for continuous injection and slug mode displacements.

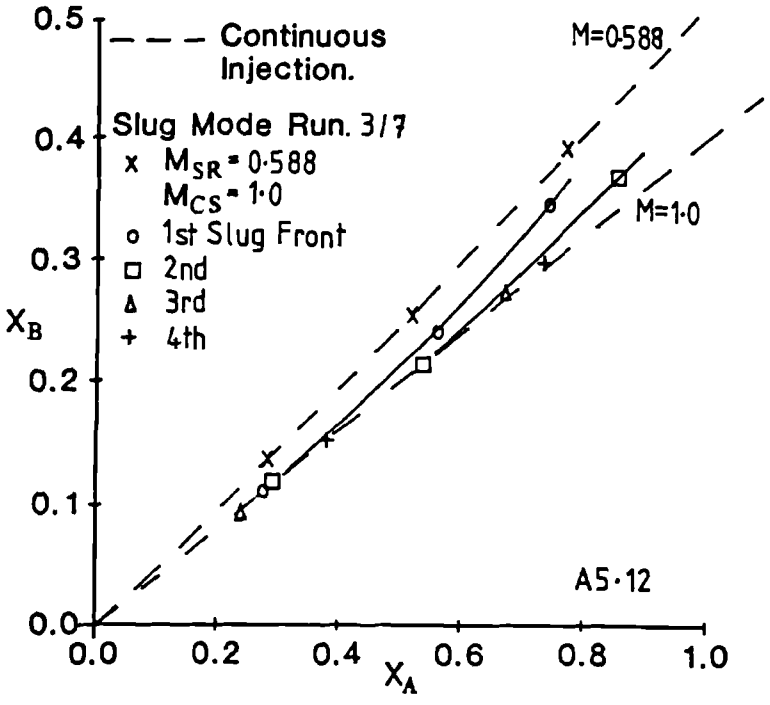

Figure 5.7 Characteristic curves for a 'stripey' displacement pattern.

A number of other points to note have been observed in experiments with displacement patterns two, six and eight; these will now be discussed.

Displacement pattern two ($M_{SR} < 1.0$, $M_{CS} = 1.0$).

Figure 5.8 shows photographs of this type of slug mode displacement at two different times. Here a favourable

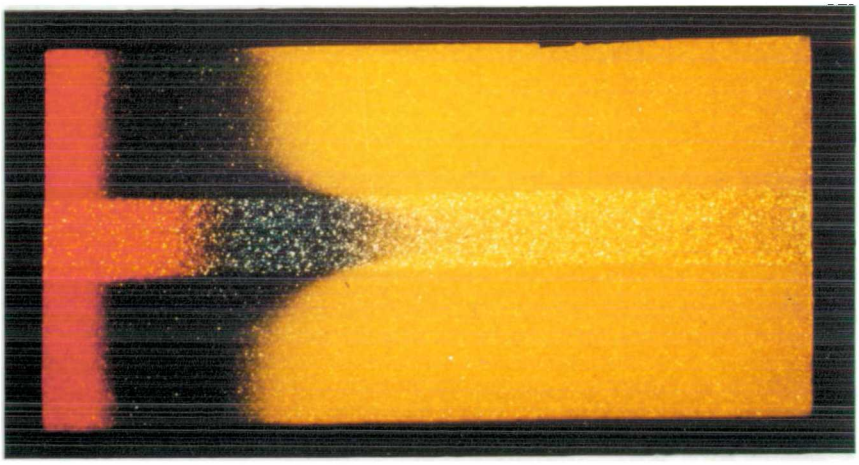

(a) Before the overtaking point.

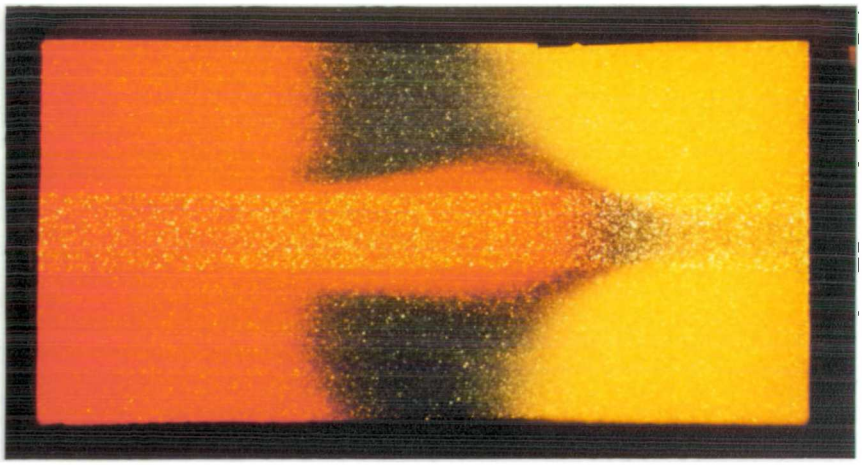

(b) After the overtaking point.

Figure 5.8 Photographs of experiment 1/12.

displacement front (M_{SR} = 0.267) is followed by an unit mobility ratio front (M_{CS} = 1.0). In figure 5.8a the rear front is beginning to channel into the slug fluid (blue), even through the chase (red) and slug fluids have the same mobility. At the later time (figure 5.8b) the chase fluid has reached the front of the slug which is now divided into two portions. Note that the transverse pressures around the favourable front cause chase fluid (red) to crossflow out of the central layer and the rear front (blue/red) now appears to have an unfavourable character.

Displacement pattern eight ($M_{SR} < 1.0$, $M_{CS} > 1.0$).

This case will occur when a polymer thickened slug fluid (red) is displaced by an unthickened chase fluid (yellow, ie. water). Here the favourable slug/resident (M_{SR} = 0.267) fluid front is followed by an unfavourable chase/slug (M_{CS} = 3.74) fluid front (figure 5.9). The unfavourable front is more bulbous than expected, due to its velocity being reduced by the favourable front, and therefore there is more time available for fluid crossflow to occur (section 4.3). While the favourable front has been elongated by the unfavourable front pushing the slug portion in the high conductance layer. After the overtaking point has occurred, the displacement behaviour will depend on the mobility ratio between the chase and resident fluids. If this is greater than unity, the chase fluid may bypass the slug portion in the high conductance layer, which may have a detrimental effect on process efficiency.

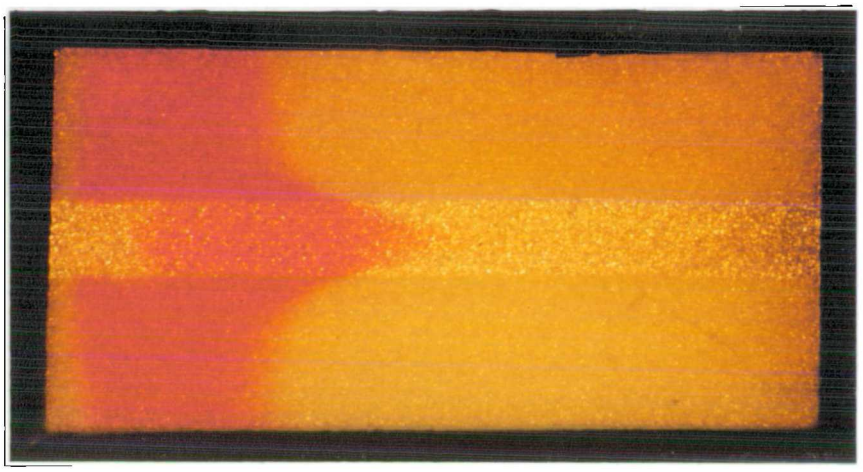

(a) Before the overtaking point.

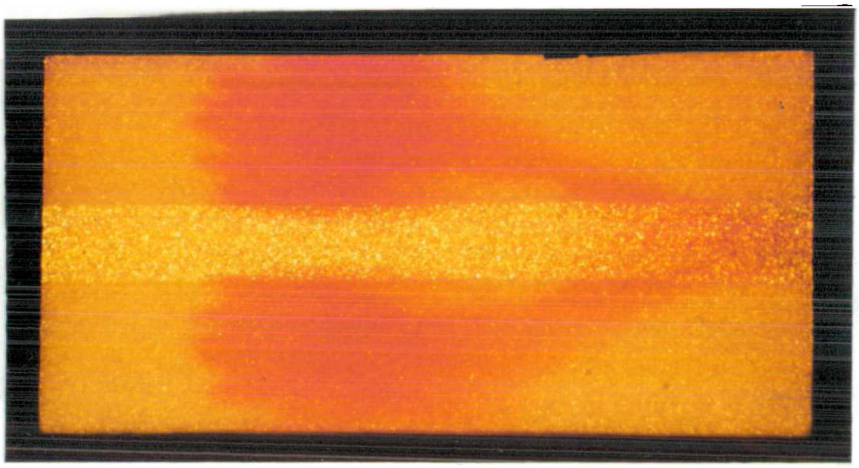

(b) After the overtaking point.

Figure 5.9 Photographs of experiment 1/7.

Displacement pattern six ($M_{SR} > 1.0$, $M_{CS} < 1.0$).

An unthickened slug fluid (yellow) displaced by a polymer thickened chase fluid (red) corresponds to this case (figure 5.10). Here very little chemical is injected into the low conductance layers during the initial stages of the process (figure 5.10a) due to the high mobility of the slug fluid. After chase fluid injection is initiated the slug fluid is forced to crossflow out of the low conductance layer and very little of the low conductance layer is swept by slug fluid (figure 5.10b).

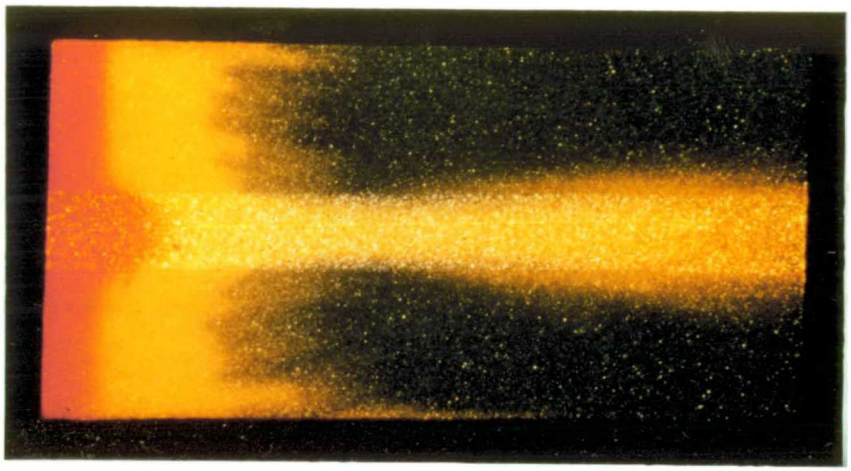

(a) Before the overtaking point.

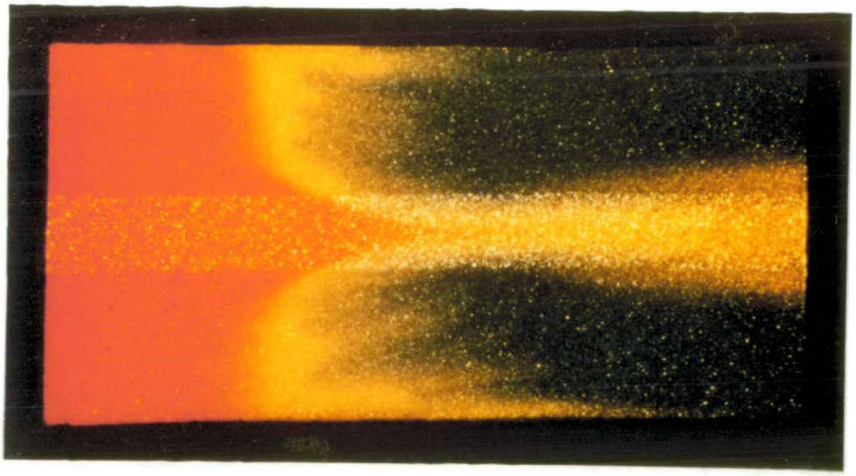

(b) After the overtaking point.

Figure 5.10 Photographs of experiment 1/10 (M_{SR} = 3.74, M_{CS} = 0.267).

5.2.2 Experimental Results.

Table 5.2 summarises the experiments undertaken to investigate non-unit mobility ratio slug mode processes. For each displacement the overtaking point was determined by the method detailed in section 5.1.1. But here the determination of frontal positions was made more difficult by the non-rectangular frontal geometries and intra-layer instabilities and a visual estimation of the average frontal position was used. The X_{A2} versus X_{B1} graphs (used to estimate X_{OT}) and the characteristic curves for these experiments are given in appendix five. Experimentally measured overtaking points (X_{OT}) are plotted against calculated slug volumes (S) for a selection of these displacements in figure 5.11. The optimum slug volume (S_{OPT}) for each combination of mobility ratios is obtained by extending the correlating lines to $X_{OT} = 1.0$. These values have been plotted against chase/slug fluid mobility ratios (M_{CS}) in figure 5.12. This parameter was used because as the chase fluid is usually water and the slug fluid an aqueous solution of chemicals, M_{CS} (the mobility of the chase fluid divided by that of the slug fluid) is a measure of how the added chemicals affect the relative mobility of these two fluids. If the relative permeabilities of the media to these fluids are the same, M_{CS} is the viscosity of the slug fluid divided by that of the chase fluid and therefore indicates how much more viscous the chase fluid is than the slug fluid.

Model Number	C_A/C_B	h_D	b	Run Number	Slug Volume(%PV)	M_{SR}	M_{CS}	X_{OT} Measured	X_{OT} Predicted	Predicted Optimum Slug Volume(%PV
1	2.45	0.1	0.2	7	22.85	0.267	3.74	0.365	0.349	66.25
				9	21.5	3.74	0.267	0.17	0.254	98.22
				10	42.54			0.485	0.458	
				12	21.92	0.267	1.0	0.34	0.435	51.14
3	2.5	0.1	0.2	4	26.64	1.0	3.74	0.28	0.287	92.80
				7_1	17.85	0.588	1.0	0.24	0.271	66.52
				7_2	31.88			0.46	0.484	
				7_3	45.5			0.69	0.687	
				7_4	57.7			0.89	0.869	
				8	25.34	1.7	0.588	0.3	0.307	84.01
				9_1	19.98	1.0	1.7	0.24	0.234	85.25
				9_2	43.1			0.475	0.506	
				9_3	61.04			0.66	0.557	
				10	21.2	0.588	1.7	0.3	0.290	73.77
6	2.6	0.1	0.8	6	47.38	1.7	0.588	0.24	0.238	205.60
				8	34.78	0.588	1.7	0.4	0.379	94.45
10	2.33	0.5	0.5	4	44.01	3.74	0.267	0.18	0.252	209.07
				6	34.24	0.267	3.74	0.53	0.793	44.29

Table 5.2 (Part I) Summary of non-unit mobility ratio slug mode displacements.

Model Number	$\frac{C_A}{C_B}$	h_D	b	Run Number	Slug Volume(%PV)	M_{SR}	M_{CS}	X_{OT} Measured	X_{OT} Predicted	Optimum Slug Volume(%
10	2.33	0.5	0.5	7_1	23.36	0.267	1.0	0.4	0.702	34.37
				7_2	51.95			> 1.0	> 1.0	
				8_1	32.15	1.0	3.74	0.285	0.306	104.96
				8_1	59.6			0.515	0.568	
				8_3	80.75			0.66	0.769	
11	2.5	0.1	0.2	3	37.4	0.267	3.74	0.57	0.563	67.23
				4	56.0			0.85	0.843	
				5	56.0	3.74	0.267	0.50	0.568	102.03
12	2.7	0.1	0.2	2	36.07	0.588	1.7	0.44	0.462	78.8
				3	54.05			0.72	0.689	
				4	35.94	1.7	0.588	0.38	0.393	92.5
				5	53.92			0.55	0.586	
15	2.55	0.1	0.2	2	18.98	0.4	2.5	0.29	0.268	71.93
				3	38.1			0.58	0.539	
				4	57.15			0.81	0.800	
				5	19.59	2.5	0.4	0.22	0.224	93.72
				6	38.57			0.4	0.425	
				7	57.74			0.6	0.614	

Table 5.2 (Part II) Summary of non-unit mobility ratio slug mode displacements.

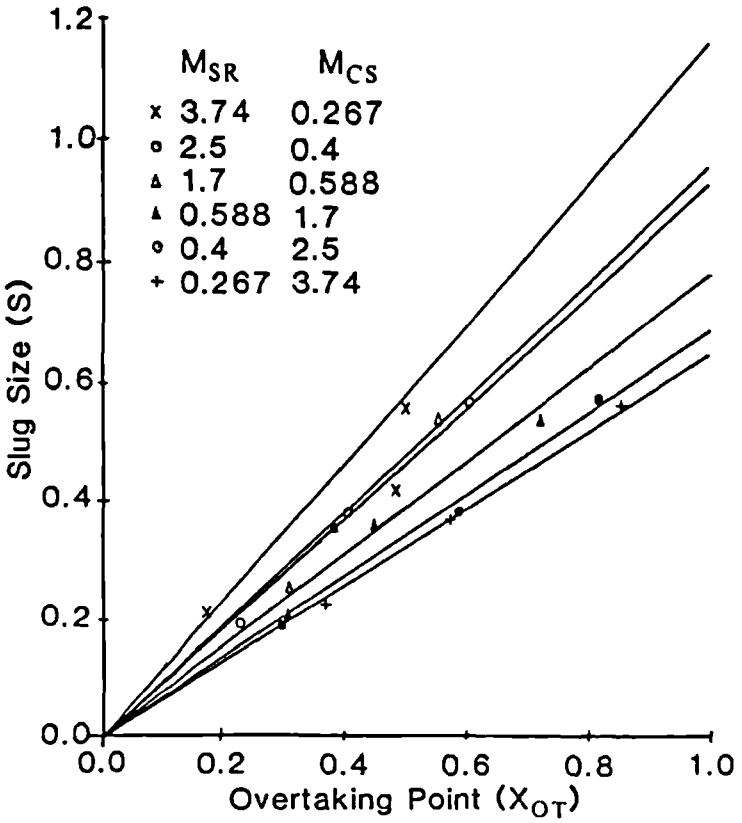

Figure 5.11 Correlation of slug volume and overtaking point for experimental displacements.

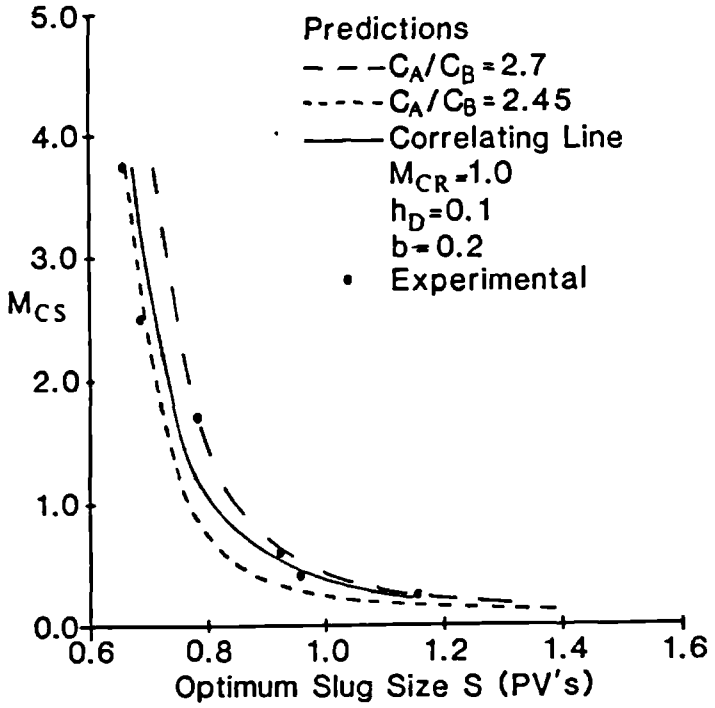

Figure 5.12 Dependence of optimum slug size on slug mobility for the experimental system used.

Figure 5.12 exhibits two distinct regions. Above a chase/slug mobility ratio of 4.0 the optimum slug volume tends towards a limited value of the order of 0.65 and therefore there appears to be no benefit in increasing the slug fluid viscosity further. This is because although a stable front has been created across the whole system (ie. a 'shock' front) at the leading slug/resident fluid boundary, severe channelling occurs at the rear of the slug which will offset this efficiency (displacement pattern eight and figure 5.9). For chase/slug mobility ratios of less than unity, the optimum slug size depends strongly on the mobility ratio and even minor viscosification of the slug fluid would cause a large decrease in slug size, and hence chemical requirements (displacement pattern six and figure 5.10). Clearly, the problem with slug mode displacements is that there are two boundaries to consider. Viscosification of the slug fluid makes the leading boundary more favourable but the trailing one more unfavourable and vice versa. However, a slug mobility which is less than that of the resident fluid (ie. viscosity greater, case eight) leads to a more favourable case because more fluid is injected into the low conductance layer during the initial stages of the process.

5.2.3 Estimation of Slug Requirements.

During the design stages of a slug mode enhanced oil recovery process it will be necessary to consider a range of design alternatives. Therefore a simple method to estimate slug volume requirements would be useful. The method presented below is based on a number of simplifying assumptions:

(a) The leading and trailing fronts do not interfere with each other. This will be true if these are widely spaced (S~1.0 PV).

(b) The relative frontal propagation of corresponding fronts in adjacent layers can be given before breakthrough by equations 2.18 and 2.20, and after breakthrough by equations 4.22 and 4.23.

(c) The complex frontal geometries due to viscous crossflow do not significantly affect the process and can therefore be considered rectangular.

(d) The overtaking point is significant.

Consider a dual layer system, where the overtaking point has occurred before slug fluid breakthrough in the high conductance layer (figure 5.1c). The volume of slug fluid (pore volumes) injected into layer A is:

$$I_A = X_{OT}(U_{A1}/U_{B1}-1)b \quad . \qquad (5.8)$$

The volume of slug fluid (pore volumes) injected into layer B is:

$$I_B = (1-b)X_{OT}(1-U_{B2}/U_{A2}) \quad . \qquad (5.9)$$

Combining equations 5.5, 5.8 and 5.9 gives the overtaking point before slug fluid breakthrough as:

$$X_{OT} = \frac{S}{b(U_{A1}/U_{B1}-1) + (1-b)(1-U_{B2}/U_{A2})} \quad . \qquad (5.10)$$

(U_{A1}/U_{B1}) and (U_{A2}/U_{B2}) can be calculated from equations 2.18 and 2.20.

If the overtaking point occurs after breakthrough (figure 5.13) a volume of slug fluid (I_P) will have been produced where:

$$I_P = b(X_{OT} - U_{B1}/U_{A1})(U_A/U_B)^* \quad . \qquad (5.11)$$

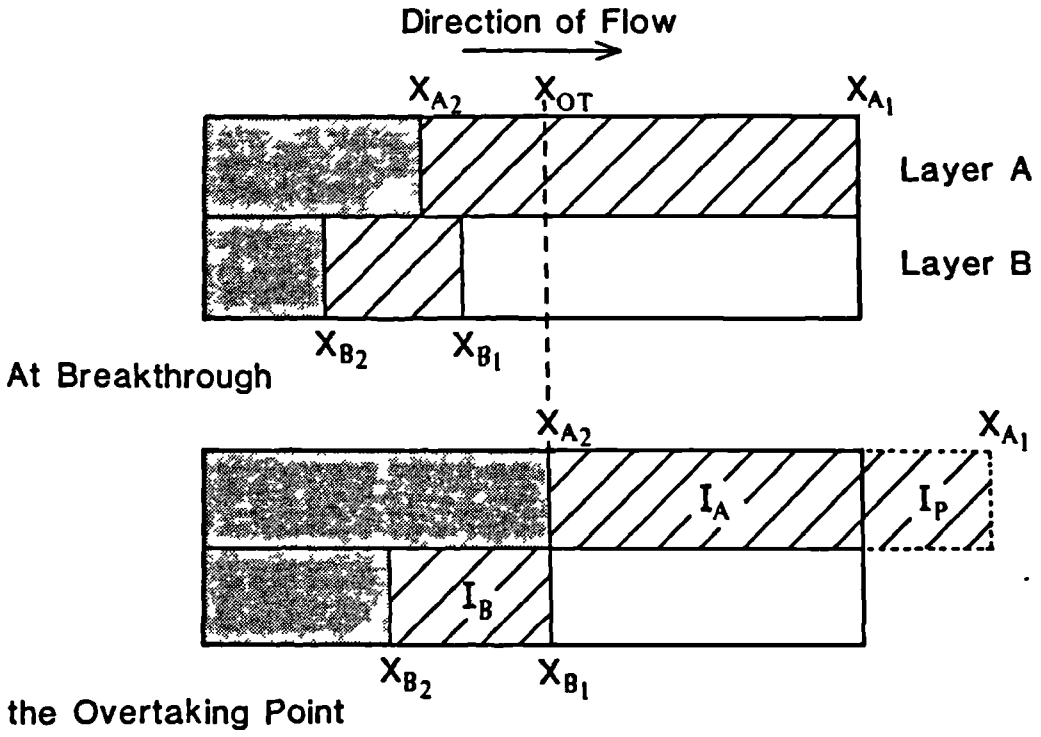

Figure 5.13 Schematic of slug mode displacement where the overtaking point occurs after breakthrough.

$(U_A/U_B)^*$ can be calculated from equations 4.22 and 4.23. The slug volume remaining in layer A in pore volumes is:

$$I_A = b(1-X_{OT}) \quad . \qquad (5.12)$$

After breakthrough: (5.13)

$$S = I_A + I_B + I_P \quad .$$

Combining equations 5.9, 5.11, 5.12 and 5.13 gives the overtaking point after slug breakthrough as:

$$X_{OT} = \frac{S - b + b(U_A/U_B)^*(U_{B1}/U_{A1})}{(1-b)(1-U_{B2}/U_{A2}) - b + b(U_A/U_B)^*} \quad . \qquad (5.14)$$

Predictions of X_{OT} by equations 5.10 and 5.14 are compared to experimentally obtained data in table 5.2. When the layer aspect ratio is low ($h_D \leqslant 0.1$) agreement between measured and predicted overtaking points is in most cases within experimental error. But when the layer aspect ratio is higher ($h_D = 0.5$) discrepancies in the order of 50.0% occur. This is because the equations used to estimate the relative frontal propagation rates (equations 2.18, 2.20, 4.22 and 4.23) are no longer valid. Nevertheless they give an order of magnitude estimation.

The minimum slug volume required to prevent X_{OT} occuring within the system (S_{OPT}) is defined as that when $X_{OT} = 1.0$; thus:

$$S_{OPT} = b(U_A/U_B)*(1-U_{B1}/U_{A1}) + (1-b)(1-U_{B2}/U_{A2}) \quad . \quad (5.15)$$

Predictions using equations 5.15 are shown for all the experiments in table 5.2, and compared with experimental values in figure 5.12. As the conductance contrast varied slightly between models, predicted curves representing the upper ($C_A/C_B = 2.7$) and lower ($C_A/C_B = 2.45$) limits have been plotted. All measured points fall within or very close to this range.

5.2.4 Discussion.

The overtaking point corresponds to the time in the displacement when recovery may begin to be seriously affected. There are two reasons for this:

1. After X_{OT} has occurred the slug portions in adjacent layers no longer laterally support each other and microscopic transverse dispersion may reduce the chemical concentration to below its effective value (discussed in chapter six).
2. Unless the process is designed to prevent X_{OT} occurring

within the system large volumes of slug and chase fluid (>> 1.0 PV) may need to be injected before the whole system is swept. Thus it is advantageous that this point does not occur within the system.

The method detailed in section 5.2.3 to estimate slug volume and mobility requirements provides good agreement with the experimental data (table 5.2). Here the arguments are extended to obtain estimates for reservoir scale processes where the only practicable injection parameters which can be altered by the engineer are the volume of the slug fluid injected and its mobility (characterised by M_{CS}). Figure 5.14 gives predictions of the optimum slug volume (S_{OPT}) correlated with M_{CS} and conductance contrast (C_A/C_B) for a range of chase/resident mobility ratios (M_{CR}). This parameter is the overall mobility ratio for the displacement and is usually unfavourable ($M_{CR} > 1.0$) because of the low relative permeability of the oil rich zone and the high relative permeability behind the slug (very low oil saturation). These curves show the same characteristics as the experimental data (figure 5.12).

The chase/resident fluid mobility ratio has a large effect on the slug volume requirements and in most cases slug volumes of greater than one pore volume are required to prevent overtaking. The overall mobility ratio (M_{CR}) may be reduced by the use of certain polymers within the slug which reduce the effective permeability of the media to subsequent chase fluid[72]. The curves in figure 5.14 illustrate the interdependence of the pertinent parameters needed for the design of a slug mode chemical EOR process. These curves may be used during the preliminary design stages to evaluate the many available options.

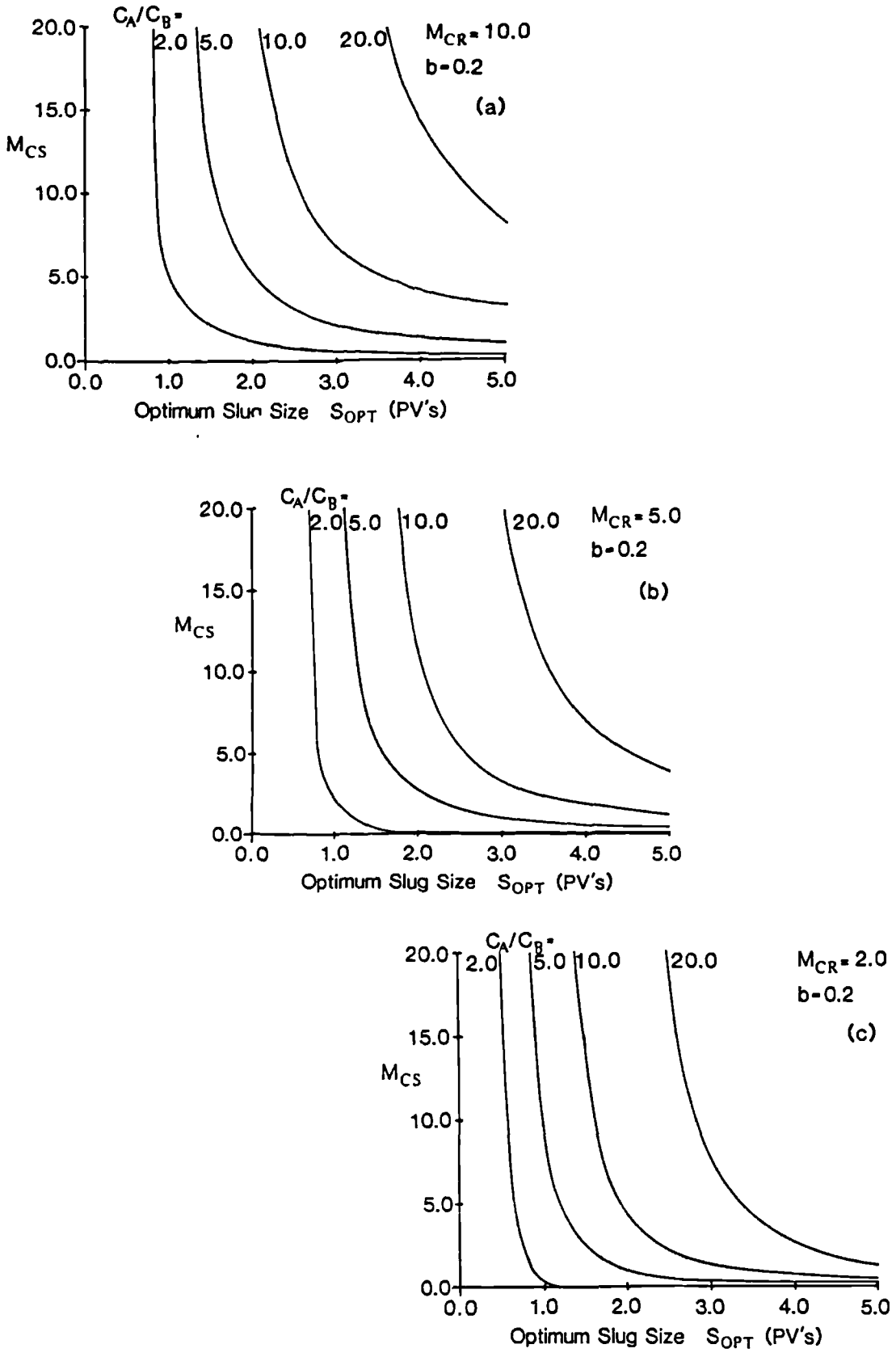

Figure 5.14 Predicted optimum slug size correlated with conductance contrast and chase/slug fluid mobility ratio.

CHAPTER SIX

THE EFFECT OF DISPERSION IN LAYERED SYSTEMS WITH FLUIDS OF EQUAL MOBILITY

The previous two chapters have shown how viscous forces may reduce the efficiency of miscible displacement processes in stratified systems. Figures 4.5 and 5.1 demonstrate how fluid/fluid interfaces are formed at the displacement fronts and at the layer boundaries. Molecular diffusion and microscopic dispersion processes will cause the transfer of fluid components across these interfaces (figure 6.1) and so modify the fluid concentration distribution in both layers (chapter two). This chapter

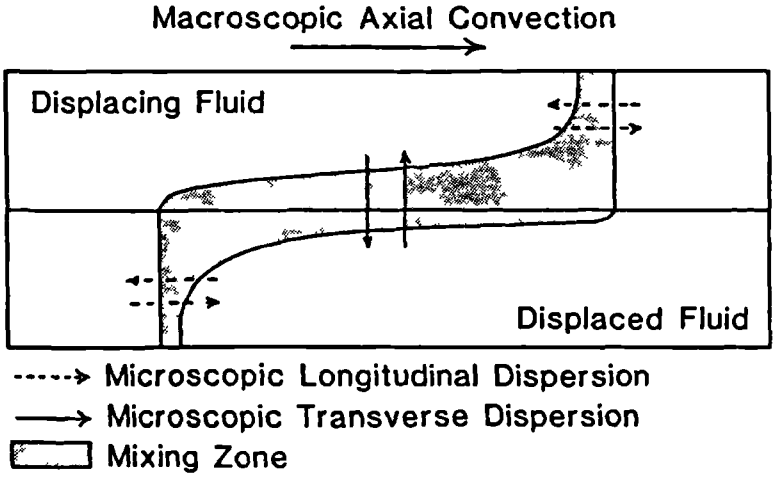

Figure 6.1 Mixing of displacing and displaced fluids in a layered system.

considers the case when the fluids have equal mobilities and therefore the fluid/fluid boundaries are rectangular (figures 4.1 and 5.2). The increased complexities when the fluids have different mobilities will be discussed in chapter seven.

6.1 Dispersion in Stratified Media.

6.1.1 Continuous Injection Displacements.

Consider initially a unit mobility ratio displacement in a dual layer model and for simplicity let there be no fluid mixing (figure 6.2). It can be seen that the length

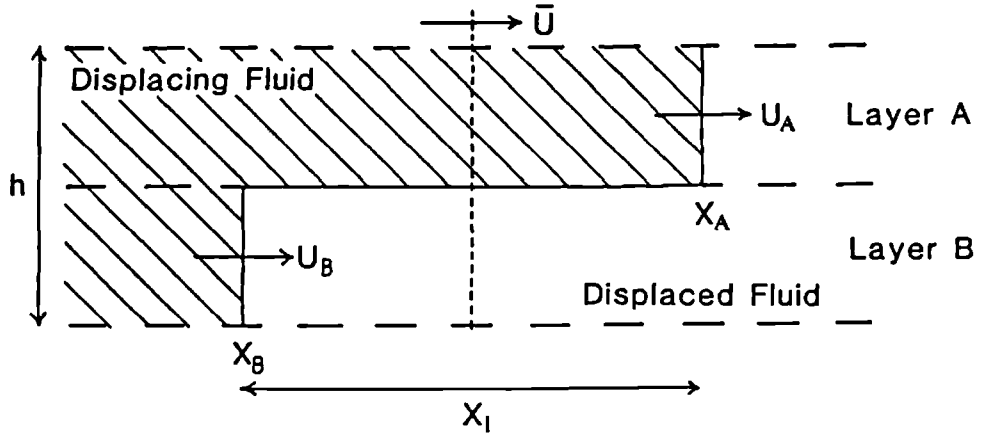

Figure 6.2 Dual layer model showing the length of the fluid/fluid interfaces.

of the lateral fluid/fluid interface across which longitudinal dispersion will act is constant and equal to h. The length of the axial fluid/fluid interface (X_I) across which transverse dispersion will act grows with time, and after time T is:

$$X_I = \frac{(U_A - U_B)T}{L} \quad . \tag{6.1}$$

As the average velocity of the fronts ($\bar{U}$) is:

$$\bar{U} = \frac{U_A + U_B}{2} = \frac{(C_A/C_B + 1)U_B}{2} \tag{6.2}$$

and for equal mobility ratio:

$$\frac{U_A}{U_B} = \frac{C_A}{C_B} \tag{5.1}$$

it follows that:

$$X_I = \frac{2\bar{U}T}{L}\left(\frac{C_A/C_B-1}{C_A/C_B+1}\right) \quad . \qquad (6.3)$$

Thus the length of the axial fluid/fluid interface is proportional to twice the average distance travelled by the fronts ($2\bar{U}T/L$) and a conductance term. This term accounts for the heterogeneity of the system. It will range from zero for homogeneous media ($C_A = C_B, X_I = 0.0$), to almost unity when layer A has a much higher conductance than layer B ($C_A >> C_B$).

If we now allow fluid mixing, the amount of microscopic dispersion will be proportional to the length of the fluid/fluid interface over which it can act. The amount of microscopic transverse dispersion compared to microscopic longitudinal dispersion will increase with increasing time and system heterogeneity (ie. as X_I increases). In a homogeneous system longitudinal microscopic dispersion will be the dominant mechanism for fluid mixing for an equal viscosity and density displacement where there will be a piston type displacement front (figure 2.2). But whenever the displacement front takes on a heterogeneous character (eg. in displacements dominated by viscous fingering, gravity tonguing or stratification) microscopic transverse dispersion effects will increase.

The component concentration, c_i, at any point and at any time in a miscible equal density displacement is given by:

$$K_L \frac{\partial^2 c_i}{\partial x^2} + K_t \frac{\partial^2 c_i}{\partial y^2} - U_x \frac{\partial c_i}{\partial x} = \frac{\partial c_i}{\partial T} \quad . \qquad (6.4)$$

Each component will have a similar equation, but for convenience the subscript i will be dropped. Defining the dimensionless parameters:

$$X = \frac{x}{L} \quad , \quad Y = \frac{y}{h} \quad , \quad T^* = \frac{TU_x}{L}$$

equation 6.4 becomes:

$$\ell \frac{\partial^2 c}{\partial X^2} + t^* \frac{\partial^2 c}{\partial Y^2} - \frac{\partial c}{\partial X} = \frac{\partial c}{\partial T^*} \qquad (6.5)$$

where: $\ell = \frac{K_L}{U_x L}$ and $t^* = \frac{LK_t}{U_x h^2}$.

ℓ and t^* are the longitudinal and transverse mixing groups respectively and are commonly used to scale the effects of dispersion [46,58,59,73] . Here t^* applies to a single layer; it is similar to t, the transverse dimensionless time defined as $LK_t / \bar{U}h^2$ (equation 2.36), which is used to scale transverse microscopic dispersion effects in stratified systems. The longitudinal mixing group, ℓ, is the ratio of the time needed for fluid to be moved axially by convection (bulk fluid movement) to that for it to be moved axially by dispersion. Similarly the tranverse mixing group is the ratio of the time needed for fluid to be moved axially by convection to that for it to be moved laterally by dispersion. Thus the larger the numerical value of these groups the greater is the importance of microscopic dispersion relative to axial convection as the mechanism for fluid movement.

Parameter	Units	Scale	
		Reservoir	Long Core Test
K_L	cm^2/sec	$4x10^{-5}$	$4x10^{-5}$
K_t	cm^2/sec	$7x10^{-6}$	$7x10^{-6}$
U_x or $\bar{U}$	cm/sec(ft/D)	$3.52x10^{-4}$(1.0)	$3.52x10^{-4}$(1.0)
L	cm(ft)	$3.05x10^4$(1000.0)	91.44 (3.0)
h	cm(ft)	25.0	0.2
ℓ	Dimensionless	$3.73x10^{-6}$	$1.243x10^{-3}$
t^* or t	Dimensionless	0.97	45.46

Table 6.1 Typical values for reservoir and laboratory long core test paramaters.

Table 6.1 gives values of ℓ and t^* and their constituent parameters for typical reservoir and long core scales. In both cases microscopic longitudinal dispersion is relatively unimportant in comparison to axial convection. On the reservoir scale microscopic transverse dispersion and axial convection are of equal importance, while on the long core test scale microscopic transverse dispersion is the most important mechanism for the movement of fluid. These differences reflect the relative distances over which these mechanisms have to act.

As the value of the longitudinal mixing group is usually small, equation 6.5 shows that the effect of longitudinal dispersion can be neglected whenever d^2c/dx^2 (rate of change of the axial concentration gradient) is small, which is everywhere except at the displacement fronts. Figure 6.3 shows numerically calculated concentration profiles for three different values of the transverse mixing group (ℓ^*) (no microscopic longitudinal dispersion has been included in these calculations; section 6.2). Here the axial dimension, X_I, has been normalised between the frontal positions (X_A and X_B) for the case when there is no fluid mixing (figure 6.2). When fluid component movement by microscopic transverse dispersion is small compared to that due to axial convection (ℓ^*=0.01, figure 6.3a), the concentration distribution is little affected in either layer. Here d^2c/dx^2 is likely to be large at the displacement fronts and so the effect of longitudinal microscopic dispersion cannot be neglected. As transverse microscopic dispersion effects increase compared to axial convection (ℓ^*=0.1, figure 6.3b) the concentration profiles become more distorted. Here d^2c/dx^2 and the effect of microscopic longitudinal dispersion will be less than the previous case. Figure 6.3c (ℓ^*=1.0) illustrates the 'long time solution' phenomenon discussed in section 2.3.5. Here the effect of transverse dispersion has been to create a constant concentration profile across the system. In this case d^2c/dx^2, and the effect of longitudinal dispersion, will be negligibly small.

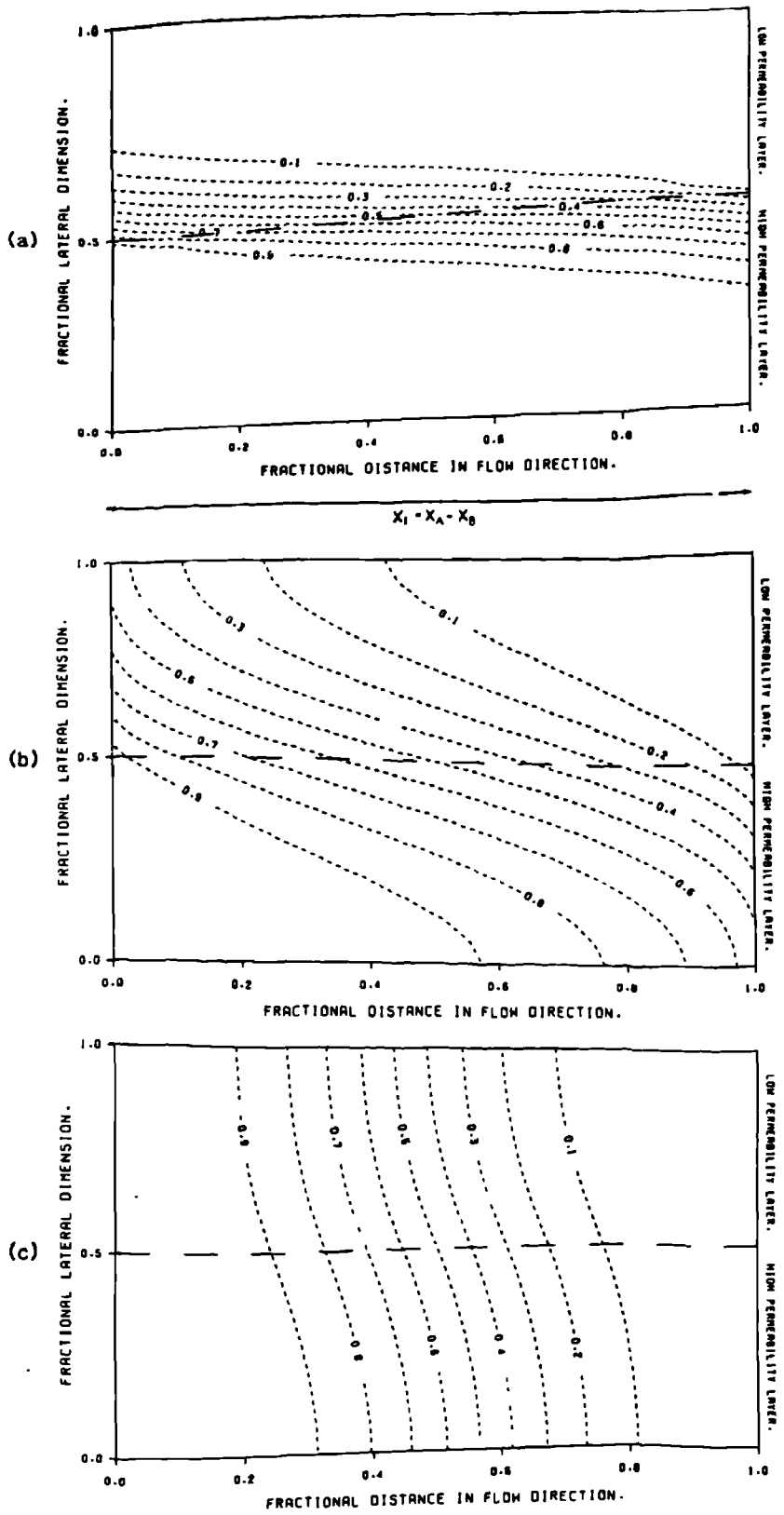

Figure 6.3 Effect of microscopic transverse dispersion on the concentration distribution in dual a layer system.

(a) $t^* = 0.001$ - Very little dispersion.

(b) $t^* = 0.1$ - Moderate dispersion.

(c) $t^* = 1.0$ - Uniform lateral concentration.

It is clear that when $t^* > 0.1$, longitudinal microscopic dispersion will not affect the concentration profiles significantly. Consequently it has been assumed negligible for a large portion of the analyses in this chapter, although it will be shown to distort a number of the effluent profiles at small values of the transverse mixing group (t^*).

6.1.2 Slug Mode Displacements.

The process efficiency of slug mode displacements in stratified systems will depend on how the chemical concentration in the separate portions of the slug are affected by fluid mixing processes after the overtaking point has occurred (figure 5.1d). Koonce and Blackwell[73] studied this case. They modelled component transfer by microscopic dispersion from the slug portion in the high conductance layer both experimentally and numerically, and produced correlations for the fraction of the high conductance layer swept by chemical of concentration above a certain fraction of the injected value; defined as the critical concentration (see figures 10 through 14 reference 73). They did not consider the interaction between the mass transfer from the slug portions in each layer, and so the beneficial effects of the long time solution phenomenon were not included.

The effect of microscopic transverse dispersion on the distribution of the slug chemical is illustrated in figure 6.4. These concentration profiles were calculated numerically (section 6.2) with microscopic longitudinal dispersion neglected. Here the axial dimension, X_{II}, has been scaled between the leading front in the low conductance layer (X_{A1}) and the trailing front in the high conductance layer (X_{B2}) for the case where there is no fluid mixing (figure 5.1). When the amount of fluid component moved laterally by microscopic dispersion is small ($t = 0.015$, figure 6.4a) the chemical concentration in the majority of

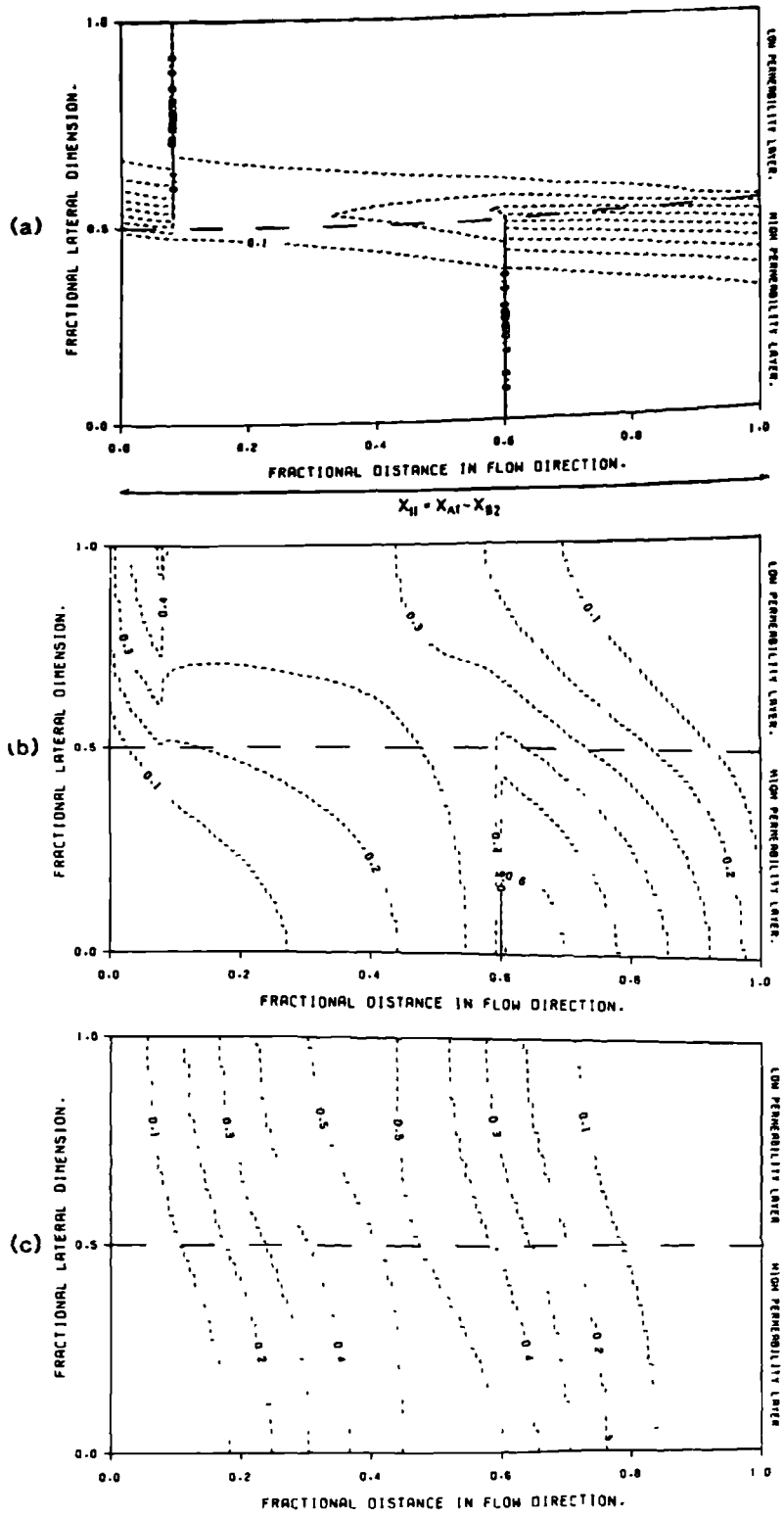

Figure 6.4 Effect of microscopic transverse dispersion on the concentration distribution in a slug mode displacement $C_A/C_B = 5.0$ and $S = 0.209$.

(a) t = 0.015 - Very little microscopic dispersion.

(b) t = 0.460 - Moderate microscopic dispersion.

(c) t = 1.533 - Uniform lateral concentration.

the slug is unaffected and it is only reduced to below the injected value close to the interlayer boundaries. Thus, provided enough chase fluid is injected to displace both slug portions to the production wells, the majority of the system will be swept with chemical equal to the injected concentration and recovery will only be lost due to the chemical being diluted to below its effective level in the region of the interlayer boundary.

As the microscopic transverse dispersion effects increase ($t \approx 0.460$, figure 6.4b) the chemical becomes more dispersed, resulting in portions of the system being swept with more dilute chemical. For example in figure 6.4b where the chemical is only effective at concentrations greater than 50% of its injected concentration (called the critical concentration) very little recovery would be achieved from the low conductance layer. On the other hand if the critical concentration was only 10% then oil would be recovered from the entire system. When the rate of axial fluid component movement by convection is slow compared to that laterally by microscopic dispersion ($t = 1.533$, figure 6.4c), the slug chemical is formed into a bank of constant lateral concentration moving with the averge velocity of the system. This is the long time solution phenomenon discussed in section 2.3.5. It can be seen that if the critical concentration for the process is less than 50% of the injected value, recovery will be achieved from a large proportion of the system. But if it is greater than 50%, oil will be recovered from very little of the system. In summary, it has been shown that as the value of the transverse dimensionless time (t)increases, recovery will initially decrease due to the slug chemical becoming more dilute, but will then increase due to the effect of the long time solution phenomenon.

6.2 Numerical Model.

The interaction between microscopic transverse dispersion and axial convection in a dual layer system has been modelled by a moving co-ordinate approach. As discussed in the previous section microscopic longitudinal dispersion has been assumed negligibly small compared to microscopic transverse dispersion. The moving co-ordinate systems that have been used for the continuous and slug mode injection cases are illustrated in figure 6.5. Note that the normalised length of these systems are equal to the

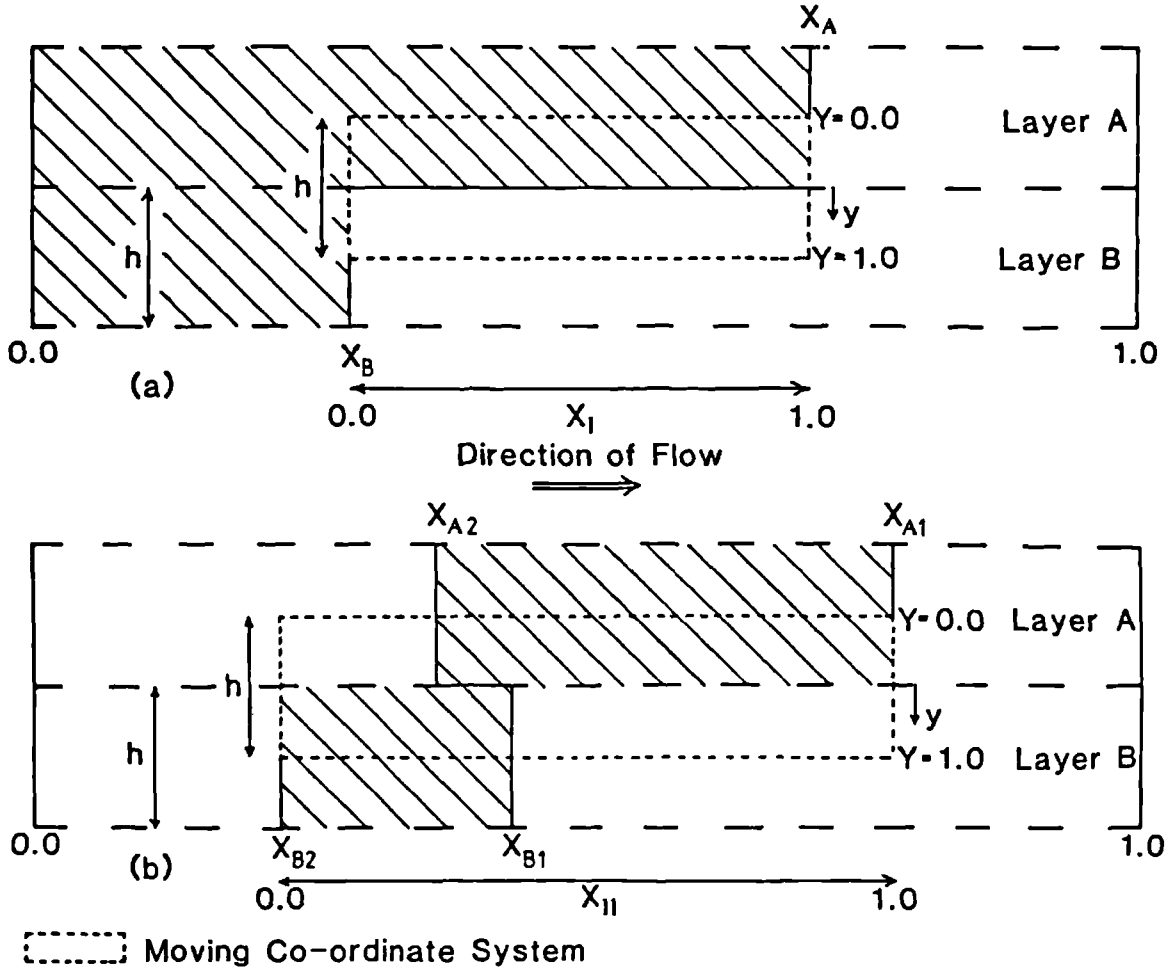

Figure 6.5 Moving co-ordinate systems used to study
(a) continuous and
(b) slug mode injection processes.

length of the longitudinal fluid/fluid interfaces across which microscopic transverse dispersion will act. Here X_I is given by equation 6.3, and X_{II} before the overtaking point occurs, is:

$$X_{II} = 2 \left\{ \frac{C_A/C_B - 1}{C_A/C_B + 1} \right\} (2P+S) \qquad (6.6)$$

and after the overtaking point occurs, becomes:

$$X_{II} = 2 \left\{ \frac{C_A/C_B - 1}{C_A/C_B + 1} \right\} (P+S) + S \qquad (6.7)$$

where S and P are dimensionless slug and chase fluid pore volumes respectively.

Garder et al[74] have shown that the equation describing the component concentration at any point and at any time (equation 6.4), can be reduced by the method of characteristics to:

$$\frac{dx}{dT} = U_x \qquad (6.8)$$

and

$$\frac{dc}{dT} = K_L \frac{\partial^2 c}{\partial x^2} + K_t \frac{\partial^2 c}{\partial y^2} \quad . \qquad (6.9)$$

As microscopic longitudinal dispersion has been neglected the first term on the right hand side of equation 6.9 is omitted, and using the dimensionless parameters Y and t from section 6.1 , equation 6.9 becomes:

$$\frac{dc}{dt} = \frac{\partial^2 c}{\partial Y^2} \quad . \qquad (6.10)$$

Equation 6.8 represents the axial convection of fluid and equation 6.10 the microscopic transverse dispersion of fluid components.

Equation 6.10 has been solved by a Crank-Nicholson procedure having been discretized as:

$$\frac{c_j^{n+1} - c_j^n}{\Delta t} = \frac{1}{2Y^2}\left\{(c_{j+1}^{n+1} - 2c_j^{n+1} + c_{j-1}^{n+1}) + (c_{j+1}^n - 2c_j^n + c_{j-1}^n)\right\} \quad (6.11)$$

giving:

$$c_{j-1}^{n+1} - c_j^{n+1}(2+(1/r)) + c_{j+1}^{n+1} = -c_{j-1}^n + c_j(2-1/r) + c_{j+1}^n \quad (6.12)$$

where j is the block number, n the time step and

$$r = (\Delta t/2Y^2) \ .$$

The necessary boundary conditions are:

$$\frac{dc}{dY} = 0 \qquad \text{at} \qquad Y = 0.0 \quad \text{and} \quad 1.0 \ ,$$

(ie. there are no flow boundaries at the top and bottom edges of the model).

The model simulates the interaction between axial convection and microscopic transverse dispersion by applying the following procedure at each time step. For the unit mobility ratio case U_x in equation 6.8 is constant and the axial convection can be simulated by moving the grid blocks representing layer A forward ($C_A/C_B - 1$) blocks relative to those representing layer B. Note that C_A/C_B in this model must be an integer. The effect of microscopic transverse dispersion is then calculated by solving equation 6.12 across the system. The grid system used in each run was 600 blocks in the x direction by 20 blocks in the y-direction. Typical concentration profiles are shown in figures 6.3 and 6.4.

The moving co-ordinate system was considered to move through a stationary system representing the reservoir (figure 6.5). Thus effluent concentration profiles were obtained as grid blocks from the moving system left the reservoir. In slug mode, the maximum concentration of slug fluid encountered by each grid block comprising the stationary reservoir system was recorded. Integration of these data gave the fraction of the system swept by any critical concentration of slug chemical.

6.3 Continuous Injection Results.

6.3.1 Numerical Calculations.

The model described in section 6.2 has been used to produce effluent profiles for a system with a conductance contrast of 3. A range of transverse dimensionless time (t) values between 0.01 and 3.0 have been studied and the resultant effluent concentration profiles are presented in appendix six. The curves are discontinuous at low values of t because longitudinal dispersion, which modifies the concentration distribution at the sharp fluid/fluid displacement fronts, has been ignored in these calculations. This is the only occasion when the assumption that longitudinal dispersion is negligible is not applicable in heterogeneous systems.

These data have been correlated by a transverse dispersion index[46] :

$$I_{TD} = \frac{q - q_N}{1.0 - q_N} \qquad (6.13)$$

where q_D is the cumulative pore volumes injection when the effluent concentration is 50% of the injection value.

and q_N is the predicted cumulative pore volumes injected in a displacement with no fluid mixing.

For a dual equal thickness layer system:

$$q_N = \frac{1}{2}\left\{1 + \frac{C_B}{C_A}\right\} \quad . \qquad (6.14)$$

When the effect of transverse dispersion is small ($t < 0.01$), q_D tends to q_N and I_{TD} tends to zero. If the effect of transverse dispersion is large ($t > 1.0$), the system acts as

a single layer due to the long time solution effect (figure 6.3c), q_D tends to one pore volume and I_{TD} tends to unity. The variation of I_{TD} with t as calculated by the model is shown in figure 6.6.

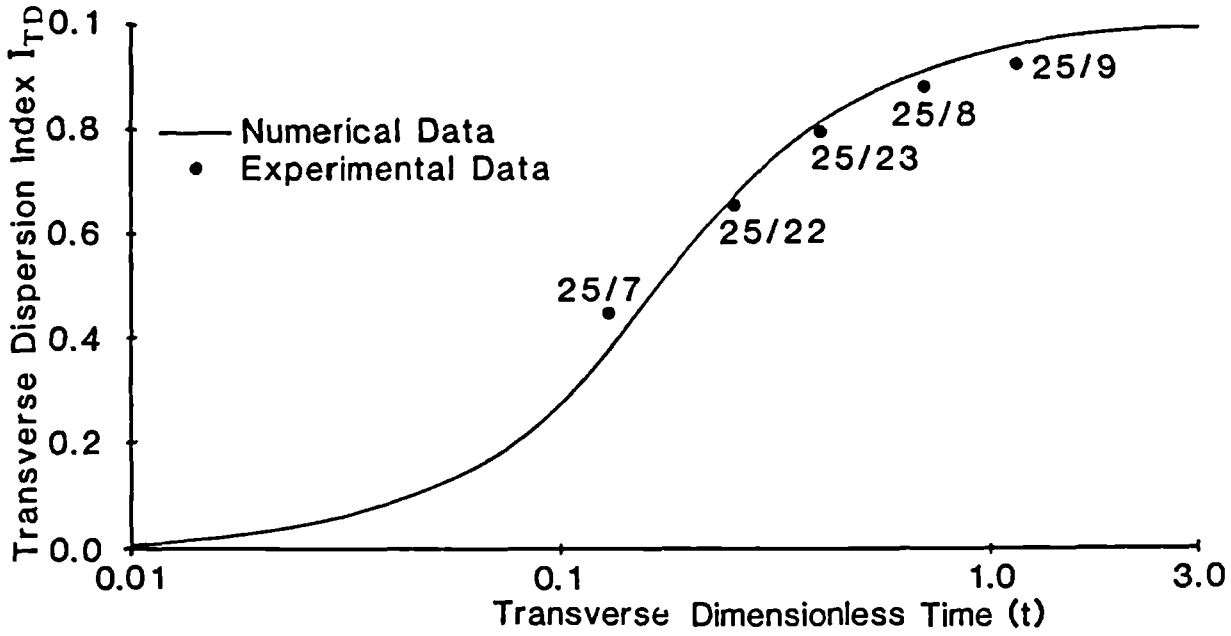

Figure 6.6 Variation of the transverse dispersion index (I_{TD}) with the transverse dimensionless time (t) for continuous injection displacements.

6.3.2 Experimental Results.

The dispersion experiments using the methodology given in chapter three were for a range of average displacement velocities ($\overline{U}$) from 5.78×10^{-4} to 2.65×10^{-2} cm/sec (1.64 to 75.26 ft/day), which are summarised in table 6.2 and the effluent concentration profiles given in appendix six. These data were obtained by a continuous monitoring technique (section 3.4.1) but are shown as points for comparison purposes.

Experimental Run	$\bar{U}$ cm/sec	t dimensionless	K_t cm^2/sec
25/7	2.65×10^{-2}	0.13	3.61×10^{-5}
25/8	1.17×10^{-3}	0.70	5.57×10^{-6}
25/9	5.78×10^{-4}	1.15	4.52×10^{-6}
25/22	6.83×10^{-3}	0.25	1.16×10^{-5}
25/23	2.85×10^{-3}	0.40	7.76×10^{-6}

Table 6.2 Continuous injection experiments to study the effect of dispersion.

The transverse dimensionless time used to scale these experiments was:

$$t = \frac{K_t L}{h^2 \bar{U}} \quad . \tag{6.15}$$

The average interstitial flow rate:

$$\bar{U} = \frac{Q}{A\phi} \tag{6.16}$$

is used here to allow systems with different conductance contrasts to be compared (section 6.6). From section 2.3.3 the microscopic transverse dispersion coefficient (K_t) has two parts; a diffusive element and a convective element:

$$K_t = \frac{D_o}{F\phi} + \alpha_t U \quad . \tag{2.30}$$

α_t contains the parameter, σ, designed to account for the local heterogeneity (pore scale) of the media, which can not be experimentally measured. Therefore it was necessary to match the experimental and numerical effluent concentration profiles, to get a value of t, from which a microscopic

transverse dispersion coefficient was estimated (equation 6.15). These values of K_t are correlated in figure 6.7 against the average displacement velocity ($\bar{U}$). They are in fact average values as the absolute values are different for each layer due to their having different conductances.

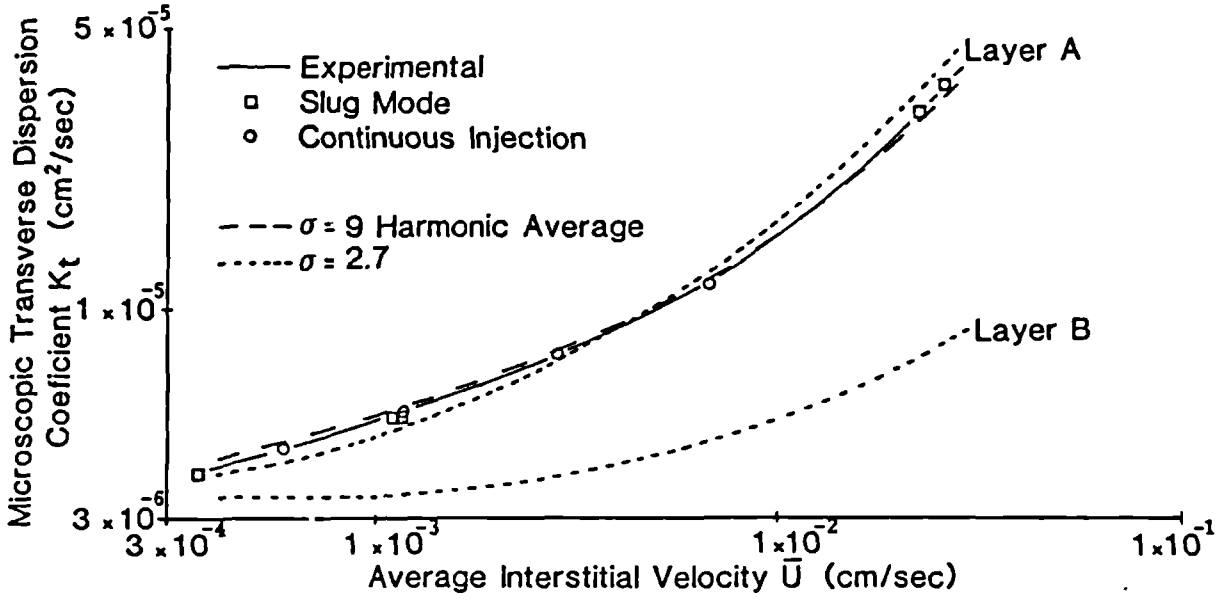

Figure 6.7 Experimentally obtained and predicted relationship between microscopic transverse dispersion coefficient and average displacement velocity.

6.3.3 Discussion of Results.

The effluent profiles in appendix six illustrate the interaction betweeen axial convection and microscopic transverse dispersion. When t is low (t=0.01, figure A6.1) a small amount of displacing fluid has been dispersed from behind X_A (figure 6.2) in the high conductance layer to ahead of X_B in the low conductance layer. As t increases more displacing fluid is dispersed in this way until, when t is large ($t > 1.0$, figures A6.12 and A6.13), the effluent fluid concentration is approximately equal in both layers. The experimental and numerical effluent profiles are

compared in appendix six. The shapes of the corresponding curves show excellent agreement, with microscopic longitudinal dispersion only affecting the experimental profiles when t is small (ie. t=0.13, figure A6.3). Figure 6.6 shows that there is good agreement between the transverse dispersion indices (I_{TD}) obtained numerically and experimentally.

In order to estimate a value for the local heterogeneity factor (σ) it is necessary to average the microscopic transverse dispersion coefficients for each layer which will have different interstitial velocities. Usually this average is taken to be the harmonic mean:

$$\overline{K_t} = \frac{2}{\frac{1}{K_{tA}} + \frac{1}{K_{tB}}} \quad . \qquad (6.17)$$

In order to match the experimental data (figure 6.7) with the harmonic mean a local heterogeneity factor of 9 is required, which is slightly larger than that given by the correlation of Perkins and Johnson (figure 18, reference 41). By assuming that the process is dominated by the dispersion within the high conductance layer the data can be matched with a local heterogeneity factor of 2.7, which is a more reasonable value. Blackwell and Koonce[73] found that this approach produced a much closer agreement between their experimental and numerical data when it was used as the interlayer boundary condition in their numerical model.

6.4 Slug Mode Injection Results.

6.4.1 Numerical Calculations.

Calculations have been performed for slug sizes of approximately 20 and 40 per cent of the pore volume, a range of transverse dimensionless times beteen 0.01 and 3.0 and a conductance contrast of 3. The effluent profiles are presented in appendix seven. They have been correlated by plotting the maximum concentration ($(c/c_o)_{MAX}$) appearing in the effluent against the dimensionless time (figure 6.8).

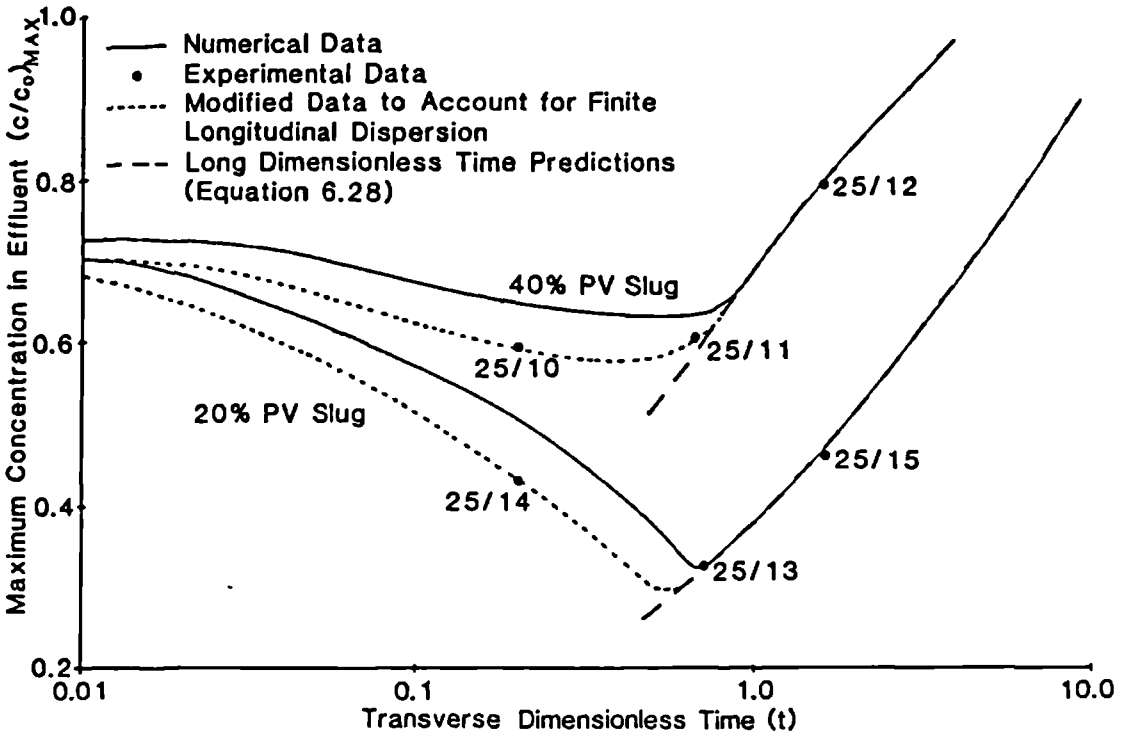

Figure 6.8 Correlation of slug mode injection data.

As longitudinal dispersion has been neglected in these calculations, the effluent profiles at low values of t are more angular and have slightly higher maxima than would be expected in practice.

6.4.2 Experimental Results.

Three experiments were performed at different rates for each slug size (20 and 40 per cent of the pore volume). These are summarised in table 6.3, correlated in figure 6.8, and the effluent profiles are presented in appendix seven. Transverse dispersion coefficients, calculated by the method discussed in section 6.3.2, are correlated with those calculated for the continuous injection experiments in figure 6.7.

Exp. Run	S Dim'less	$\overline{U}$ cm/sec	t Dim'less	K_t cm^2/sec	$(c/c_o)_{MAX}$ Dim'less
25/10	0.40	2.29×10^{-2}	0.20	3.12×10^{-5}	0.59
25/11	0.40	1.19×10^{-3}	0.65	5.43×10^{-6}	0.60
25/12	0.40	3.59×10^{-4}	1.60	3.91×10^{-6}	0.79
25/13	0.20	1.13×10^{-3}	0.70	5.38×10^{-6}	0.33
25/14	0.20	2.65×10^{-2}	0.20	3.61×10^{-5}	0.41
25/15	0.20	3.60×10^{-4}	1.60	3.92×10^{-6}	0.45

Table 6.3 Slug mode injection experiments to study the effect of dispersion.

6.4.3 Discussion of Results.

The effluent concentration profiles for slug mode displacements in appendix seven are summarised in figure 6.9. Although microscopic longitudinal dispersion has been neglected in these calculations it is instructive to consider its effects if it were included. Therefore the influence of this mechanism has been included in the following discussion. Figure 6.9 demonstrates the increasing importance microscopic transverse dispersion plays in the distribution of slug fluid as the transverse dimensionless time (t) increases. When the process is dominated by axial convection ($t \sim 0.0$) the effluent profile can be calculated from simple flow theory (figure 6.9a). Here the initially sharp fluid/fluid interfaces at each end of the slug portions will be modified slightly by microscopic longitudinal dispersion. Provided the slug volumes in each layer are large enough so that the longitudinal mixing zones at each end of a slug portion do not interact,

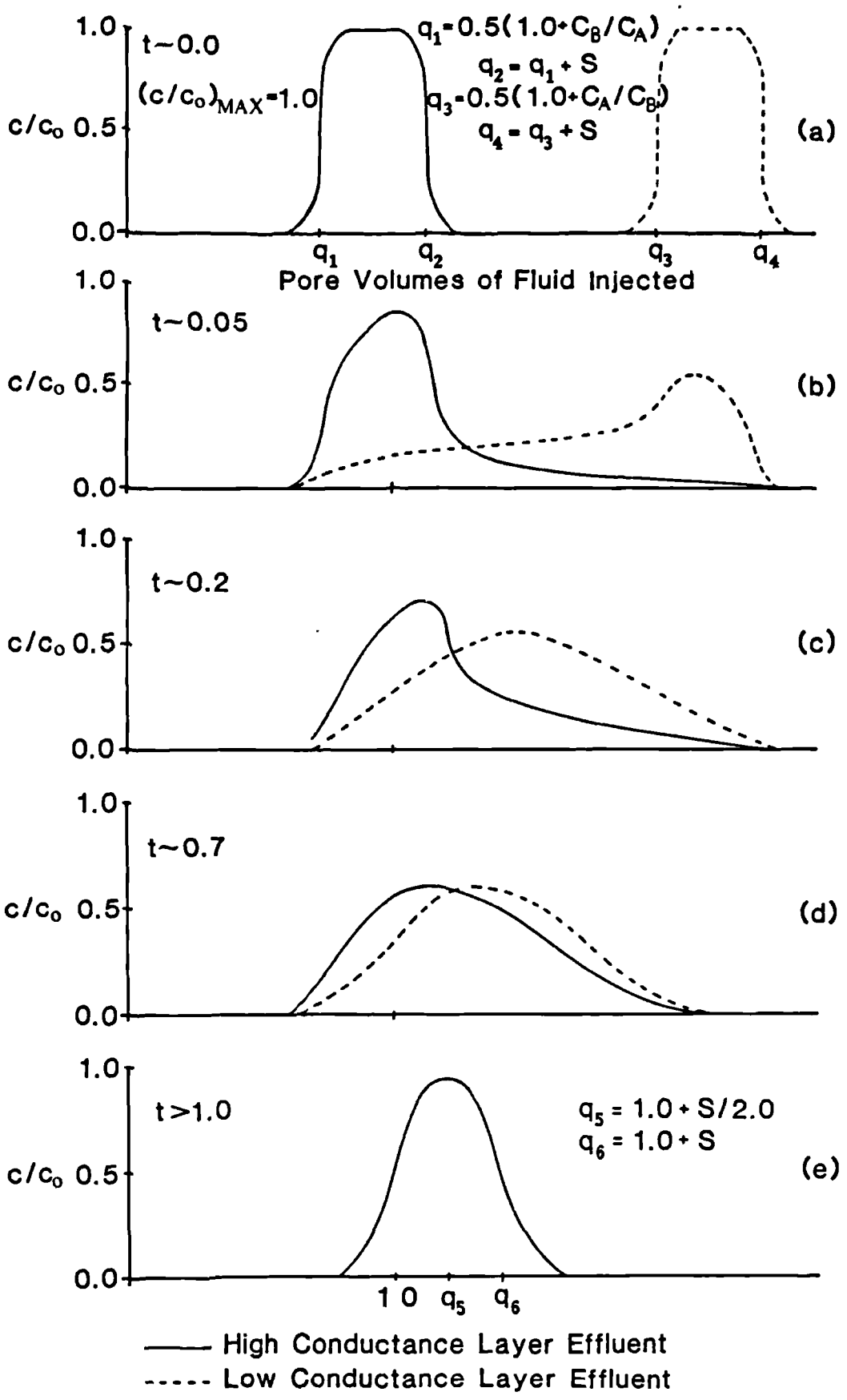

Figure 6.9 Schematic of slug mode effluent concentration profiles.

their maximum concentration will not be affected. However as the slug fluid is not distributed evenly between the layers (figure 5.1) in some cases (large conductance contrasts and/or small slug sizes) the maximum slug concentration in the low conductance layer may be reduced by microscopic longitudinal dispersion alone. To avoid this occurring, slug volumes used in this work were large enough to withstand the deteriorating effect of this mechanism.

As t increases slug chemical is dispersed from the areas of the slug portions next to the interlayer boundary into the adjacent layers (figure 6.4a). This reduces the maximum chemical concentration within each slug portion in the effluent stream (figures 6.9b and 6.9c), with the dispersed fluid component produced at a time intermediate between that of the main slug portions. As the slug portion in the low conductance layer is smaller than that in the high conductance layer, microscopic transverse dispersion has a greater deteriorating effect on it. When t is of the order of 0.7 the majority of chemical has dispersed out of the two main portions of the slug and this dispersed fluid component is produced at an intermediate time (figure 6.9d). It is here that $(c/c_o)_{MAX}$ (the maximum chemical concentration appearing in the effluent) reaches a minimum. Above t= 0.7 the slug fluid appears to become more concentrated in a small area of the system and the maximum concentration in the effluent increases. When t is greater than 1.0 the slug fluid concentration is laterally uniform (figure 6.4c) and the effluent profile (figure 6.9e) has the form of a slug in a one layer system but with an increased degree of longitudinal dispersion.

This variation of the maximum slug chemical concentration in the effluent stream $(c/c_o)_{MAX}$ with the transverse dimensionless time is illustrated in figure 6.8. Here the small amount of longitudinal dispersion in the experimental results has been included; although neglected in the

numerical study as discussed earlier in this chapter. The slug mode experimental and numerical effluent concentration profiles presented in appendix seven show excellent agreement.

6.5 Large Dimensionless Time Models.

When the transverse dimensionless time is greater than 1.0, the two layer system behaves as a single layer system with a larger longitudinal dispersion coefficient (figures 6.3c, 6.4c and 6.9e). This section examines how the effluent profiles for these dimensionless times may be predicted.

6.5.1 Continuous Injection.

For a system consisting of two layers of equal width and porosity, the effective longitudinal dispersion coefficient (K_{Leff}) describing the increased dispersion at large transverse dimensionless times is[46,50] :

$$K_{Leff} = \bar{K}_L + \frac{1}{12}\frac{L\bar{U}}{t}\left(\frac{C_A/C_B-1}{C_A/C_B+1}\right)^2 \qquad (2.37)$$

where $\bar{K}_L$ is the thickness-weighted average longitudinal dispersion coefficient. This equation consists of a longitudinal and a transverse dispersion term. In the numerical model (section 6.2) longitudinal dispersion has been neglected, and it can be seen when this assumption is justified by comparing the magnitude of the two constituent parts of equation 2.37. From table 6.4 it is clear that while the longitudinal microscopic dispersion effect can be neglected on the field scale it must be taken into account in the experimental displacements, although its effect may be small.

Equation 2.24 describes the concentration distribution in one dimension due to longitudinal dispersion (figure 2.13). This equation can be modified to give the effluent

Units cm^2/sec	$\bar{K}_L$	$\frac{1}{12}\frac{L\bar{U}}{t}\left(\frac{C_A/C_B-1}{C_A/C_B+1}\right)^2$
Laboratory Scale	$1x10^{-5}$	$7x10^{-5}$
Field Scale	$1x10^{-5}$	0.1

Table 6.4 Comparision of the magnitude of the constituent parts of equation 2.37 (C_A/C_B=3.0, t=3.0).

concentration profile due to the long time solution phenomenon, such that:

$$\frac{c}{c_o} = \frac{1}{2}\left[1.0 - \text{erf}\left\{\frac{1.0-q}{2\sqrt{q\ell_{eff}}}\right\}\right] \qquad (6.18)$$

where q is the dimensionless pore volumes injected and ℓ_{eff} is the effective longitudinal mixing group:

$$\ell_{eff} = \frac{K_{Leff}}{\bar{U}L} \quad . \qquad (6.19)$$

Neglecting the longitudinal term in equation 2.37, equation 6.19 becomes:

$$\ell_{eff} = \frac{1}{12t}\left\{\frac{C_A/C_B-1}{C_A/C_B+1}\right\}^2 \quad . \qquad (6.20)$$

Effluent profiles calculated numerically and by equations 6.20 and 6.18 are compared in figure 6.10.

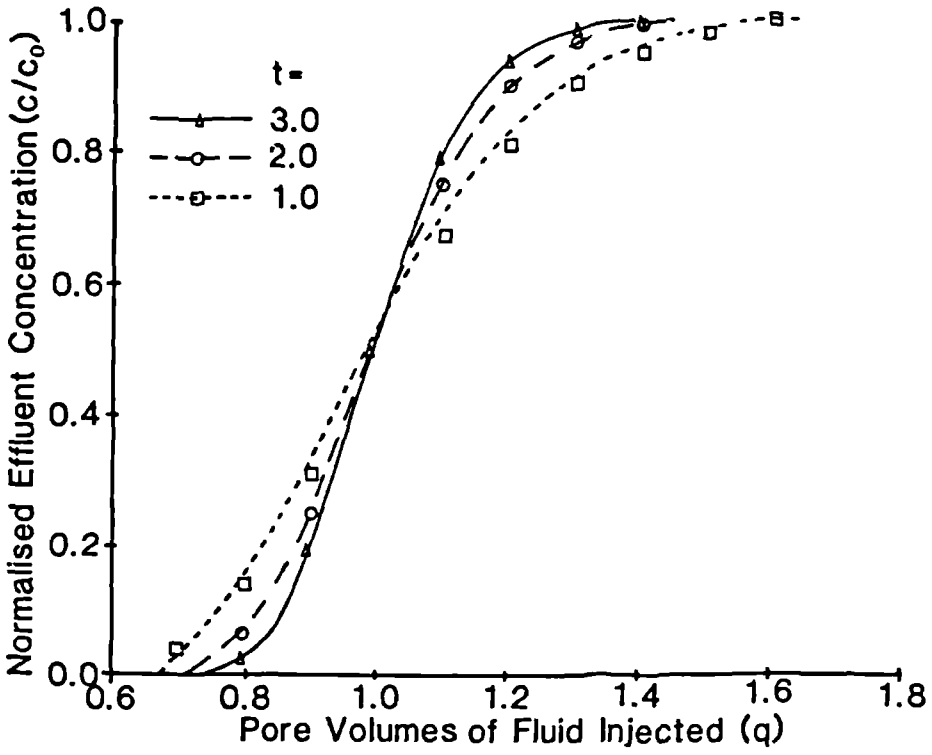

Figure 6.10 Comparison of numerically (lines) and analytically (points) calculated effluent profiles for continuous injection (C_A/C_B = 3.0).

The length of the longitudinal mixing zone due to longitudinal dispersion alone (defined as between c/c_o=0.1 and c/c_o=0.9) is given by:

$$X_m = 3.625\sqrt{\ell} \quad . \tag{6.21}$$

For the typical reservoir parameters in table 6.1:

$$X_m \sim 7 \times 10^{-3} \quad . \tag{6.22}$$

The length of the mixing zone due to the long time solution phenomenon is obtained by combining equations 6.19 and 6.21:

$$X_{meff} = 1.046 \left\{\frac{C_A/C_B-1}{C_A/C_B+1}\right\} \frac{1}{\sqrt{t}} \tag{6.23}$$

where X_{meff} is the length of the longitudinal mixing zone created by the long dimensionless time phenomenon. For a reservoir heterogeneity of C_A/C_B=10.0:

$$X_{meff} \sim \frac{0.856}{\sqrt{t}} \quad . \qquad (6.24)$$

Therefore as t increases the length of this mixing zone decreases (figure 6.10), and comparison with equation 6.22 shows that the effective longitudinal mixing zone due to the long dimensionless time phenomenon will be much larger than that due to longitudinal dispersion alone. As mentioned in section 2.3.4 this may account for the large values of longitudinal dispersivity measured in the field[43,44].

In section 6.1.1 the distance between the fronts in a non-dispersing displacement was given by equation 6.3, which in dimensionless form is:

$$X_{ID} = 2 \left\{ \frac{C_A/C_B - 1}{C_A/C_B + 1} \right\} \quad . \qquad (6.25)$$

Dividing equation 6.23 by equation 6.25 gives:

$$\frac{X_{meff}}{X_{ID}} = \frac{0.523}{\sqrt{t}} \quad . \qquad (6.26)$$

This result is independent of the degree of heterogeneity of the system (ie. C_A/C_B) and shows that for t=1.0, the mixing zone length due to the long dimensionless time phenomenon is approximately half that for a non-dispersing displacement.

6.5.2 Slug Mode Injection.

The effluent concentration profile for a slug mode displacement is given by:

$$\frac{c}{c_o} = \frac{1}{2}\left[\text{erf}\left\{\frac{q-1.0}{2\sqrt{\ell_{eff}q}}\right\} - \text{erf}\left\{\frac{(q-S)-1.0}{2\sqrt{\ell_{eff}(q-S)}}\right\}\right] \quad . \quad (6.27)$$

Figure 6.11 shows effluent profiles calculated numerically and by equations 6.20 and 6.27. It can be shown[58,75] that the maximum concentration in the effluent is given by:

$$\left(\frac{c}{c_o}\right)_{MAX} = \text{erf}\left[\frac{S}{4\sqrt{\ell_{eff}}}\right] \quad . \quad (6.28)$$

$(c/c_o)_{MAX}$ values calculated by equations 6.20 and 6.28 are compared to the numerical and experimental data in figure 6.8. Equation 6.28 gives good agreement when $t > 1.0$. The slug volume required to sweep the entire system with a chemical concentration of $(c/c_o)_{CRIT}$ is obtained by rearranging equation 6.28, thus:

$$S_{OPT} = 4(\text{erf}^{-1}(c/c_o)_{CRIT})\sqrt{\ell_{eff}} \quad . \quad (6.29)$$

Equation 6.29 is presented graphically in figure 6.12 for conductance contrasts of 3 and 11 and a range of $(c/c_o)_{CRIT}$ values from 0.1 to 0.9. Clearly the required slug volume increases as $(c/c_o)_{CRIT}$ and (C_A/C_B) increases and t decreases and $(c/c_o)_{CRIT}$ is an important parameter.

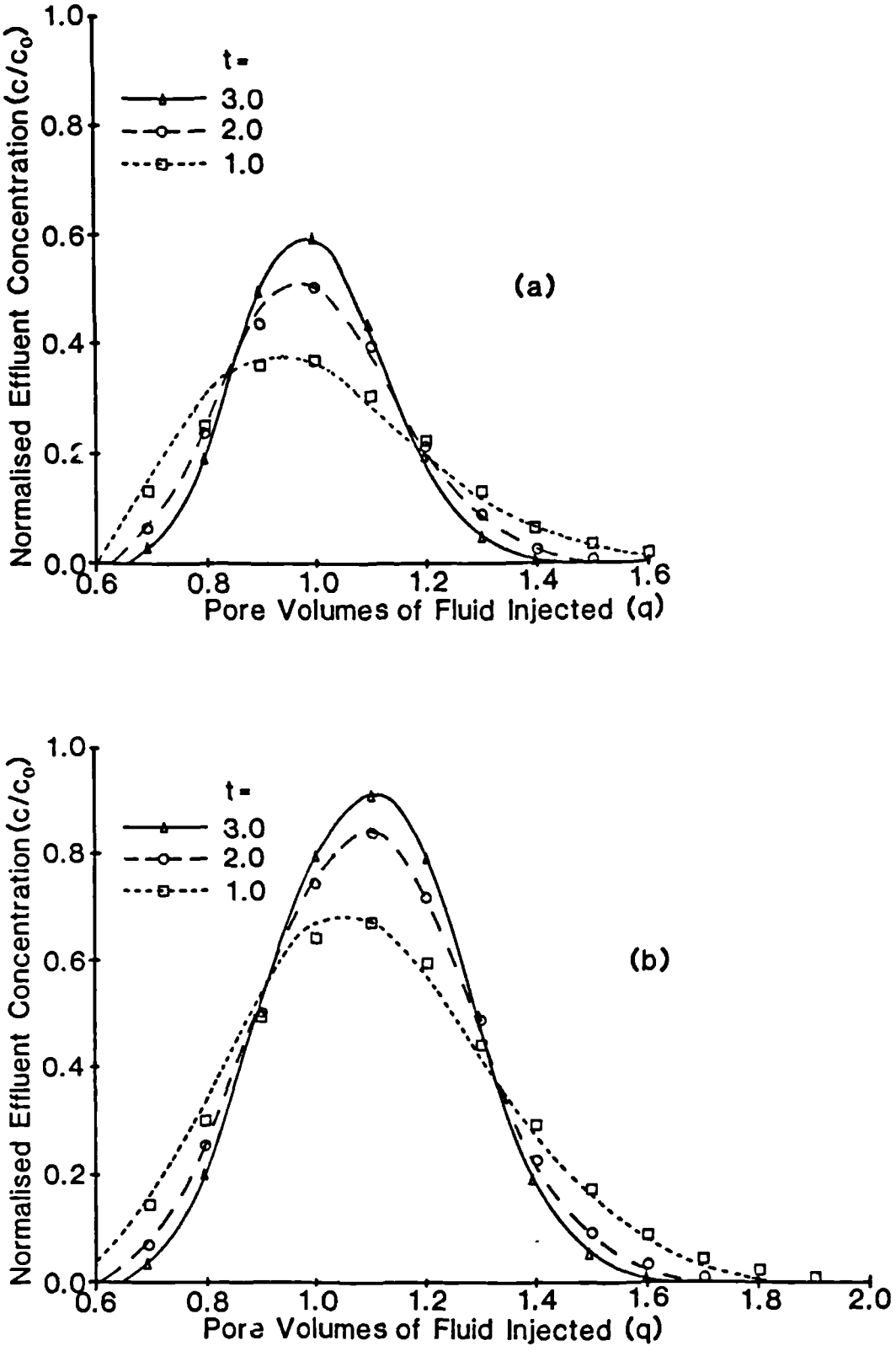

Figure 6.11 Comparison of numerical (lines) and analytical (points) effluent profiles for displacements with slug volumes of (a) 19.92 and (b) 39.83 per cent of the pore volume (C_A/C_B = 3.0).

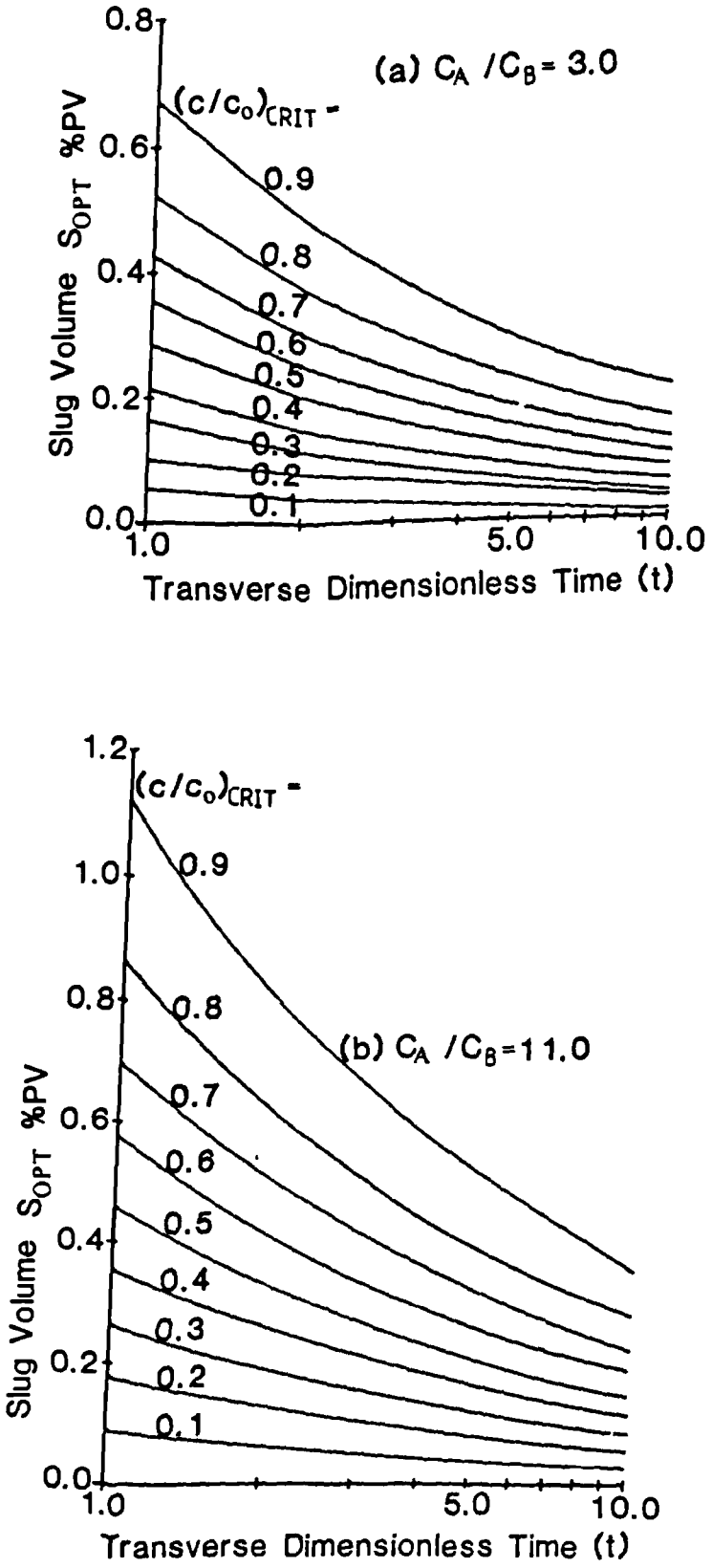

Figure 6.12 Graphical representation of equation 6.29.

6.6 Prediction of the Volume of the Reservoir Swept in Slug Mode Processes.

When the concentration of a chemical in an EOR chemical process is reduced to below a critical value, $(c/c_o)_{CRIT}$, residual oil will not be mobilised and the additional enhanced recovery will not be achieved. During the planning stage of an EOR process it is necessary therefore to calculate the volume and injection concentration of chemical (c_o) of the slug such that it will sweep the reservoir satisfactorily. This section examines this problem.

The numerical model (section 6.2) has been used to predict the proportion of a layered system swept by various slug sizes, where the critical concentration of chemical ranges from $0.1c_o$ to $0.9c_o$ for a number of conductance contrasts. These results are presented graphically in appendix seven, after one pore volume of fluid (slug plus chase) has been injected and when all the slug fluid has been displaced from the system; which can be a number of pore volumes in some cases. This later stage is called ultimate injection (q_{ULT}) and for a dual layer system is:

$$q_{ULT} = (1-b) + \frac{bC_A}{C_B} + S \quad . \qquad (6.30)$$

For both one pore volume injected and ultimate injection, the area of the system over which a certain critical concentration is effective is an inverse function of the critical value for all t values. For example, for the ultimate injection case when C_A/C_B =11.0, S= 0.39 and t=0.5 the area swept by a critical concentration of $0.7c_o$ is 46% PV while the area swept by a critical concentration of $0.4c_o$ is 91% PV. The area swept is also a function of the transverse dimensionless time (t), and

hence the average flow rate ($\overline{U}$), microscopic transverse dispersion coefficient (K_t), layer width (h) and system length (L). For the ultimate injection case, at low ($t < 0.09$) and high ($t > 1.0$) values of t the areas swept are greater than at the intermediate times ($0.09 < t < 1.0$). This is due to the microscopic transverse dispersion effects discussed in section 6.1.2 and 6.4, ie. at low times little transverse dispersion occurs and at long times the lateral concentrations are held constant. The minimum value for the area swept which occurs for t values between 0.09 and 1.0 is very important as it represents the layer width (equation 6.15) which produces the smallest fraction of the system swept, and hence lowest recovery. The graphs in appendix seven show that this value of t increases with increasing slug size and decreasing conductance contrast and critical concentration.

Numerical calculations after one pore volume of fluid has been injected are also presented in appendix seven. These may be useful for field applications since the reservoir may have to be abandoned due to economic factors before ultimate injection is achieved. Here the curves for $t > 0.1$ are similar to those for ultimate injection. For $t > 1.0$ this occurs because the bank of constant lateral concentration which is maintained by transverse dispersion for those values of t moves at the average velocity of the system, therefore the majority of the system will have been swept by chemical when one pore volume of fluid (slug plus chase) has been injected. Between t=0.1 and 1.0 the maximum recovery for each critical concentration is achieved before one pore volume of fluid has been injected due to the unfavourable fluid mixing which occurs in this region. As t decreases below 0.1 the curves for each critical concentration tend towards the value of the system swept at one pore volume injected for a non dispersing system ($E_{1.0}$), which for a

dual layer system is:

$$E_{1.0} = b + \frac{(1-b)}{(1-b) + \frac{bC_A}{C_B}} \quad . \qquad (6.31)$$

Figure 6.13 shows layer widths (h) as a function of transverse dimensionless time (t) calculated from equation 6.15, with the time to inject one pore volume of slug and chase fluid ($L/\overline{U}$) as a variable. In reservoir rock and at reservoir rates (< 1ft/day) and conditions, the microscopic transverse dispersion coefficient is of the order of $7 \times 10^{-6} cm^2/sec$ (section 2.3.3). As the value of t which causes the minimum fraction of the system to be swept lies between 0.09 and 1.0, figure 6.13a shows the range of layer widths which will cause the lowest recovery. For example, when the time to inject one pore volume of fluid ($L/\overline{U}$) is three years, layer widths between 21.0 and 70.0 cm, with conductance contrasts less than 20.0, may cause the most detrimental fluid mixing. Conductance contrasts larger than about 20 will need to be treated with pore blocking polymers if they are not to negate the use of EOR processes altogether. Figure 6.13b shows that in long core test experiments where the media is stratified, microscopic transverse dispersion will be the dominant mechanism influencing chemical concentration distribution, even if the stratification is only a few millimeters.

During the planning stages of a chemical EOR process both slug volume(s) and the chemical injection concentration are variables. If, for example, the chosen chemical needs to contact the residual oil at a concentration of X g/l, then for a fixed quantity of chemical there will be a range of injection policies. Two of these are given in table 6.5 as examples.

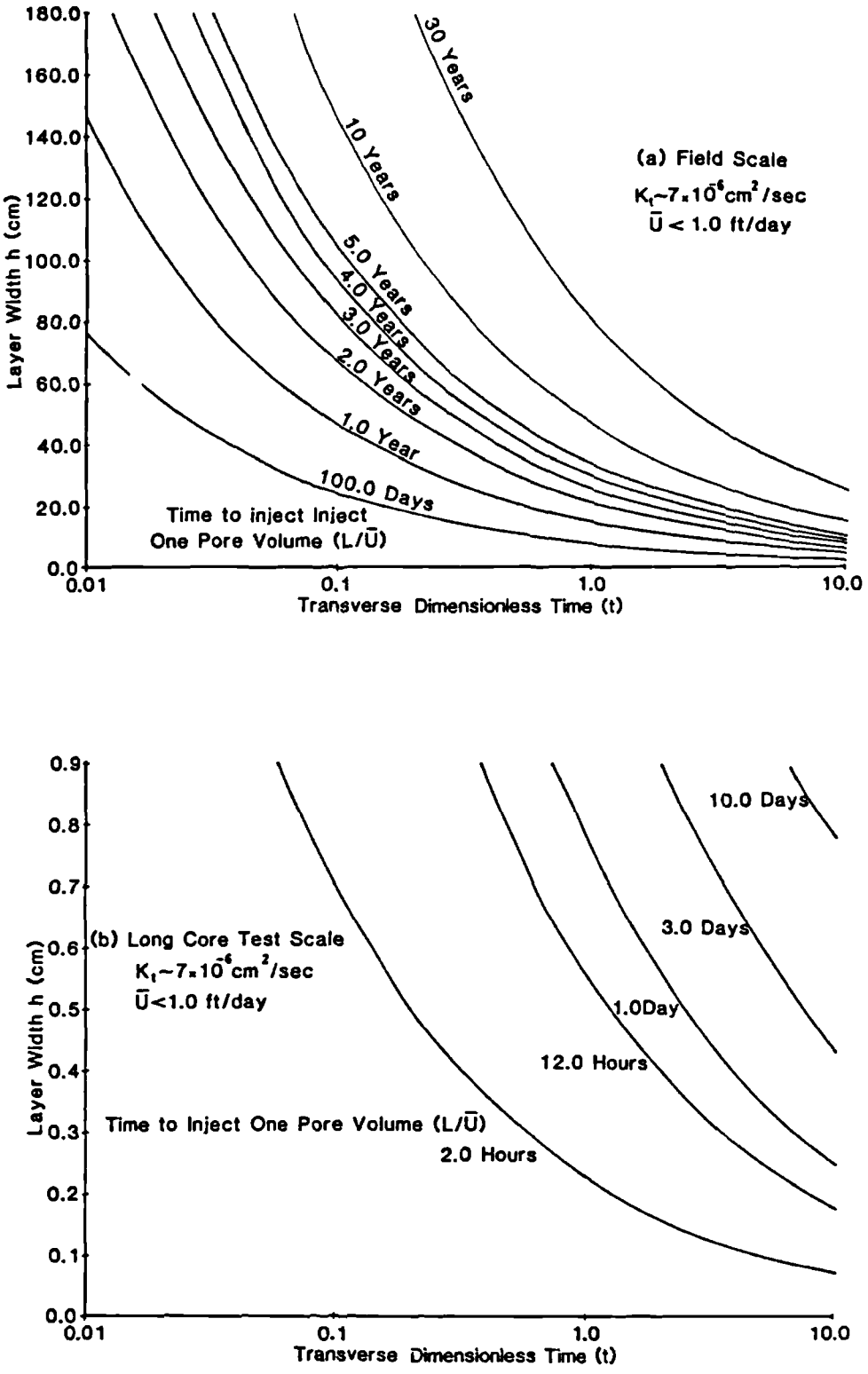

Figure 6.13 Layer width as a function of transverse dimensionless time for the field and long core test scales.

Critical Concentration	Slug Volume	Injection Concentration
$(c/c_o)_{CRIT}$	S	(g/l)
Case One		
1.0	1.0	X
0.8	0.8	1.25X
0.6	0.6	1.67X
0.4	0.4	2.5X
0.2	0.2	5.0X
Case Two		
1.0	0.5	X
0.8	0.4	1.25X
0.7	0.35	1.43X
0.6	0.3	1.67X
0.5	0.25	2.0X
0.4	0.2	2.5X

Table 6.5 Possible injection policies for slug mode injection (c_{CRIT} = X g/l).

Figure 6.14 shows data cross-plotted from the numerical model results in appendix seven, for a conductance contrast of 11.0. Comparison of the injection policies in table 6.5 and figure 6.14 show that, for the range of data considered, it may be more advantageous to inject small concentrated slugs of chemical rather than large dilute slugs. For example, in a reservoir in which it takes 3 years to inject one pore volume of fluid, transverse dimensionless times of 0.05, 0.2, 0.5 and 2.0 correspond to layer widths of 94.0 cm, 58.5 cm, 42.5 cm and 18.5 cm respectively (while if it takes 30 years the corresponding

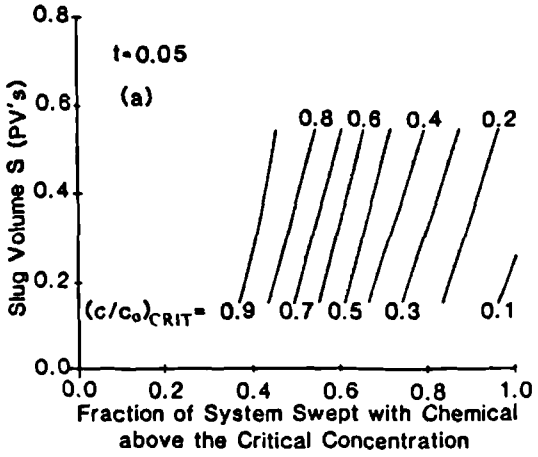

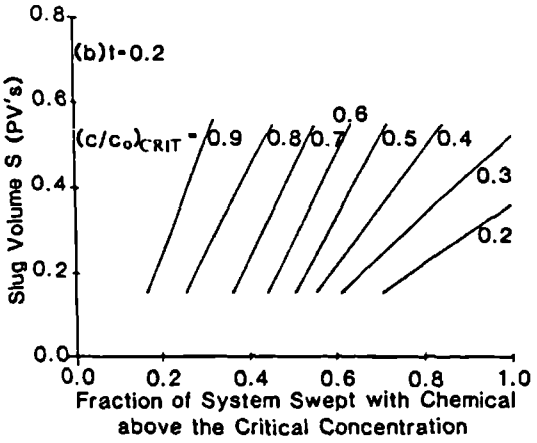

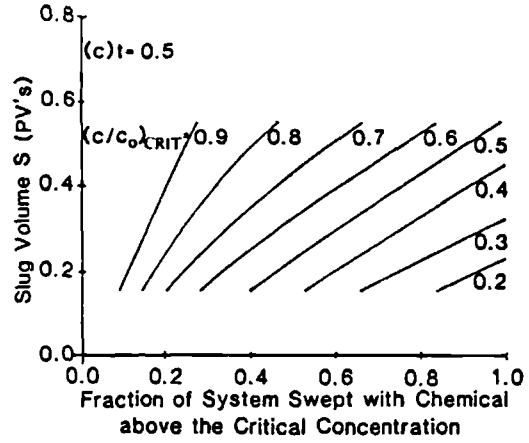

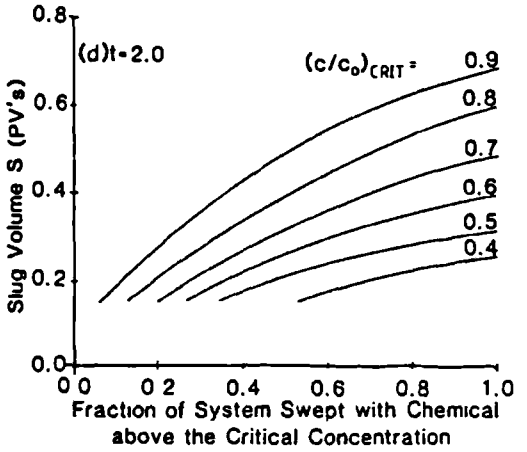

Figure 6.14 Proportion of the system swept by chemical as a function of slug volume for a range of transverse dimensionless times (C_A/C_B = 11.0).

layer widths are approximately three times larger). For these layer widths 68.5, 59.5, 60.5 and 67.0 per cent of the system respectively would be swept by a 20 per cent pore volume slug with critical concentration of $0.4c_o$, while 50.5, 38.5, 32.0 and 51.5 per cent of the system respectively would be swept by a 40 per cent pore volume slug with a critical concentration of $0.8c_o$. Although when a reservoir contains thick layers (ie. $t < 0.1$, $h > 66.5$ cm) large volumes of fluid (equation 6.30) may need to be injected before the maximum sweep is achieved.

CHAPTER SEVEN

THE EFFECT OF DISPERSION IN MISCIBLE LAYERED SYSTEMS WITH FLUIDS OF UNEQUAL MOBILITY

Heterogeneity channelling (chapter four) and viscous fingering are both instabilities in the fluid/fluid displacement front. The rate of growth of the fingered region ($X_A - X_B$) is affected by viscous crossflow and the value of the mobility ratio. In each case axial fluid/fluid interfacial boundaries are produced over which transverse microscopic dispersion may occur. This fluid mixing may alter the effective value of the mobility ratio and in turn further modify the rate of growth of the fingered region. Usually the effects of heterogeneity channelling dominate reservoir displacements, but for unfavourable mobility ratios viscous fingering can also occur, but usually has less influence on gross fluid movement. However much of the published work on this subject has concentrated on the growth of viscous fingers in homogeneous systems, and has been recently reviewed by Stalkup [68]. Here, the more important effect of channelling in heterogeneous reservoirs is examined.

7.1 Previous Work.

When simulating miscible displacements, current computer limitations require that coarse grids are used. This means that the detailed shape of the displacement front within a grid block is not included, and a basic assumption is usually made that the displacing and displaced fluids are homogeneously mixed within the block. This introduces an artificially high level of dispersion into the system which considerably reduces the rate of growth of viscous fingers and heterogeneity channels, resulting in highly optimistic predictions of oil recovery.

Todd and Longstaff[31] proposed to improve the simulation of miscible processes dominated by instabilities in the displacement front with a modified black-oil simulator by assuming partial mixing when calculating fluid viscosities. They considered the flow of displacing and displaced phases in the presence of an immobile water phase, and recommended modifying the relative permeabilities of the mobile phases to:

$$k_{rR} = \frac{S_R}{S_{nw}} \cdot k_{rnw}$$

$$k_{rD} = \frac{S_D}{S_{nw}} \cdot k_{rnw} \qquad (7.1)$$

where $S_{nw} = S_R + S_D$ and $k_{rnw} = k_{rnw}(S_w)$ is the imbibition relative permeability of the non-wetting phase. The degree of mixing of the displacing and displaced phases within each grid block due to microscopic dispersion is characterised by a mixing parameter ω. A value of ω=1.0 corresponds to complete mixing within a grid block, whereas a value of ω=0.0 corresponds to negligible mixing. The effective viscosities are given by:

$$\mu_{Reff} = \mu_R^{1-\omega}\mu_m^{\omega}$$

and (7.2)

$$\mu_{Deff} = \mu_D^{1-\omega}\mu_m^{\omega}$$

where μ_m is given by:

$$\frac{1}{\mu_m} = \left\{ \left(\frac{c_D}{c_o}\right)\left(\frac{1}{\mu_D}\right)^{\frac{1}{4}} + \left(\frac{c_R}{c_o}\right)\left(\frac{1}{\mu_R}\right)^{\frac{1}{4}} \right\}^4 . \qquad (7.3)$$

c_D and c_R are the concentrations of the displacing and resident fluid components respectively. Thus when ω has a value less than one, the effective viscosity of the displacing phase in a given block will be less than the effective viscosity of the oil phase. Displacing phase

will then flow out of the block at a higher velocity than the oil phase, thereby simulating the behaviour of viscous fingering and heterogeneity channelling. Interblock heterogeneities are incorporated in this model by using pseudo-relative permeability curves.

The mixing parameter model is limited by the lack of a theoretical basis for an estimation of ω. Todd and Longstaff [31] estimated ω values that characterised unfavourable displacements in homogeneous laboratory five-spots models with various packings, by comparing computed and experimental recovery data (figure 7.1). The degree of

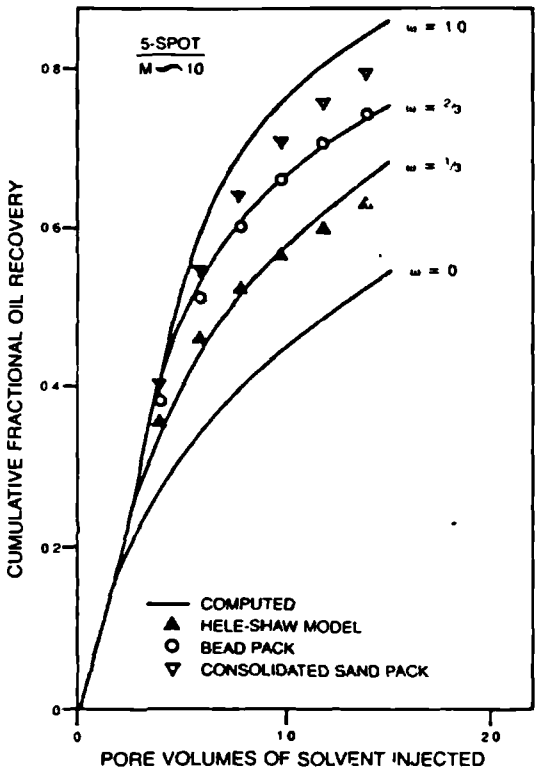

Figure 7.1 Miscible displacement performance in a confined five-spot pattern (after reference 31).

reservoir mixing modelled by these experiments ranged from mixing due to molecular diffusion (Hele-Shaw model) to mixing large enough to be caused by a large degree of macroscopic dispersion (consolidated sand pack). The mixing parameter ranged from a third to greater than two-thirds for the Todd-Longstaff model to span the range of experimental data.

In chapter six it has been shown that the degree of fluid mixing in a layered system increased with increasing time (T), microscopic transverse dispersion coefficient (K_t) and distance travelled (x), and decreasing average interstitial velocity ($\overline{U}$) and wavelength of the instability (h)*. It is therefore reasonable to assume that the mixing parameter for a layered system should be a function of the transverse dimensionles time (t, equation 6.15). For instance when $t < 0.01$, which corresponds to a very early stage in the displacement or to a system with very thick layers, transverse fluid mixing will have little effect, the effective mobility ratio will equal the initial mobility ratio and ω will be very close to zero. On the other hand if $t > 1.0$, which corresponds to the later stages of a displacement in a system with thin layers, transverse fluid mixing will have had a large effect, the effective mobility ratio will be much less than the initial mobility ratio and ω will tend to unity. A relationship between the transverse dimensionless time and the Todd-Longstaff mixing parameter for layered systems is suggested in section 7.3.2.

*For heterogeneity channelling the wavelength of the instability is constant and equal to the layer width (h), but for viscous fingering it is equal to the average finger width which has been shown[25] to increase with time.

7.2 Experimental Results.

Continuous and slug mode experiments (table 3.5) were performed in packing 25 (pattern H, figure 3.2) with fluids of unequal viscosity. Here both viscous crossflow and microscopic transverse dispersion occurred. A tracer monitoring technique (section 3.4.1) was used to follow the concentration variations in the effluent stream. The corresponding effluent profiles are presented in appendix eight.

7.2.1 Continuous Injection Results.

Figures A8.1 through A8.5 show the effect of varying the mobility ratio, for displacements at approximately equal rates. In each case the unfavourable mobility ratio displacement produces earlier breakthrough and a prolonged period of production compared to the unit mobility ratio displacement. While the favourable mobility ratio displacements show the opposite characteristic. This is consistent with the results of viscous crossflow effects given in chapter four.

Figures A8.6 through A8.8 show the effect of varying the average displacement rate for constant mobility ratio. Here the fastest rate produces the earliest breakthrough but longest production period. This is consistent with the fact that the amount of dispersion is inversely proportional to the flow rate; ie. time (chapter six).

7.2.2 Slug Mode Injection Results.

In figures A8.9 through A8.13 displacements with 40% pore volume slug fluid are compared. Cases where the slug fluid is more, less and of equal mobility to the resident

fluid (figure 5.5) are considered. The resident and chase fluids have equal mobilities in all cases (ie. $M_{CR} = 1.0$). Displacements at approximately equal flow rates are shown in figures A8.9 through A8.11. Here the effect of mobility ratio variation is the same as for continuous injection, with the effluent curve portions representing the favourable fronts having steeper gradients than those representing the unfavourable fronts. As the flow rate is decreased the level of dispersion increases and the mobility ratio effects become less pronounced. The maximum concentration in the effluent does not appear to be affected by variation of the mobility ratio.

The effect of varying the flow rate is shown in figures A8.12 and A8.13. Here the pore volumes of fluid injected at breakthrough appears to be only slightly affected by flow rate; which is contrary to the continuous injection results (figures A8.6 through A8.8). This is probably due to the more complex pressure fields produced in slug mode injection processes (chapter five). The maximum concentration of slug fluid in the effluent and the period of production are both clearly affected by displacement rate.

7.3 Modelling Viscous and Dispersive Effects.

7.3.1 The Numerical Model.

The interaction between heterogeneity channelling (chapter four) and microscopic dispersion (chapter six) was examined in a linear two layer system by a numerical model, which is detailed below:

Viscous Forces.

The relative frontal propagation (U_A/U_B) was assumed to be given by equations 2.18 and 2.20 before breakthrough, and equations 4.22 and 4.23 after breakthrough. The value

of the mobility ratio (M) was, as will be shown later, affected by the fluid mixing processes which occurred. Although these approximations assume infinitely thin layers (ie. $h_D \rightarrow 0.0$) they have been shown to give reasonable agreement with the experimental data for h_D values less than 0.1 (figure 4.22); a range of values into which reservoir structures can fall.

Microscopic Transverse Dispersion.

In chapter six it was shown that in stratfied systems, microscopic dispersion in the lateral direction compared to the axial direction had a much greater effect on component distributions. This transverse fluid mixing effect was incorporated in the model by solving equation 6.13 across a grid system between the leading (X_A) and trailing (X_B) displacement fronts (figure 6.5a, section 6.2). This provided a component concentration distribution within the system at each time step.

Coupling Viscous and Dispersive Effects.

Equation 7.3 for the viscosity of the fluid mixture (μ_m) can be rearranged to give:

$$VR_{eff} = \frac{\mu_{MB}}{\mu_{MA}} = \left(\frac{\left(\frac{C_{DA}}{C_o}\right)(VR^{\frac{1}{4}}-1)+1}{\left(\frac{C_{DB}}{C_o}\right)(VR^{\frac{1}{4}}-1)+1} \right)^4 \qquad (7.4)$$

where $VR = \mu_R/\mu_D$.

This relates the effective viscosity ratio between the layers (VR_{eff}) to the average displacing fluid concentration in each layer. Thus in order to calculate a value for the effective viscosity ratio at each time step it was necessary to have an averaged value for the displacing fluid concentration in each layer. Several methods of averaging the component distribution in each layer were tested, the most successful was to average the concentrations at the lateral

edges of the numerical model (figure 6.5a). This would represent the concentrations along the middle of the complete layers if the dual layer model was an element in a repeating series. Figure 7.2 shows how these averaged displacing fluid concentrations vary with the transverse dimensionless time. The resulting relationship between

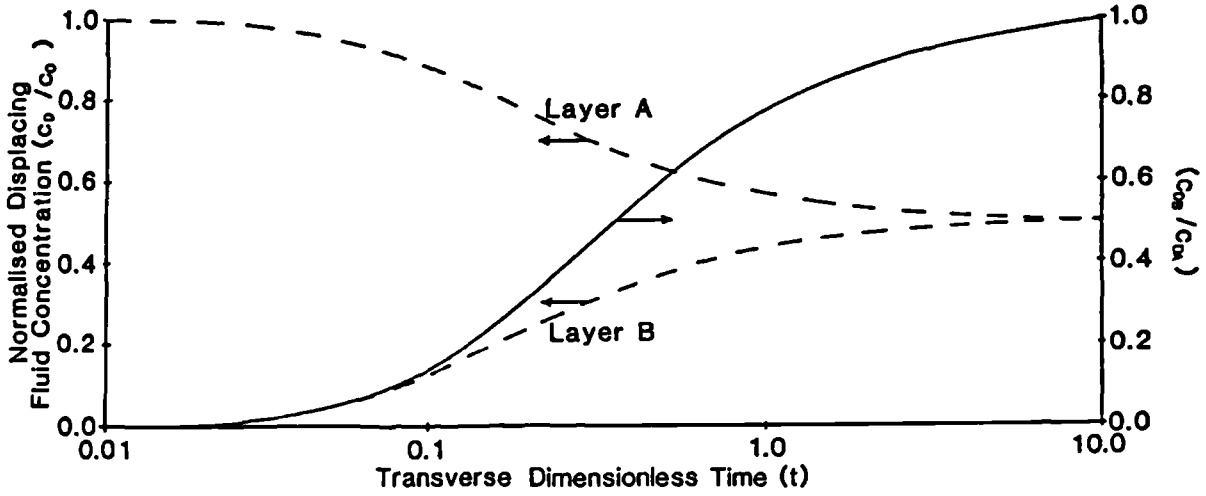

Figure 7.2 Calculated variation of the average displacing fluid concentration with the transverse dimensionless time.

the effective viscosity ratio and t is shown in figure 7.3 for initial viscosity ratios of 2.0 and 10.0. It can be seen that when there is negligible fluid mixing ($t \sim 0.01$) the effective viscosity ratio equals its initial value, but when there is complete mixing ($t > 1.0$) the effective viscosity ratio tends to unity.

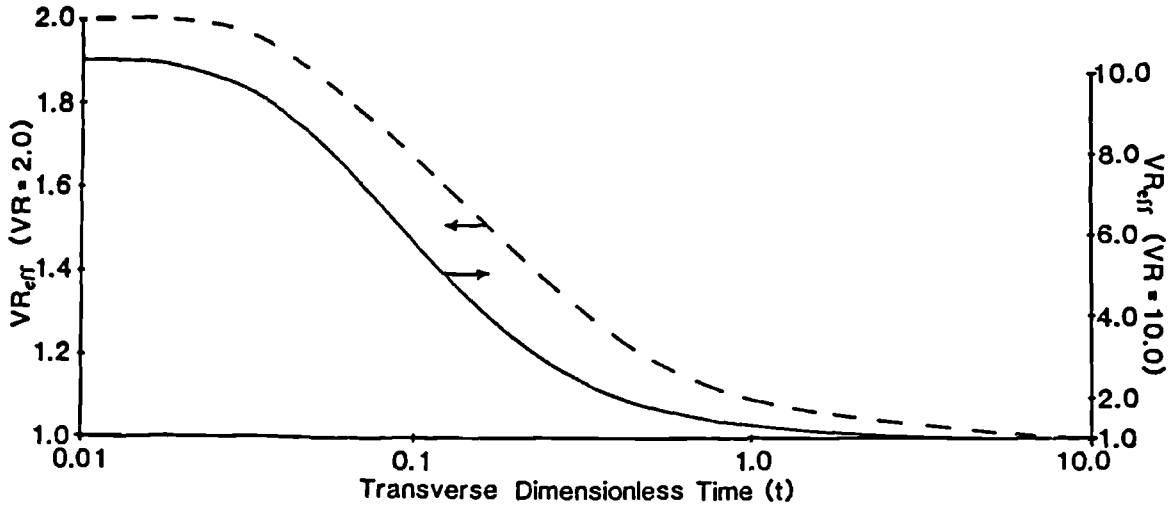

Figure 7.3 Correlation of effective viscosity ratio and transverse dimensionless time for initial viscosity ratios of 2.0 and 10.0.

7.3.2 Comparison with the Mixing Parameter Approach.

From equation 7.2 the effective viscosity ratio following the Todd and Longstaff[31] approach is:

$$VR_{eff} = \frac{\mu_{Reff}}{\mu_{Deff}} = \left(\frac{\mu_R}{\mu_D}\right)^{1-\omega}. \qquad (7.5)$$

Therefore the mixing parameter, ω, can be related to the transverse dimensionless time, t, using equations 7.4 and 7.5 and figure 7.2. The relationship is shown in figure 7.4 for a range of initial viscosity ratios between 1000.0 and 0.001. It can be seen that the mixing parameter varies only slightly with viscosity ratio and can therefore be approximated by:

$$\omega = \frac{B}{B + 1.0} \qquad (7.6)$$

where $B = (t/0.195)^{1.476}$.

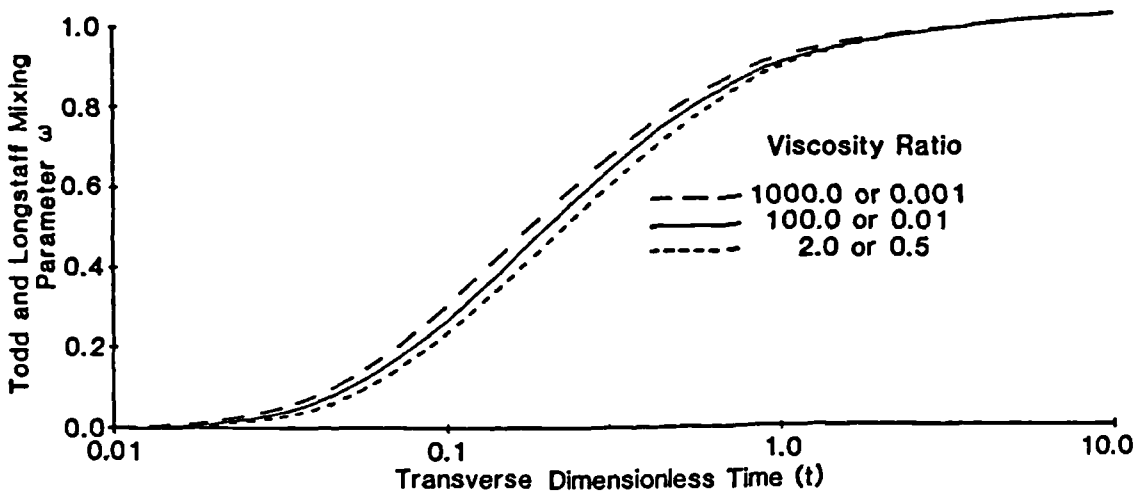

Figure 7.4 Correlation of the Todd and Longstaff mixing parameter with the transverse dimensionless time.

7.3.3 Numerical Results.

The numerical model detailed in section 7.3.1 was validated by using M=1.0. Calculated effluent profiles were compared to those obtained in section 6.3.1 for the effects of dispersion only (figure 7.5). It can be seen that agreement is excellent, although as M=1.0 in these cases fluid mixing has no effect on the viscous forces. Figures 7.6 and 7.7 show the effect of varying the mobility ratio. As this parameter increases, the number of pore volumes of fluid injected to breakthrough decreases and the production period increases. These figures show that this model gives qualitatively good results. In figure 7.8 effluent profiles for a range of t values are compared for non-unit mobility ratio displacements. Here the change

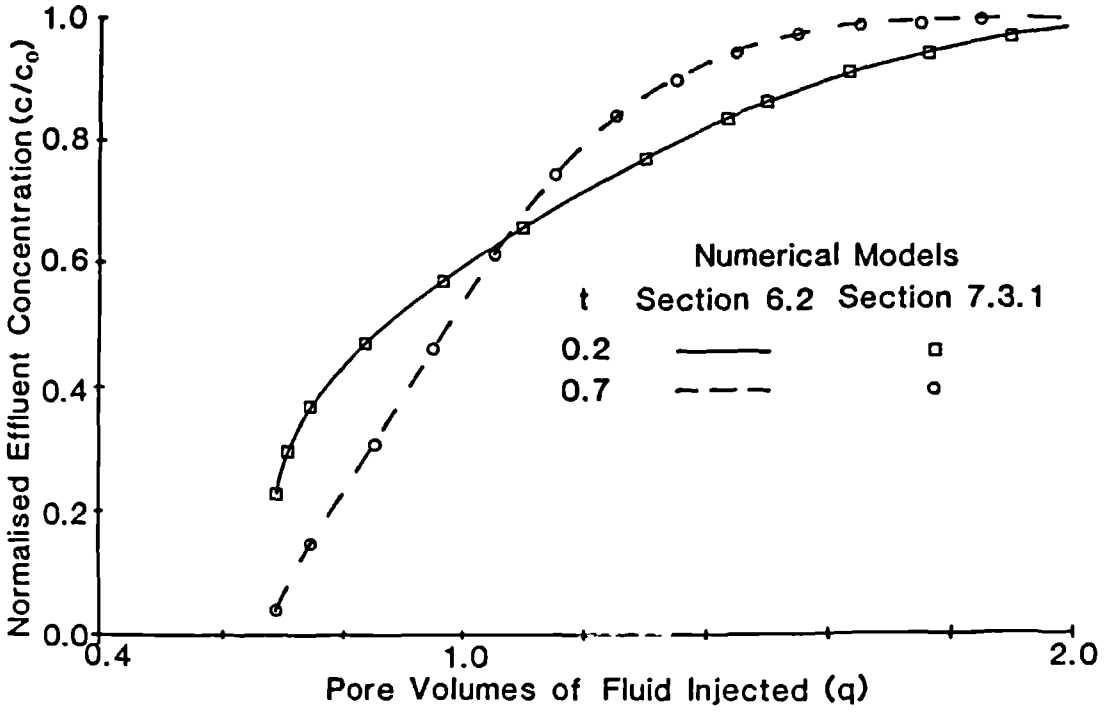

Figure 7.5 Comparison of effluent profiles calculated by the numerical models detailed in sections 6.2 and 7.3.1 (M=1.0, C_A/C_B =3.0).

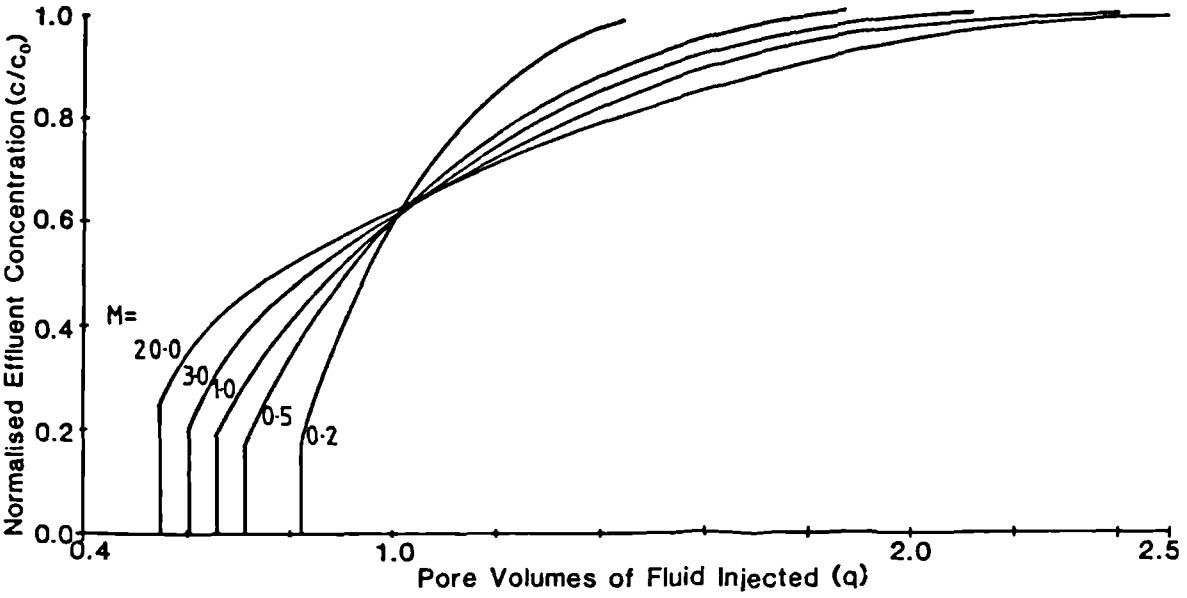

Figure 7.6 Predicted effect of varying the mobility ratio on the effluent curve (C_A/C_B =3.3, t=0.3).

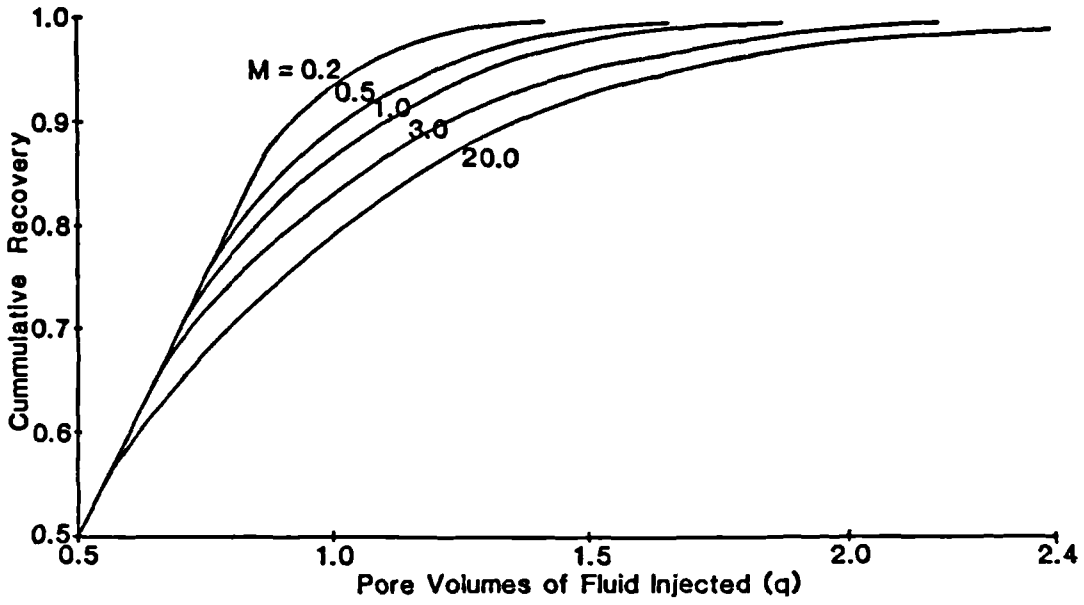

Figure 7.7 Predicted effect of varying the mobility ratio on the cumulative recovery of resident fluid. (C_A/C_B =3.3, t=0.3).

in the relative 'frontal' propagation rate (hence breakthrough time) due to the mobility modifications caused by fluid mixing appear small in comparison to the gross redistribution of injection fluid between the layers due to microscopic dispersion.

An important parameter used to quantify the effects of viscous crossflow in chapters two and four was the fraction of the low conductance layer swept at breakthrough in the high conductance layer; defined as X_B^*. Due to the fluid mixing, fluid fronts are defined here as points of 50% of the injection concentration. Figure 7.9 shows how fluid mixing affects the value of X_B*. When microscopic transverse dispersion is negligible (t < 0.01), X_B* is correctly predicted by equations 2.18 and 2.20, which do not allow for any fluid mixing. As t increases, the

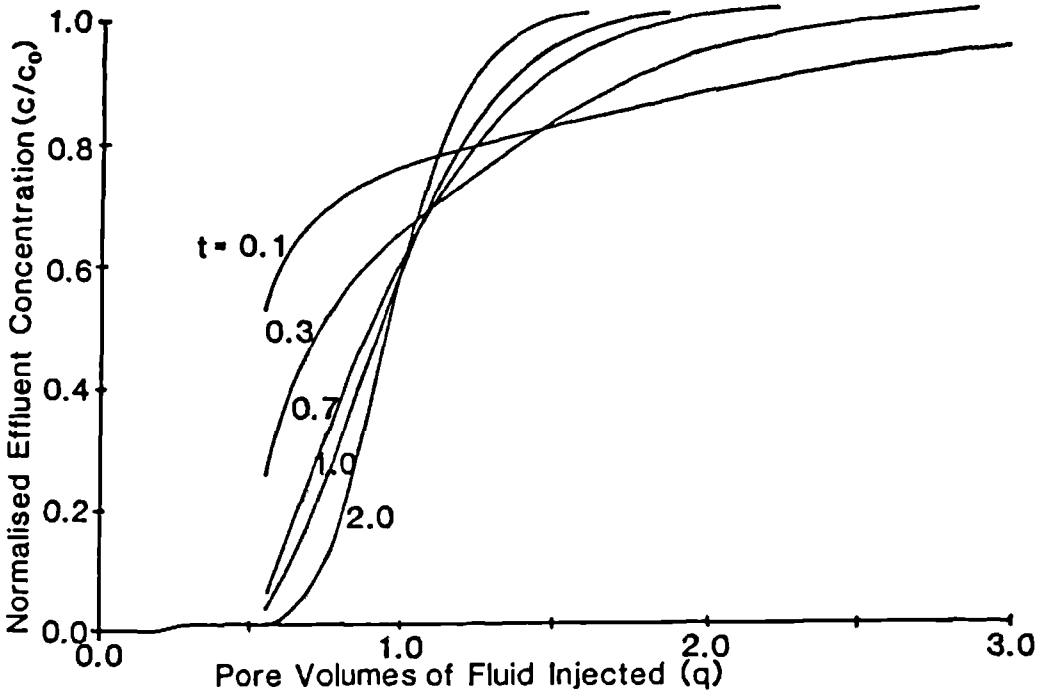

Figure 7.8 Predicted effluent profiles for non-unit mobility ratio displacements (M=10.0, C_A/C_B=5.0).

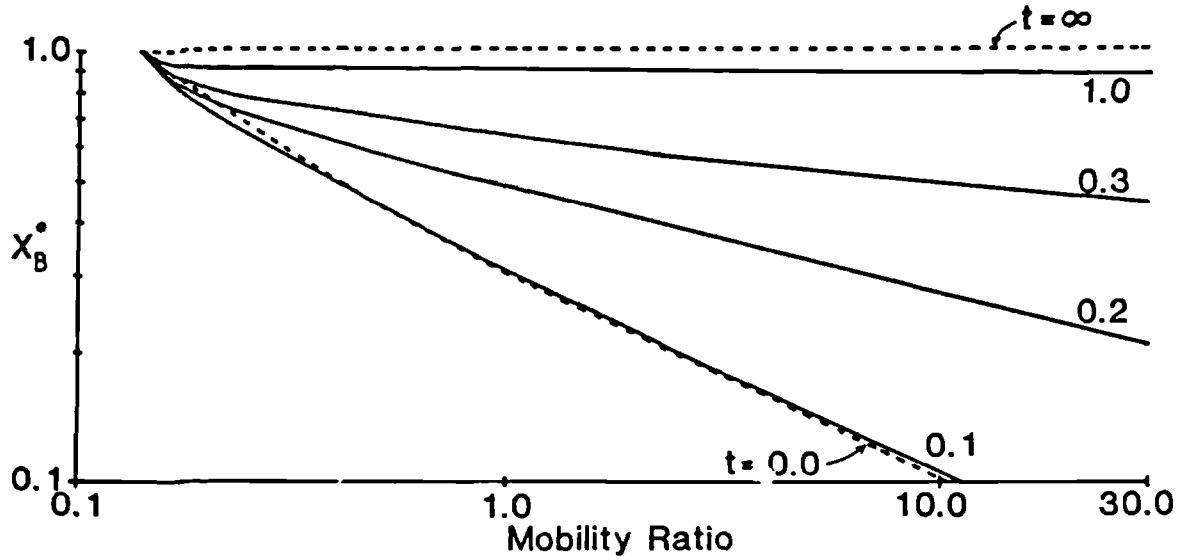

Figure 7.9 Correlation of X_B* against mobility ratio for a range of transverse dimensionless times (C_A/C_B =3.3).

displacements become more favourable with more of the low conductance layer being swept at breakthrough (ie. X_B* increases). When t>1.0, microscopic transverse dispersion dominates the displacement and X_B* tends toward unity (ie. breakthrough occurs simultaneously in all layers). For the conductance contrast considered in figure 7.9, C_A/C_B=3.3, equations 2.18 and 2.20 predict that favourable viscous crossflow will cause a shock front to occur across the system (ie. X_B* =1.0) for a mobility ratio of 0.138. Here there are no axial fluid/fluid boundaries and therefore no transverse fluid mixing may occur. For this reason all the constant t curves converge at X_B* =1.0 and M=0.138. For favourable mobility ratios between 0.138 and 0.3, X_B* values are less than those predicted by the non-dispersing displacement equations (ie. 2.18 and 2.20). In this region the fluid mixing increases the channelling in the high conductance layer above that which would be expected if there was no transverse microscopic dispersion.

7.4 Discussion.

The interaction between viscous forces and microscopic dispersive phenomena in non-unit mobility ratio displacements in stratified media is complex, due to the coupling of these mechanisms. This interrelation is illustrated in figure 7.10. Fluid mixing by microscopic transverse dispersion has two main effects. When t> 0.1 it causes a gross redistribution of fluid components between the layers, the magnitude of which depends on the value of t. This component exchange also modifies the fluid compositions of which the fluid viscosities and hence mobilities are functions.

The effective value of the mobility ratio will modify the value of the effective microscopic dispersion coefficients and the amount of lateral component transfer. In

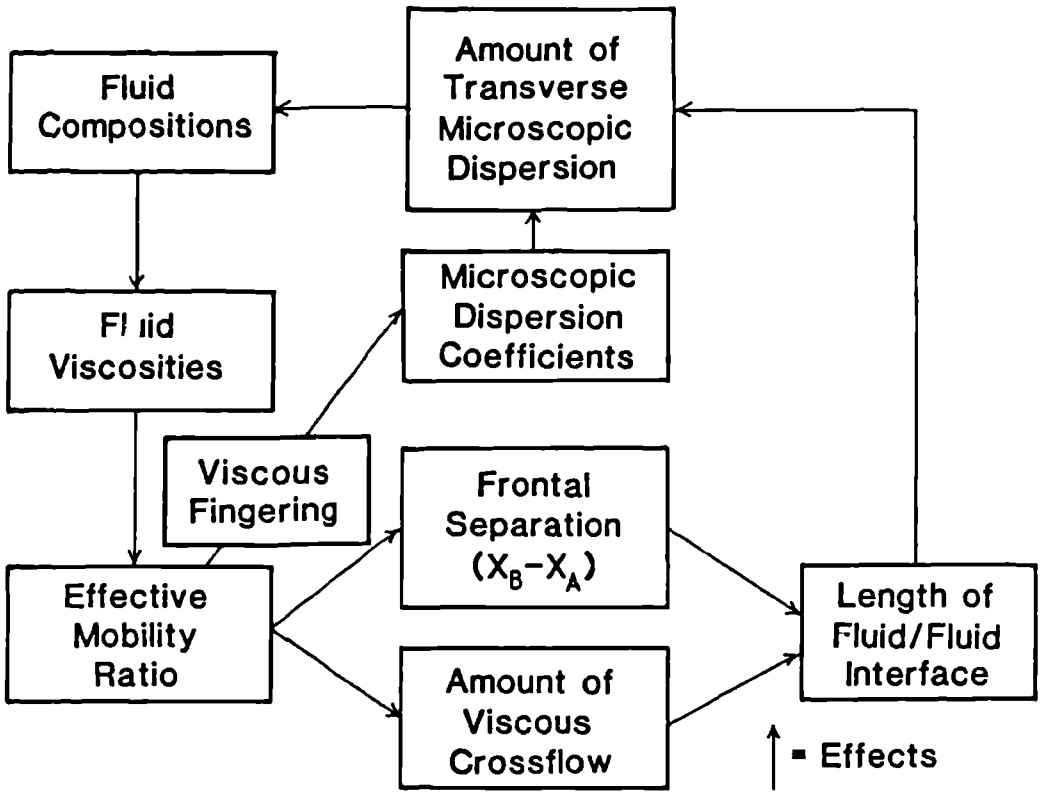

Figure 7.10 Flow chart showing the interaction between viscous forces and microscopic dispersive phenomena.

unfavourable mobility ratio displacements intralayer instabilities occurring at fluid/fluid boundaries will increase the microscopic area for component transfer and hence increase the value of the microscopic dispersion coefficients compared to those expected for equiviscous displacements. Favourable mobility ratios will decrease the value of the effective microscopic dispersion coefficients by reducing the separation between fluid/fluid interfaces inside the pore spaces[41] (ie. reduces the

convective element of dispersion). The length of the axial fluid/fluid boundaries over which lateral component transfer will occur and hence the amount of microscopic transverse dispersion, will be altered by changes in the effective value of the mobility ratio in two ways. Firstly by affecting the relative frontal propagation rate (U_A / U_B) and hence the frontal separation ($X_A - X_B$); and secondly by affecting the amount of viscous crossflow and hence the shape of the interfacial boundaries.

The experimental and numerical effluent profiles are compared in appendix eight. Agreement is good; although it must be noted as the model does not yet fully incorporate all the coupling effects, it was necessary to modify slightly the values for t used in the model to achieve this fit (figure 7.11).

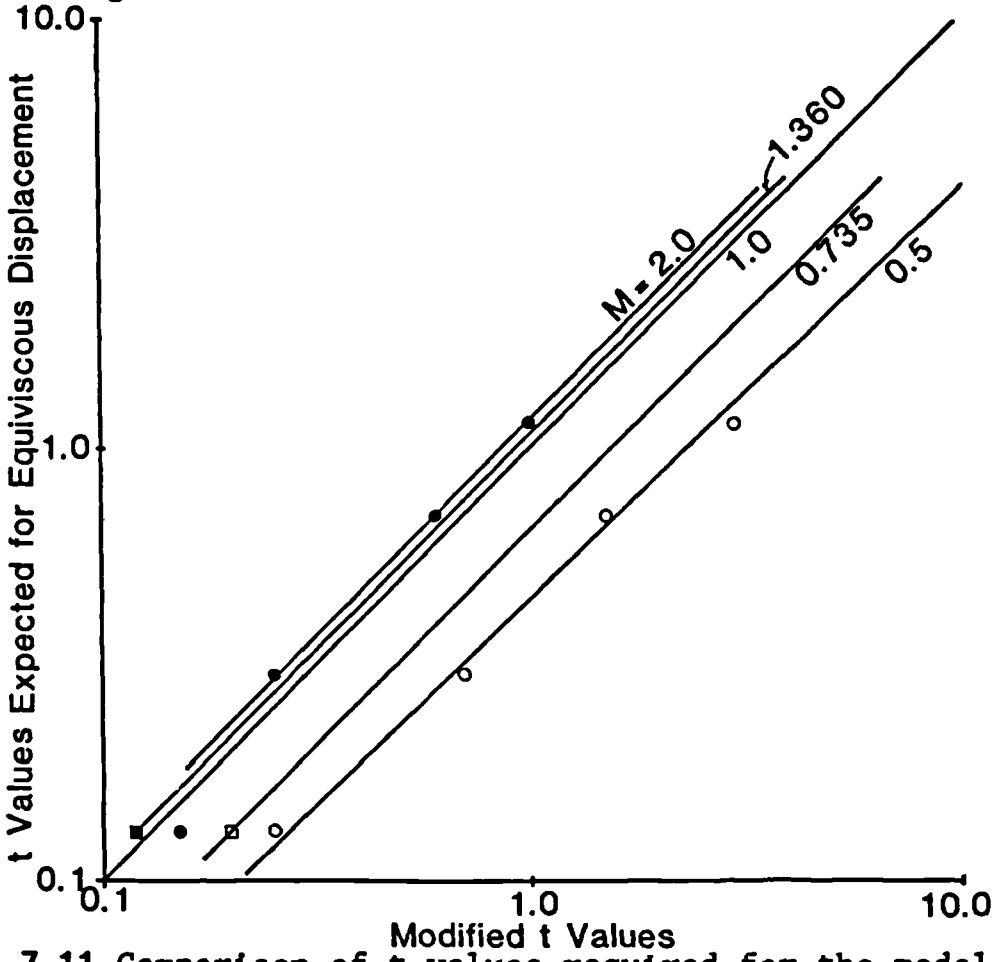

Figure 7.11 Comparison of t values required for the model to fit the experimental data and those expected for an equiviscous displacement (C_A/C_B = 3.3).

CHAPTER EIGHT

MISCIBLE FLUID FLOW IN A SYSTEM CONTAINING A LENS

So far fluid flow in layered heterogeneities have been examined, but non-continuous heterogeneities (eg. lenses) also occur in reservoir structures. Parameters determined from tests on core samples (eg. absolute permeability, relative permeability, residual saturations etc.) normally assume homogeneous core properties, but heterogeneities within the core must affect fluid flow and hence the reliability of these parameters. Also it is necessary to know how reservoir sweep patterns are affected by heterogeneities. Huppler[77] studied the effect of layers and lenses on the determination of relative permeabilities in core samples. He calculated dynamic relative permeability functions[78] from numerical waterflood data for systems with specified heterogeneities. Comparison of input and calculated relative permeability curves provided a quantitative indication of the affect of these non-uniformities. He found that lenses can seriously affect the determination of residual saturations. Small well distributed lenses however appear to have little effect on waterflood behaviour, but increase in significance as they become more continuous between inlet and outlet.

Warren and Skiba[45] and Schwartz[79] have used numerical methods to investigate how randomly distributed lenses create macroscopic dispersion (section 2.3.4). Moulu[80] used favourable mobility ratio displacements in laboratory visual models containing a single lens (similar to the models reported in this work) to study how this heterogeneous system affects the mixing zone between two miscible fluids. Rosman and Simon[81] have suggested an experimental method to characterise core scale heterogeneities. Their method involves miscibly displacing helium from a core with nitrogen, and using the effluent profile to infer the

heterogeneity of the sample. Before such a 'black box' method can be useful it is necessary to 'calibrate' the method using well defined heterogeneities. This chapter presents an experimental (using visual models) and theoretical study of how a single lens will modify displacement patterns.

8.1 Unit Mobility Ratio Displacements.

Miscible displacements in systems containing a lens with either higher or lower conductance than the surrounding media (figure 3.2 C and D, table 3.3) have been studied. Experimental fluid/fluid interfacial geometries at various

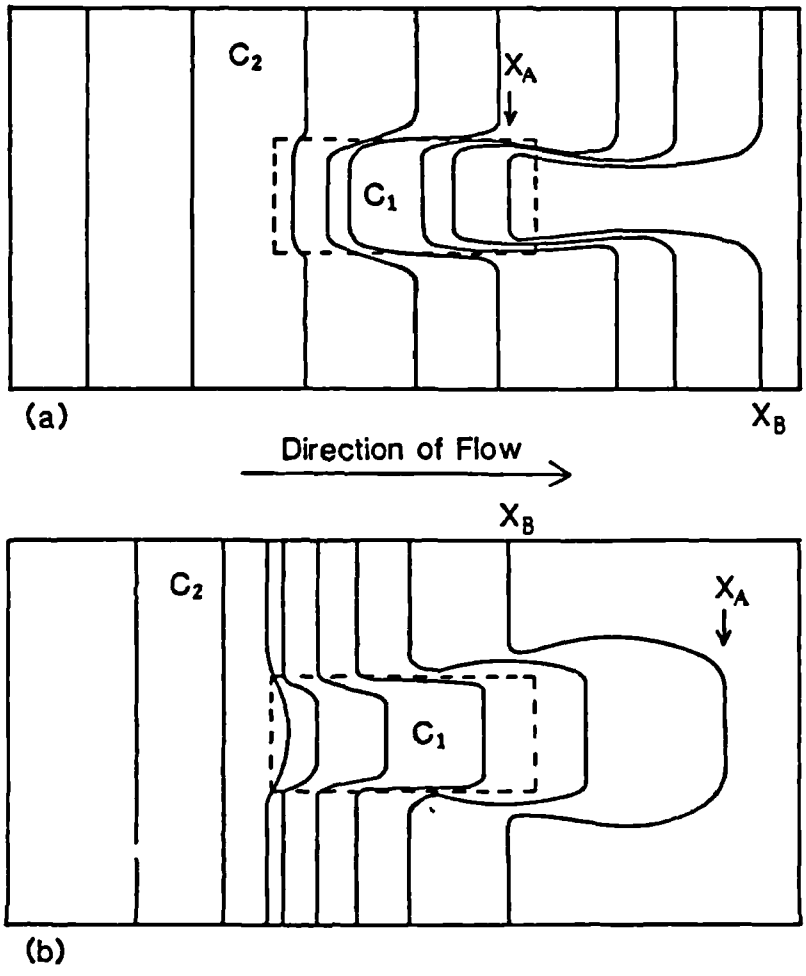

Figure 8.1 Experimental fluid/fluid interfacial geometries for miscible displacements (M=1.0) in systems containing (a) a low ($C_1 < C_2$) and (b) a high ($C_1 > C_2$) conductance lens.

stages of displacement are shown in figure 8.1 for both these systems and experimentally observed fluid streamlines for a system containing a high conductance lens are shown in figure 8.2. Characteristic curves (frontal position in

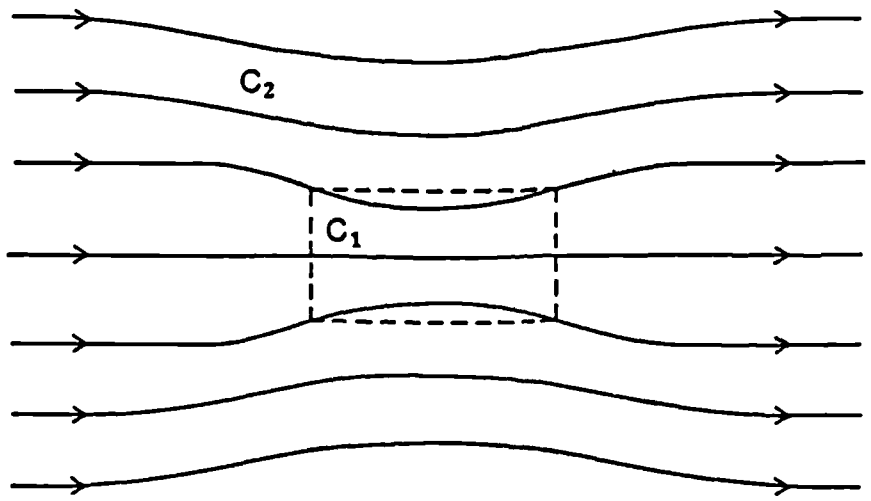

Figure 8.2 Experimental fluid streamlines in a high conductance lens ($C_1 > C_2$) system (M=1.0).

the centre of the system (X_A) against those in the surrounding media (X_B) for unit mobility ratio displacements are presented in appendix nine.

The streamlines in figure 8.2 show that the fluid streamlines in a system containing a high conductance lens are distorted. This causes the fluid/fluid interface (figure 8.1b) to pinch into the lens as it enters and bulge out as it leaves. This behaviour can be explained by considering a non-communicating two layer system, where one layer contains a lens (figure 8.3a). As layer B has a uniform conductance the pressure gradient is constant along its length (figure 8.3b). But layer A is non-uniform and the majority of the normalised pressure drop is through the low conductance media (C_2); thus the pressure gradient through each section is different. This means that there are lateral pressure differences between adjacent points in the two layers (figure 8.3b). Therefore there will be a tendency for fluid to flow from layer B

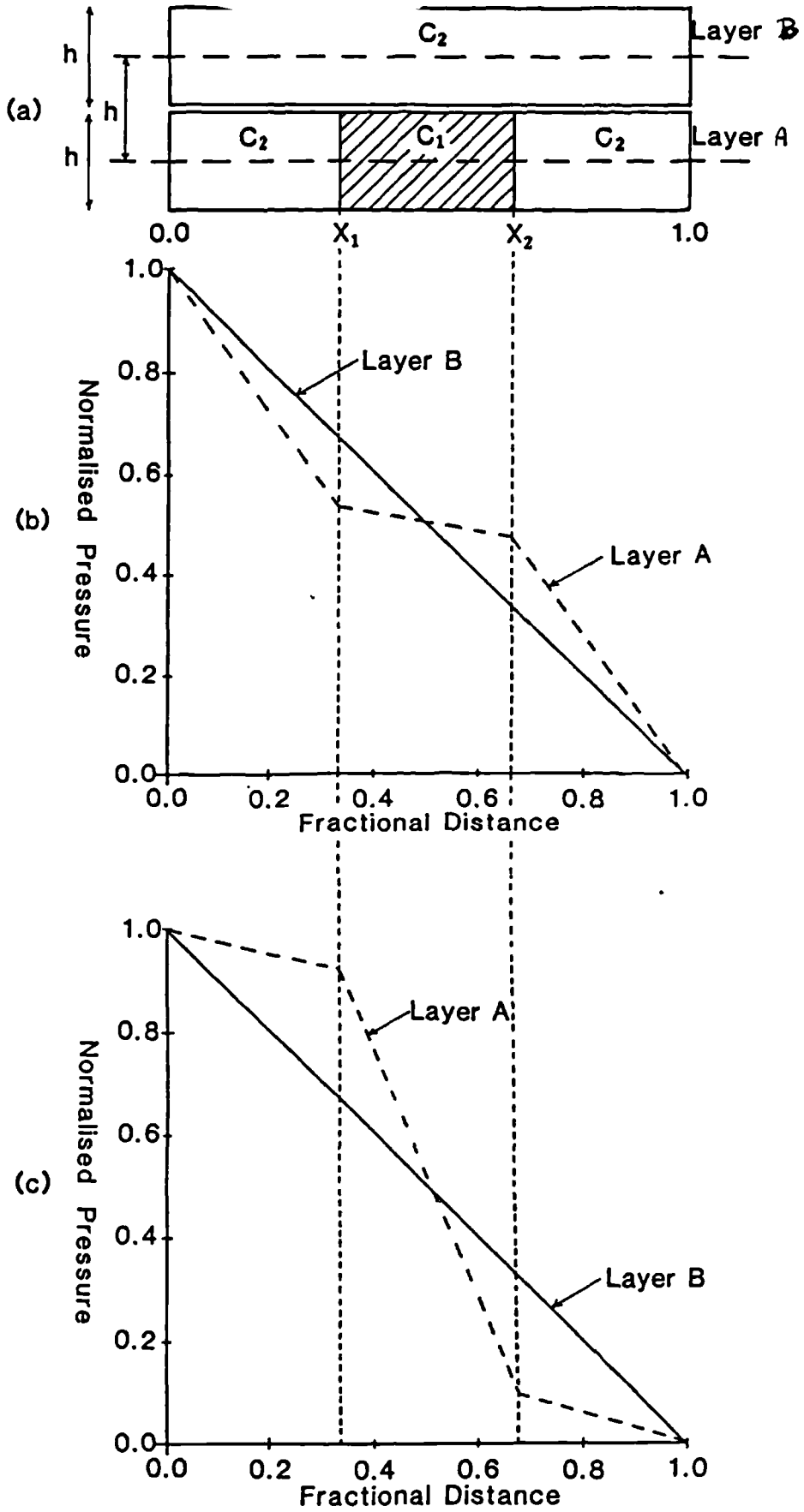

Figure 8.3 (a) Non-communication lens system.
(b) and (c) Axial pressure profiles in systems with high ($C_1 > C_2$) and low ($C_1 < C_2$ conductance lenses respectively.

to layer A at the beginning of the lens ($X=X_1$), and from layer A to layer B at the end of the lens ($X=X_2$), if the layers were able to communicate.

The axial pressure profiles for a system with a low conductance lens are illustrated in figure 8.3c. Here the majority of the pressure drop is through the central portion of layer A, and means that the tendency for flow is in the opposite direction to that in the high conductance lens system. The displacement patterns this produces are illustrated in figure 8.1a. The off axial flow of fluid in lensed systems is analogous to the viscous crossflow discussed in chapter four, but can also occur for unit mobility ratio displacements.

Flow in lensed systems can be analysed by a method similar to that used to study the finite viscous crossflow of fluid in layered systems; discussed in chapter four. The effect of fluid crossflow on the axial pressure profile within layer A is calculated when layer B is wide relative to layer A. The flow rate within layer B is assumed constant and unaffected by fluid crossflow. The necessary equations are derived in appendix ten. These give axial pressure distributions, such as shown in figure 8.4 for any value of h, the distance between the pressure axes. When h_D (h/L) is large (~10.0) the amount of fluid crossflowing is small and the axial pressure profile within layer A is unaffected and the non-communicating lens case (figure 8.3b) is approached. When h_D is small (~ 0.001) the amount of fluid crossflowing approaches a maximum and the pressures in the two layers are almost equalised. For h_D values between 10.0 and 0.001 the axial pressure gradient within layer A varies continuously with distance.

The instantaneous velocities of the fluid fronts can be calculated because the axial pressure gradient at any distance along the length of either layer is known. Thus

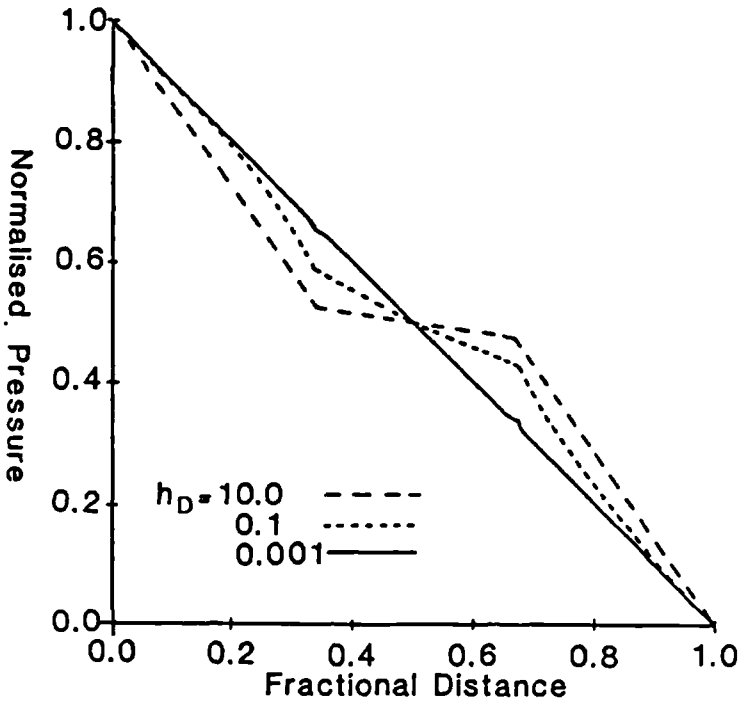

Figure 8.4 Calculated normalised axial pressure profiles within layer A for a unit mobility ratio displacement in a system containing a high conductivity lens (C_1/C_2=10.0) and a range of h_D values.

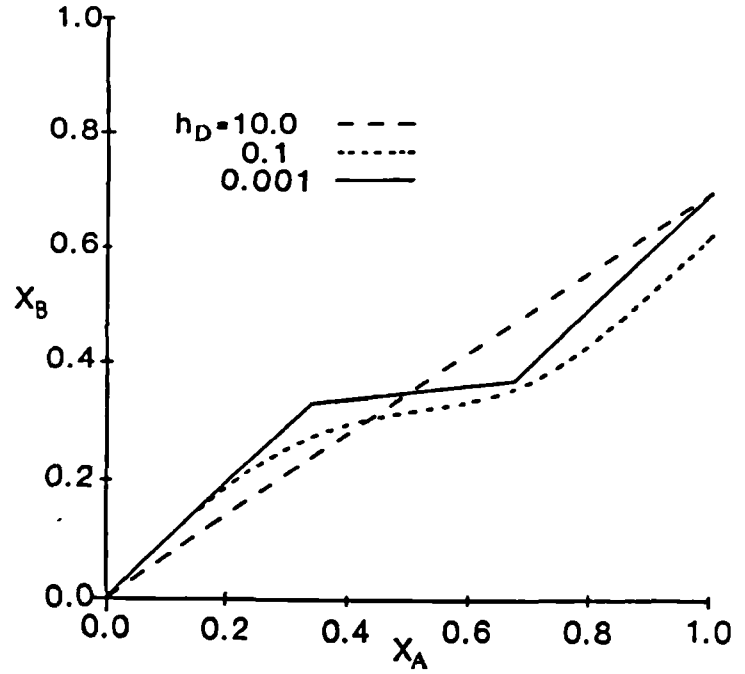

Figure 8.5 Predicted characteristic curves for unit mobility ratio displacements in a system containing a high conductivity lens (C_1/C_2=10.0).

characteristic curves for unit mobility ratio displacements in lensed systems can be predicted (figure 8.5). When h_D is large (ie. the non-communicating layer case) the front in layer A travels at a constant velocity relative to that in layer B. For this case X_B^* (defined in section 2.2.2) and similarly X_A^* are given by:

$$X_B^* = (X_2-X_1)(C_2/C_1-1.0) + 1.0 \quad , \quad C_1/C_2 > 1.0$$

$$X_A^* = \frac{1.0}{(X_2-X_1)(C_2/C_1-1.0) + 1.0} \quad , \quad C_1/C_2 < 1.0 \qquad (8.1)$$

When h_D is small (ie. maximum crossflow case) the velocity of the front in layer A is constant within each media but is different for each. Once again X_A^* and X_B^* are given by equation 8.1. For h_D values between 10.0 and 0.001 the velocity of the front in layer A varies continuously

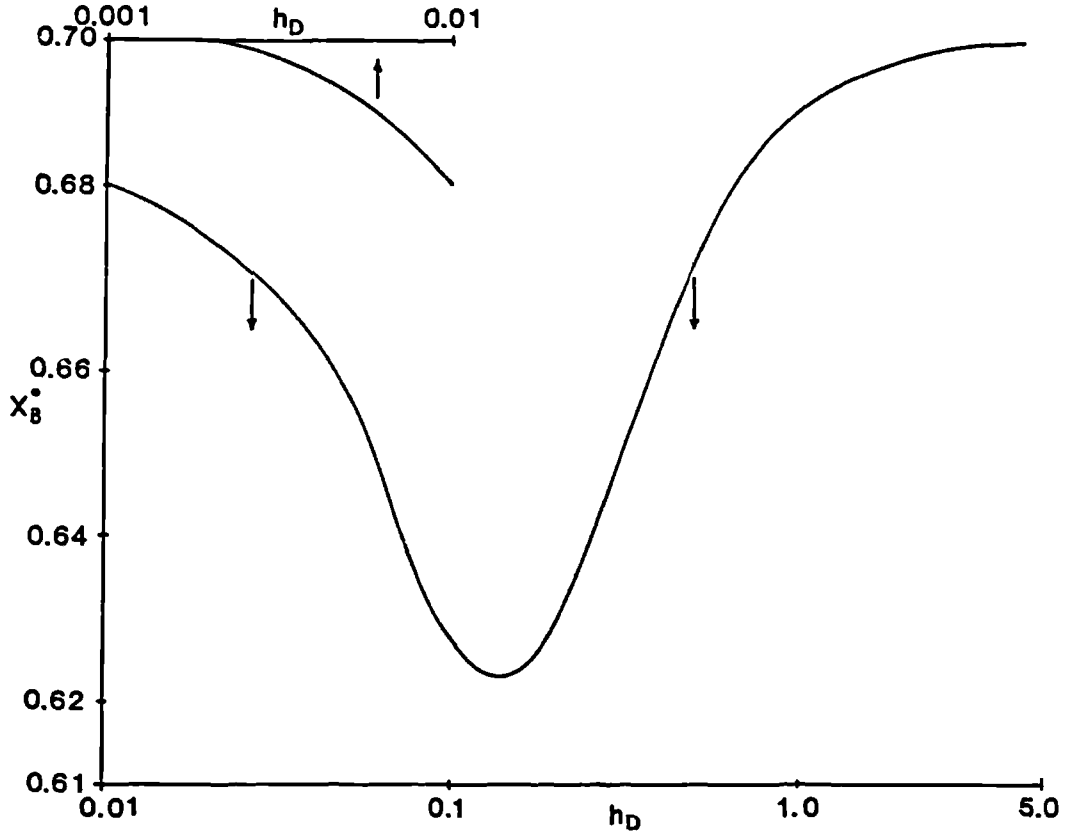

Figure 8.6 Variation of X_B^* with h_D (C_1/C_2=10.0).

relative to that in layer B. In these cases X_B^* and X_A^* are not given by equation 8.1 but equals some value less than this. The variation of X_B^* with h_D is shown in figure 8.6. Here X_B^* is a minimum value of 0.623 when h_D equals 0.14. Therefore the effect of an intermediate amount of viscous crossflow is to cause the front in layer A to breakthrough earlier, relative to the front in layer B, than occurs for either the non-communicating layer or maximum crossflow cases.

The experimental characteristic curves are compared to those predicted by the above method in appendix nine. The agreement is very good for all but the last portion of the high conductance lens system curve, where the predicted values are higher than the experimental. This part of the curve represents the movement of the front in layer A after it has left the lens. For the low conductance lens system the front in layer B breaks through before the front in layer A has reached the end of the lens. Therefore it appears that the prediction method may be inadequate in exactly representing the propagation of the front in layer A after it has left the lens (between $X_A = X_2$ and $X_A = 1.0$).

Equation 8.1 and figure 8.5 show that for the two limiting cases ($10.0 < h_D < 0.001$) the fraction of the system swept at breakthrough depends only on the conductance contrast (C_1/C_2) and the length of the lens, and not on its axial position in the system. To investigate whether this is also the case for finite communication ($10.0 > h_D > 0.001$) between the layers, two cases were examined; when the lens is located near the beginning of the model ($X_1 = 0.1$, $X_2 = 0.433$) and when it is near the end of the model ($X_1 = 0.567$, $X_2 = 0.9$). The normalised pressure distributions within layer A calculated for these cases are shown in figure 8.7 and the characteristic curves are compared to that for a centrally located lens ($X_1 = 0.333$, $X_2 = 0.667$) in figure 8.8. Here although the characteristic

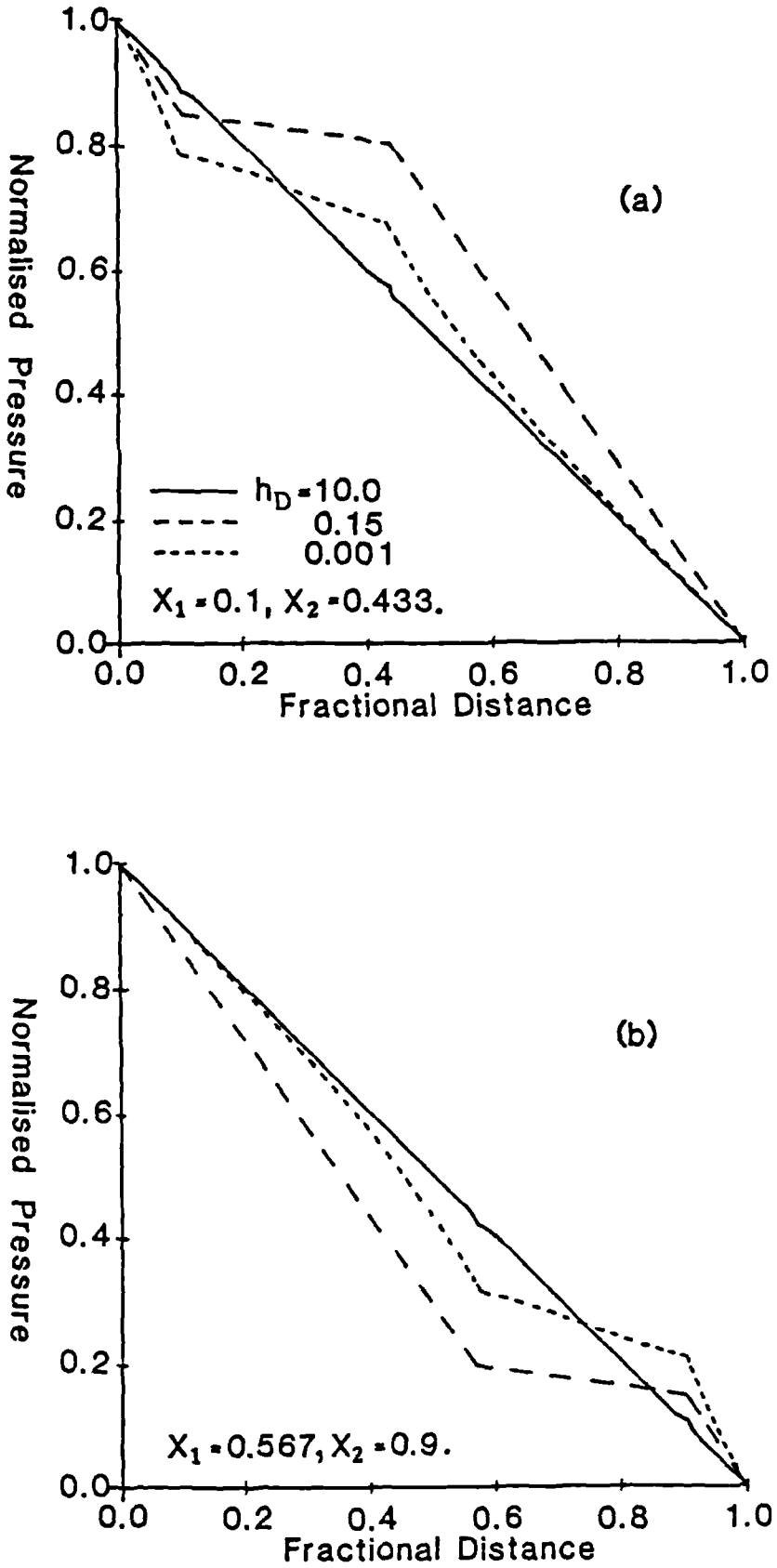

Figure 8.7 Calculated normalised pressure profiles within layer A for two different axial lens positions.

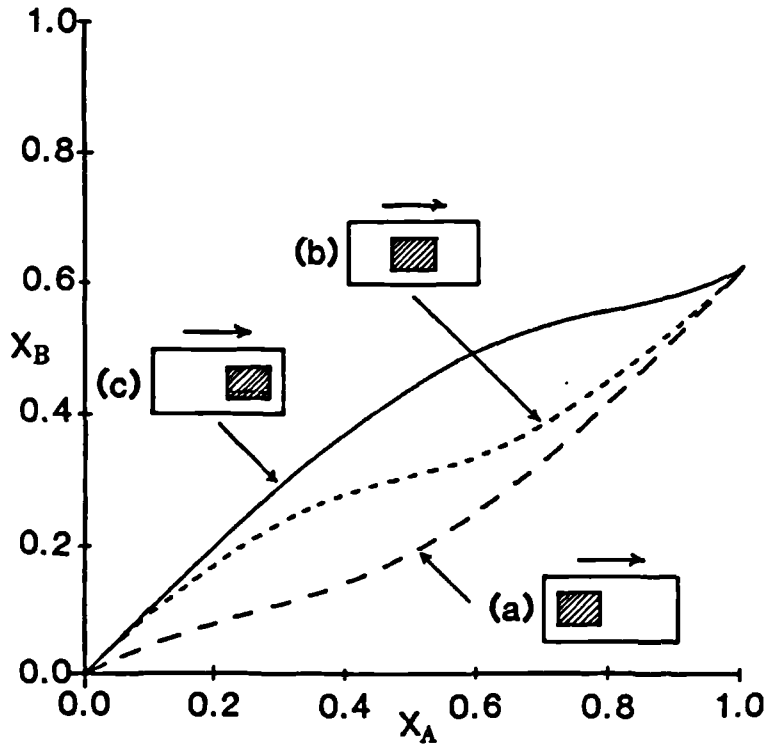

Figure 8.8 Predicted characteristic curves for a lens in three different axial positions (C_1/C_2=10.0). (a) X_1 =0.1, X_2 =0.433 (b) X_1 =0.333, X_2 =0.667 (c) X_1 =0.569, X_2 =0.9.

curves are different for each case, they all converge when X_A =1.0 and thus have the same value of X_B*. In summary, for a unit mobility ratio displacement in a lensed system the fraction of the system swept at breakthrough depends only on the length of the lens and the conductance contrast.

8.2 Non-Unit Mobility Ratio Displacement.

The previous section has shown that when a system contains a lens whose conductivity differs from that of the surrounding matrix, the fluid flow patterns are distorted from those which would be expected for a homogeneous system (figure 8.1). Additional modifications to the displacement patterns occur when the mobility ratio differs from unity (figures 8.9 and 8.10). The frontal separations ($X_A - X_B$) in the favourable mobility ratio

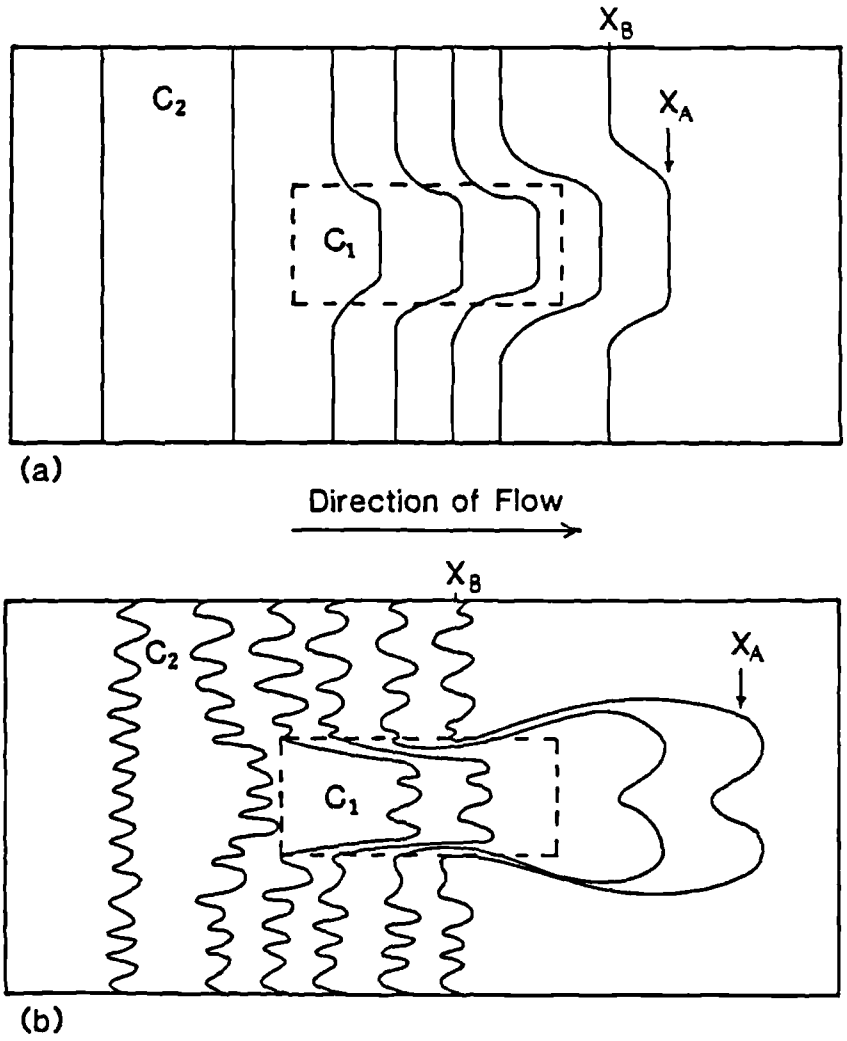

Figure 8.9 Experimental displacement patterns in a high conductivity lens system (C_1/C_2=2.5) with (a) a favourable (M=0.267) and (b) an unfavourable (M=3.74) mobility ratio.

displacements (figures 8.9a and 8.10a) can be seen to be less than those for the unit mobility displacement (figure 8.1), while those in the unfavourable mobility ratio displacements (figures 8.9b and 8.10b) are greater. In the latter displacements viscous fingering caused distortion of the fluid/fluid displacement front which made observation of this boundary difficult in some cases. The experimental characteristic curves for unit, favourable and unfavourable mobility ratio displacements are compared in figure 8.11. As expected the fraction of the system swept at breakthrough

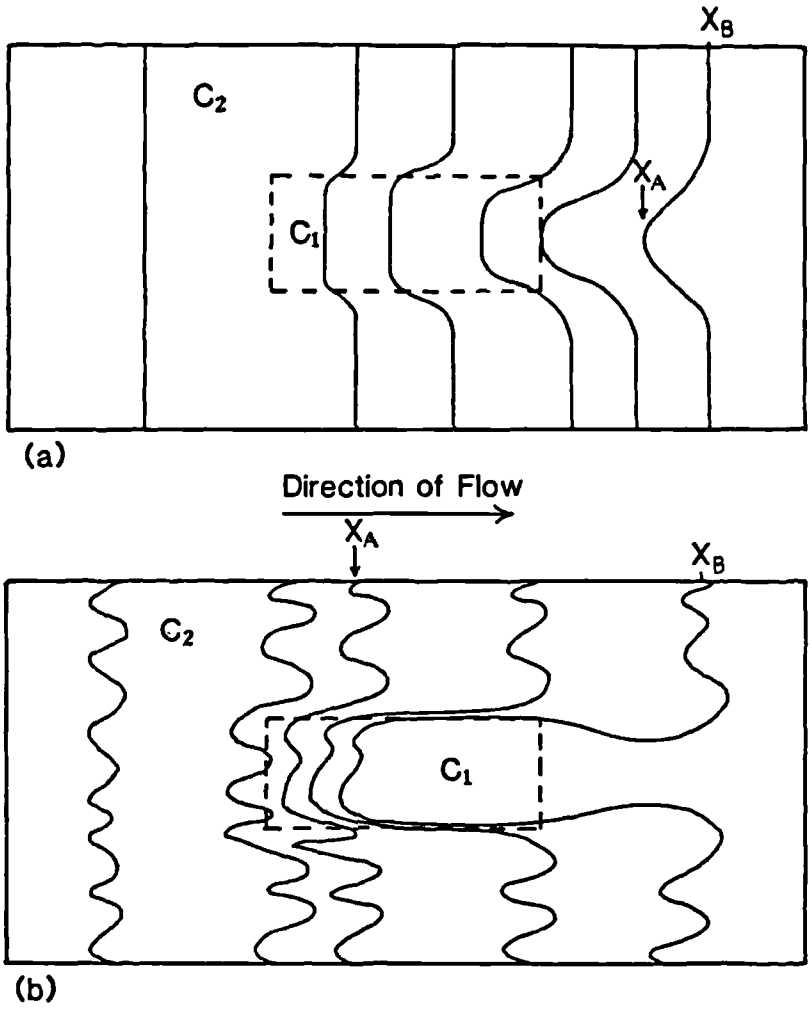

Figure 8.10 Experimental displacement patterns in a low conductivity lens system with (C_1/C_2=0.4) (a) a favourable (M=0.267) and (b) an unfavourable (M=3.74) mobility ratio.

decreases as the mobility ratio increases, while in the favourable case breakthrough occurs almost simultaneously in both the central (containing the lens) and the outer (homogeneous) portions of the system.

Consideration of the normalised pressure profiles for the non-communicating lens case (figure 8.3a) can help to explain the experimental fluid/fluid interfacial geometries for the displacements illustrated in figures 8.9 and 8.10. Figure 8.12 shows the off-axial directions that fluid would tend to flow if communication between the central and outer portions of the system was possible.

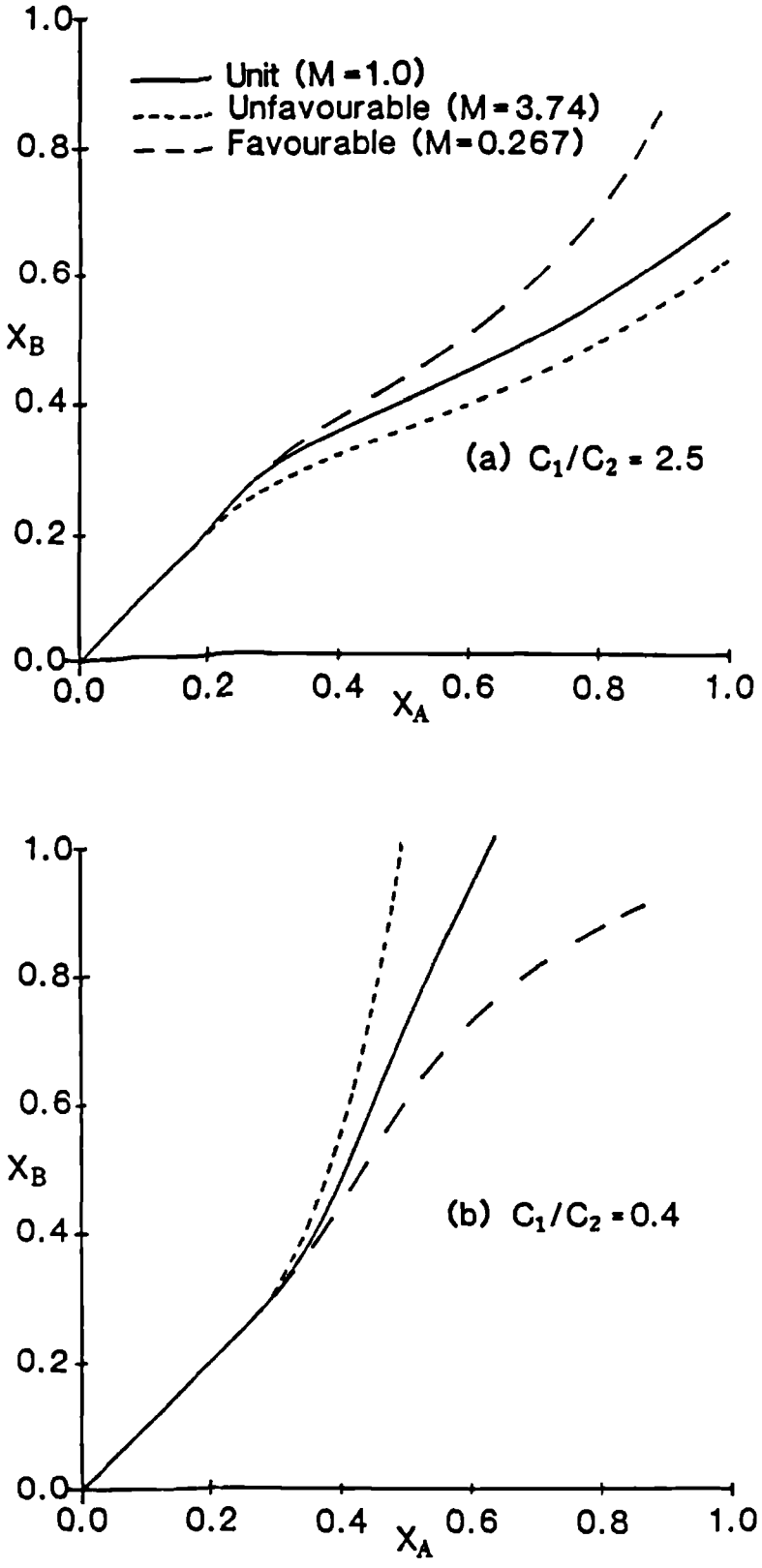

Figure 8.11 Comparison of experimental characteristics curves for (a) a high (C_1/C_2 =2.5) and (b) a low (C_1/C_2 =0.4) conductivity lens system (X_1=0.333, X_2=0.667)

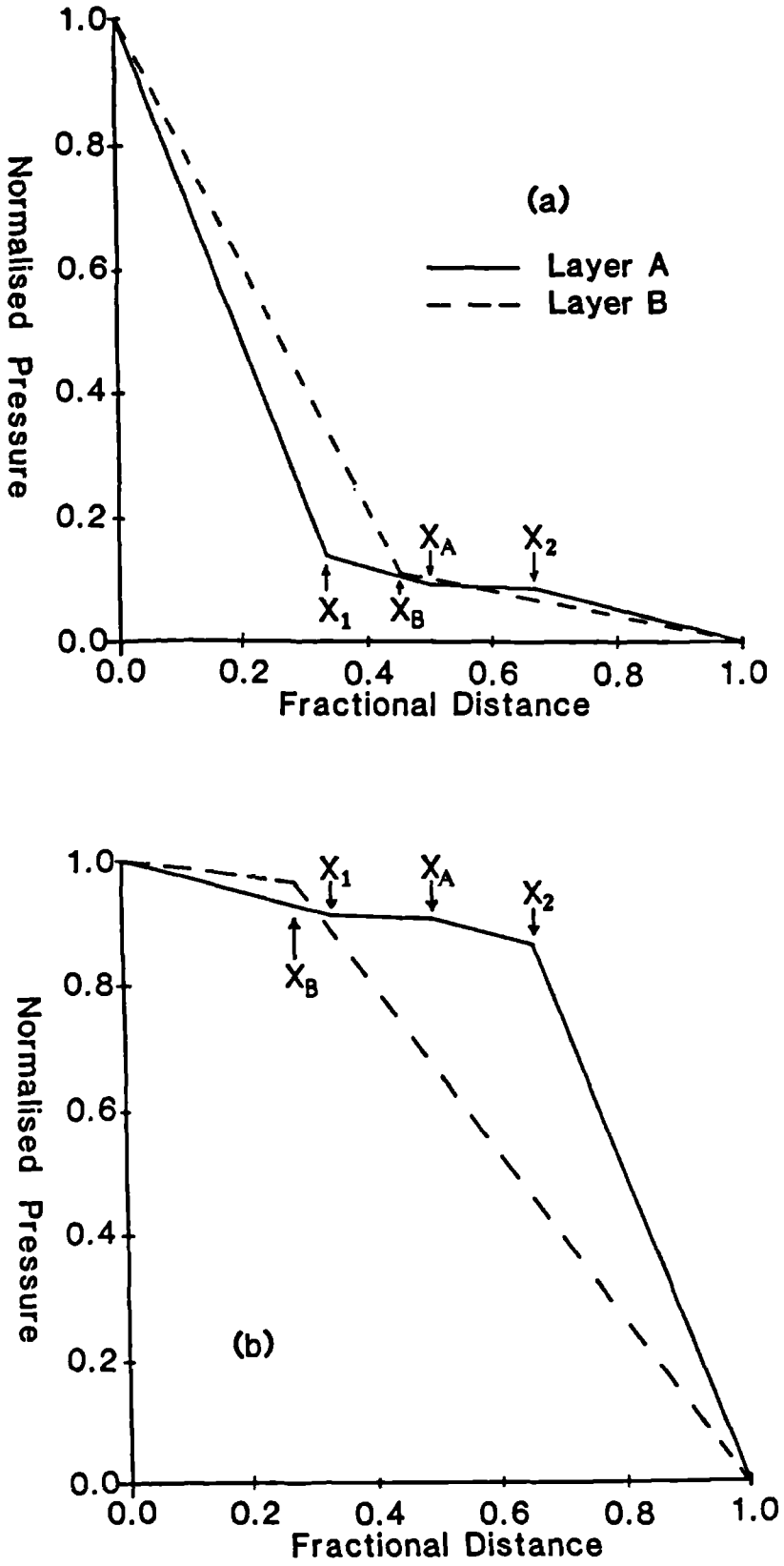

Figure 8.12 Normalised pressure profiles for a non-communicating high conductivity lens (C_1/C_2 =10.0) system for (a) a favourable (M=0.1) and (b) an unfavourable (M=10.0) mobility ratio displacements.

An analysis similar to that used in section 8.1 which is valid for any h_D value (ie. which allows for finite communication between layers) is not possible for non-unit mobility ratio displacements due to the complexity of the normalised pressure profiles (figure 8.12). Therefore the non-communicating lens case will be used to highlight some of the features. The necessary equations for this case are derived in appendix eleven. It should be noted that as there is a distinct front moving through the system, different equations are required to describe the movement of the fronts, when the front in layer A is in each section of that layer (figure 8.3a). Characteristic curves predicted by this method are shown in figure 8.13 and compared to the experimental data in appendix nine. Figure 8.13 shows that the mobility ratio has a large effect on the characteristic curves for lens systems. Although the shape of the predicted and experimental characteristic curves (appendix nine) are different, the predicted curves can be seen to provide a reasonable approximation. The effect of varying the mobility ratio and conductance contrast in a system with a centrally located lens is correlated in figure 8.14.

Whereas for a unit mobility ratio displacement the axial position of the lens did not affect X_B* or X_A* (figure 8.8), in the non-unit mobility ratio case X_B* and X_B* are dependent on the axial position of the lens, as well as the conductivity contrast and the length of the lens. This is shown in figure 8.15.

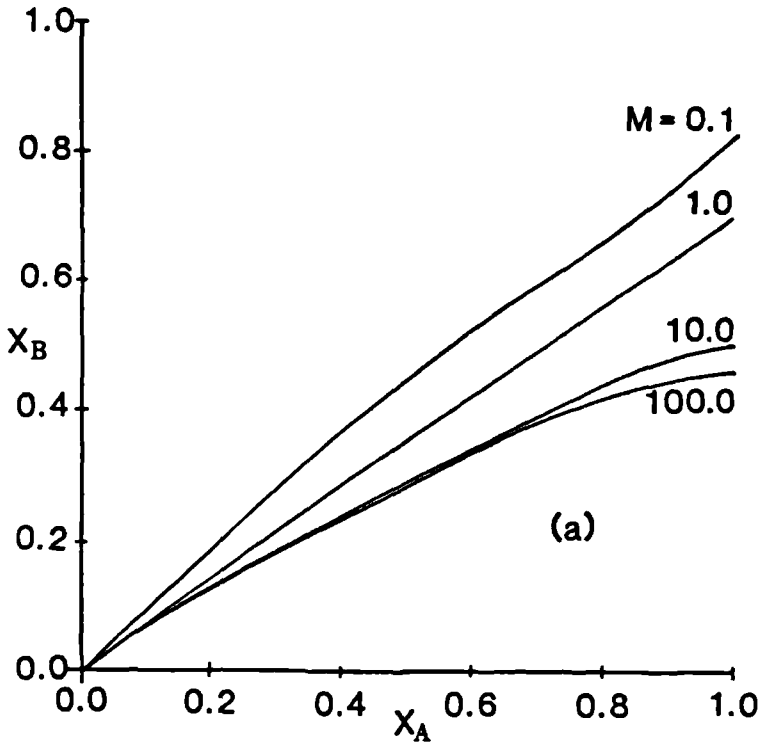

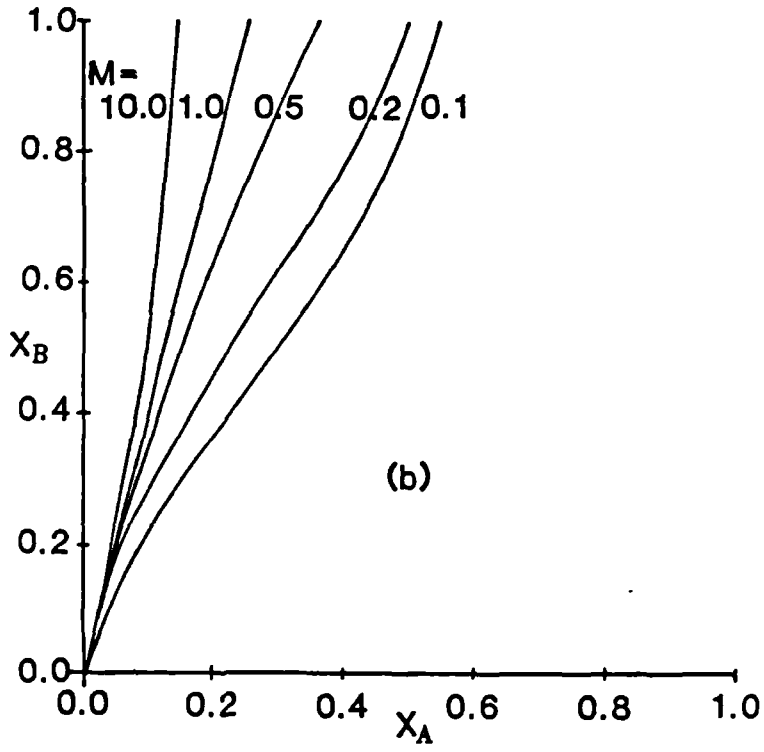

Figure 8.13 Calculated characteristic curves for the non-communicating lens case (X_1 =0.333, X_2 = 0.667) for a range of mobility ratios in a system with
(a) a high (C_1/C_2=10.0) and
(b) low (C_1/C_2=0.1) conductivity lens.

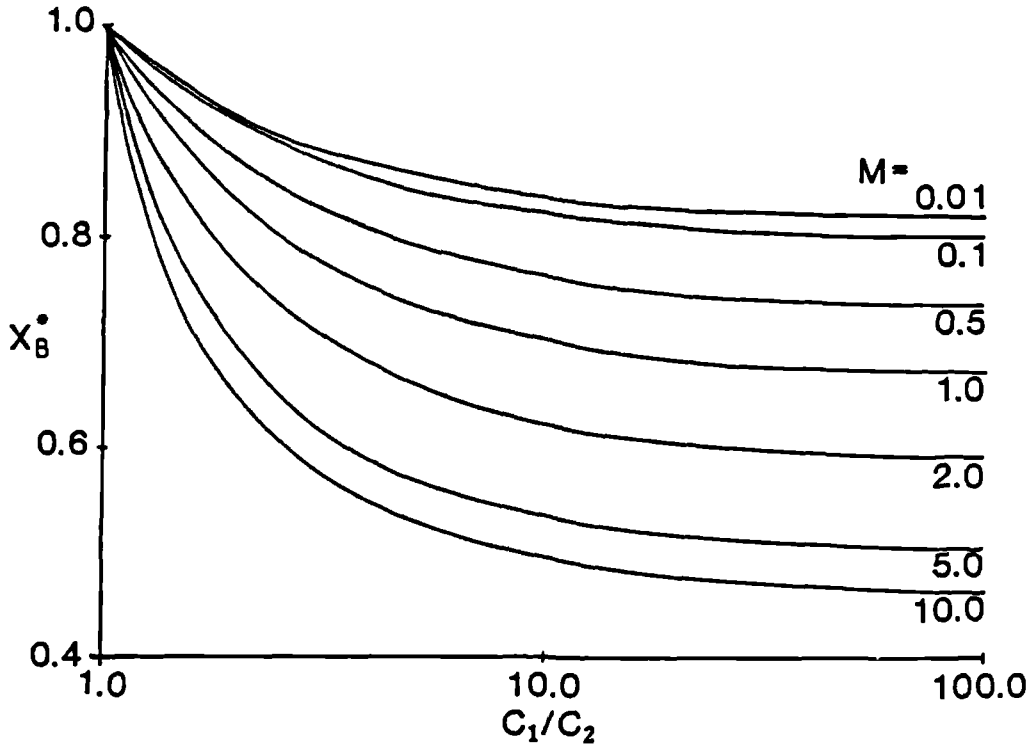

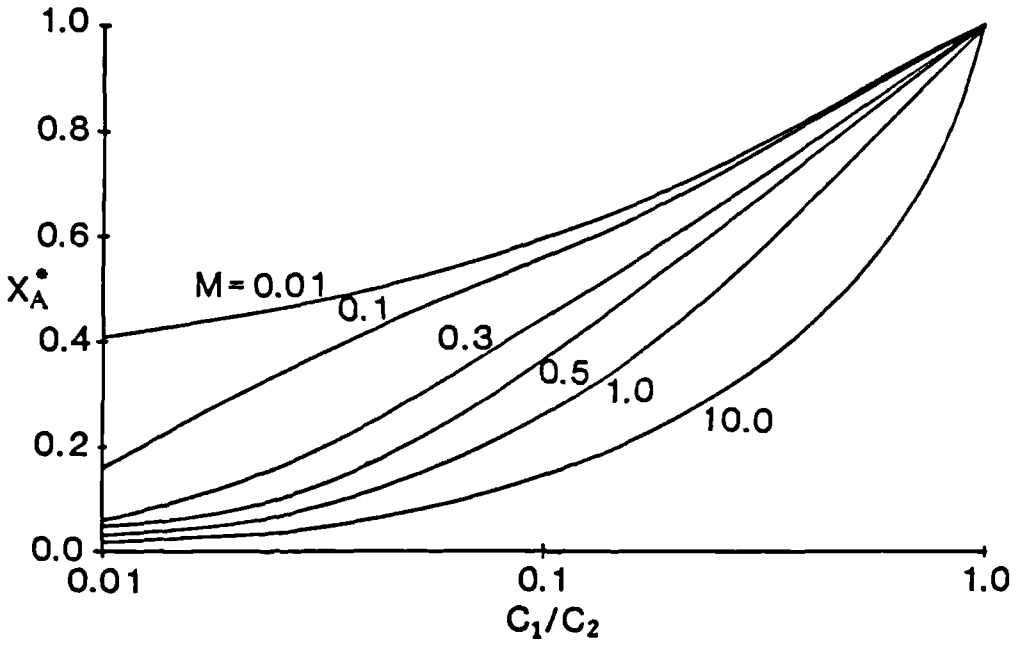

Figure 8.14 Predicted correlation between conductance contrast and mobility ratio for the non-communicating lens case (X_1=0.333, X_2=0.667).

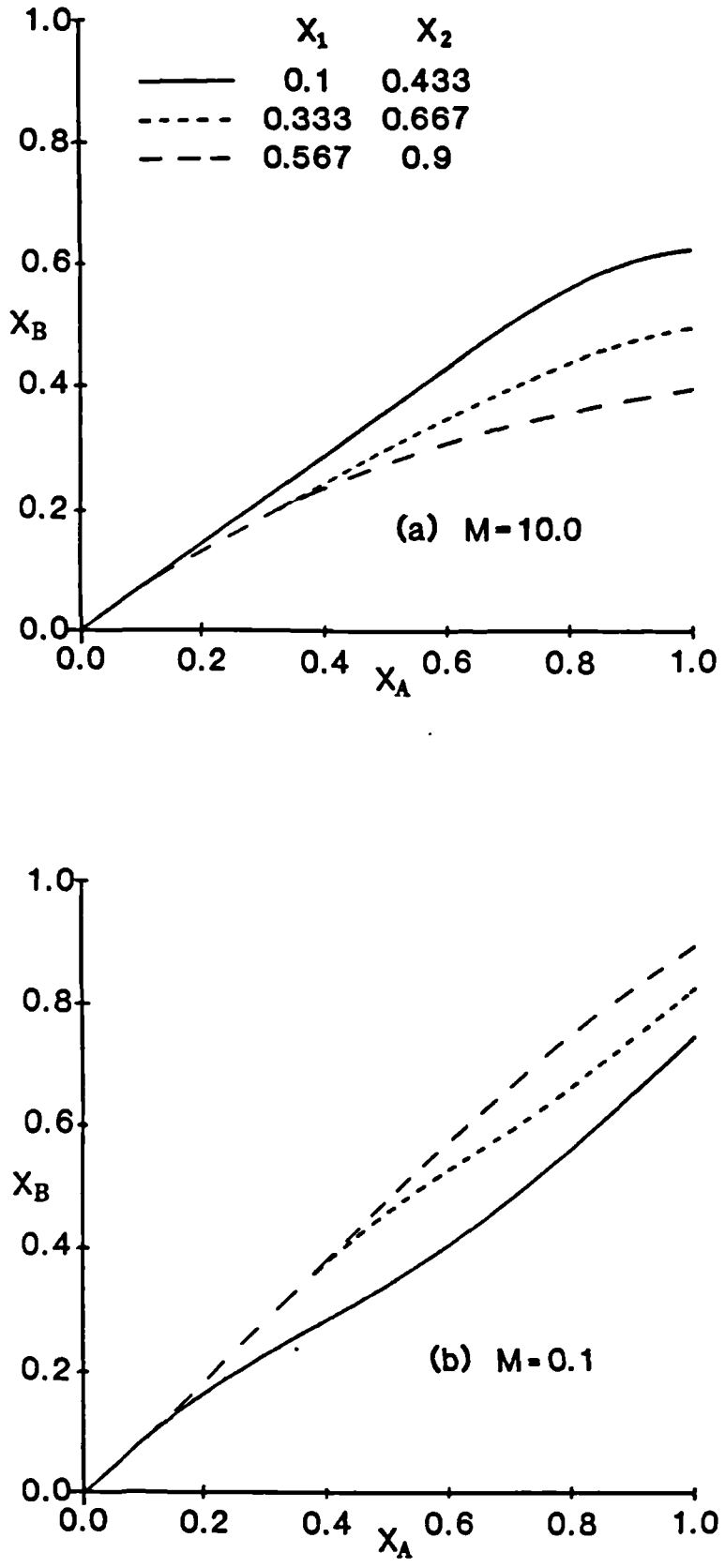

Figure 8.15 Predicted characteristic curves for a non-communicating high conductivity lens ($C_1/C_2 = 10.0$) illustrating the effect of axial lens position.

8.3 Effluent Analysis and Fractional Flow Curves.

The analysis of frontal displacement patterns in a lenced system can be extended by observing the effluent concentration from the model (figure 8.16a) and from this the fractional flow functions (figure 8.16b) can be calculated by the method given in section 4.4. The unit and unfavourable mobility ratio effluent curves both differ from that which would be expected for a homogeneous system (figure 2.13). The reason for this can be seen from the experimental displacement patterns (figure 8.1a and 8.10b). Here the production period of displaced fluid is extended due to the low conductivity lens delaying breakthrough in the central portion of the model. As with the unfavourable effluent profile for the layered system (figure 4.19a) there is a bulbous nature to the unfavourable effluent profile. This is because the displacement pattern (figure 8.10b) 'pinches in' after the lens. Compared to the layered case this occurs later in the displacement and at a high concentration because the overall conductance of the central portion of the system is lower than the layered model. The favourable effluent profile shows a homogeneous nature, as breakthrough occurs almost simultaneously at all points at the production end of the system (figure 8.10a). The heterogeneous nature of the unit and unfavourable mobility ratio effluent profiles and the homeogeneous nature of the favourable effluent profile are further emphasised in the fractional flow curves (figure 8.15b).

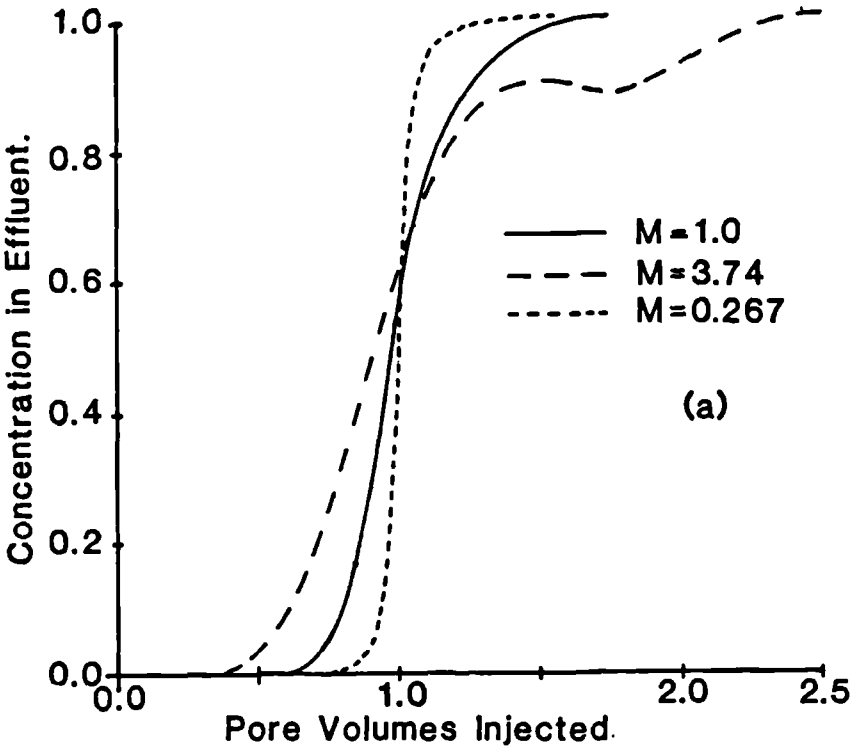

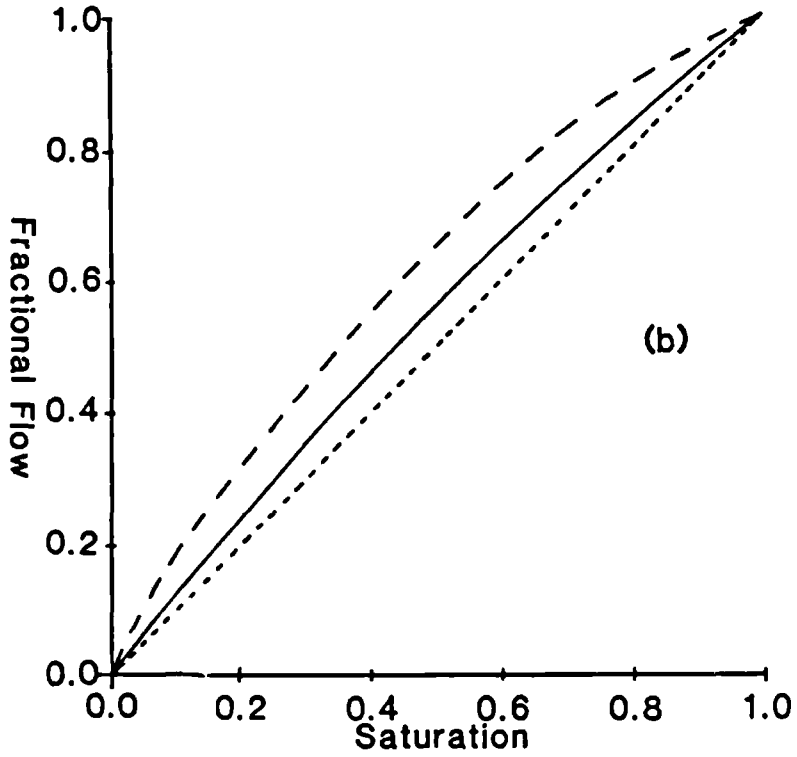

Figure 8.16 (a) Experimentally obtained effluent concentration profile for a low conductivity lens system.
(b) Calculated fractional flow curves.

CHAPTER NINE

CAPILLARY PRESSURE EFFECTS IN IMMISCIBLE DISPLACEMENTS

This work has concentrated on miscible displacements or the miscible stages of complex EOR schemes. However the displacement of oil by immiscible processes accounts for a large proportion of the total oil recovery (ie. water and gas flooding) and also many EOR processes contain an immiscible stage (eg. chase water displacing a solvent slug or after the overtaking point has occurred). It is therefore important to understand not only the miscible displacement processes but also the mechanism of immiscible displacement.

There are major differences in immiscible and miscible displacements. The most important is that in immiscible multi-phase flow processes saturation effects, and hence relative permeability concepts, are involved. Capillary pressure effects (section 2.4) are also strongly apparent. These will be important at saturation discontinuities where the capillary forces change over a few grain diameters and can give rise to large pressure gradients. In homogeneous media such discontinuities may occur at displacement fronts and the effluent end of the system. In heterogeneous media they are also created at the boundaries between media with different properties; such as permeability, porosity or wettability changes. Dispersive phenomena will be strongly modified due to the mass transfer processes having to pass through the interface.

In immiscible displacements it is difficult to isolate the individual effects and this chapter concentrates on lensed and layered systems, and investigates how the

capillary pressure differences at matrix boundaries modifies the fluid flow patterns. Subsequently the differences between miscible and immiscible displacements are highlighted.

9.1 Lensed Systems.

A series of immiscible displacement experiments (packings 20,21,22 and 24, model type β) were undertaken to investigate the effects of capillary forces in lensed systems (table 3.6). The experimental procedures, packing details and fluid properties are given in chapter three. In each case both oil and waterfloods were carried out in the water-wet media with and without an initial residual fluid saturation. However experimental difficulties were experienced in obtaining uniform residual saturations and in most cases the colour intensity (hence saturation) of the residual fluid was observed to increase from model inlet to outlet ends, similar to the trailing edge of a Buckley Leverett type displacement[14]. This has also been noted by Bentsen and Saeedi[18] and Parsons[82].

9.1.1 Packing Number 20 - Pattern C, figure 3.2.
- Lens of higher conductance than that of the surrounding media.

(a) Waterflooding.

In the absence of capillary forces the water would be expected to channel into the higher conductance lens, as discussed in chapter eight (figure 8.1b). But in these displacements, both with and without an initial residual water saturation, the water initially bypassed the lens (figure 9.1). This was because the water phase pressure on the inside of the lens boundary was greater than on the outside (figure 2.16b) due to the larger capillary pressure

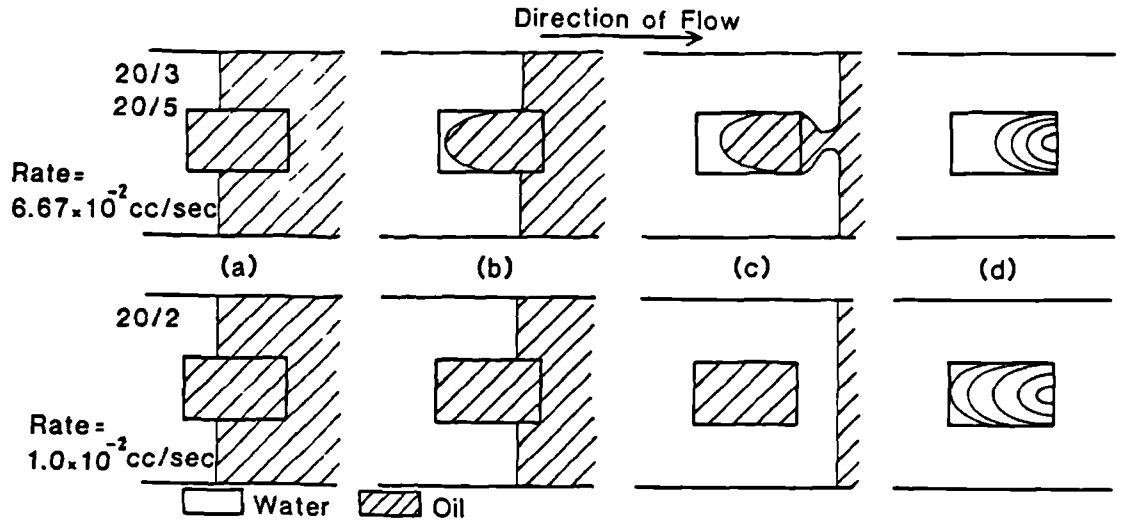

Figure 9.1 Waterflooding packing number 20.

difference between the fluids in the tighter packing. In the displacements 20/3 and 20/5 the water began to enter the lens before the displacement front reached the end of the lens (figure 9.1b). But in displacement 20/2 where the displacement rate was slower, water did not enter the lens until the displacement front had almost reached the end of the system. Here the capillary forces exerted a greater influence on the fluid distribution due to the slower displacement rate. In each experiment a large portion of oil was left in the lens after the displacment front had passed; this was then gradually displaced from

the lens (figure 9.1d). As no bulk fluid movement was observed behind the displacement front, oil must have moved to the outlet end of the model as discrete droplets.

(b) Oilflooding.

Unlike the waterfloods just discussed, where water (the wetting fluid) initially bypassed the lens due to capillary forces, here the oil (the non-wetting fluid) readily entered when the displacement front reached the lens. In fact the oil flowed into the lens at a faster rate than would be expected due to viscous forces only and appeared to be 'sucked' in. This was because the oil phase pressure on the inside of the lens was less than that on the outside because of the capillary pressure differences. When there was no initial oil saturation (20/6), oil did not start entering the lens until the displacement front had reached the lens (figure 9.2a). Whereas when there was an initial residual oil saturation (20/1, 20/4) oil was observed to enter the lens before the front had been reached the lens. Here the residual oil in runs 20/1 and 20/4 allowed pressure communication, so that the strong capillary forces could draw the oil into the lens. In each case when the lens was completely filled with oil (forming a 'finger' of displacing fluid, figure 9.2b), the oil flowed out of the sides of the lens as well as the front (figure 9.2c). This expansion of the displacing fluid 'finger' continued until the lateral edges of the model were encountered, at which point the front of the finger became the new displacement front.

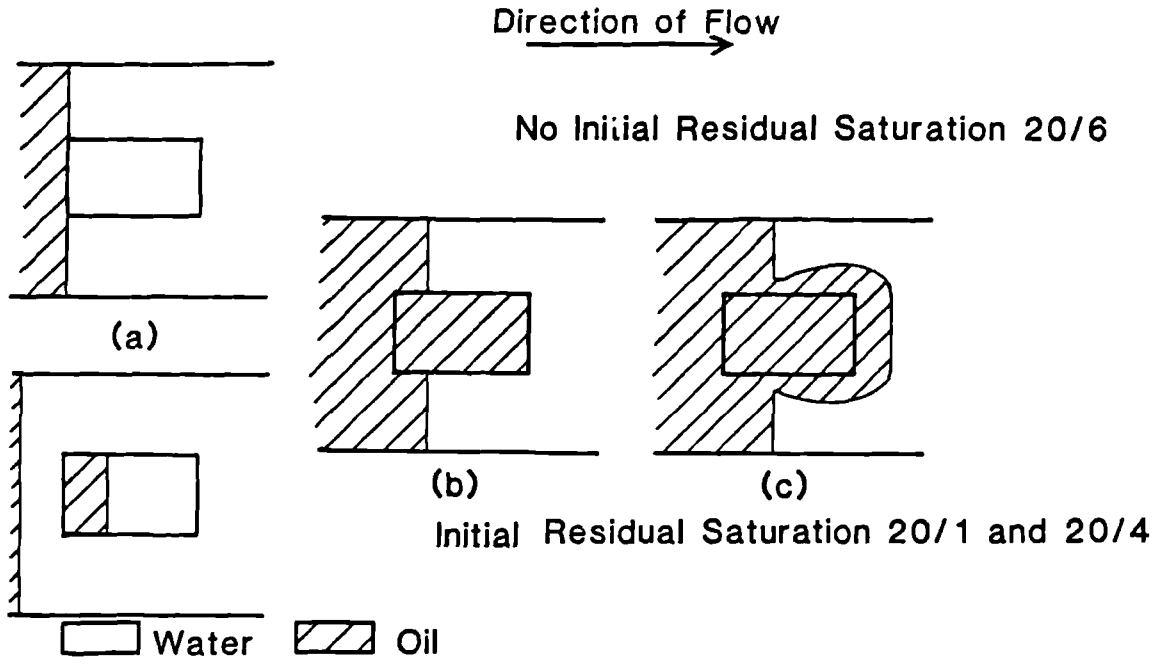

Figure 9.2 Oilflooding packing number 20.

9.1.2 Packing Number 21 - Pattern D, figure 3.2.
- Lens of lower conductance than that of the surrounding media.

(a) Waterflooding.

In this packing (number 21) the lens permeability is lower than the surrounding media and so has the opposite configuration compared with that in packing number 20. The water (wetting fluid) now has a greater affinity for the lens than the surrounding media due to the strong capillary forces in this highly water-wet system. The

experimental observations made while waterflooding in this packing were similar to those for oilflooding packing number 20; (b) above. When there was an initial water saturation (run 21/2) water started to enter the lens before it was reached by the main displacement front (figure 9.3a), while this did not occur in the absence

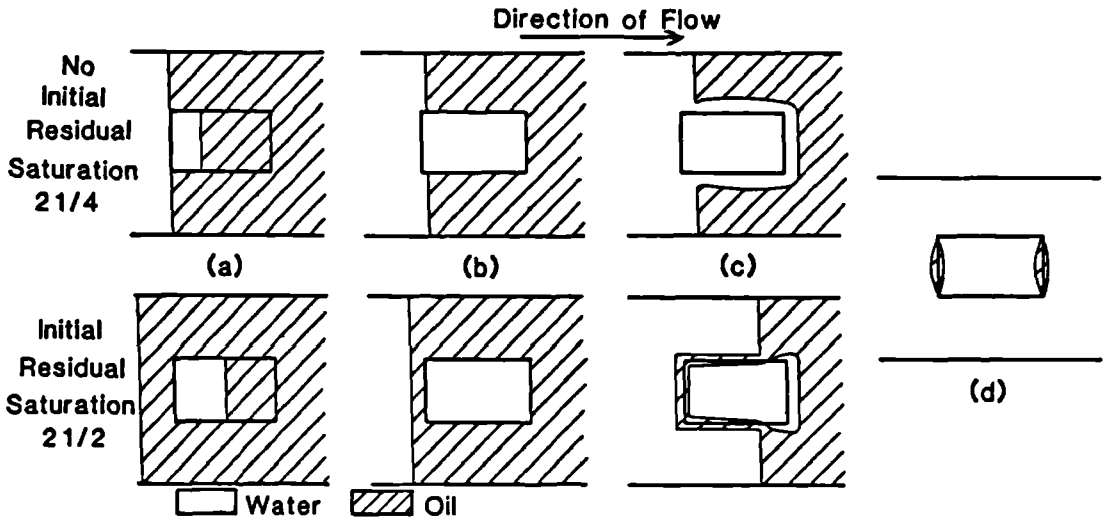

Figure 9.3 Waterflooding packing number 21.

of an initial water saturation (run 21/4). In run number 21/4 a finger of displacing fluid, water in this case, was formed once the lens was full which expanded upon further injection (figure 9.3c). In run number 21/2 (initial water saturation) as the displacement front passed the lens

a band of oil was left at the matrix boundary (figure 9.3c), which reduced to a band at each end of the lens (figure 9.3d) as the displacement proceeded.

(b) Oilflooding.

The oilfloods, both with (run 21/3) and without (run 21/1) an initial oil saturation produced the same effect in this packing (number 21). These were almost identical to those observed in packing number 20, although here the mobile displaced fluid (water) was never totally removed from the lens even after ten pore volumes of displacing fluid (oil) has been injected.

9.1.3 Packing Number 22 - Pattern D, figure 3.2.
- Lens of lower conductance than that of the surrounding media, with the lens beads coated with a water repellent chemical.

Experimental observations made in this packing were similar to those for packing number 20, as here the wetting fluid (water) had a slightly greater affinity for the surrounding media than the lens media due to the chemical treatment of the lens beads.

(a) Waterflooding.

When there was no initial water saturation (run 22/4) the displacing fluid only entered a small band of the lens (figure 9.4 a and b) at the matrix boundary. A substantial quantity of oil remained trapped in the lens (figure 9.4c) after the displacement front had passed. This oil gradually seeped out and had all been displaced when 1.6 pore volumes of water had been injected. On the other hand when there was an initial water saturation (run 22/2) the

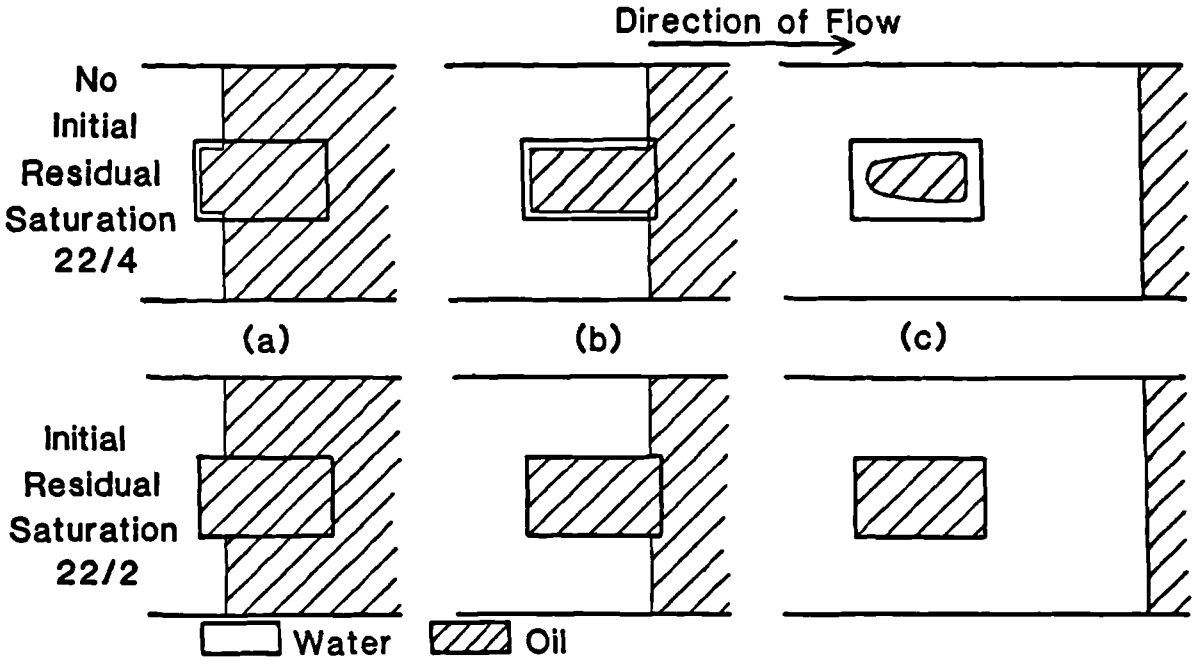

Figure 9.4 Waterflooding in packing number 22.

displacing fluid bypassed the lens (figure 9.4). Here 1.0 pore volume displacing fluid was injected before water started to enter the lens and the mobile oil was never totally removed.

(b) Oilflooding.

The initial stages of these experiments with (run 22/3) and without (run 22/1) an initial residual oil saturation were unexpectedly different (figure 9.5). In run 22/1 the displacement front outside the lens advanced

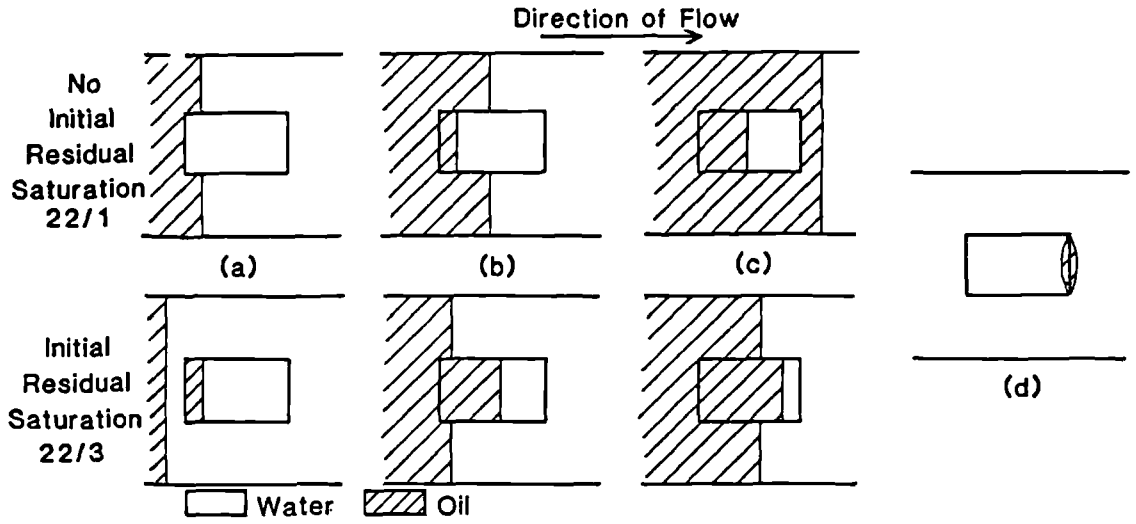

Figure 9.5 Oil flooding in packing number 22.

fastest (figure 9.5a and b), so trapping a large portion of water in the lens (figure 9.5c). This gradually seeped to the outlet of the system leaving a band of water at the end of the non-uniformity (figure 9.5d). In contrast in run 22/3 (initial oil saturation) oil started to enter the lens before the displacement front reached the lens (figure 9.5a). Here the front in the lens was advancing ahead of the front outside (figure 9.5b). As the fronts reached the end of the lens they coincided and again left a thin band of water at the end of the lens (figure 9.5d).

9.1.4 Packing Number 24 - Pattern G, figure 3.2.
- This is a uniformly packed model, with the lens beads coated with water repellent chemical.

In this packing the changes in capillary forces were very large due to the chemical treatment of the lens beads. Run 24/2 was an oilflood with no initial oil saturation. When the displacement front reached the beginning of the lens, oil imbibed very quickly and no expanding finger phenomenon (figure 9.2 and 9.3) occurred. A subsequent waterflood (24/3) failed to displace any oil from the lens even after 20 pore volumes of water had been injected. The oil was miscibly displaced from the lens with absolute alcohol. In runs 24/5 and 24/6 the reverse displacement order was attempted; here no water entered the lens.

9.2 Layered Systems.

In the previous section capillary forces were shown to be important in determining the distribution of fluid within a lensed system. As discussed in section 2.4.1 Richardson and Perkins[53] have shown experimentally that capillary forces are also important in modifying the relative frontal propagation rate (U_A / U_B) in a layered system during an imbibition process. In the work reported in this section a series of immiscible experiments in layered systems were undertaken to study further this modifying effect and to contrast the characteristics of miscible (chapters four through seven) and immiscible displacements. Drainage and imbibition processes with and without an initial residual fluid saturation have been studied for a variety of flow rates.

9.2.1 Waterflooding.

In all the waterflooding experiments reported here the water front in the low conductance layers (X_B) advanced ahead of the front in the higher conductance layer (X_A). This is the opposite to that observed by Richardson and Perkins and possibly reflects the difference in wettability of our media (water-wet glassbeads) compared to theirs (sand). Figure 9.6 shows the characteristic displacement

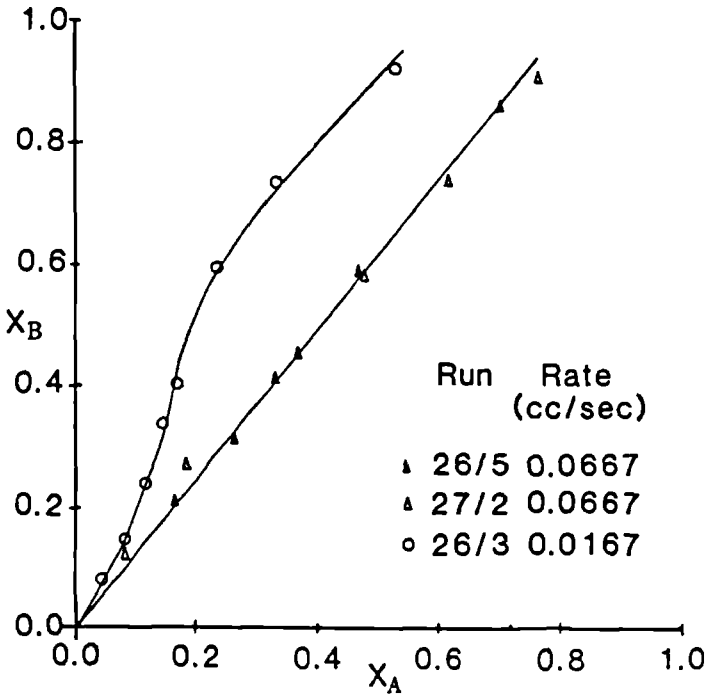

Figure 9.6 Waterflood characteristic curves.

curves at two displacement rates. Here the frontal separation ($X_A - X_B$) is greater for the slower rate displacement. As discussed in section 2.4.1 this is because at the slower rate there is more time for the capillary forces to act to transfer water from the high conductance media (higher water phase pressure) to the low conductance media (lower water phase pressure). This is illustrated in figure 2.18.

The rate dependence of the capillary forces is further emphasised in figures 9.7 and 9.8.

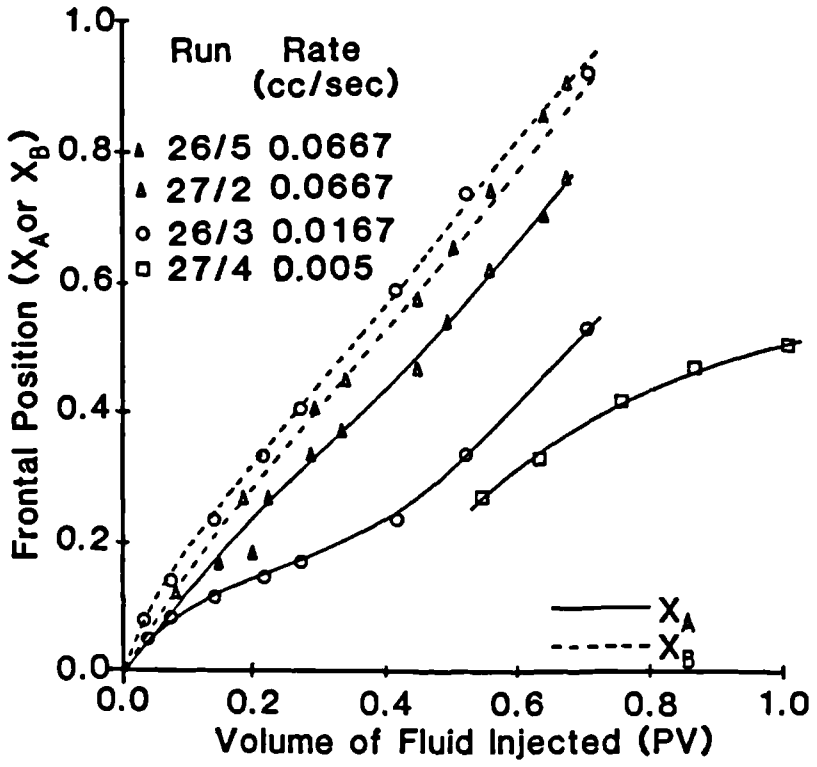

Figure 9.7 Correlation of frontal position versus pore volumes injected for waterfloods.

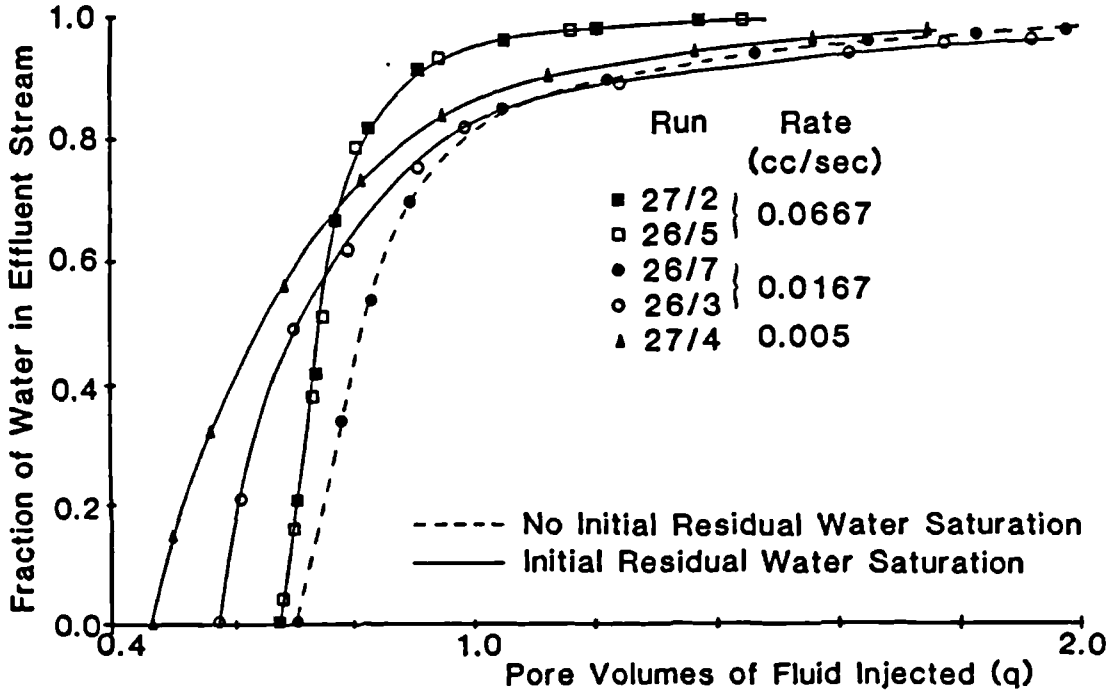

Figure 9.8 Effluent profiles for waterflooding experiments in layered systems.

In figure 9.7 the rate of frontal advance of X_B can be seen to increase with decreasing rate, while that of X_A decreases. Figure 9.8 shows that breakthrough occurs earlier (on a pore volume basis) and the production period becomes longer as the injection rate decreases. Both these observations support Othe above discussion. This figure also shows that when there was no initial residual saturation (run 26/7) breakthrough occurred later than it did for the experiments with an initial residual saturation. In this displacement the central layer was only flooded over its whole width close to the injection end of the model. Over the rest of its length only the boundary area was swept until after breakthrough when the oil from the central area of the layer was recovered as this area slowly contracted. This observation is similar to that in run 22/4 and is due to the lack of an initial residual fluid saturation which would allow pressure communication between the layers.

9.2.2 Oilflooding.

Most of the oilflooding experiments had the characteristic pointed shape of a favourable mobility ratio displacement (chapter four). Here the end point mobility ratios were 0.789 with an initial residual fluid saturation and 0.530 without. The effect of capillary forces in these displacements was to tend to force the oil (non-wetting fluid) into the central layer and the water (wetting fluid) into the outer layers of tighter media; which tended to push the fronts in each layer apart. As with the waterfloods the effect of the capillary forces was inversely proportional to the displacement rate. This is shown in figure 9.9 where the largest frontal separation occurred in the displacement at the slower rate. Also shown in these figures are the predicted (chapter four) characteristic curves for a miscible displacement. All

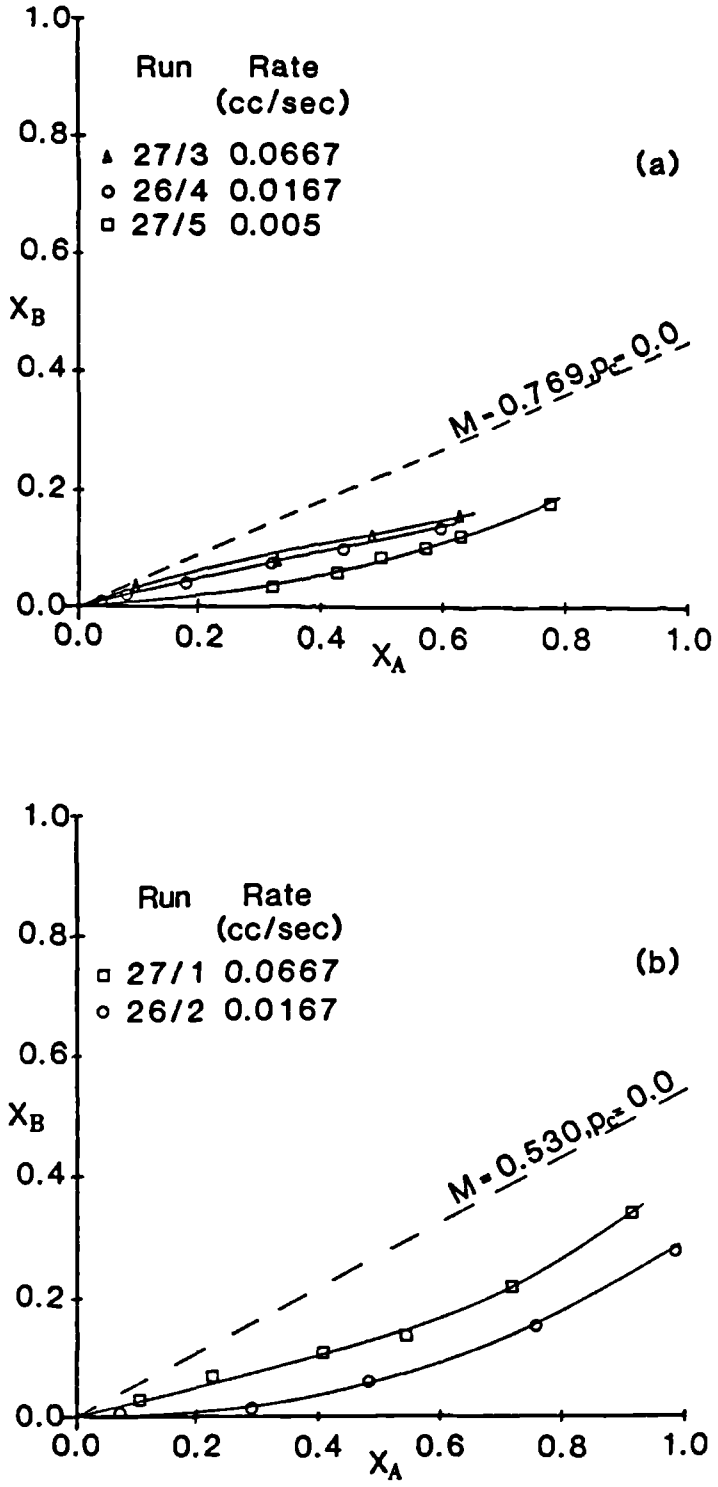

Figure 9.9 Oilflooding characteristic curves for displacements (a) with and (b) without an initial residual oil saturation.

the immiscible experiment data show a greater frontal separation than predicted for the miscible case, although this is approached as the displacement rate increases (figure 9.9). Thus it may be expected that the immiscible and miscible cases would coincide when the rate is large enough (ie. capillary forces are negligible compared to the viscous forces).

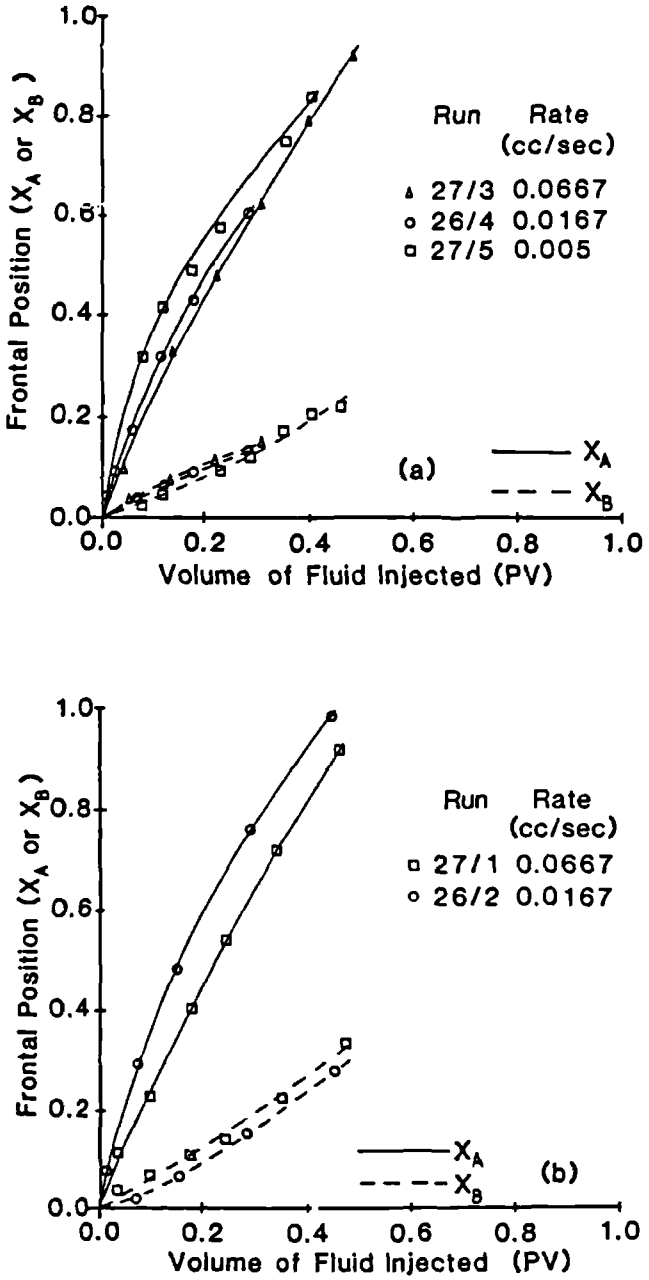

Figure 9.10 Correlation of frontal position versus pore volumes injected for oil floods (a) with and (b) without an initial residual oil saturation.

In figure 9.11 the effluent profiles for the oil-flooding experiments show that the pore volumes injected at breakthrough increases and production period decreases with increasing injection rate. This reflects the rate dependence of the capillary effects. Breakthrough for the displacements without an initial residual fluid saturation is later than for those with, due to the more favourable end point mobility ratios in these cases.

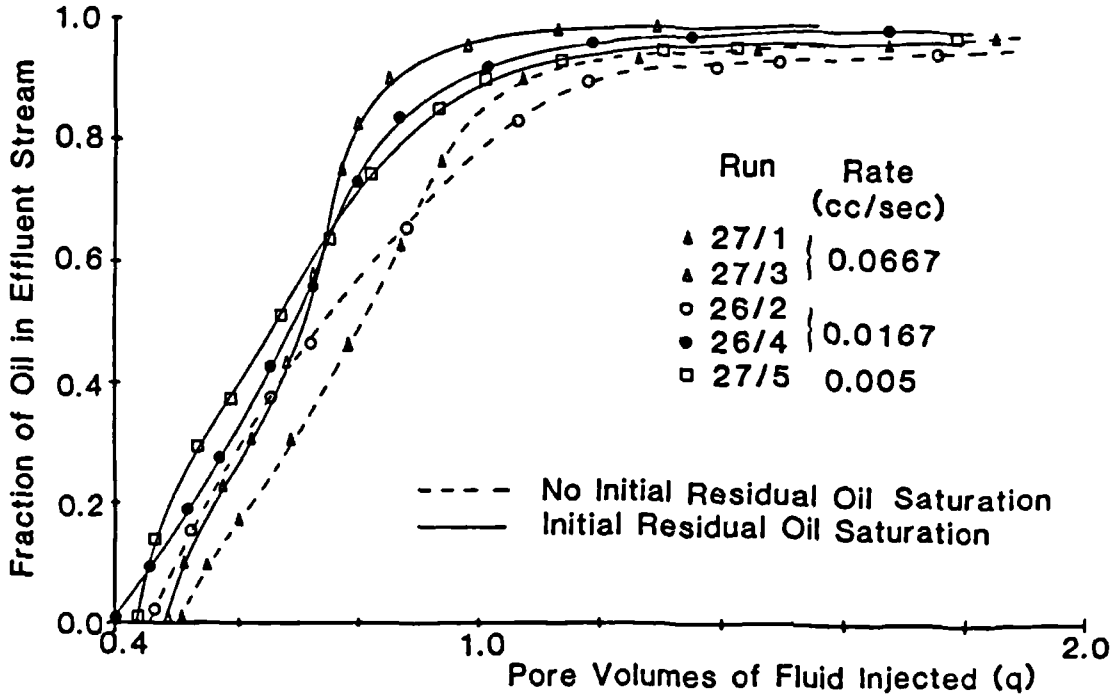

Figure 9.11 Effluent profiles for oilflooding experiments in layered systems.

9.3 Comparison of Miscible and Immiscible Displacements.

The experiments described in this chapter have demonstrated the effect that capillary forces have over localised events (eg. in the vicinity of the lens) and how they affect the relative frontal velocities in a stratified media. In chapter four it was shown that the displacing

fluid tended to channel through the high conductance media. In the waterflooding experiments with layered packings reported here, capillary forces were strong enough to make the displacement front advance faster in the low conductance media. In the oilflooding experiments the displacement front advanced faster in the higher conductance media than would be predicted due to viscous forces alone (figure 9.9). Here, due to the favourable end point mobility ratio in these displacements, the pointed displacement front characteristic of favourable viscous crossflow was observed.

In the miscible displacements in lensed systems reported in chapter eight, the fluid displacement fronts were observed to travel smoothly through the system, although their shape and instantaneous velocities were affected by the lens. The experiments reported in section 9.1 for immiscible displacements in lensed systems show contrasting characteristics. Here the displacements were dominated by the capillary effects around the lens. In some cases the displacement front in the surrounding media was observed to stop moving while the displacing fluid entered the lens. On the other hand in some cases the capillary forces at the lens boundary stopped the displacement front in the centre of the system from moving forward. In these experiments fluid was trapped both in the lens and at the matrix boundaries due to capillary forces.

This work shows that there are major differences between miscible and immiscible displacements and more work needs to be done in this area. This is being attempted in a parallel research project[76] .

CHAPTER TEN

SUMMARY AND CONCLUSIONS

The effects of heterogeneity channelling, viscous crossflow and microscopic transverse dispersion in both continuous injection and slug mode processes of relevance to oil recovery have been investigated. The objective has been to understand the mechanisms affecting fluid flow in heterogeneous porous media so that more efficient computer modelling of reservoirs and long core experiments can be achieved.

To this end fluid flow has been studied in laboratory bead pack models (described in chapter three) with a variety of packing structures and fluid systems. The displacement data have been matched by numerical and theoretical models which allow scaling to the reservoir or the long core tests. Additionally fluid flow in lensed systems were considered. Lenses cause increased disturbances of the streamline patterns. Modelling of the unit mobility ratio case has been achieved, while approximations have been used to study non-unit mobility ratio cases. Finally a number of carefully chosen experiments in both layered and lensed models have highlighted the differences between the miscible and the immiscible cases.

10.1 Viscous Crossflow in Continuous Injection Processes in Layered Systems.

10.1.1 Summary.

Viscous crossflow effects in layered media have been demonstrated to occur in miscible fluid displacements. Measurements show the relationship between the relative displacement ratio in the layers, U_A/U_B, the conductance

(permeability/porosity) contrast between the layers, C_A/C_B, the mobility ratio M (which for the miscible systems used in this study is the ratio of displaced to displacing fluid viscosity), and the layer aspect ratio, h_D (system length to layer thickness ratio). These data have validated a mathematical model[37] which predicts the relative displacement ratio based on the axial pressure distributions in a dual layer system. This model has been extended to approximate the relative advance of the front in the low conductance layer (X_B) after breakthrough has occurred in the high conductance layer. This is given by:

$$\left(\frac{U_B}{U_A}\right)^* = \frac{C_B}{C_A M}\left[\frac{1.0+Z^*}{(1/M)+Z^*}\right] \qquad (4.22)$$

where

$$Z^* = \left(\frac{C_A/C_B + 1/M}{C_A/C_B + 1.0}\right)^{\frac{1}{2}} \qquad (4.23)$$

Additionally a method has been developed to calculate the modified shape of the fluid/fluid interfacial geometries due to viscous crossflow. The distance the interface moves relative to the interlayer boundary is given by:

$$\left.\frac{x_L}{h}\right|_{dx,dT} = \frac{C_A}{C_B}\frac{dX_B}{2}\left(\frac{d^2P_A}{dX^2}\right)[X_B(1-M)+M] \quad , \quad X_{CR} \leq X \leq X_A \qquad (4.17)$$

$$\left.\frac{x_L}{h}\right|_{dx,dT} = \frac{C_B}{C_A}\frac{dX_A}{2}\left(\frac{d^2P_B}{dX^2}\right)\left[\frac{X_A(1-M)+M}{M}\right] \quad , \quad X_B \leq X \leq X_{CR} \qquad (4.18)$$

and an example is shown in figure 4.19. This method has allowed the mechanism of viscous crossflow to be more fully understood.

10.1.2 Conclusions.

(i) Layered heterogeneities cause lower sweep efficiency for the number of pore volumes injected than for the homogeneous case. For unit mobility ratio case,

figure 4.2 shows that for conductance contrasts greater than 10.0 and a layer to system width ratio of 0.5, less than 55% of the system will be swept at breakthrough compared to 100% for the uniform case.

(ii) This sweep efficiency is affected by the mobility ratio, M, and is further modified by viscous crossflow. When $M < 1.0$ the sweep efficiency is greater than the unit mobility ratio case, while when $M > 1.0$ it is less.

(iii) Favourable viscous crossflow may be used to stabilize a displacement front against the heterogeneous media, although to achieve this very high viscosification of displacing fluid may be necessary.

10.2 Slug Degradation Due to Viscous Forces.

10.2.1 Summary.

Miscible slug mode displacements in layered systems have been studied experimentally. High conductance layer width to total system width ratio (b), layer aspect ratio (h_D), slug volume and fluid mobilities have been varied, and a number of interesting observations have been made. The overtaking point (defined in chapter five), which indicates when recovery is likely to start to be impaired, has been introduced. For maximum efficiency this point should not occur within the system. Slug flow has been evaluated by considering the relative displacement values for the front (U_{A1}/U_{B1}) and trailing (U_{A2}/U_{B2}) edges separately. The optimum size of the slug, in pore volumes designed to avoid the overtaking point occurring within the system is:

$$S_{OPT} = b(U_A/U_B)*(1-U_{B1}/U_{A1}) + (1-b)(1-U_{B2}/U_{A2}) \qquad (5.15)$$

which is given as a function of the chase/slug mobility ratio in figure 5.14.

10.2.2 Conclusions.

(i) The transverse pressure fields created around each non-unit mobility ratio displacement front interfere with each other in slug mode processes and modify both the interfacial geometries (figure 5.8 through 5.10) and relative displacement rate (figure 5.6) compared to those expected for continuous injection processes. These modifying effects decrease with increasing distance from the non-unit mobility ratio front (figure 5.7).

(ii) Viscosification of the slug fluid promotes a more stable leading front but destabilities the rear of the slug. But a slug fluid whose mobility is less than that of the resident fluid leads to a more favourable case, as more fluid is injected into the low conductance layers during the initial stages of the process (displacement pattern 8, figure 5.5).

(ii) Slug sizes of greater than one pore volume may be required to prevent the overtaking point occurring within the system. Thus it may be prudent to consider the recycling of produced slug fluid as an option in field processes.

10.3 The Effects of Dispersion in Layered Systems with Fluids of Equal Mobility.

10.3.1 Summary.

Mixing of chemicals is needed to promote residual oil recovery. However excessive dilution of the chemical to below the 'effective level' will negate the process. Fluid mixing in layered media has been investigated, with an ultra-violet tracer monitoring technique (section 3.4.1) being used to obtain experimental effluent concentration profiles. These data have validated a numerical model based on a moving co-ordinated approach. For slug mode processes this has allowed the fraction of the system

swept by any critical concentration of chemical to be predicted (figure A7.21 through A7.33). Transverse microscopic dispersion is the dominant mixing mechanism in layered media, since the areas over which it can occur are large. It is scaled by the transverse dimensionless time, t,

$$t = \frac{K_t L}{h^2 U} \quad . \qquad (6.15)$$

When $t > 1.0$ the lateral concentrations are maintained constant by transverse microscopic dispersion and the subsequent effluent profiles are characteristic of a one layer system, but with a larger longitudinal dispersion coefficient. Under these conditions analytical predictions are possible for the effluent concentration profiles,

$$\frac{c}{c_o} = \frac{1}{2}\left[\text{erf}\left\{\frac{q-1.0}{2\sqrt{\ell_{eff} q}}\right\} - \text{erf}\left\{\frac{(q-S)-1.0}{2\sqrt{\ell_{eff}(q-S)}}\right\}\right] \qquad (6.27)$$

and the slug volume required to sweep the system with chemical above a certain value, $(c/c_o)_{CRIT}$:

$$S_{OPT} = 4(\text{erf}^{-1}(c/c_o)_{CRIT})\sqrt{\ell_{eff}} \quad . \qquad (6.29)$$

10.3.2 Conclusions.

(i) When $t < 0.01$ fluid mixing may be negligible and the displacement efficiency may be calculated from simple flow mechanics (section 4.1).

(ii) When $t > 1.0$ transverse microscopic dispersion maintains the fluid component concentrations constant over any cross-section of the system.

(iii) When $0.09 \leq t \leq 1.0$ the minimum fraction of the system is swept with chemical above any critical concentration. For a reservoir with conductance contrasts of less than 20.0, in which it would take 3 years to inject one pore volume of fluid, this range of t values corresponds to layer widths between 21.0 and 70.0 cm. For a long core test where 2 hours are required to inject one pore volume of fluid layers

less than 2.25 mm will be characterised by a transverse dimensionless time of greater than 1.0. As this represents a thick layer at the core scale, transverse dispersion will dominate fluid component distributions in these tests.

(iv) This work has shown that it might be more efficient to inject a small concentrated chemical slug (low critical concentration) rather than a large dilute one (high critical concentration).

(v) In multi-well tracer tests, which have been proposed [75,83] to determine interwell matrix properties prior to the application of EOR processes, transverse microscopic dispersion will cause a redistribution of fluid components between the layers. The field implication of these tests have been limited by the lack of mathematical models with which to deconvolute the resultant effluent profiles. It is hoped that this work may clarify the understanding of the mechanisms involved and thus aid in the development of an effective mathematical model.

10.4 The Effect of Dispersion in Layered Systems with Fluids of Unequal Mobilities.

10.4.1 Summary.

The coupling between viscous forces and microscopic dispersive phenomena were investigated by numerical and experimental methods. Non-unit mobility ratio displacements in a multi-layered laboratory model (packing 25) were conducted at rates where the transverse dispersion of fluid components was important. The concentration of the effluent stream was monitored by an ultra-violet monitoring technique for both continuous injection and slug mode processes. A numerical method was developed to model the channelling of displacing fluid in a dispersion sensitive process. Here the effective value of the mobility ratio used to calculate the viscous effects was affected by the

redistribution of fluid components due to transverse microscopic dispersion. This approach to the calculation of the effective mobility ratio has suggested a possible relationship between the transverse dimensionless time, t, and the Todd and Longstaff mixing parameter, ω [31] .

10.4.2 Conclusions.

(i) As t (and hence the amount of fluid mixing) increases, the channelling in an unfavourable mobility ratio displacement decreases; while that in a favourable mobility ratio displacement increases.

(ii) As t tends to 1.0 the effects of varying the mobility ratio becomes less pronounced, as transverse microscopic dispersion begins to dominate the process and becomes more important than the viscous forces.

(iii) The coupling of the forces is not just a simple case of the fluid mixing modifying the effective mobility ratio, but as figure 7.10 illustrates involves a complicated interaction of processes.

(iv) In slug mode, the processes appear further complicated by the more complex pressure fields which occur around the non-unit mobility ratio displacement fronts.

10.5 Miscible Fluid Flow in a System Containing a Lens.

10.5.1 Summary.

Lens structures cause additional streamline modifications compared to layered media (figure 8.2), and further modifications to the shape of the displacement front are caused by non-unit mobility ratios (figures 8.9 and 8.10). These effects have been studied in laboratory models containing lenses of either higher or lower conductance than the surrounding media. The unit mobility ratio displacement data have been matched by a finite crossflow

analysis similar to that used in chapter four. A non-communicating channel theoretical model was developed to highlight the important effects in the non-unit mobility ratio case.

10.5.2 Conclusions.

(i) For the unit mobility ratio case, the fraction of the system swept at breakthrough is very sensitive to the layer aspect ratio, h_D (figure 8.6), the conductance contrast and the length of the lens, but does not appear to be affected by the axial lens position (figure 8.8).

(ii) For the non-unit mobility ratio cases, the fraction of the system swept at breakthrough is sensitive to all these variables (figure 8.13 through 8.15).

10.6 Capillary Pressure Effects in Immiscible Displacement.

10.6.1 Summary.

Immiscible displacements bring wettability effects, capillary pressure and relative permeability phenomena into the analysis. Carefully chosen water and oilfloods were conducted in layered and lensed systems with the aim of highlighting the differences between miscible and immiscible displacements. Experiments with and without an initial residual fluid saturation were carried out. These displacements were followed photographically and the effluent saturation profiles were recorded for the layered systems. Additionally systems where the lens wettability differed from that of the surrounding matrix were studied. Here the lens beads were treated with dimethyldichlorosilane.

10.6.2 Conclusions.

(i) The balance between capillary and viscous forces is rate dependent, with capillary forces becoming of greater importance as the flow rate decreases. At high enough flow rates an immiscible displacement may have the same characteristics as a miscible displacement as capillary forces will be negligible in comparison to viscous forces.

(ii) The displacements in lens systems have shown that capillary forces dominate localized events.

(iii) In the displacements in layered systems capillary forces, (imbibition and drainage) strongly influenced the rate of frontal advance in each layer.

10.7 Final Remarks.

This work has demonstrated that heterogeneous media can have a profound effect on the distribution of fluids and their components within the system. There are large differences between miscible and immiscible displacements which cannot be ignored when modelling reservoir behaviour. These two processes must therefore be treated differently. If the physics assumed to represent the transmission of fluids from block to block is not correct, then the reservoir simulation results could lead to gross miscalculations and wrong recovery forecasts.

APPENDIX ONE

A1.1 Air/Water Capillary Pressure Measurement.

The apparatus consisted of a capillary pressure cell connected to a bur ette through a 2 way valve (A) in a U-tube arrangement (figure A1.1).

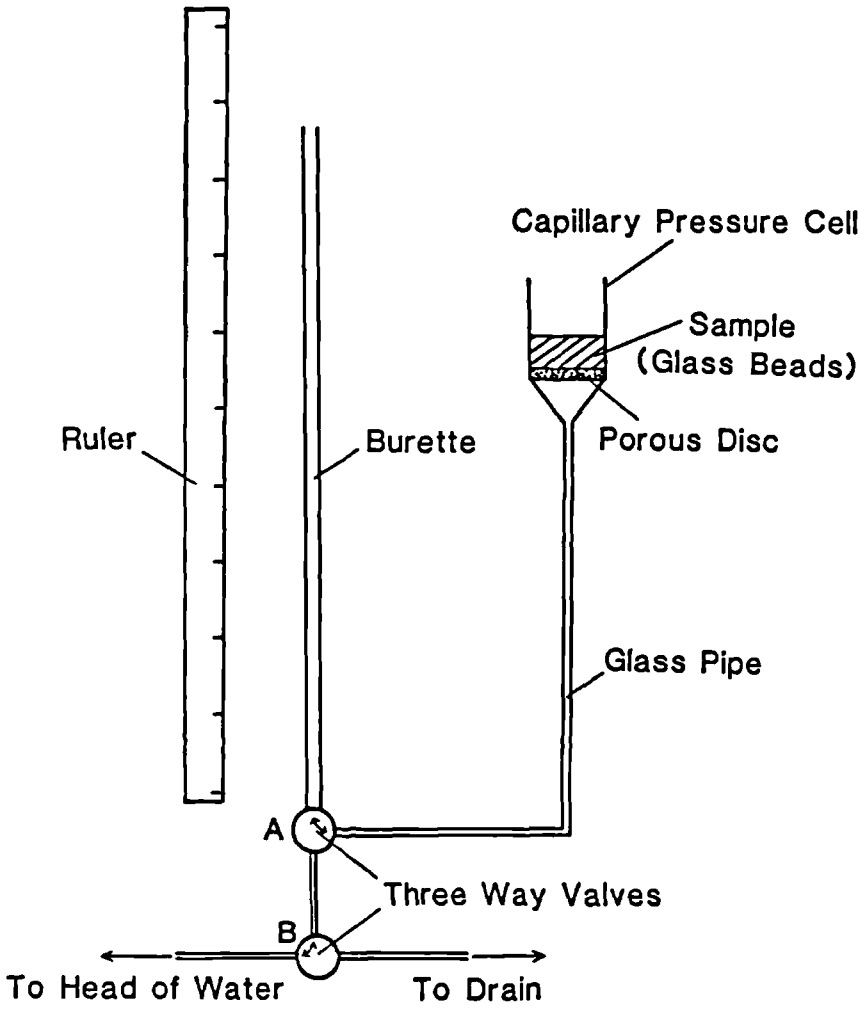

Figure A1.1 Air/water capillary pressure apparatus.

The third outlet of valve A was connected to valve B so that water could be added to or withdrawn from the system, via the bur ette. Therefore when valve A connected valve B and the bur ette, the water level in the bur ette could be

altered without the fluids in the cell being affected, and when it connected the bur ette to the cell, the fluid potentials could equilibriate. Initially the apparatus was filled with water so that there was a known volume of water above the porous disc in the cell (~30cc). A known volume of glass beads (~10cc) was then added to the cell. This was done slowly and the bead/water mixture stirred continuously to prevent air becoming trapped. By careful use of the burette and valve A, known volumes of water were withdrawn from the cell until the water just covered the sample of beads. The porosity of the sample was calculated at this point from the ratio of the pore volume to the total sample volume. The water level in the bur ette was then set equal to that in the cell.

A drainage experiment was conducted first; here valve B was connected to the drain (figure A1.1). A known volume of water (~1cc) was then withdrawn from the burrette and the system allowed to equilibrate (~10 mins). The height difference (ΔH) between the initial and equilibrium bur ette levels was noted, and is related to the capillary pressure (p_c) by:

$$p_c = \Delta H g \rho_w \qquad \text{(A1.1)}$$

The new water saturation (S_w) in the sample was calculated from a material balance and was plotted against p_c. This procedure was repeated until no further change in level was detected in the bur ette. At this stage the residual water saturation had been reached and the complete drainage capillary pressure curve obtained. Valve B was then adjusted to allow the bur ette to be filled with water and the procedure reversed to obtain the imbibition curve.

A1.2 Contact Angle Measurement.

The contact angles were measured using a commercial contact angle apparatus (from Kruss of Hamburg) and a piece of 'frosted' soda glass (since this best represented the surface of the Ballotini used in the experiments). The glass was cleaned with acid, a small drop of water was placed on it and the air/water contact angle measured (figure A1.2). The oil/water contact angle was measured by trapping a drop of soltron underneath the glass, which was now suspended in a small tank of water. The measured contact angles are given in figure A1.2 where the two experimental set-ups are illustrated.

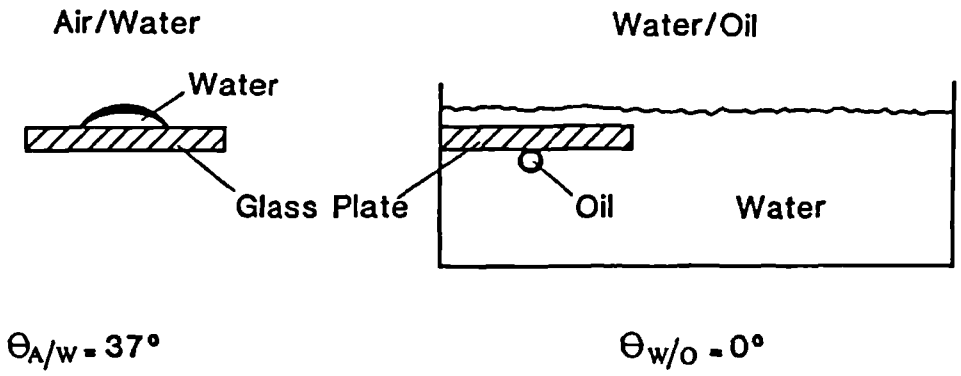

Figure A1.2 Contact angle measurement.

A1.3 Surface and Interfacial Tension Measurement.

Surface and interfacial tensions were measured in a Kruss Tensiometer using the Du Nouy Ring method[69]. The results obtained at 20.0±0.1°C were:

Surface tension of distilled water = 73.0 mN/m.

Surface tension of soltrol = 28.8 mN/m.

Interfacial tension between water and soltrol= 23.0 mN/m.

Thus, for the soltrol/water system using equation 3.1,

$$P_{c\ OIL/W} = 0.393\ P_{c\ AIR/W} \qquad (A1.2)$$

Drainage and imbibition curves for grade 6 and 9 Ballotini glass beads are given in figure 3.11.

APPENDIX TWO

DATA FOR STUDY OF VISCOUS CROSSFLOW IN LAYERED SYSTEMS

This appendix contains experimental and analytical characteristic curves (X_A vs. X_B graphs) for the continuous injection displacements conducted to study viscous crossflow and heterogeneity channelling. These data are discussed in chapter four.

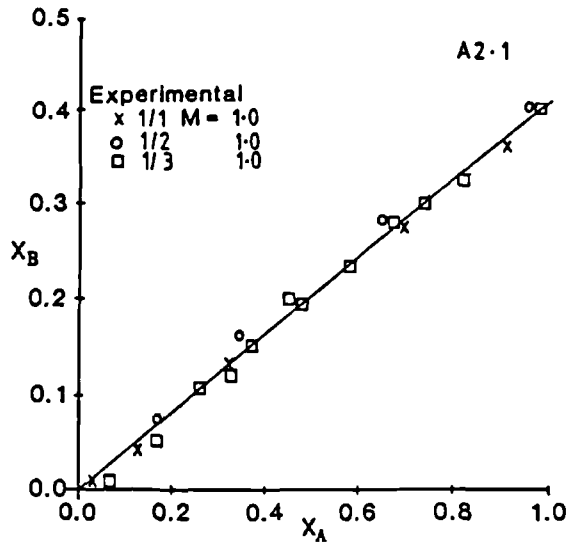

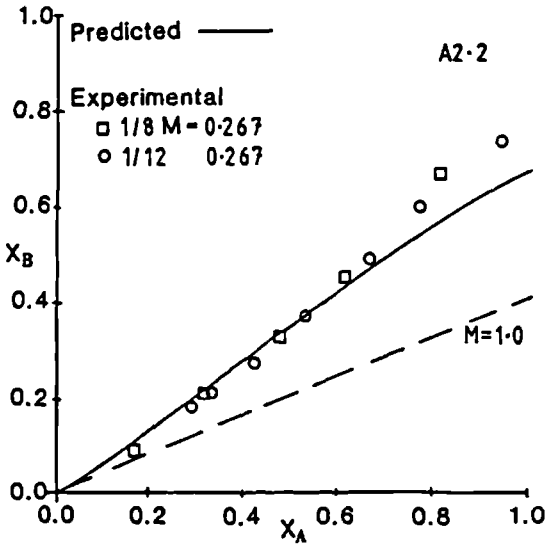

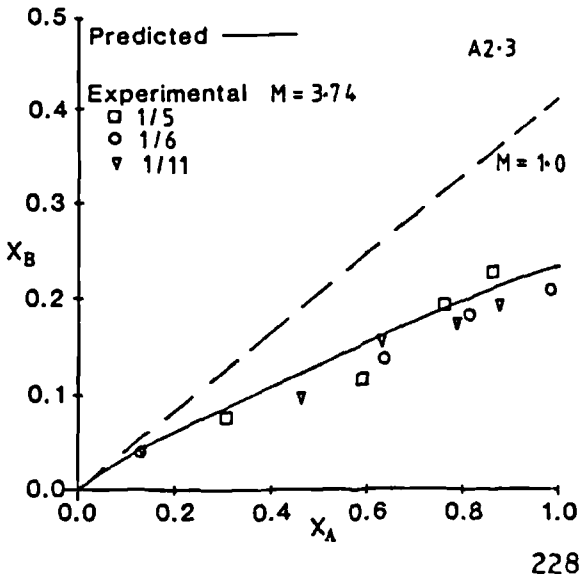

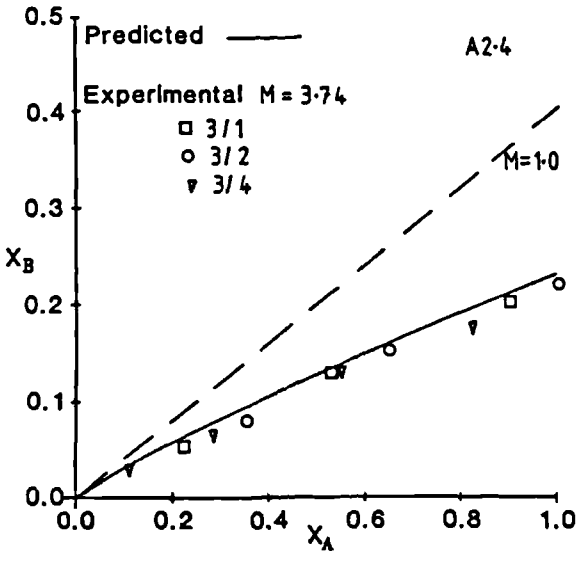

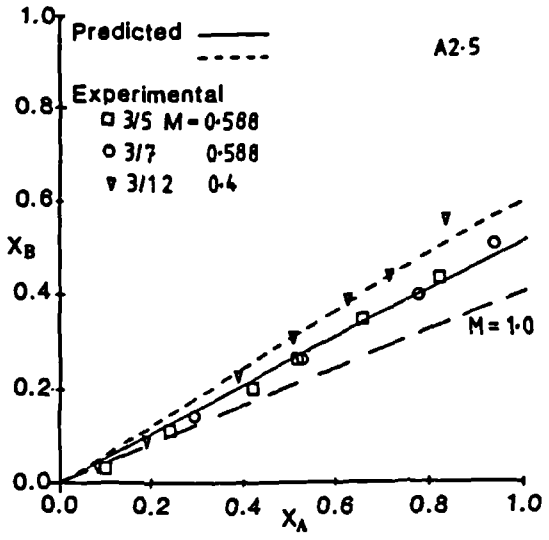
Predicted
A2·5
Experimental
□ 3/5 M = 0·588
○ 3/7 0·588
▼ 3/12 0·4
M = 1·0
X_B
X_A

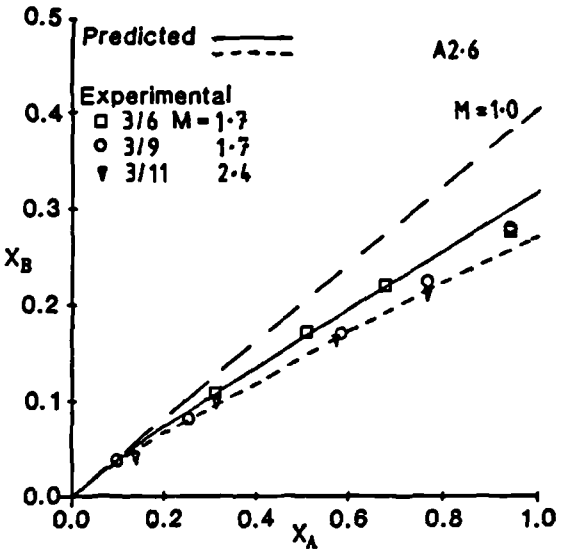
Predicted
A2·6
Experimental
□ 3/6 M = 1·7
○ 3/9 1·7
▼ 3/11 2·4
M = 1·0
X_B
X_A

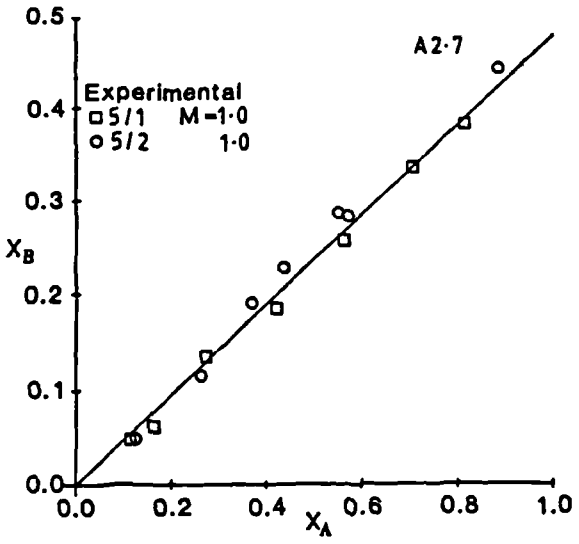
A2·7
Experimental
□ 5/1 M = 1·0
○ 5/2 1·0
X_B
X_A

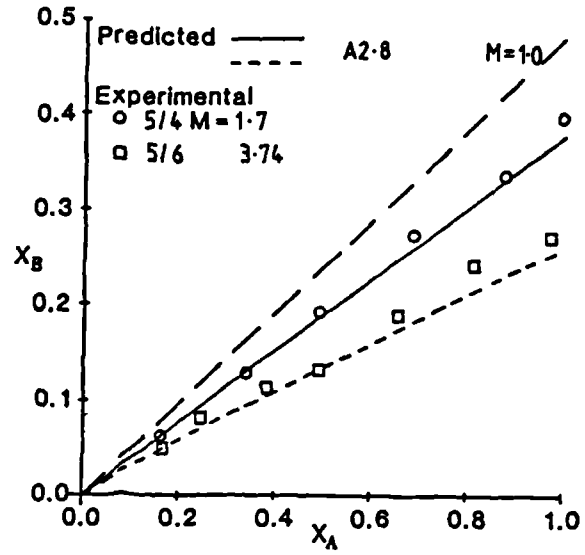
Predicted
A2·8
M = 1·0
Experimental
○ 5/4 M = 1·7
□ 5/6 3·74
X_B
X_A

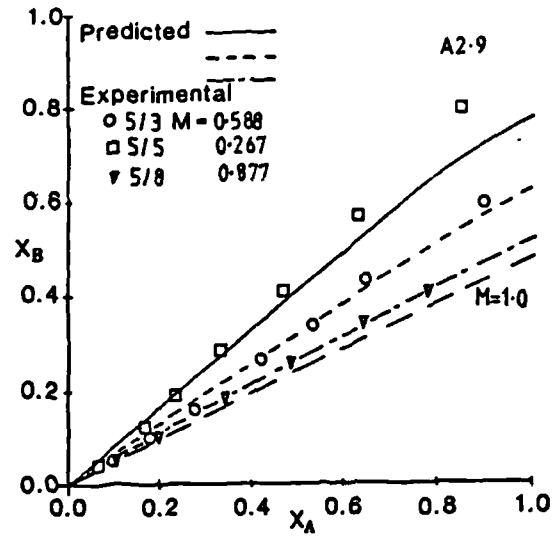
Predicted
A2·9
Experimental
○ 5/3 M = 0·588
□ 5/5 0·267
▼ 5/8 0·877
M = 1·0
X_B
X_A

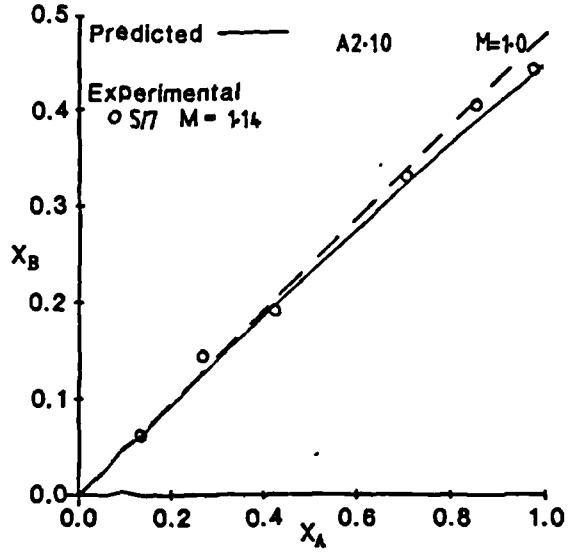
Predicted
A2·10
M = 1·0
Experimental
○ 5/7 M = 1·14
X_B
X_A

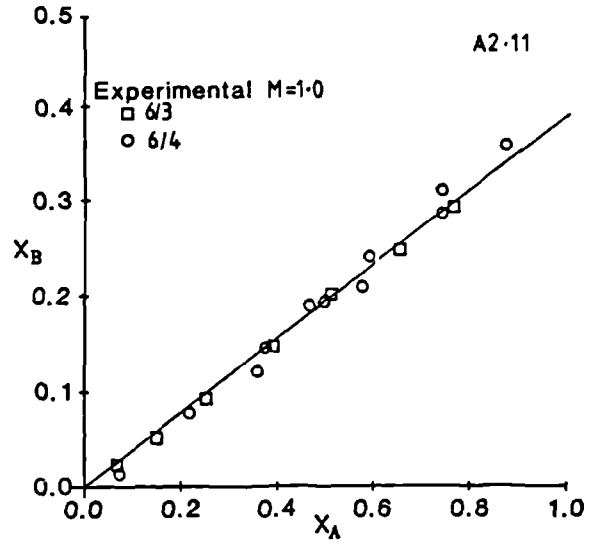
A2·11
Experimental M=1·0
□ 6/3
○ 6/4
X_B
X_A
0.0
0.1
0.2
0.3
0.4
0.5
0.6
0.8
1.0

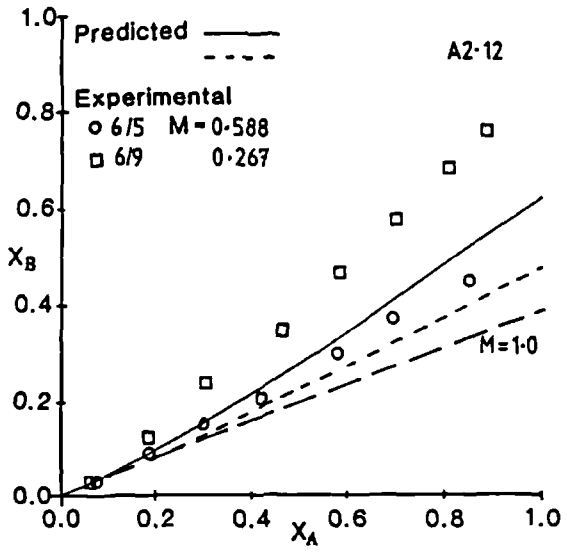
Predicted
A2·12
Experimental
○ 6/5 M = 0·588
□ 6/9 0·267
M=1·0
X_B
X_A
0.0
0.2
0.4
0.6
0.8
1.0

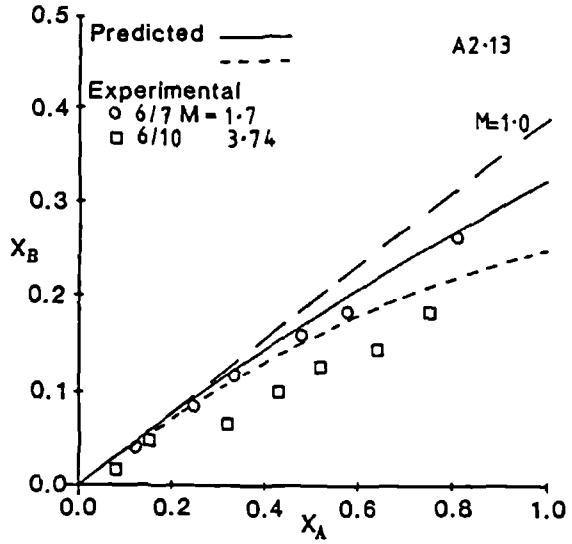
Predicted
A2·13
Experimental
○ 6/7 M = 1·7
□ 6/10 3·74
M=1·0
X_B
X_A
0.0
0.1
0.2
0.3
0.4
0.5
0.6
0.8
1.0

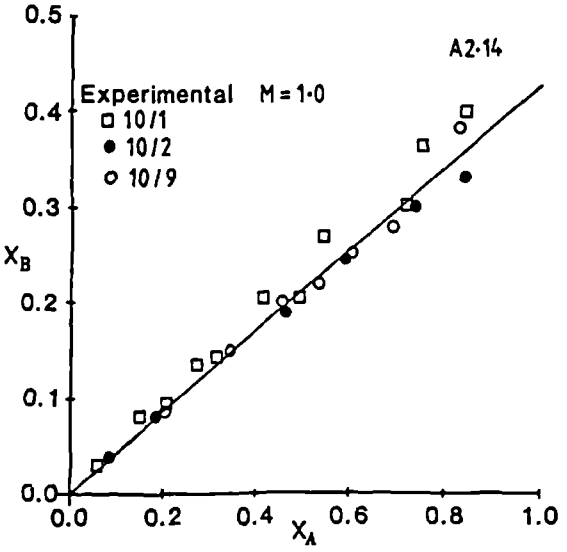
A2·14
Experimental M = 1·0
□ 10/1
● 10/2
○ 10/9
X_B
X_A
0.0
0.1
0.2
0.3
0.4
0.5
0.6
0.8
1.0

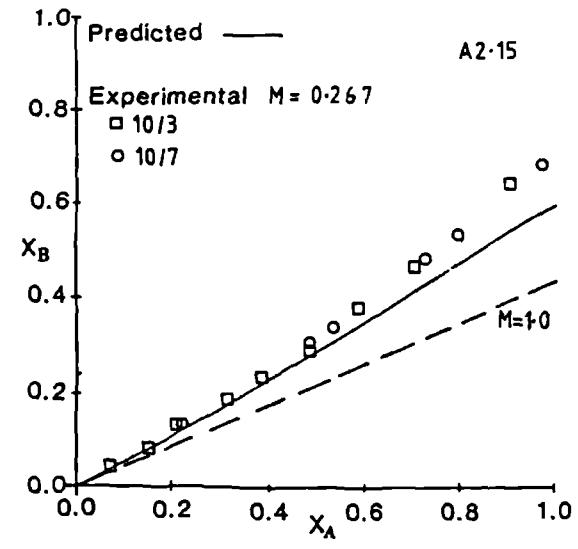
Predicted
A2·15
Experimental M = 0·267
□ 10/3
○ 10/7
M=1·0
X_B
X_A
0.0
0.2
0.4
0.6
0.8
1.0

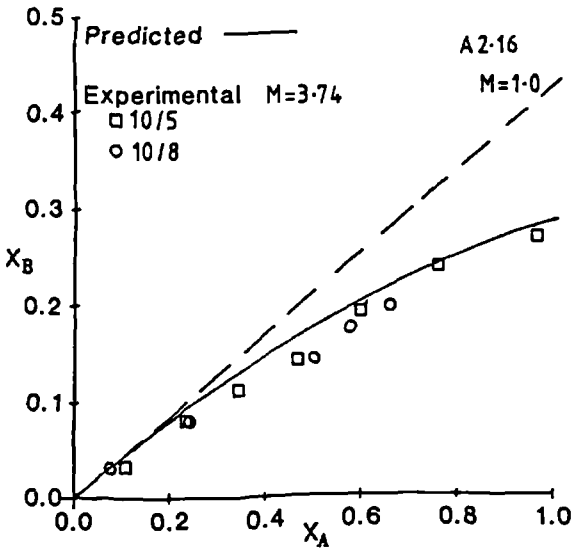
Predicted
A2·16
Experimental M=3·74
□ 10/5
○ 10/8
M=1·0
X_B
X_A
0.0
0.1
0.2
0.3
0.4
0.5
0.6
0.8
1.0

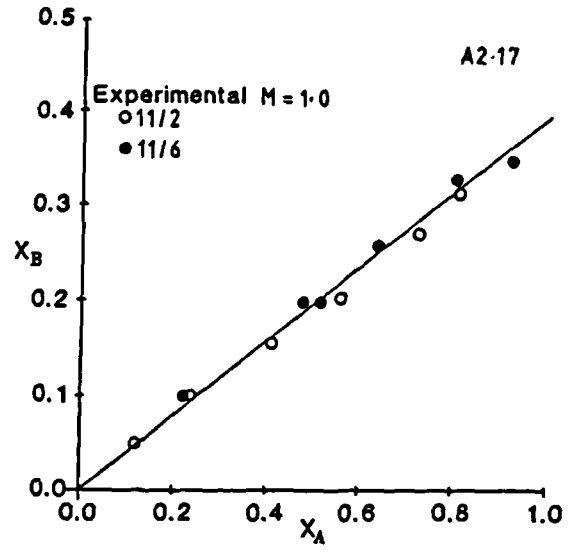
A2·17
Experimental M = 1·0
o 11/2
• 11/6
X_B
X_A
0.0
0.1
0.2
0.3
0.4
0.5
0.6
0.8
1.0

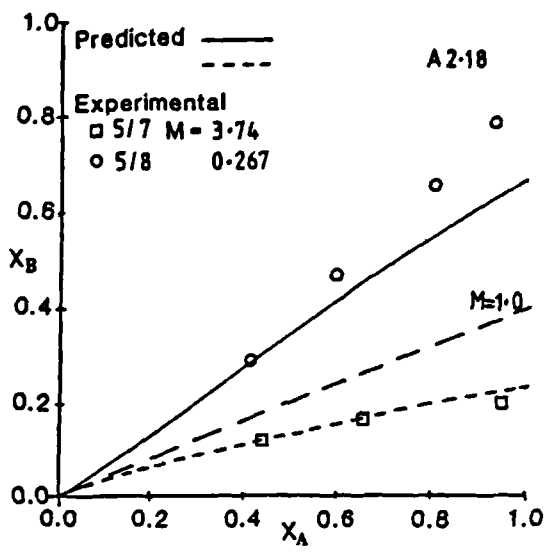
A2·18
Predicted
Experimental
□ 5/7 M = 3·74
o 5/8 0·267
M=1·0
X_B
X_A
0.0
0.2
0.4
0.6
0.8
1.0

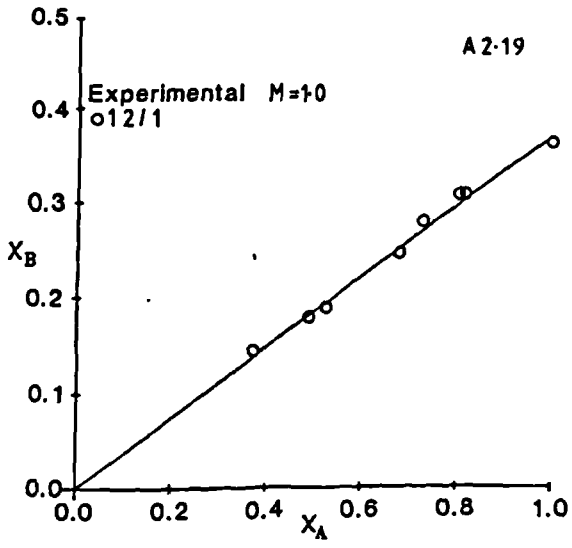
A2·19
Experimental M=1·0
o 12/1
X_B
X_A
0.0
0.1
0.2
0.3
0.4
0.5
0.6
0.8
1.0

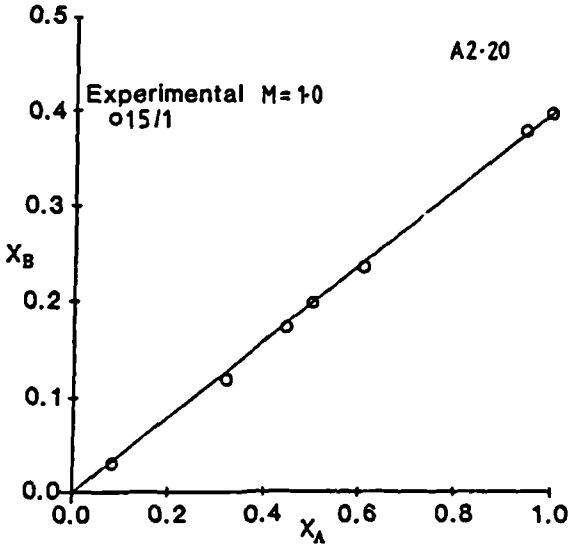
A2·20
Experimental M= 1·0
o 15/1
X_B
X_A
0.0
0.1
0.2
0.3
0.4
0.5
0.6
0.8
1.0

APPENDIX THREE

DERIVATION OF EQUATIONS TO APPROXIMATE VISCOUS CROSSFLOW EFFECTS IN SYSTEMS WHERE LAYER A IS WIDER THAN LAYER B

For the case where layer A (the high conductance layer) is wide relative to layer B (the low conductance layer), the flow rate within layer B cannot be assumed constant and unaffected by fluid crossflowing from layer A , and so the method of Wright and Dawe [37] is not valid. Here it is necessary to assume constant flow rate within layer A and calculate how the crossflow of fluid affects the axial pressure profiles within layer B . The fronts in layers A and B are further assumed to be widely spaced.

A differential mass balance on an element of the system (similar to that in figure 4.14) gives:

$$\frac{d^2P_B}{dX^2} - \alpha' P_B = \alpha'(X-1) \qquad \text{(A3.1)}$$

where $$\alpha' = \frac{4}{h_D^2 \left\{ 1 + \frac{C_B}{C_A} \frac{\mu_A}{\mu_B} \right\}}$$

Equation A3.1 is solved upstrea $(0.0 \leq X \leq X_B)$ and downstream $(X_B \leq X \leq X_{CR})$ of the displacement front X_B , to give the axial pressure profile within layer B :

$$P_B = B[\exp(-X\gamma')-\exp(X\gamma)] + 1 - X \quad , \qquad 0.0 \leq X \leq X_B \tag{A3.2}$$

where $$\gamma' = \frac{2}{h_D\left\{1 + \frac{C_B}{C_A}\right\}^{\frac{1}{2}}}$$

$$P_B = A[\exp(X\beta')-\exp(\beta'(2X_{CR}-X))] + 1 - X \quad , \qquad X_B \leq X \leq X_{CR} \tag{A3.3}$$

where $$\beta' = \frac{2}{h_D\left\{1 + \frac{C_B}{MC_A}\right\}^{\frac{1}{2}}} \quad .$$

Using the boundary conditions:

$$\left.\begin{aligned} P_{B,UPSTREAM} &= P_{B,DOWNSTREAM} \\ M\left(\frac{dP_B}{dX}\right)_{UPSTREAM} &= \left(\frac{dP_B}{dX}\right)_{DOWNSTREAM} \end{aligned}\right\} X = X_A \tag{A3.4}$$

the constants A and B can be evaluated as:

$$A = \frac{H(1-M)}{H\beta'G+M\gamma'IF} \quad ; \quad B = \frac{F(1-M)}{H\beta'G+M\gamma'IF} \tag{A3.5}$$

where $$F = \exp(X_B\beta') - \exp(\beta'(2X_{CR}-X_B))$$

$$G = \exp(X_B\beta') + \exp(\beta'(2X_{CR}-X_B))$$

$$H = \exp(-X_B\gamma') - \exp(X_B\gamma')$$

$$I = \exp(-X_B\gamma') + \exp(X_B\gamma) \quad .$$

The instantaneous rate of advance of X_B is given by:

$$\left(\frac{U_B}{U_A}\right) = -\frac{C_B}{C_A}\ \frac{1}{M}\left(\frac{dP_B}{dX}\right)_{X_B,DOWNSTREAM} \quad . \qquad (A3.6)$$

From equation A3.3:

$$\left(\frac{dP_B}{dX}\right)_{X_B,DOWNSTREAM} = -\left(\frac{1+Z'}{1/M+Z'}\right) \qquad (A3.7)$$

where

$$Z' = \frac{\gamma'[\exp(X_B\beta')-\exp(\beta'(2X_{CR}-X_B))][\exp(-X_B\gamma')+\exp(X_B\gamma')]}{\beta'[\exp(X_B\beta')+\exp(\beta'(2X_{CR}-X_B))][\exp(-X_B\gamma')-\exp(X_B\gamma')]} \quad .$$

Equation A3.6 has been used to predict the characteristic curves for packing six which are presented in appendix two and discussed in chapter four.

APPENDIX FOUR

DERIVATION OF EQUATIONS TO APPROXIMATE POST BREAKTHROUGH BEHAVIOUR

The advance of the front in the lower conductance layer (X_B) after breakthrough has occurred in the high conductance layer can be calculated. This is necessary in order to predict the fraction of the system swept after breakthrough and the number of pore volumes of fluid needed to be injected to sweep the entire system. As breakthrough has already occurred in the high conductance layer, a constant flow rate is assumed within layer A to obtain this approximation. The analysis is then similar to that in appendix three, but here the axial pressure profile in layer B is derived between X = 0.0 and X = 1.0 . In this case:

$$Z^* = \frac{\gamma'[\exp(X_B\beta')-\exp(\beta'(2-X_B))]\,[\exp(-X_B\gamma')+\exp(X_B\gamma')]}{\beta'[\exp(X_B\beta'+\exp(\beta'(2-X_B))]\,[\exp(-X_B\gamma')+\exp(X_B\gamma')]} \quad . \quad (A4.1)$$

As h_D tends to zero:

$$Z^* \rightarrow \left(\frac{\gamma'}{\beta'}\right) = \left\{\frac{C_A/C_B+1/M}{C_A/C_B+1.0}\right\}^{\frac{1}{2}} \quad . \quad (A4.2)$$

The post breakthrough advance of X_B is given by:

$$\left(\frac{U_B}{U_A}\right) = M\frac{C_B}{C_A}\left(\frac{1+Z^*}{1/M+Z^*}\right) \quad . \quad (A4.3)$$

Equations A4.2 and A4.3 have been used to model the post breakthrough behaviour in this work.

APPENDIX FIVE

EXPERIMENTAL DATA FOR STUDY OF SLUG DEGRADATION DUE TO VISCOUS FORCES

This appendix contains both characteristic curves and X_{A2} versus X_{B1} graphs for slug mode experimental displacements conducted to study the effects of viscous forces. These data are discussed in chapter five.

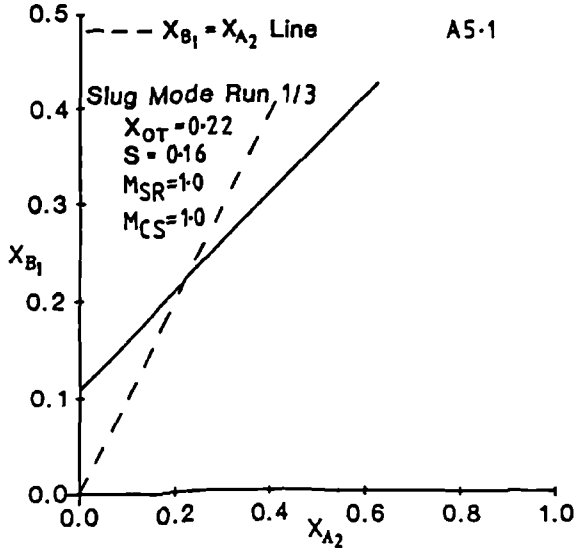

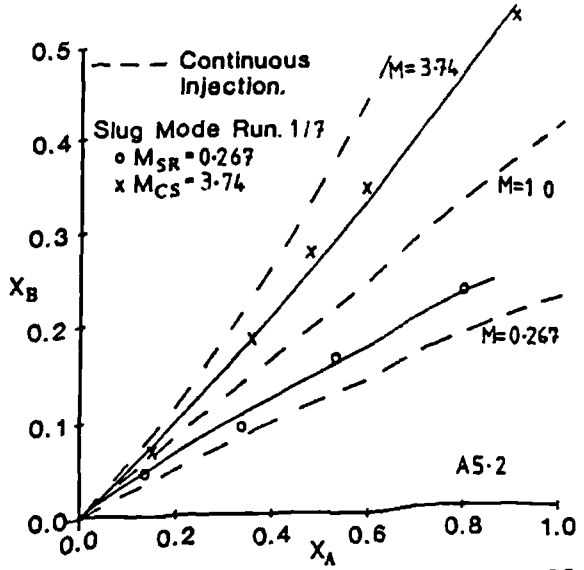

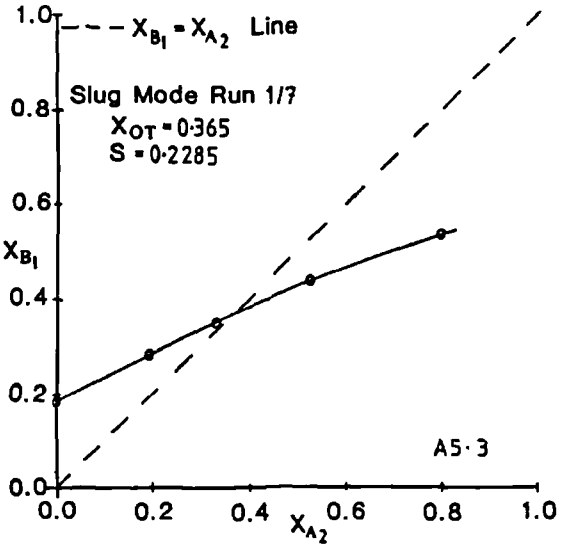

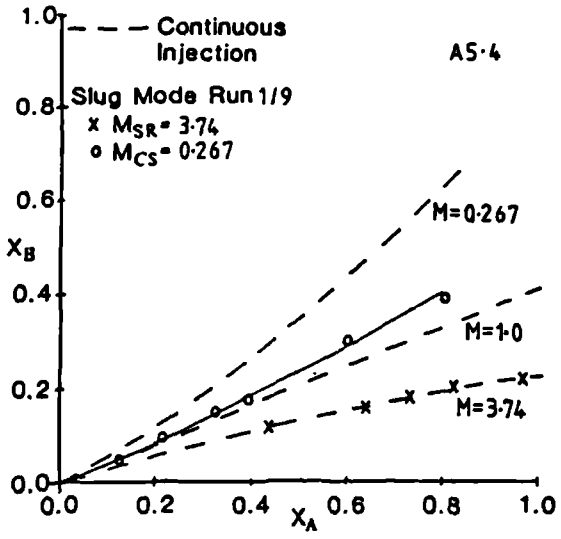
Continuous Injection
A5·4
Slug Mode Run 1/9
x M_{SR} = 3·74
o M_{CS} = 0·267
M=0·267
M=1·0
M=3·74
X_B
X_A
0.0
0.2
0.4
0.6
0.8
1.0

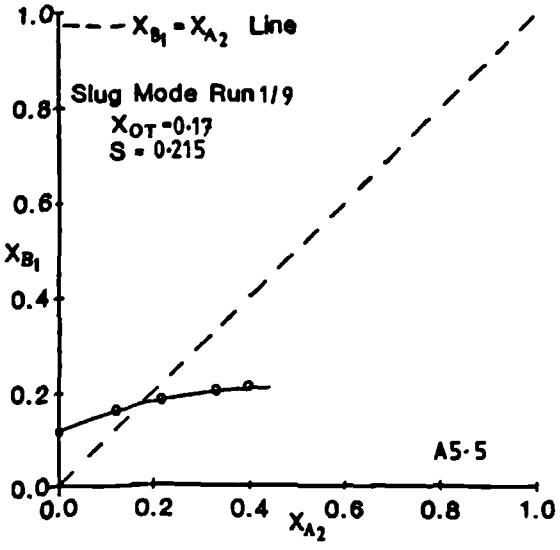
$X_{B_1} = X_{A_2}$ Line
Slug Mode Run 1/9
X_{OT} = 0·17
S = 0·215
A5·5
X_{B_1}
X_{A_2}
0.0
0.2
0.4
0.6
0.8
1.0

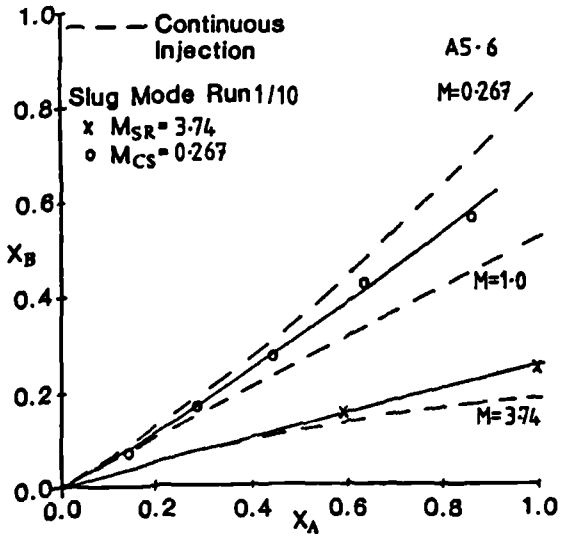
Continuous Injection
A5·6
Slug Mode Run 1/10
x M_{SR} = 3·74
o M_{CS} = 0·267
M=0·267
M=1·0
M=3·74
X_B
X_A
0.0
0.2
0.4
0.6
0.8
1.0

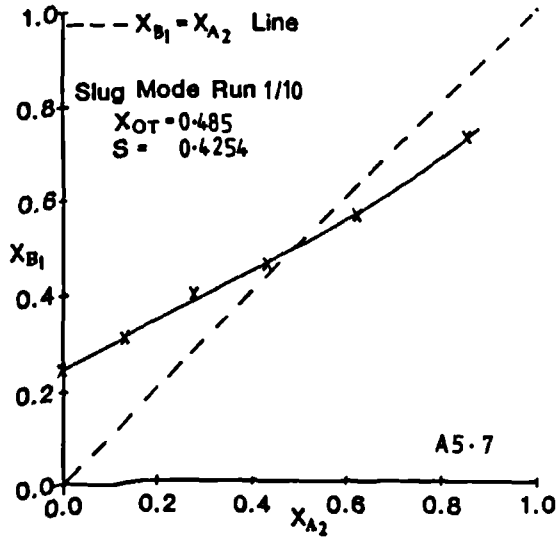
$X_{B_1} = X_{A_2}$ Line
Slug Mode Run 1/10
X_{OT} = 0·485
S = 0·4254
A5·7
X_{B_1}
X_{A_2}
0.0
0.2
0.4
0.6
0.8
1.0

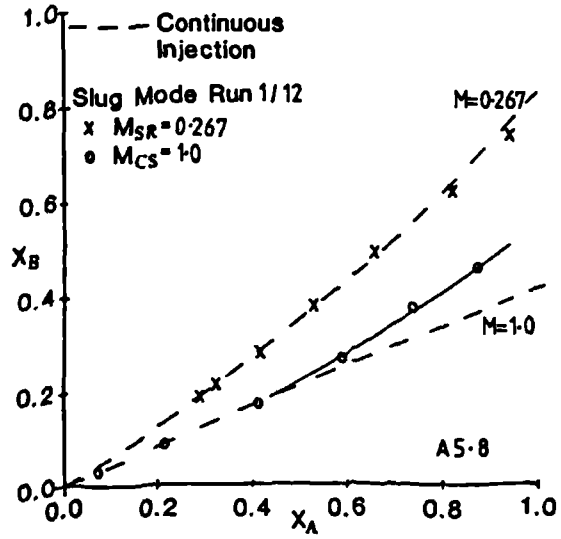
Continuous Injection
Slug Mode Run 1/12
x M_{SR} = 0·267
o M_{CS} = 1·0
M=0·267
M=1·0
A5·8
X_B
X_A
0.0
0.2
0.4
0.6
0.8
1.0

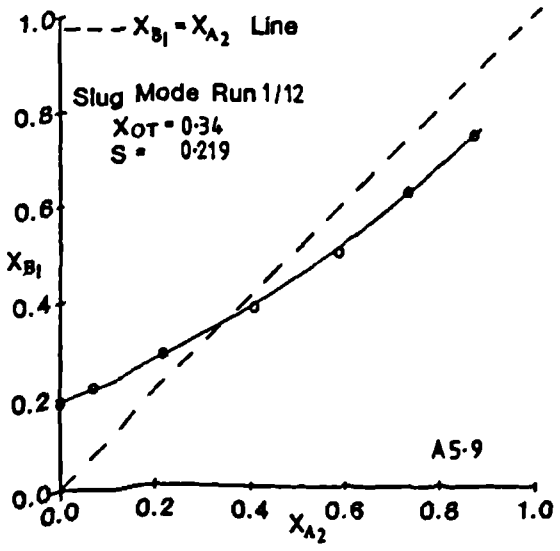
$X_{B_1} = X_{A_2}$ Line
Slug Mode Run 1/12
X_{OT} = 0·34
S = 0·219
A5·9
X_{B_1}
X_{A_2}
0.0
0.2
0.4
0.6
0.8
1.0

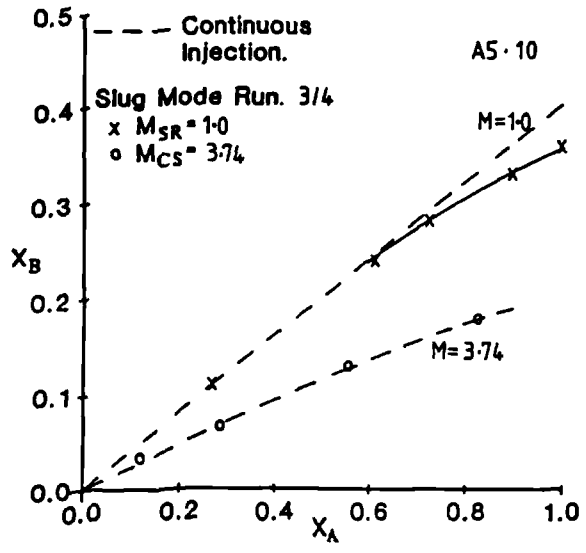
Continuous Injection.
Slug Mode Run. 3/4
x M_{SR} = 1·0
o M_{CS} = 3·74
M=1·0
M=3·74
A5·10
X_B
X_A

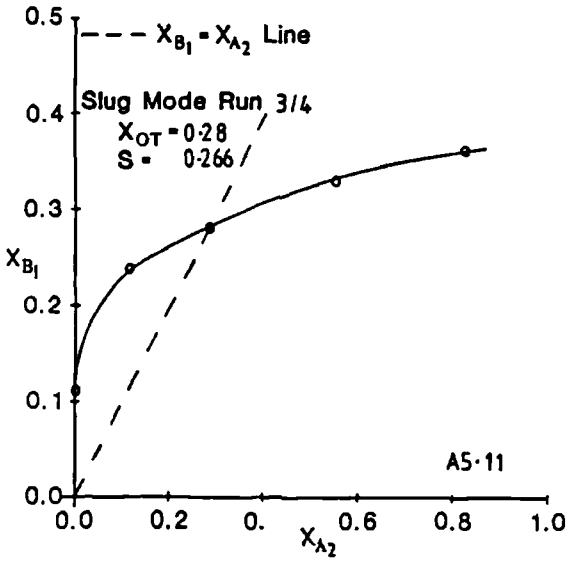
$X_{B_1} = X_{A_2}$ Line
Slug Mode Run 3/4
X_{OT} = 0·28
S = 0·266
A5·11
X_{B_1}
X_{A_2}

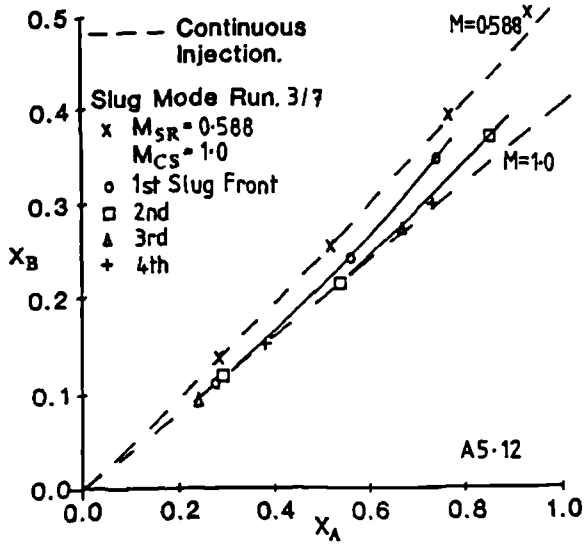
Continuous Injection.
Slug Mode Run. 3/7
x M_{SR} = 0·588
M_{CS} = 1·0
o 1st Slug Front
□ 2nd
▲ 3rd
+ 4th
M=0588
M=1·0
A5·12
X_B
X_A

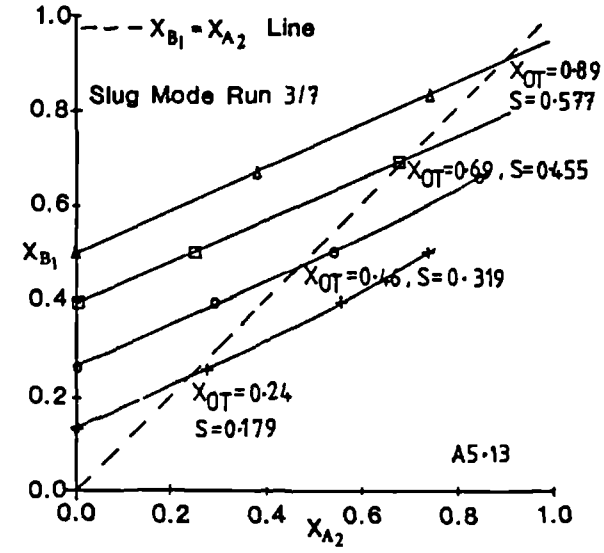
$X_{B_1} = X_{A_2}$ Line
Slug Mode Run 3/7
X_{OT}=0·89
S=0·577
X_{OT}=0·69, S=0·455
X_{OT}=0·46, S=0·319
X_{OT}=0·24
S=0·179
A5·13
X_{B_1}
X_{A_2}

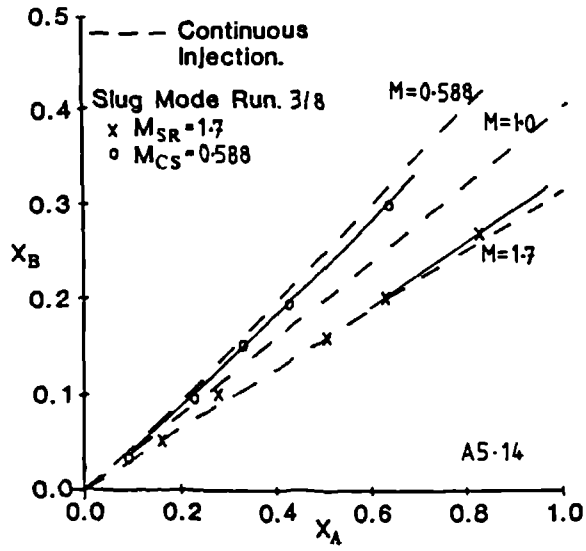
Continuous Injection.
Slug Mode Run. 3/8
x M_{SR} = 1·7
o M_{CS} = 0·588
M=0·588
M=1·0
M=1·7
A5·14
X_B
X_A

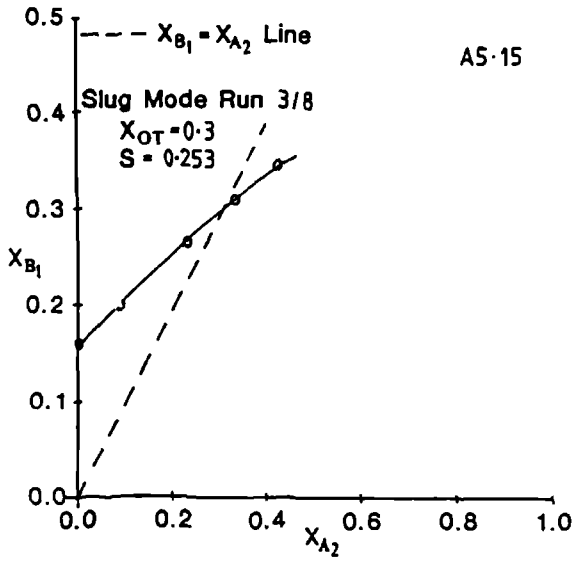
$X_{B_1} = X_{A_2}$ Line
A5·15
Slug Mode Run 3/8
X_{OT} = 0·3
S = 0·253
X_{B_1}
X_{A_2}

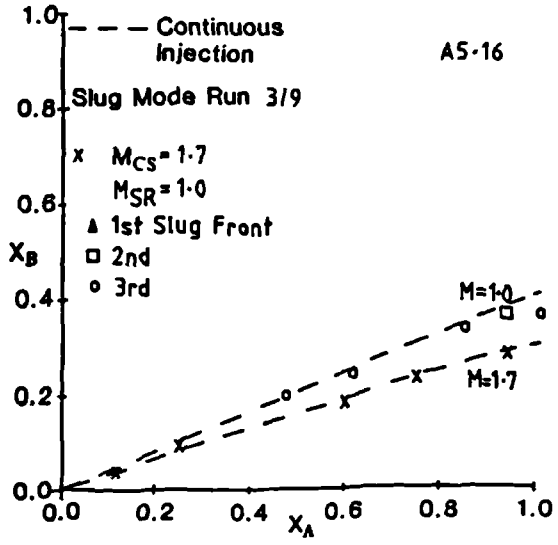
Continuous injection
A5·16
Slug Mode Run 3/9
x M_{CS} = 1·7
M_{SR} = 1·0
▲ 1st Slug Front
□ 2nd
o 3rd
M=1·0
M=1·7
X_B
X_A
0.0
0.2
0.4
0.6
0.8
1.0

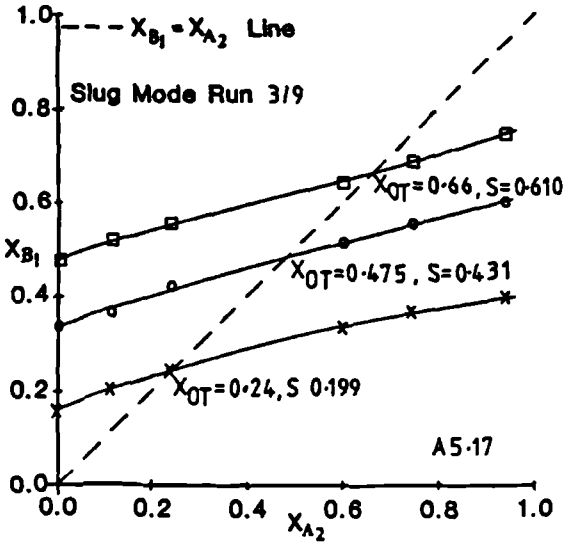
$X_{B_1} = X_{A_2}$ Line
Slug Mode Run 3/9
X_{OT}=0·66, S=0·610
X_{OT}=0·475, S=0·431
X_{OT}=0·24, S 0·199
A5·17
X_{B_1}
X_{A_2}
0.0
0.2
0.4
0.6
0.8
1.0

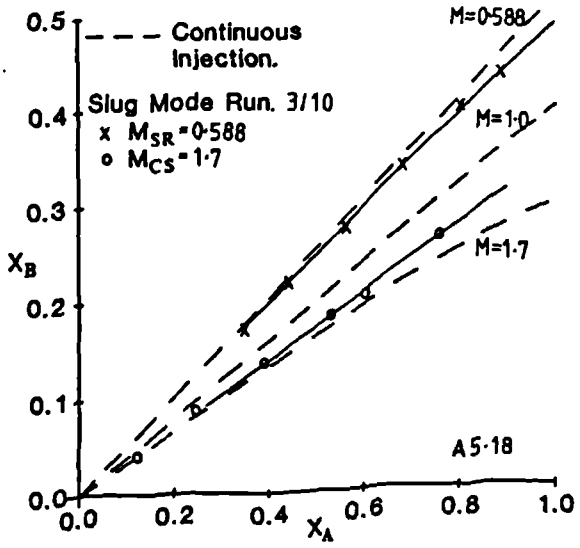
Continuous injection.
Slug Mode Run. 3/10
x M_{SR} = 0·588
o M_{CS} = 1·7
M=0·588
M=1·0
M=1·7
A5·18
X_B
X_A
0.0
0.1
0.2
0.3
0.4
0.5
0.6
0.8
1.0

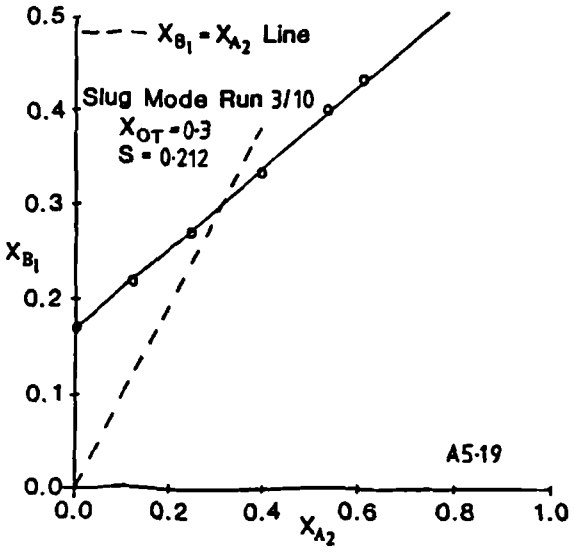
$X_{B_1} = X_{A_2}$ Line
Slug Mode Run 3/10
X_{OT} = 0·3
S = 0·212
A5·19
X_{B_1}
X_{A_2}
0.0
0.1
0.2
0.3
0.4
0.5
0.6
0.8
1.0

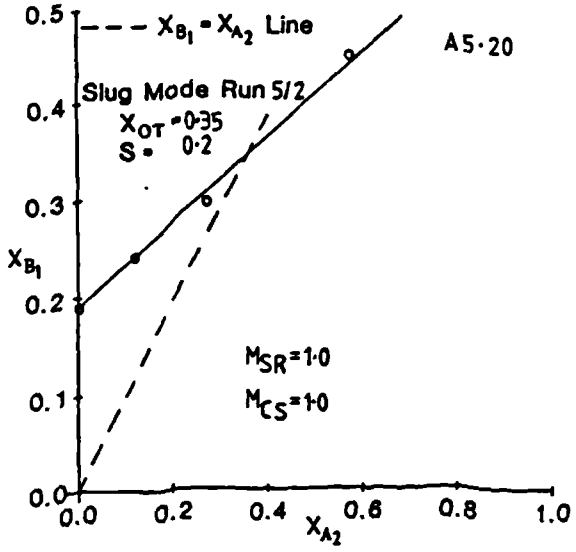
$X_{B_1} = X_{A_2}$ Line
A5·20
Slug Mode Run 5/2
X_{OT} = 0·35
S = 0·2
M_{SR} = 1·0
M_{CS} = 1·0
X_{B_1}
X_{A_2}
0.0
0.1
0.2
0.3
0.4
0.5
0.6
0.8
1.0

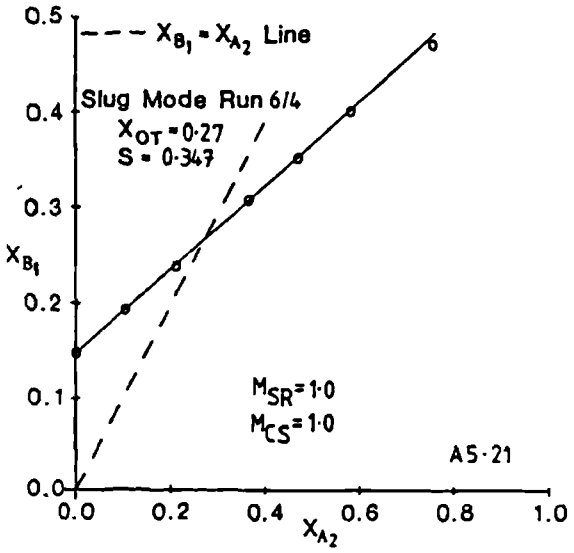
0.5
0.4
0.3
0.2
0.1
0.0
X_{B_1}
$X_{B_1} = X_{A_2}$ Line
Slug Mode Run 6/4
X_{OT} = 0·27
S = 0·347
M_{SR} = 1·0
M_{CS} = 1·0
A5·21
0.0
0.2
0.4
0.6
0.8
1.0
X_{A_2}

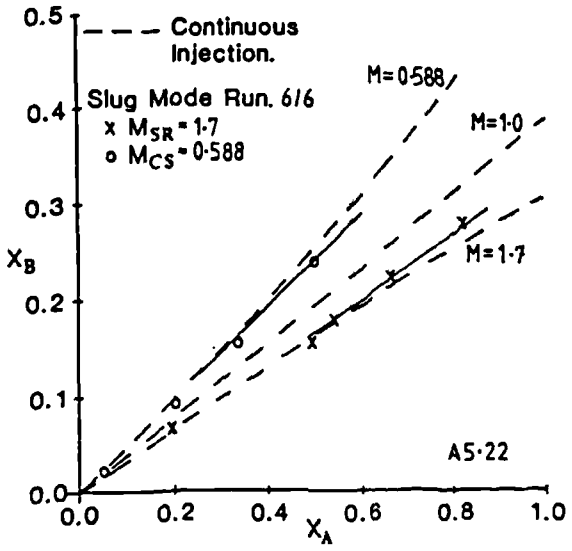
0.5
0.4
0.3
0.2
0.1
0.0
X_B
Continuous Injection.
Slug Mode Run. 6/6
x M_{SR} = 1·7
o M_{CS} = 0·588
M=0·588
M=1·0
M=1·7
A5·22
0.0
0.2
0.4
0.6
0.8
1.0
X_A

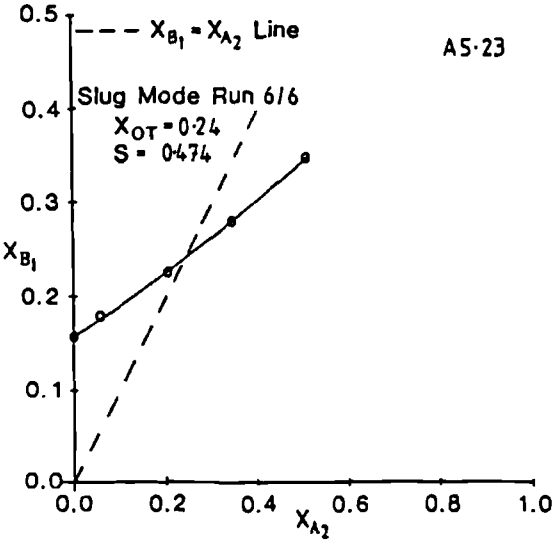
0.5
0.4
0.3
0.2
0.1
0.0
X_{B_1}
$X_{B_1} = X_{A_2}$ Line
A5·23
Slug Mode Run 6/6
X_{OT} = 0·24
S = 0·474
0.0
0.2
0.4
0.6
0.8
1.0
X_{A_2}

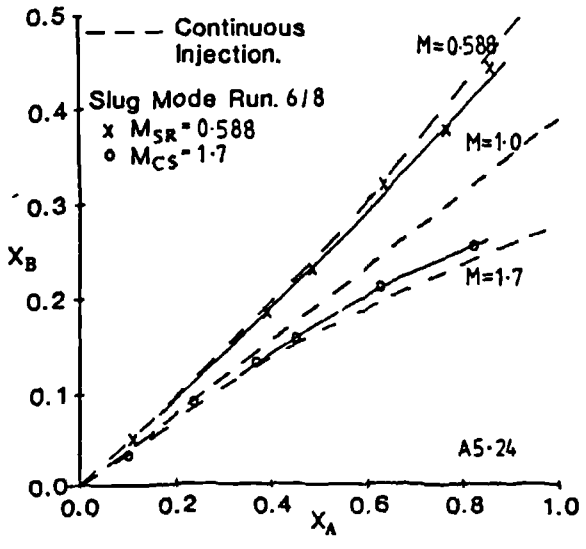
0.5
0.4
0.3
0.2
0.1
0.0
X_B
Continuous Injection.
Slug Mode Run. 6/8
x M_{SR} = 0·588
o M_{CS} = 1·7
M=0·588
M=1·0
M=1·7
A5·24
0.0
0.2
0.4
0.6
0.8
1.0
X_A

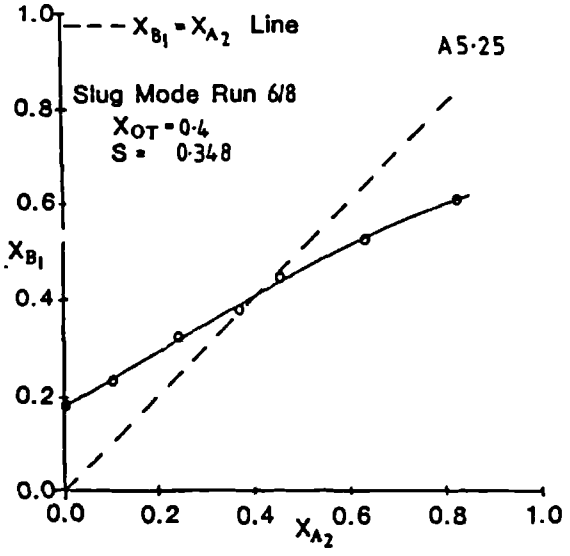
1.0
0.8
0.6
0.4
0.2
0.0
X_{B_1}
$X_{B_1} = X_{A_2}$ Line
A5·25
Slug Mode Run 6/8
X_{OT} = 0·4
S = 0·348
0.0
0.2
0.4
0.6
0.8
1.0
X_{A_2}

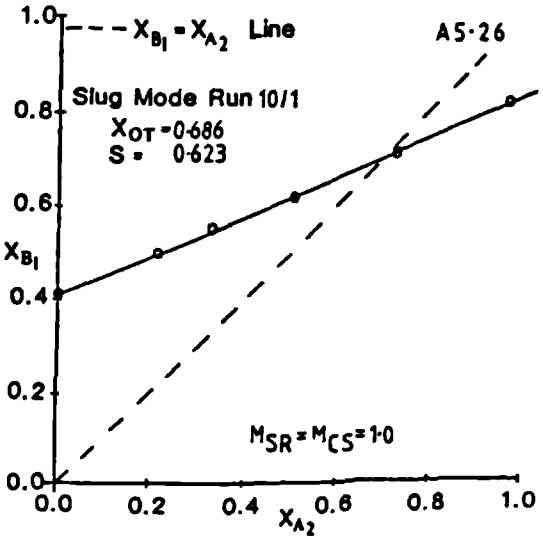
A5·26
$X_{B_1} = X_{A_2}$ Line
Slug Mode Run 10/1
X_{OT} = 0·686
S = 0·623
$M_{SR} = M_{CS} = 1·0$
X_{B_1}
X_{A_2}
0.0
0.2
0.4
0.6
0.8
1.0

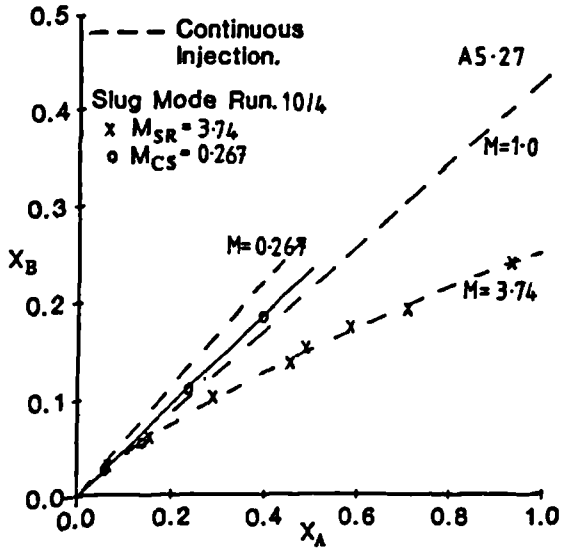
A5·27
Continuous Injection.
Slug Mode Run. 10/4
x M_{SR} = 3·74
o M_{CS} = 0·267
M=1·0
M=0·267
M=3·74
X_B
X_A
0.0
0.1
0.2
0.3
0.4
0.5
0.6
0.8
1.0

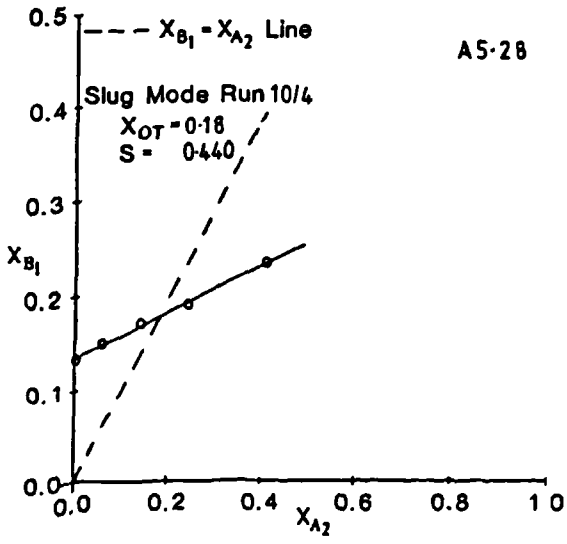
A5·28
$X_{B_1} = X_{A_2}$ Line
Slug Mode Run 10/4
X_{OT} = 0·18
S = 0·440
X_{B_1}
X_{A_2}
0.0
0.1
0.2
0.3
0.4
0.5
0.6
0.8
1.0

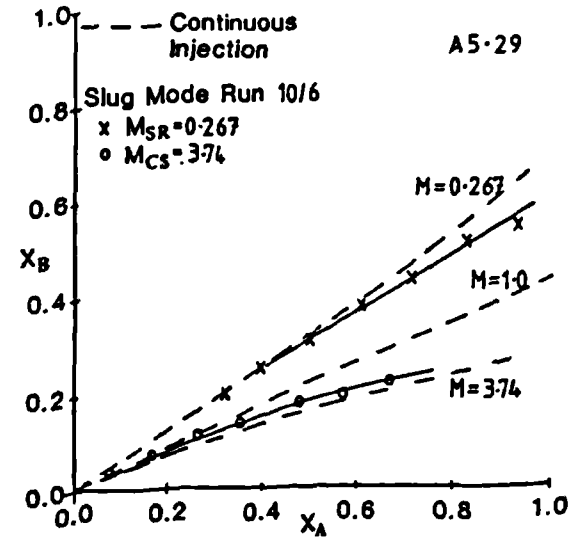
A5·29
Continuous Injection
Slug Mode Run 10/6
x M_{SR} = 0·267
o M_{CS} = 3·74
M=0·267
M=1·0
M=3·74
X_B
X_A
0.0
0.2
0.4
0.6
0.8
1.0

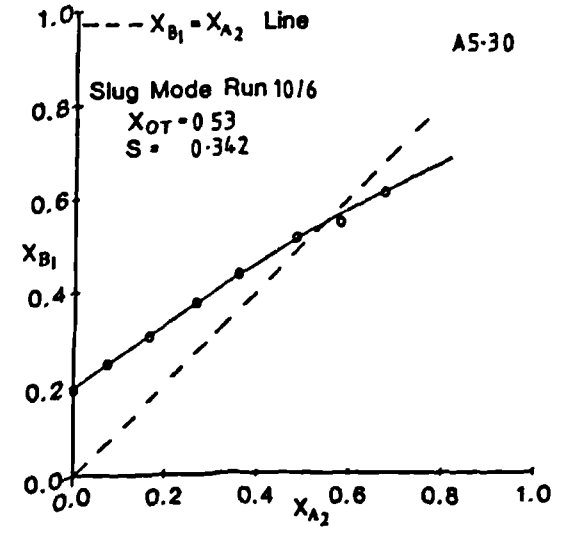
A5·30
$X_{B_1} = X_{A_2}$ Line
Slug Mode Run 10/6
X_{OT} = 0·53
S = 0·342
X_{B_1}
X_{A_2}
0.0
0.2
0.4
0.6
0.8
1.0

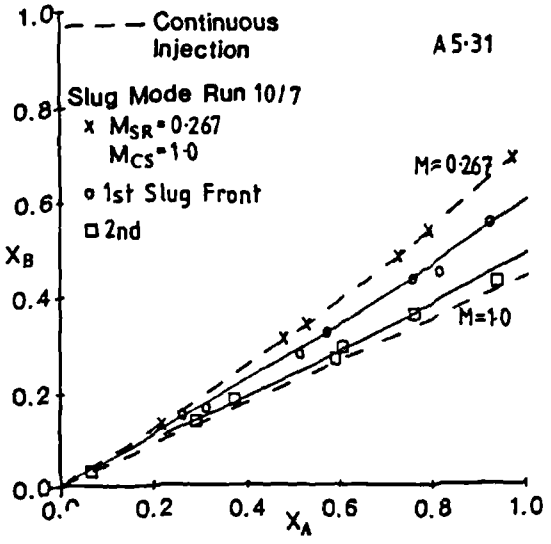
Continuous Injection
A5·31
Slug Mode Run 10/7
x M_{SR} = 0·267
M_{CS} = 1·0
o 1st Slug Front
□ 2nd
M=0·267
M=1·0
X_B
X_A

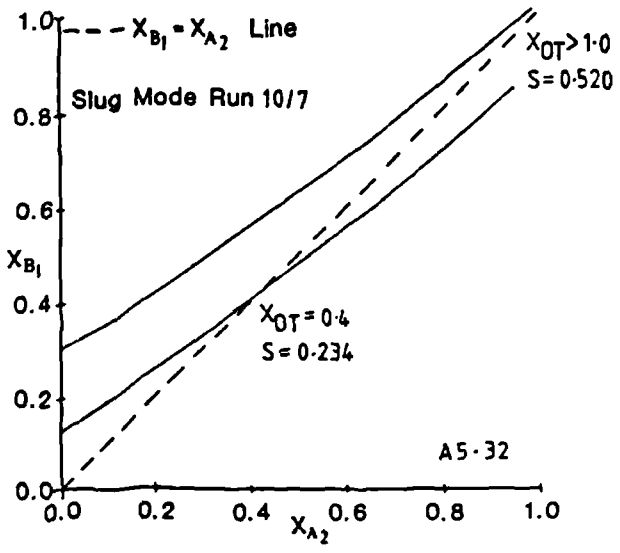
$X_{B_1} = X_{A_2}$ Line
Slug Mode Run 10/7
X_{OT} > 1·0
S = 0·520
X_{OT} = 0·4
S = 0·234
A5·32
X_{B_1}
X_{A_2}

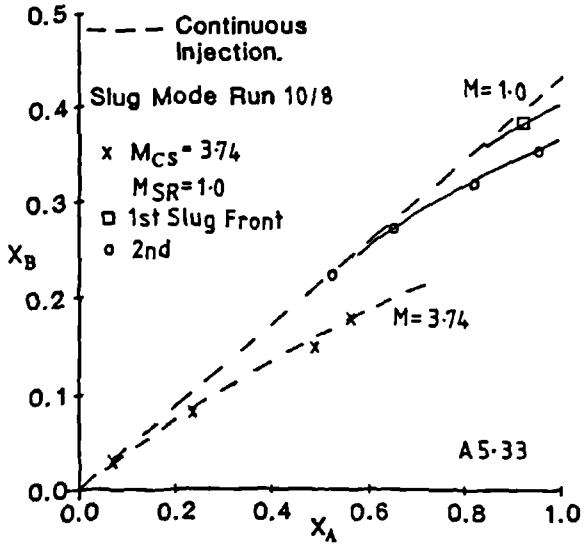
Continuous Injection.
Slug Mode Run 10/8
x M_{CS} = 3·74
M_{SR} = 1·0
□ 1st Slug Front
o 2nd
M= 1·0
M= 3·74
A5·33
X_B
X_A

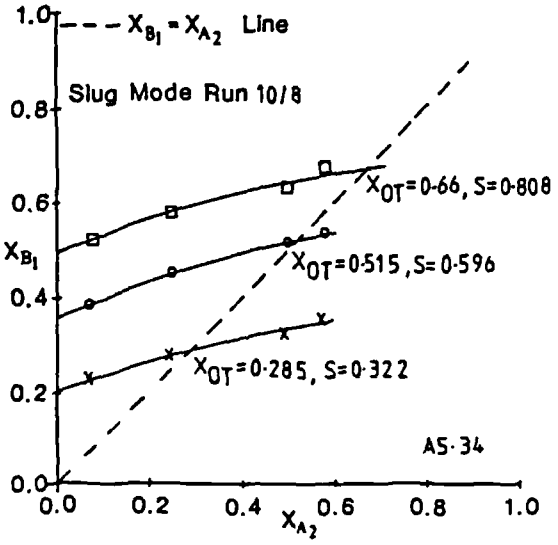
$X_{B_1} = X_{A_2}$ Line
Slug Mode Run 10/8
X_{OT} = 0·66, S = 0·808
X_{OT} = 0·515, S = 0·596
X_{OT} = 0·285, S = 0·322
A5·34
X_{B_1}
X_{A_2}

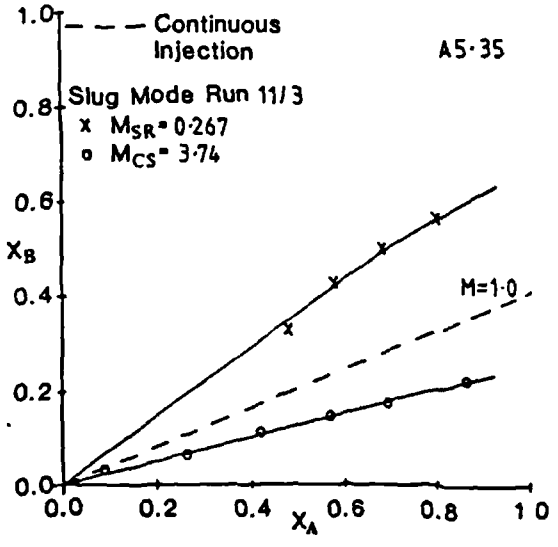
Continuous Injection
A5·35
Slug Mode Run 11/3
x M_{SR} = 0·267
o M_{CS} = 3·74
M=1·0
X_B
X_A

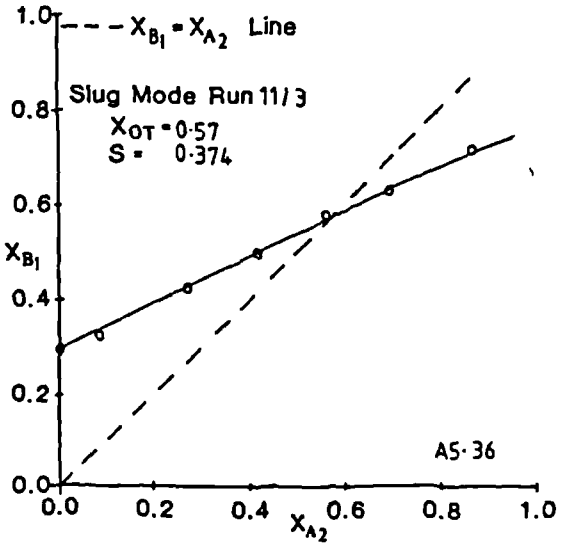
$X_{B_1} = X_{A_2}$ Line
Slug Mode Run 11/3
X_{OT} = 0·57
S = 0·374
A5·36
X_{B_1}
X_{A_2}

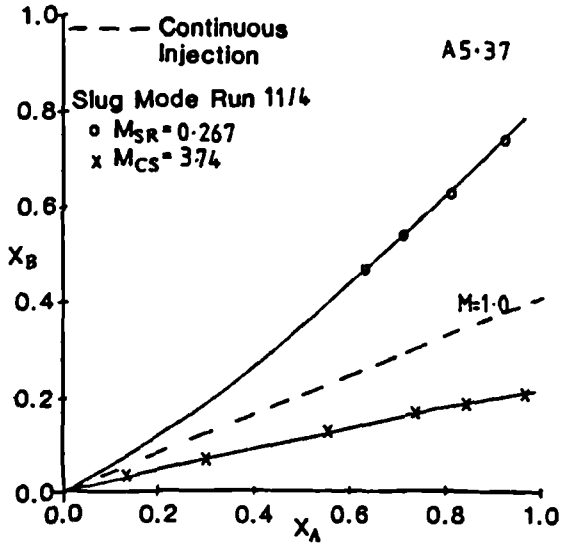
Continuous Injection
A5·37
Slug Mode Run 11/4
o M_{SR} = 0·267
x M_{CS} = 3·74
M=1·0
X_B
X_A
0.0
0.2
0.4
0.6
0.8
1.0

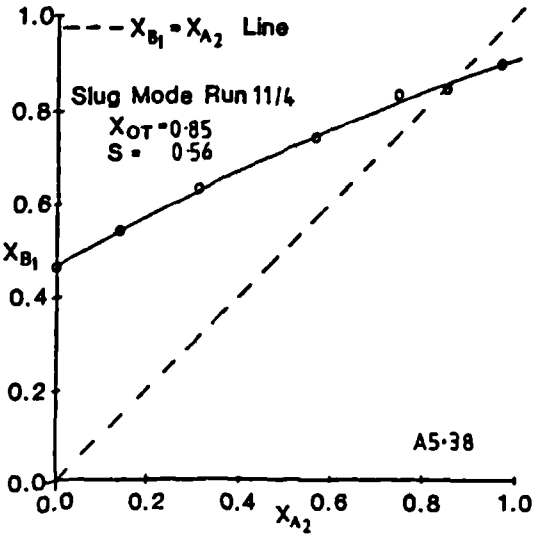
$X_{B_1} = X_{A_2}$ Line
Slug Mode Run 11/4
X_{OT} = 0·85
S = 0·56
A5·38
X_{B_1}
X_{A_2}
0.0
0.2
0.4
0.6
0.8
1.0

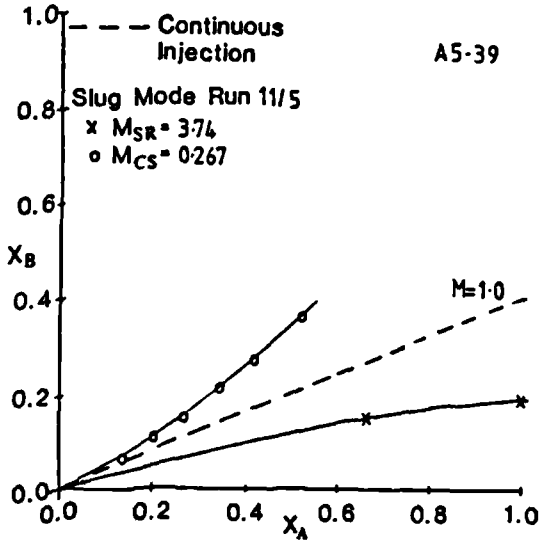
Continuous Injection
A5·39
Slug Mode Run 11/5
x M_{SR} = 3·74
o M_{CS} = 0·267
M=1·0
X_B
X_A
0.0
0.2
0.4
0.6
0.8
1.0

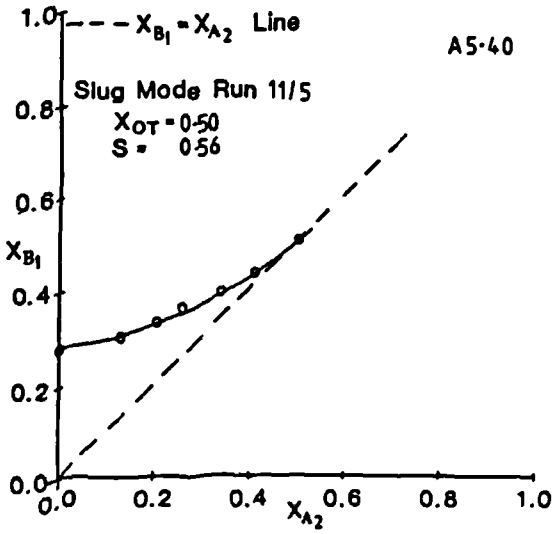
$X_{B_1} = X_{A_2}$ Line
A5·40
Slug Mode Run 11/5
X_{OT} = 0·50
S = 0·56
X_{B_1}
X_{A_2}
0.0
0.2
0.4
0.6
0.8
1.0

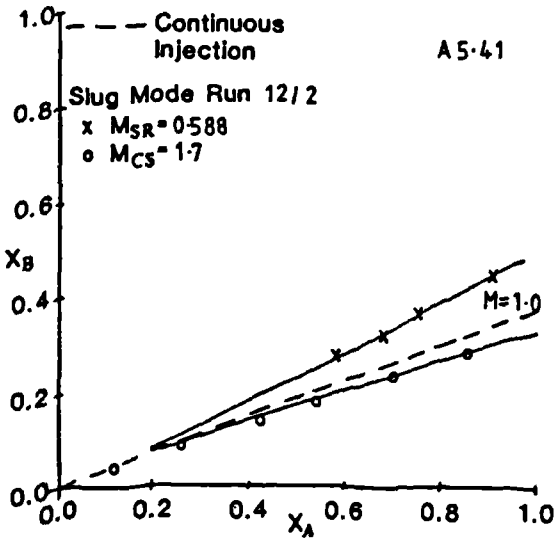
Continuous Injection
A5·41
Slug Mode Run 12/2
x M_{SR} = 0·588
o M_{CS} = 1·7
M=1·0
X_B
X_A
0.0
0.2
0.4
0.6
0.8
1.0

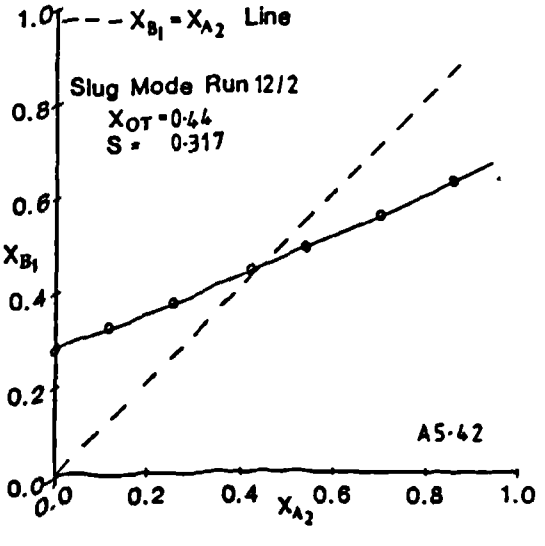
$X_{B_1} = X_{A_2}$ Line
Slug Mode Run 12/2
X_{OT} = 0·44
S = 0·317
A5·42
X_{B_1}
X_{A_2}
0.0
0.2
0.4
0.6
0.8
1.0

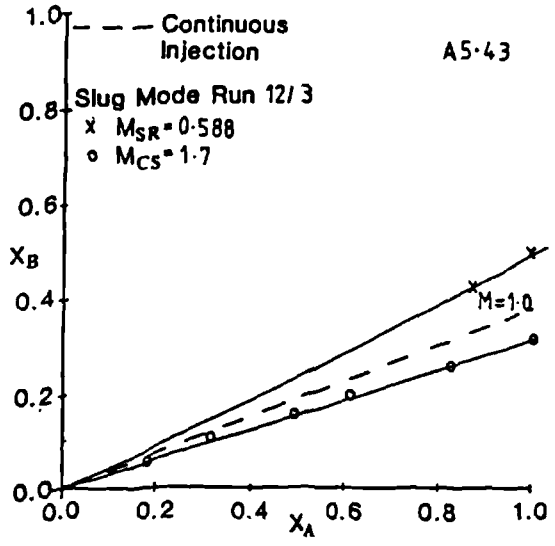
— — — Continuous Injection
A5·43
Slug Mode Run 12/3
x M_{SR} = 0·588
o M_{CS} = 1·7
M=1·0
X_B
X_A
0.0
0.2
0.4
0.6
0.8
1.0

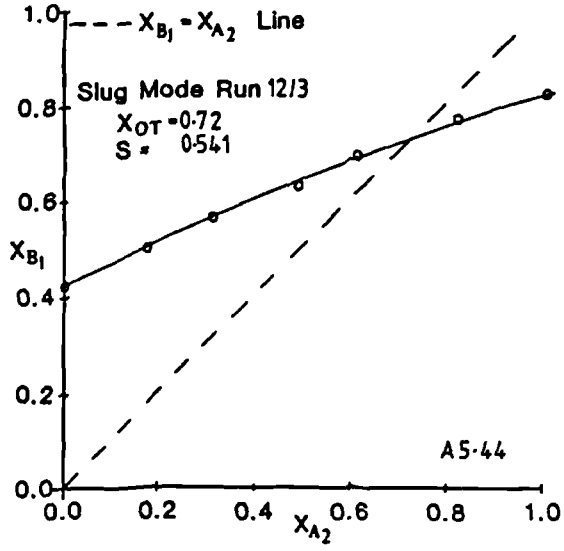
— — — $X_{B_1} = X_{A_2}$ Line
Slug Mode Run 12/3
X_{OT} = 0·72
S = 0·541
A5·44
X_{B_1}
X_{A_2}
0.0
0.2
0.4
0.6
0.8
1.0

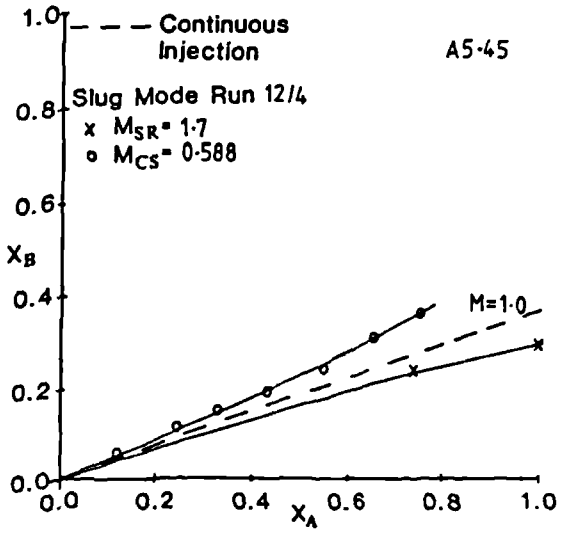
— — — Continuous Injection
A5·45
Slug Mode Run 12/4
x M_{SR} = 1·7
o M_{CS} = 0·588
M=1·0
X_B
X_A
0.0
0.2
0.4
0.6
0.8
1.0

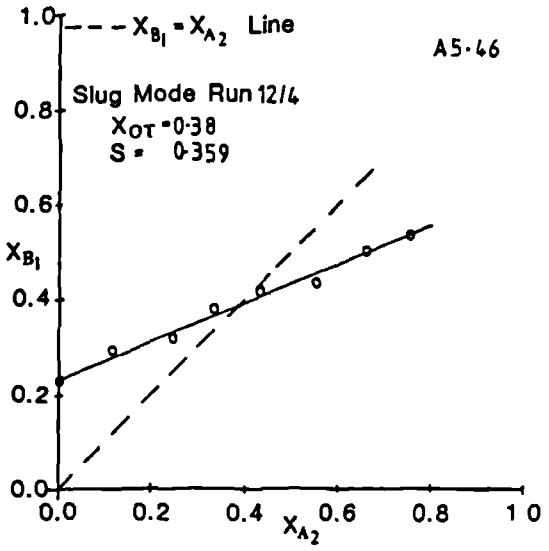
— — — $X_{B_1} = X_{A_2}$ Line
A5·46
Slug Mode Run 12/4
X_{OT} = 0·38
S = 0·359
X_{B_1}
X_{A_2}
0.0
0.2
0.4
0.6
0.8
1.0

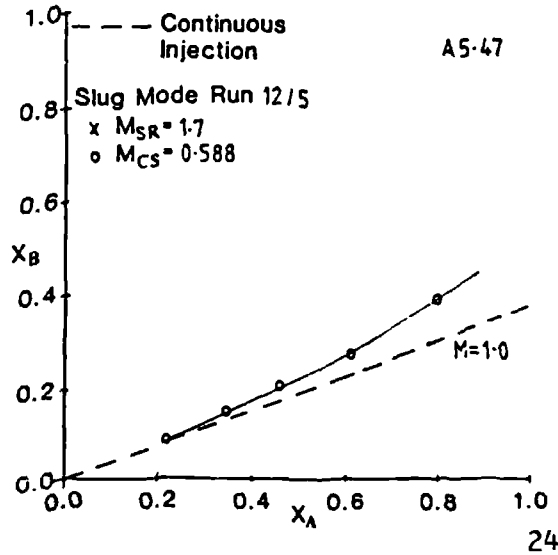
— — — Continuous Injection
A5·47
Slug Mode Run 12/5
x M_{SR} = 1·7
o M_{CS} = 0·588
M=1·0
X_B
X_A
0.0
0.2
0.4
0.6
0.8
1.0

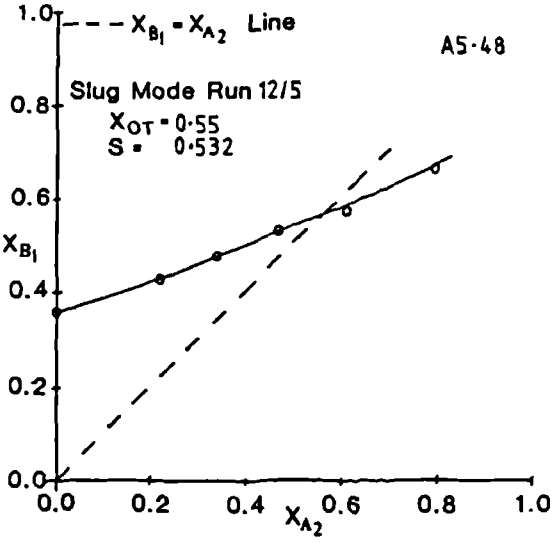
— — — $X_{B_1} = X_{A_2}$ Line
A5·48
Slug Mode Run 12/5
X_{OT} = 0·55
S = 0·532
X_{B_1}
X_{A_2}
0.0
0.2
0.4
0.6
0.8
1.0

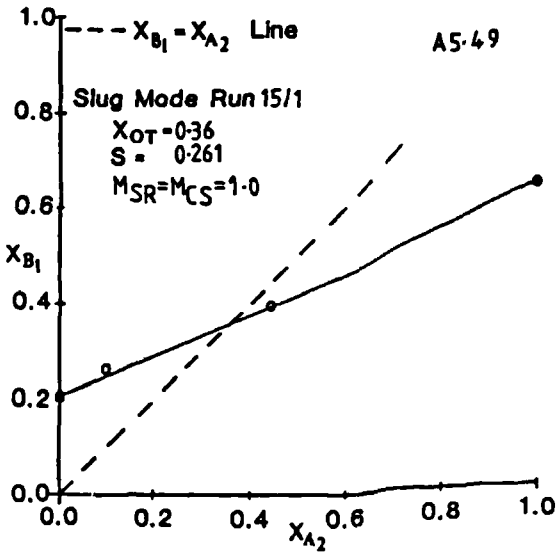
1.0
0.8
0.6
0.4
0.2
0.0
X_{B_1}
$X_{B_1} = X_{A_2}$ Line
A5·49
Slug Mode Run 15/1
X_{OT} = 0·36
S = 0·261
$M_{SR} = M_{CS} = 1·0$
0.0
0.2
0.4
0.6
0.8
1.0
X_{A_2}

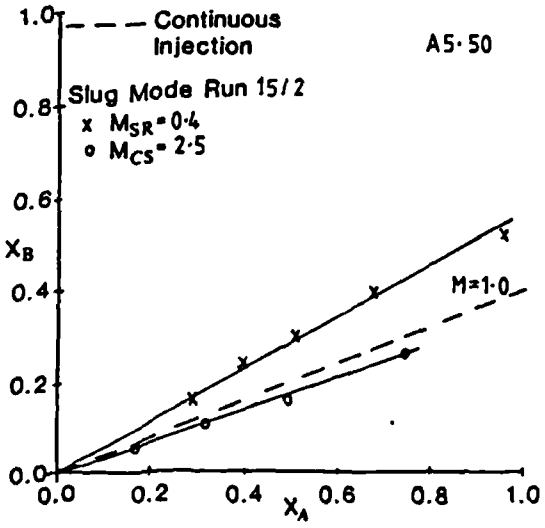
1.0
0.8
0.6
0.4
0.2
0.0
X_B
Continuous Injection
A5·50
Slug Mode Run 15/2
x M_{SR} = 0·4
o M_{CS} = 2·5
M=1·0
0.0
0.2
0.4
0.6
0.8
1.0
X_A

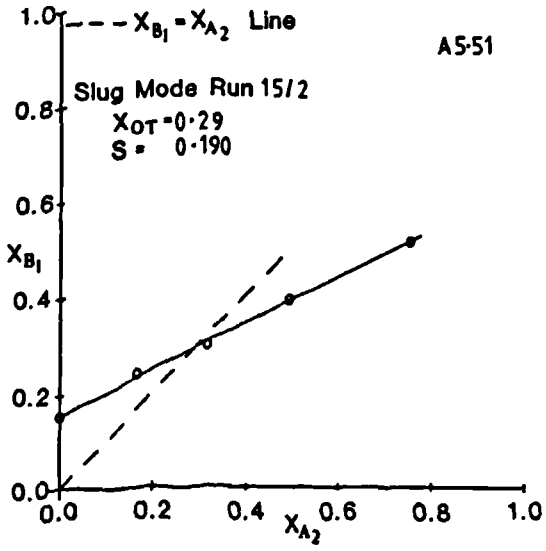
1.0
0.8
0.6
0.4
0.2
0.0
X_{B_1}
$X_{B_1} = X_{A_2}$ Line
A5·51
Slug Mode Run 15/2
X_{OT} = 0·29
S = 0·190
0.0
0.2
0.4
0.6
0.8
1.0
X_{A_2}

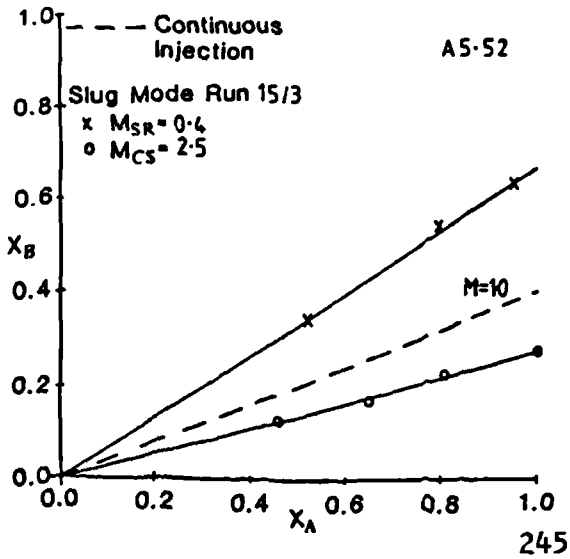
1.0
0.8
0.6
0.4
0.2
0.0
X_B
Continuous Injection
A5·52
Slug Mode Run 15/3
x M_{SR} = 0·4
o M_{CS} = 2·5
M=1·0
0.0
0.2
0.4
0.6
0.8
1.0
X_A

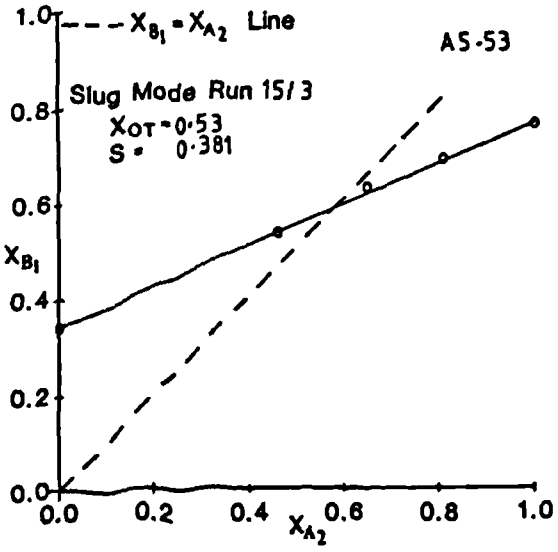
1.0
0.8
0.6
0.4
0.2
0.0
X_{B_1}
$X_{B_1} = X_{A_2}$ Line
A5·53
Slug Mode Run 15/3
X_{OT} = 0·53
S = 0·381
0.0
0.2
0.4
0.6
0.8
1.0
X_{A_2}

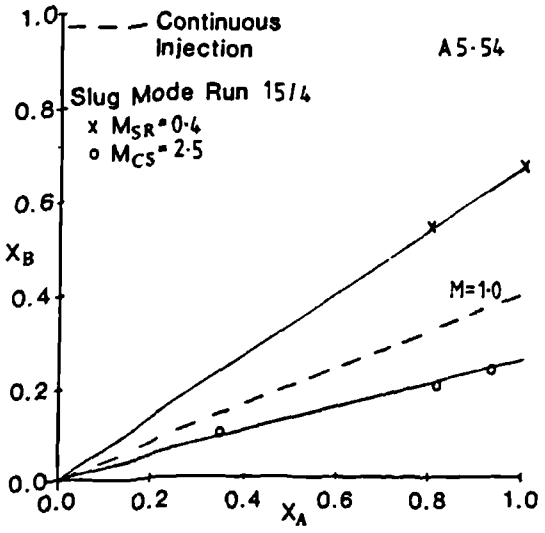
Continuous Injection
A5·54
Slug Mode Run 15/4
x M_{SR} = 0·4
o M_{CS} = 2·5
M=1·0
X_B
X_A
0.0
0.2
0.4
0.6
0.8
1.0

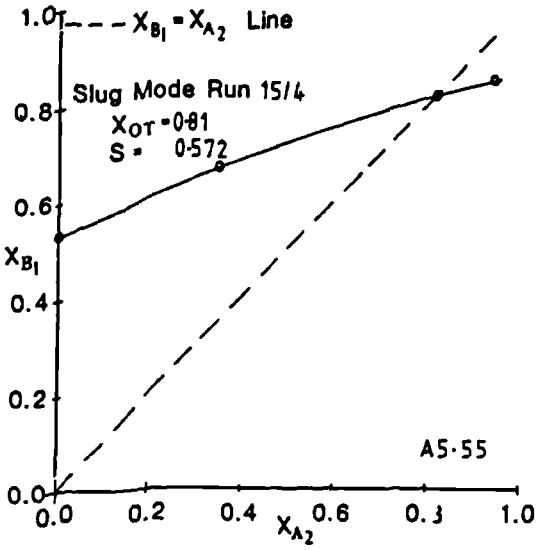
$X_{B_1} = X_{A_2}$ Line
Slug Mode Run 15/4
X_{OT} = 0·81
S = 0·572
A5·55
X_{B_1}
X_{A_2}
0.0
0.2
0.4
0.6
0.8
1.0

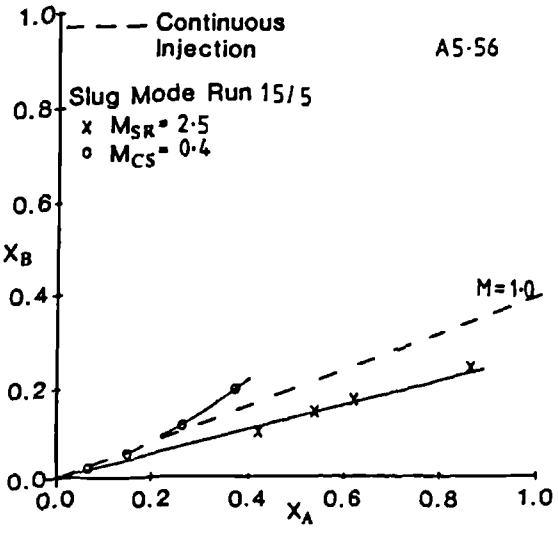
Continuous Injection
A5·56
Slug Mode Run 15/5
x M_{SR} = 2·5
o M_{CS} = 0·4
M=1·0
X_B
X_A
0.0
0.2
0.4
0.6
0.8
1.0

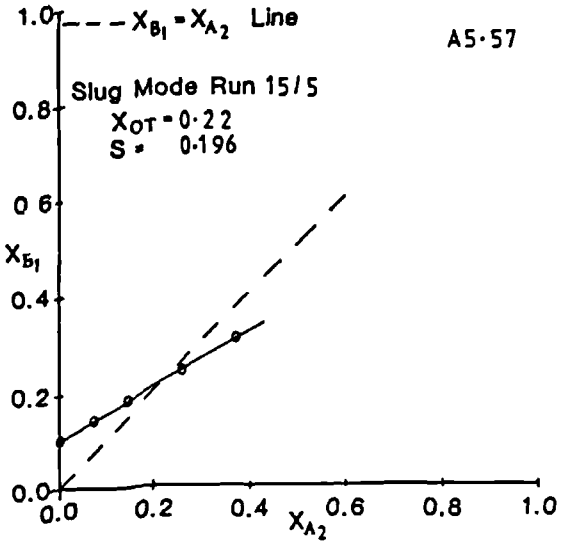
$X_{B_1} = X_{A_2}$ Line
A5·57
Slug Mode Run 15/5
X_{OT} = 0·22
S = 0·196
X_{B_1}
X_{A_2}
0.0
0.2
0.4
0.6
0.8
1.0

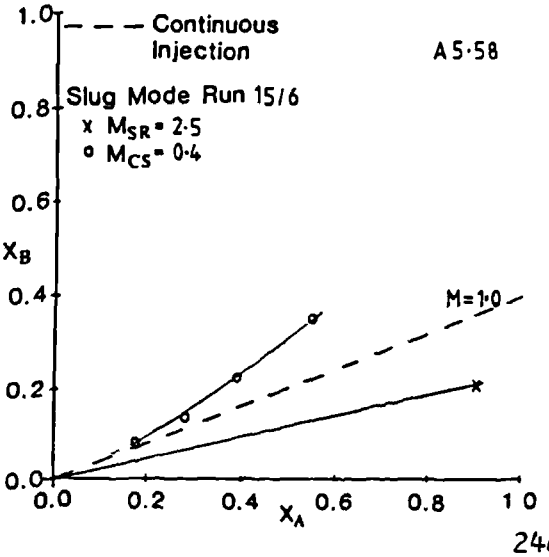
Continuous Injection
A5·58
Slug Mode Run 15/6
x M_{SR} = 2·5
o M_{CS} = 0·4
M=1·0
X_B
X_A
0.0
0.2
0.4
0.6
0.8
1.0

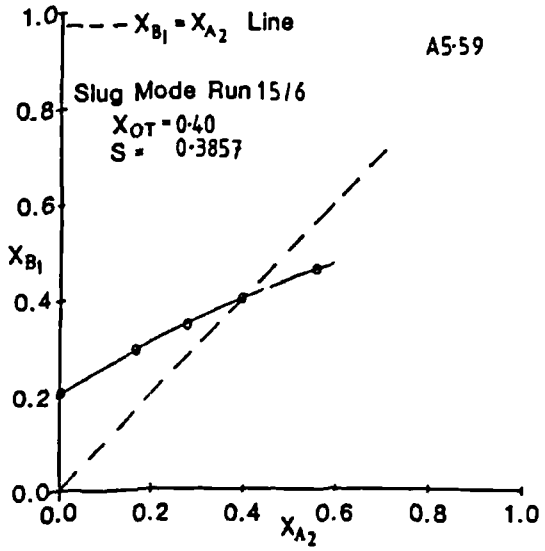
$X_{B_1} = X_{A_2}$ Line
A5·59
Slug Mode Run 15/6
X_{OT} = 0·40
S = 0·3857
X_{B_1}
X_{A_2}
0.0
0.2
0.4
0.6
0.8
1.0

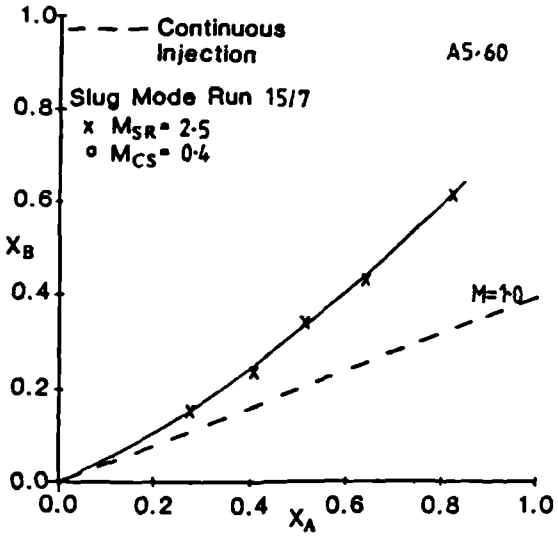
1.0
0.8
0.6
0.4
0.2
0.0
X_B
Continuous Injection
A5·60
Slug Mode Run 15/7
x M_{SR} = 2·5
o M_{CS} = 0·4
M=1·0
0.0
0.2
0.4
X_A
0.6
0.8
1.0

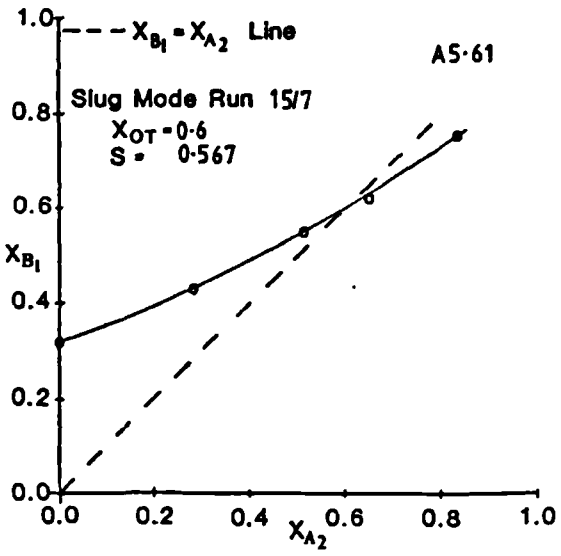
1.0
0.8
0.6
0.4
0.2
0.0
X_{B_1}
$X_{B_1} = X_{A_2}$ Line
A5·61
Slug Mode Run 15/7
X_{OT} = 0·6
S = 0·567
0.0
0.2
0.4
X_{A_2}
0.6
0.8
1.0

APPENDIX SIX

CONTINUOUS INJECTION DATA FROM EQUIVISCOUS DISPERSION SENSITIVE EXPERIMENTS

This appendix contains numerical effluent profiles for equiviscous continuous injection displacements used to study the effects of transverse microscopic dispersion in layered systems. These are compared with experimental displacements in figures A6.3 (experimental run 25/7), A6.5 (run 25/22), A6.7 (run 25/23), A6.9 (run 25/8) and A6.11 (run 25/9). These data are discussed in chapter six.

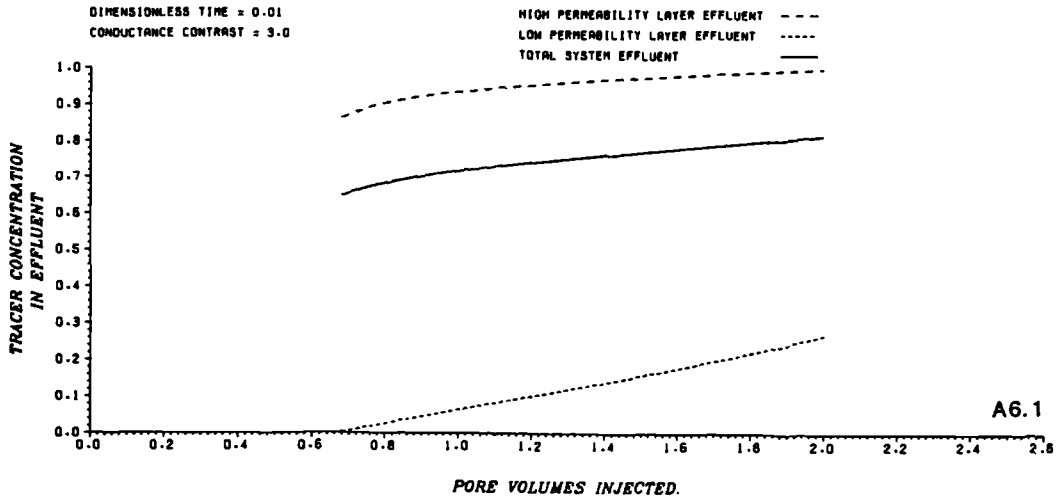

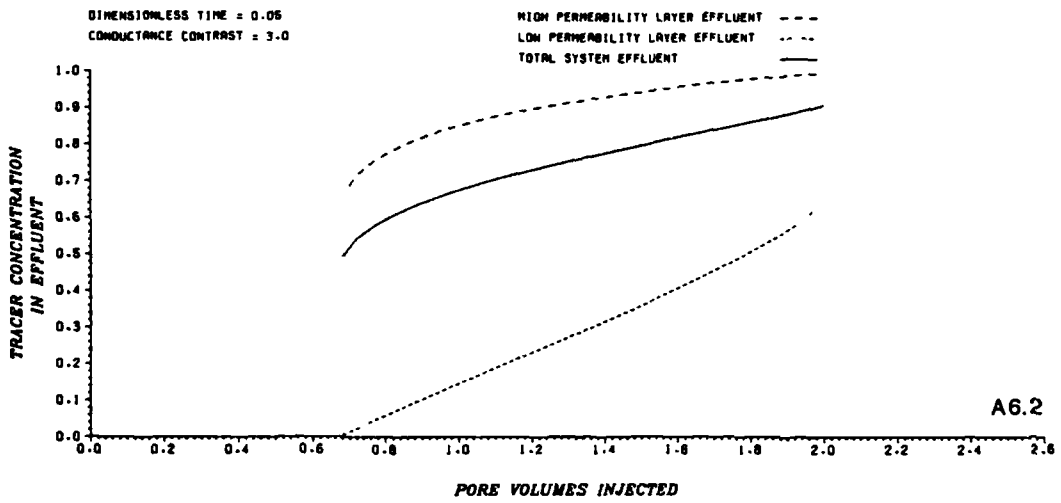

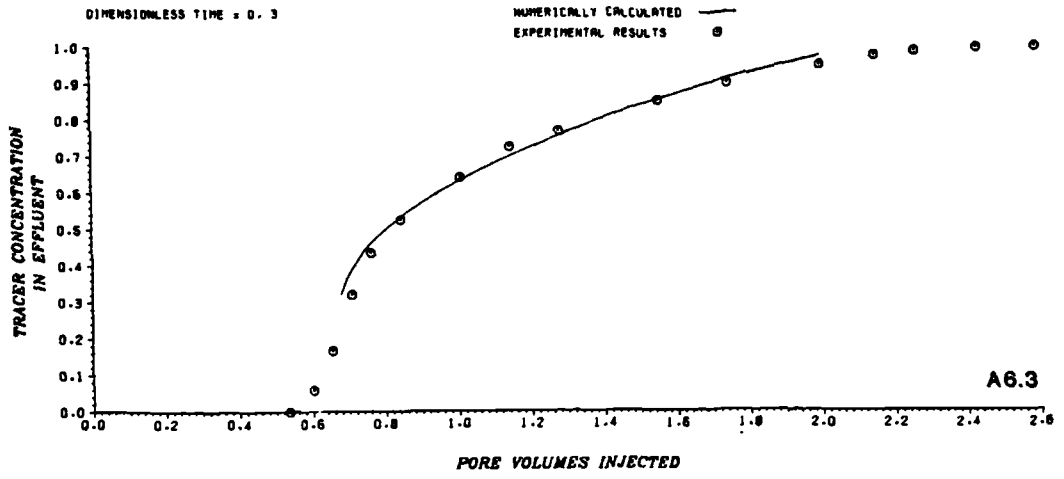
DIMENSIONLESS TIME = 0. 3
NUMERICALLY CALCULATED
EXPERIMENTAL RESULTS
TRACER CONCENTRATION IN EFFLUENT
A6.3
PORE VOLUMES INJECTED

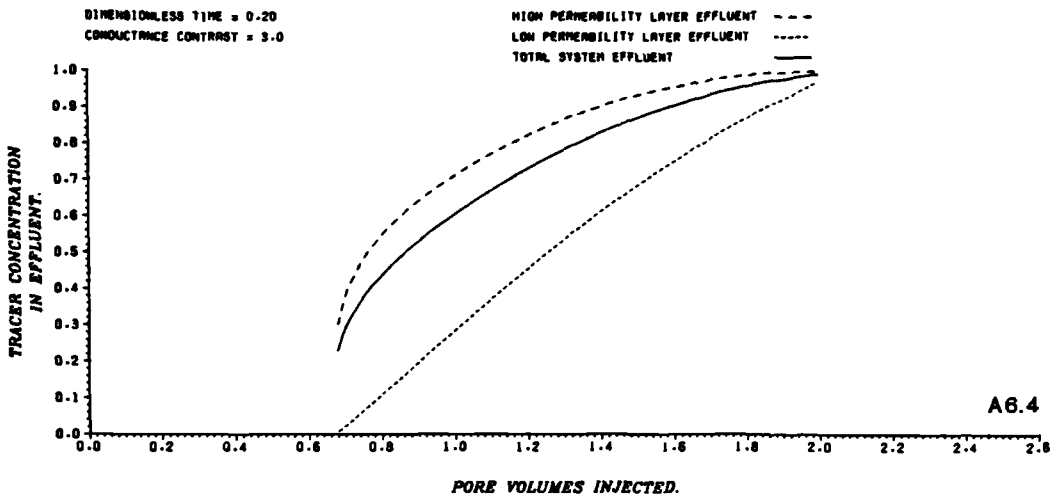
DIMENSIONLESS TIME = 0.20
CONDUCTANCE CONTRAST = 3.0
HIGH PERMEABILITY LAYER EFFLUENT
LOW PERMEABILITY LAYER EFFLUENT
TOTAL SYSTEM EFFLUENT
TRACER CONCENTRATION IN EFFLUENT.
A6.4
PORE VOLUMES INJECTED.

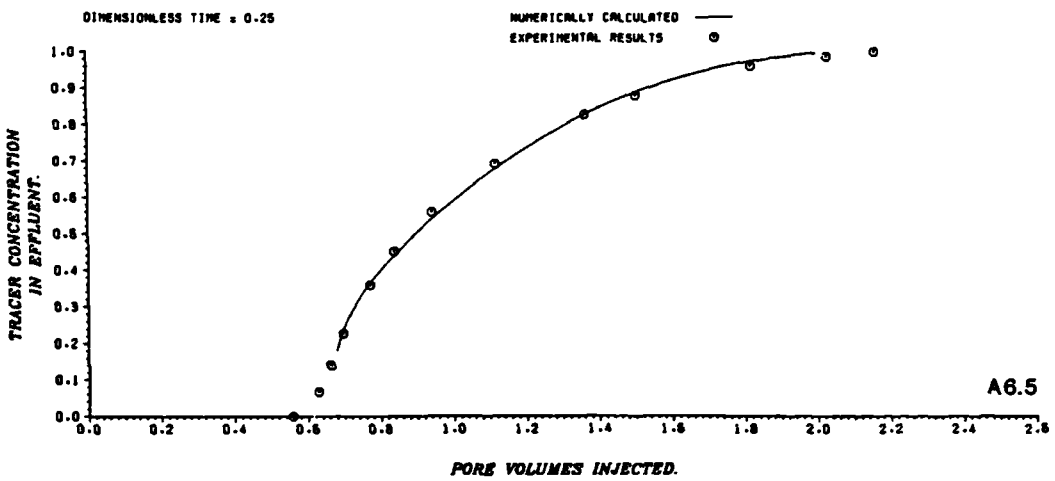
DIMENSIONLESS TIME = 0.25
NUMERICALLY CALCULATED
EXPERIMENTAL RESULTS
TRACER CONCENTRATION IN EFFLUENT.
A6.5
PORE VOLUMES INJECTED.

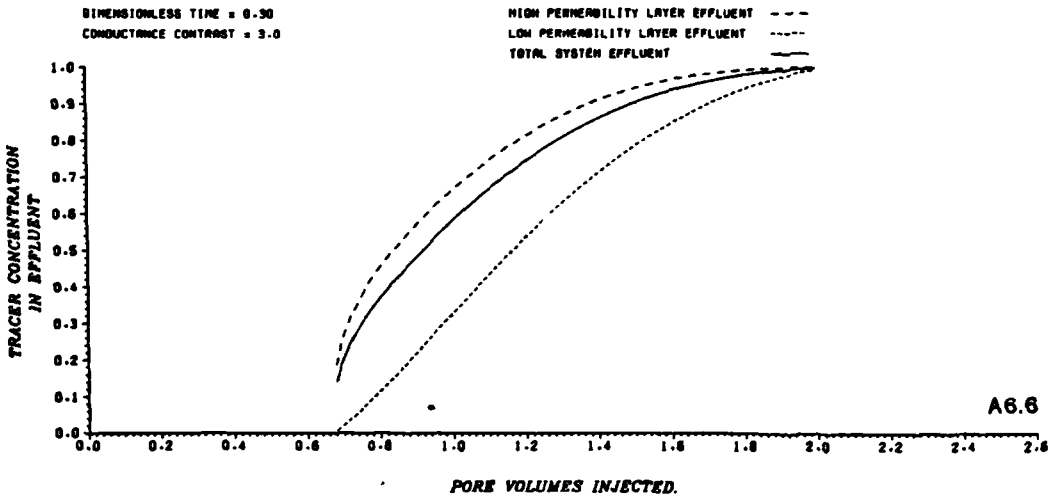
DIMENSIONLESS TIME = 0.50
CONDUCTANCE CONTRAST = 3.0
HIGH PERMEABILITY LAYER EFFLUENT
LOW PERMEABILITY LAYER EFFLUENT
TOTAL SYSTEM EFFLUENT
TRACER CONCENTRATION IN EFFLUENT
A6.6
PORE VOLUMES INJECTED.

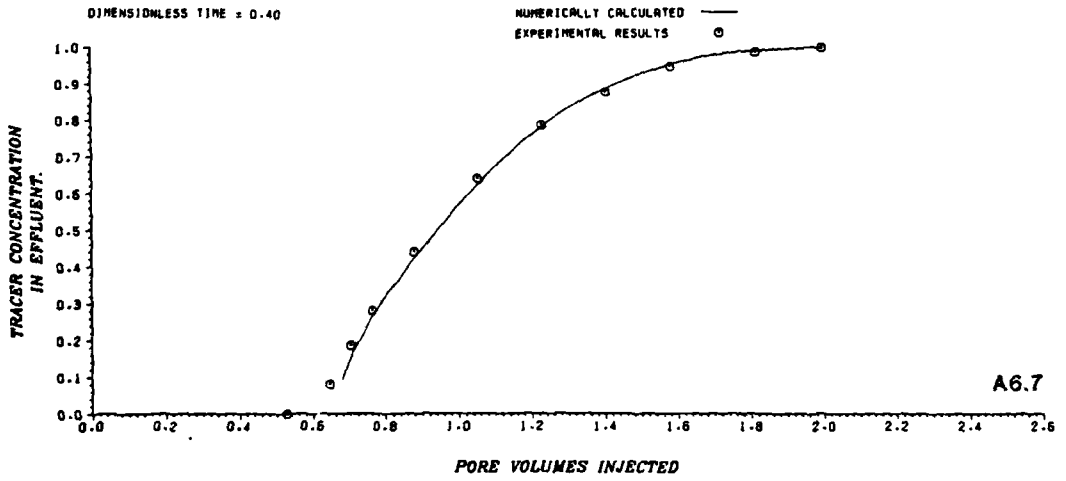
DIMENSIONLESS TIME = 0.40
NUMERICALLY CALCULATED
EXPERIMENTAL RESULTS
TRACER CONCENTRATION IN EFFLUENT.
A6.7
PORE VOLUMES INJECTED

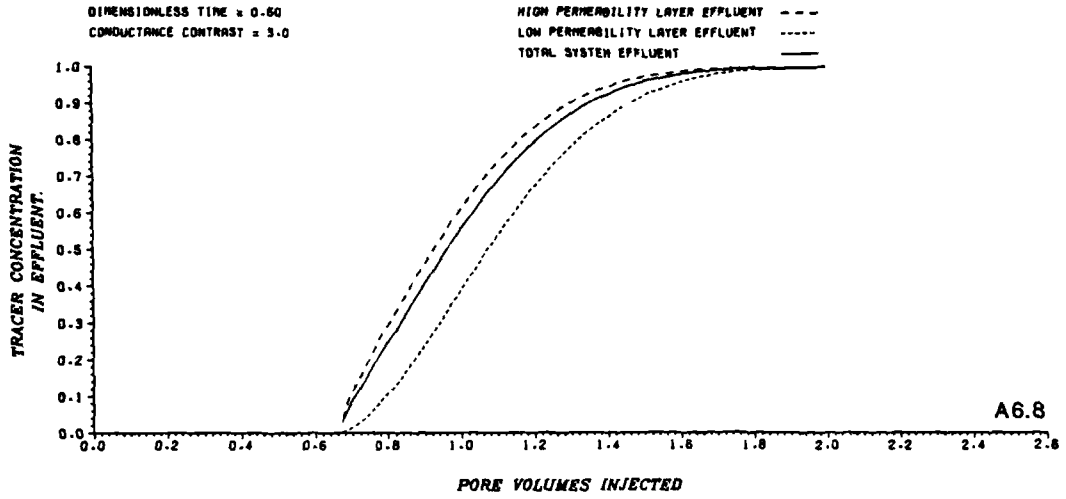
DIMENSIONLESS TIME = 0.60
CONDUCTANCE CONTRAST = 3.0
HIGH PERMEABILITY LAYER EFFLUENT
LOW PERMEABILITY LAYER EFFLUENT
TOTAL SYSTEM EFFLUENT
TRACER CONCENTRATION IN EFFLUENT.
A6.8
PORE VOLUMES INJECTED

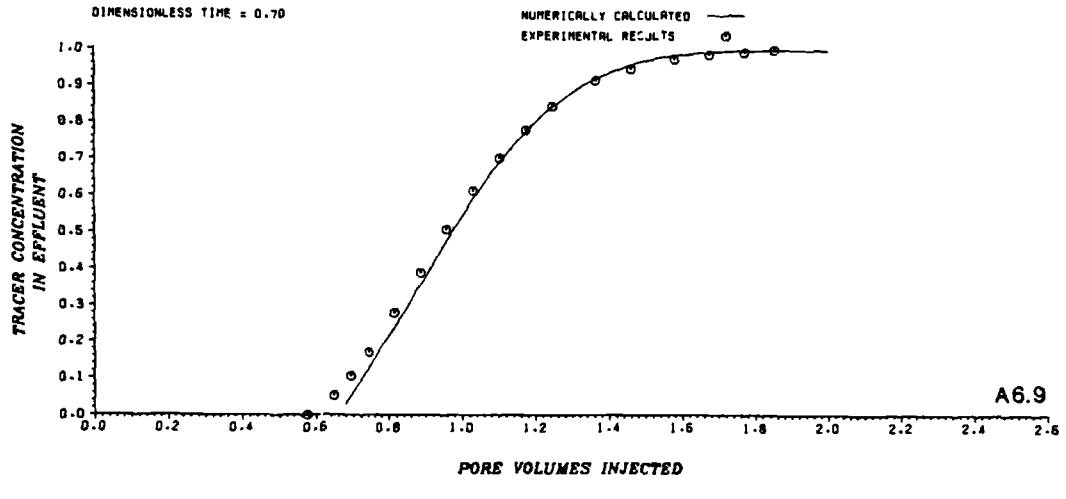
DIMENSIONLESS TIME = 0.70
NUMERICALLY CALCULATED
EXPERIMENTAL RESULTS
TRACER CONCENTRATION IN EFFLUENT
A6.9
PORE VOLUMES INJECTED

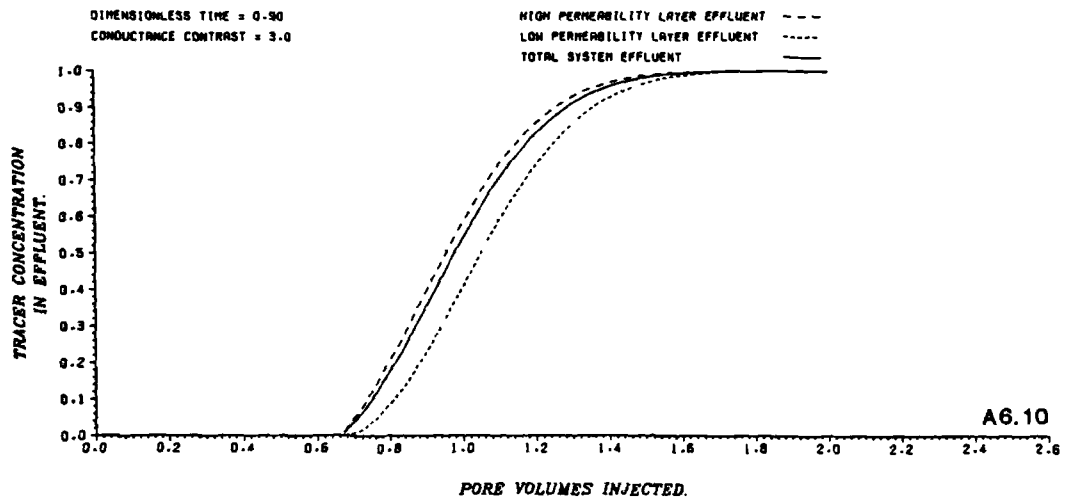
DIMENSIONLESS TIME = 0.90
CONDUCTANCE CONTRAST = 3.0
HIGH PERMEABILITY LAYER EFFLUENT
LOW PERMEABILITY LAYER EFFLUENT
TOTAL SYSTEM EFFLUENT
TRACER CONCENTRATION IN EFFLUENT.
A6.10
PORE VOLUMES INJECTED.

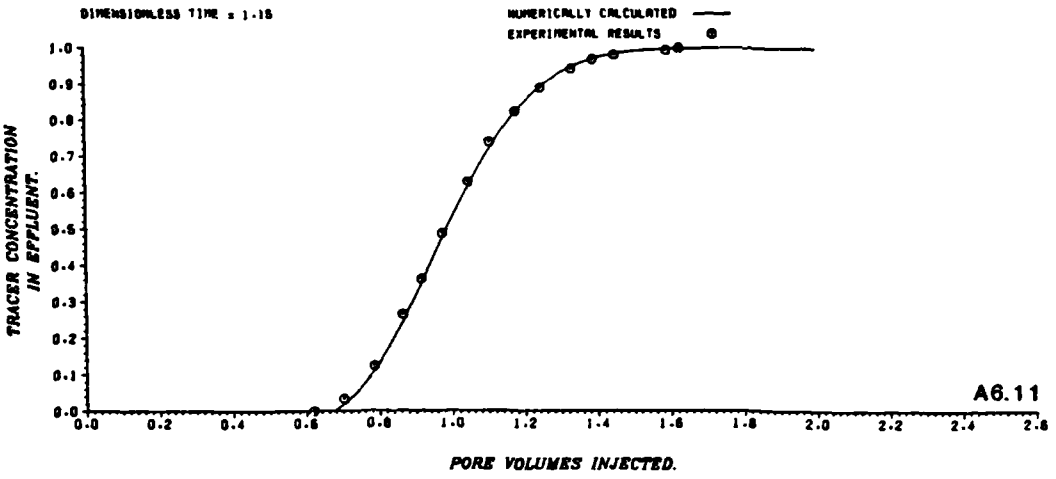
DIMENSIONLESS TIME = 1.15
NUMERICALLY CALCULATED
EXPERIMENTAL RESULTS
TRACER CONCENTRATION IN EFFLUENT.
PORE VOLUMES INJECTED.
A6.11

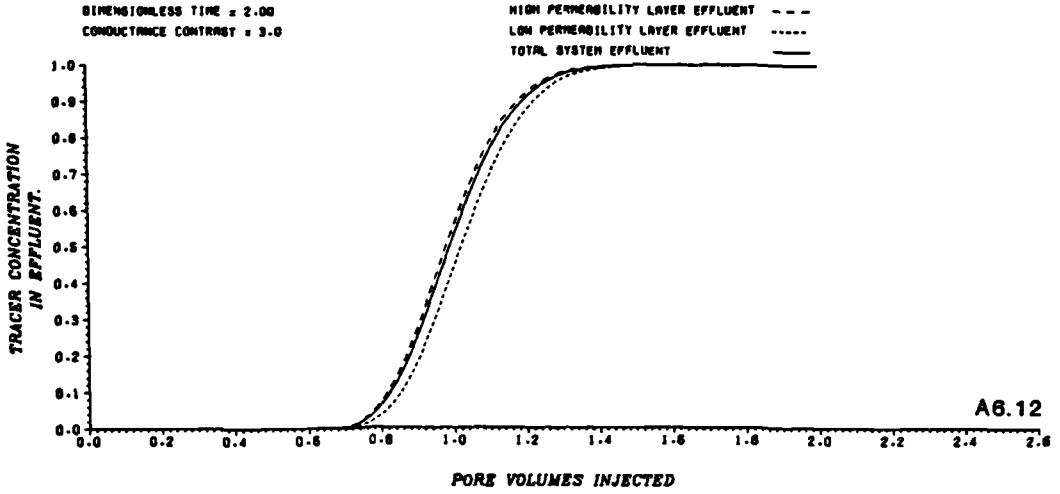
DIMENSIONLESS TIME = 2.00
CONDUCTANCE CONTRAST = 9.0
HIGH PERMEABILITY LAYER EFFLUENT
LOW PERMEABILITY LAYER EFFLUENT
TOTAL SYSTEM EFFLUENT
TRACER CONCENTRATION IN EFFLUENT.
PORE VOLUMES INJECTED
A6.12

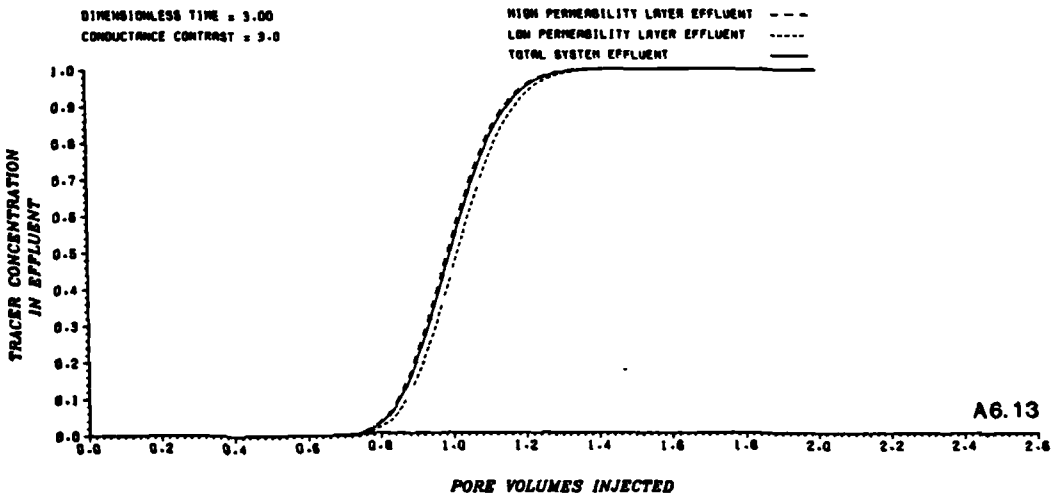
DIMENSIONLESS TIME = 3.00
CONDUCTANCE CONTRAST = 9.0
HIGH PERMEABILITY LAYER EFFLUENT
LOW PERMEABILITY LAYER EFFLUENT
TOTAL SYSTEM EFFLUENT
TRACER CONCENTRATION IN EFFLUENT
PORE VOLUMES INJECTED
A6.13

APPENDIX SEVEN

SLUG MODE DATA FROM EQUIVISCOUS DISPERSION SENSITIVE EXPERIMENTS

The data in this appendix are discussed in chapter seven.

A7.1 Effluent Profiles

This section contains numerical effluent profiles for equiviscous slug mode displacements used to study the effects of transverse microscopic dispersion in layered systems. These are compared with experimental displacements in figures A7.4 (experimental run 25/14), A7.7 (run 25/13), A7.9 (run 25/15), A7.14 (run 25/10), A7.17 (run 25/11) and A7.19 (run 25/12).

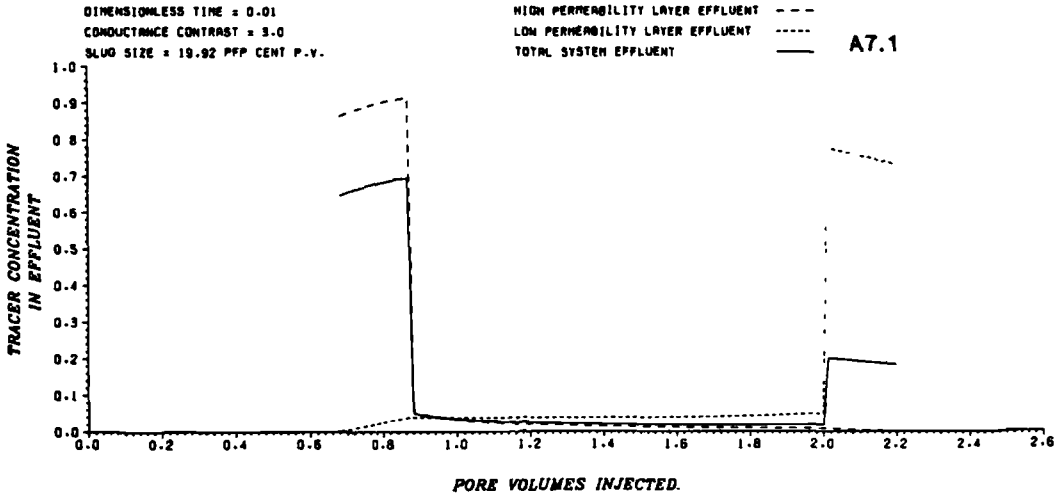

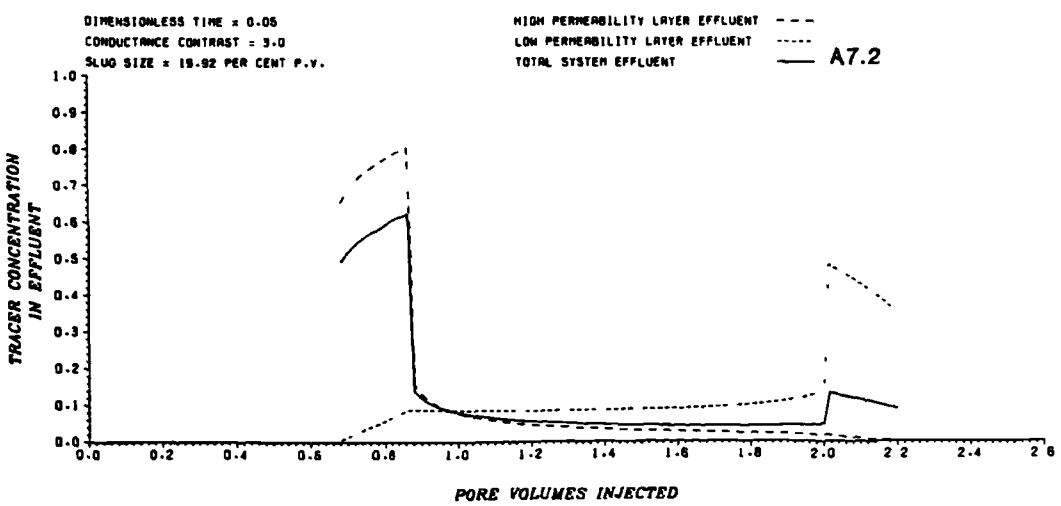

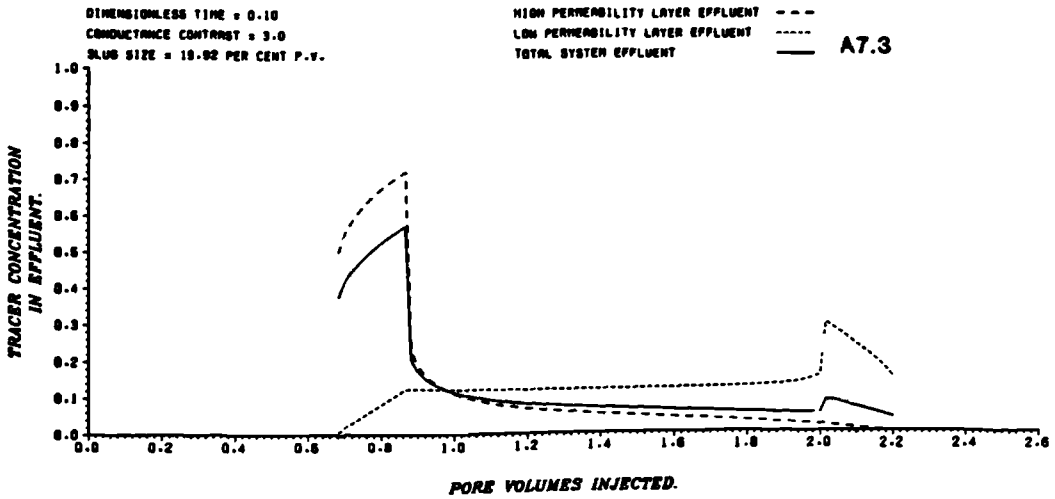
DIMENSIONLESS TIME = 0.10
CONDUCTANCE CONTRAST = 3.0
SLUG SIZE = 19.92 PER CENT P.V.
HIGH PERMEABILITY LAYER EFFLUENT
LOW PERMEABILITY LAYER EFFLUENT
TOTAL SYSTEM EFFLUENT
A7.3
TRACER CONCENTRATION IN EFFLUENT.
PORE VOLUMES INJECTED.

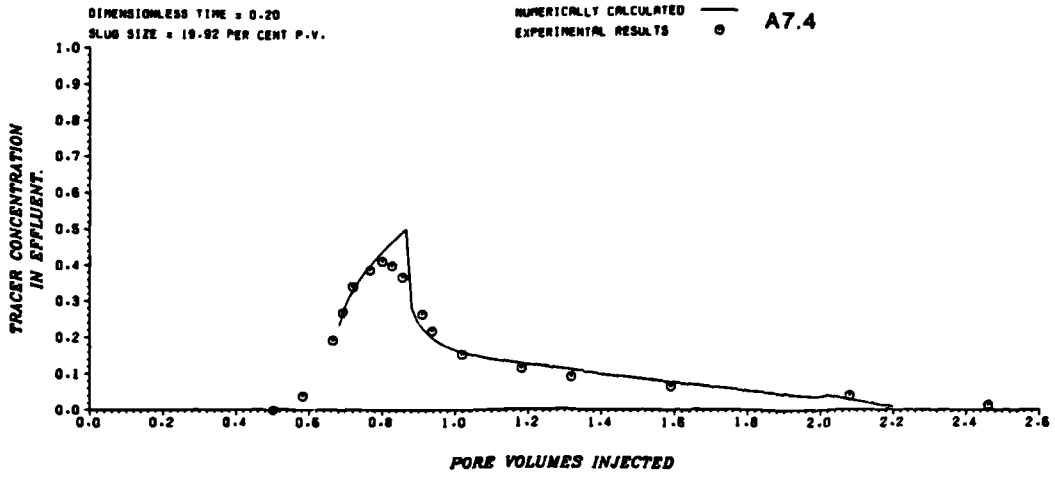
DIMENSIONLESS TIME = 0.20
SLUG SIZE = 19.92 PER CENT P.V.
NUMERICALLY CALCULATED
EXPERIMENTAL RESULTS
A7.4
TRACER CONCENTRATION IN EFFLUENT.
PORE VOLUMES INJECTED

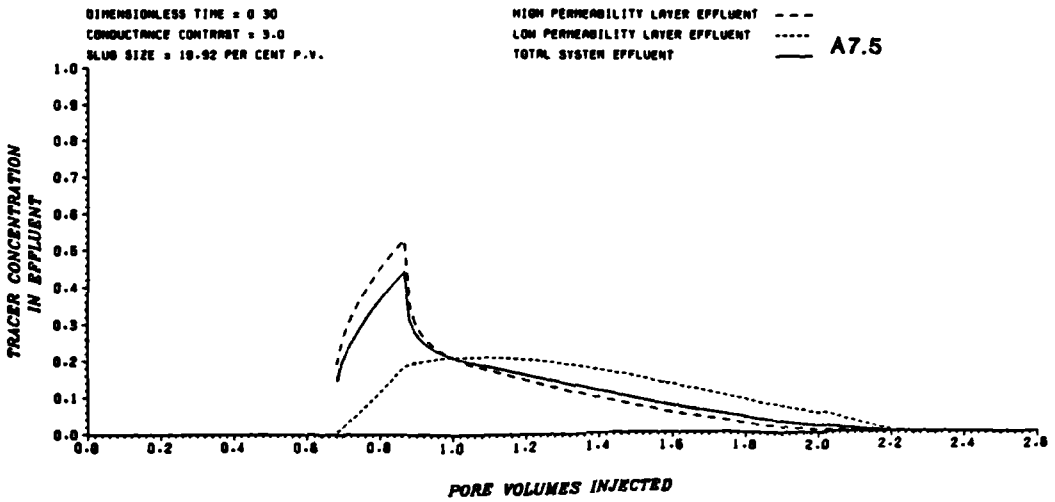
DIMENSIONLESS TIME = 0.30
CONDUCTANCE CONTRAST = 3.0
SLUG SIZE = 19.92 PER CENT P.V.
HIGH PERMEABILITY LAYER EFFLUENT
LOW PERMEABILITY LAYER EFFLUENT
TOTAL SYSTEM EFFLUENT
A7.5
TRACER CONCENTRATION IN EFFLUENT
PORE VOLUMES INJECTED

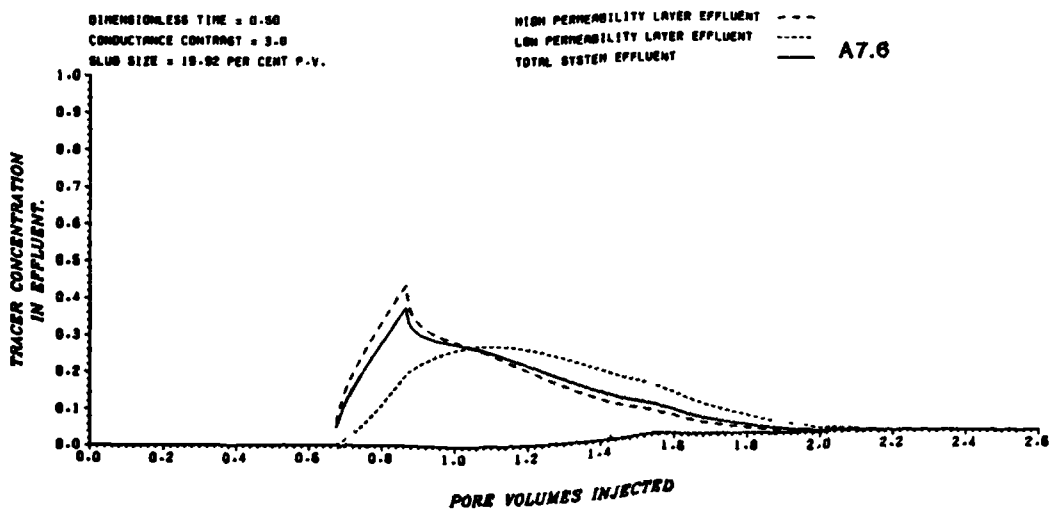
DIMENSIONLESS TIME = 0.50
CONDUCTANCE CONTRAST = 3.0
SLUG SIZE = 19.92 PER CENT P.V.
HIGH PERMEABILITY LAYER EFFLUENT
LOW PERMEABILITY LAYER EFFLUENT
TOTAL SYSTEM EFFLUENT
A7.6
TRACER CONCENTRATION IN EFFLUENT.
PORE VOLUMES INJECTED

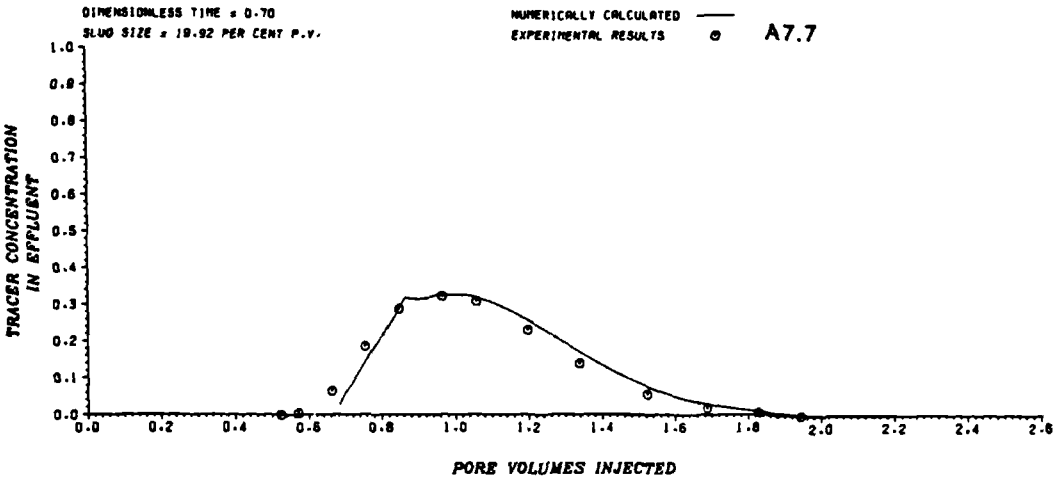
DIMENSIONLESS TIME = 0.70
SLUG SIZE = 19.92 PER CENT P.V.
NUMERICALLY CALCULATED
EXPERIMENTAL RESULTS
A7.7
TRACER CONCENTRATION IN EFFLUENT
PORE VOLUMES INJECTED

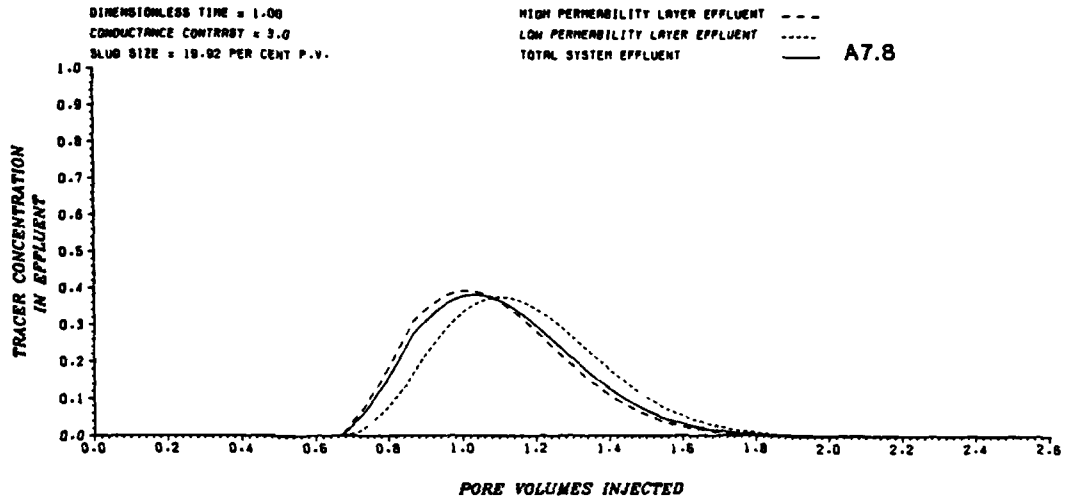
DIMENSIONLESS TIME = 1.00
CONDUCTANCE CONTRAST = 3.0
SLUG SIZE = 19.92 PER CENT P.V.
HIGH PERMEABILITY LAYER EFFLUENT
LOW PERMEABILITY LAYER EFFLUENT
TOTAL SYSTEM EFFLUENT
A7.8
TRACER CONCENTRATION IN EFFLUENT
PORE VOLUMES INJECTED

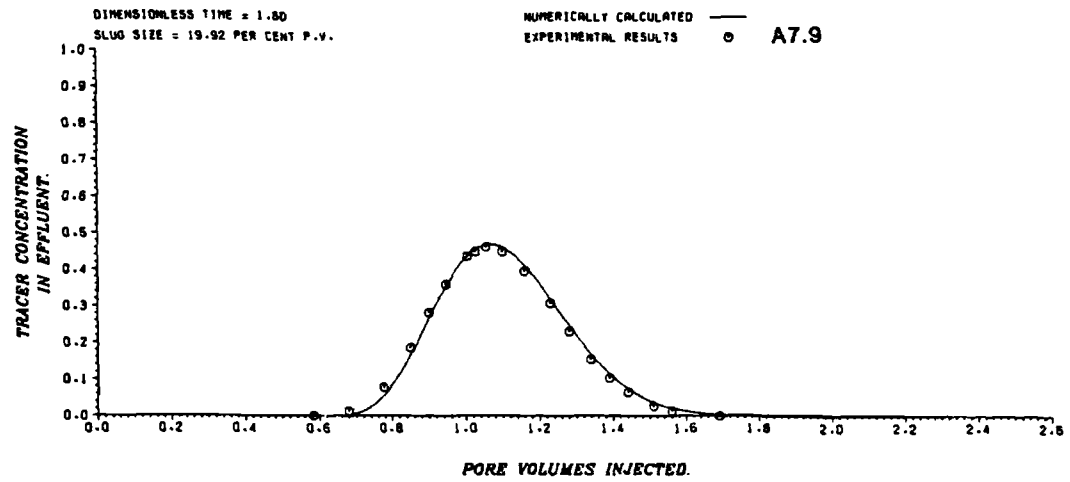
DIMENSIONLESS TIME = 1.80
SLUG SIZE = 19.92 PER CENT P.V.
NUMERICALLY CALCULATED
EXPERIMENTAL RESULTS
A7.9
TRACER CONCENTRATION IN EFFLUENT.
PORE VOLUMES INJECTED.

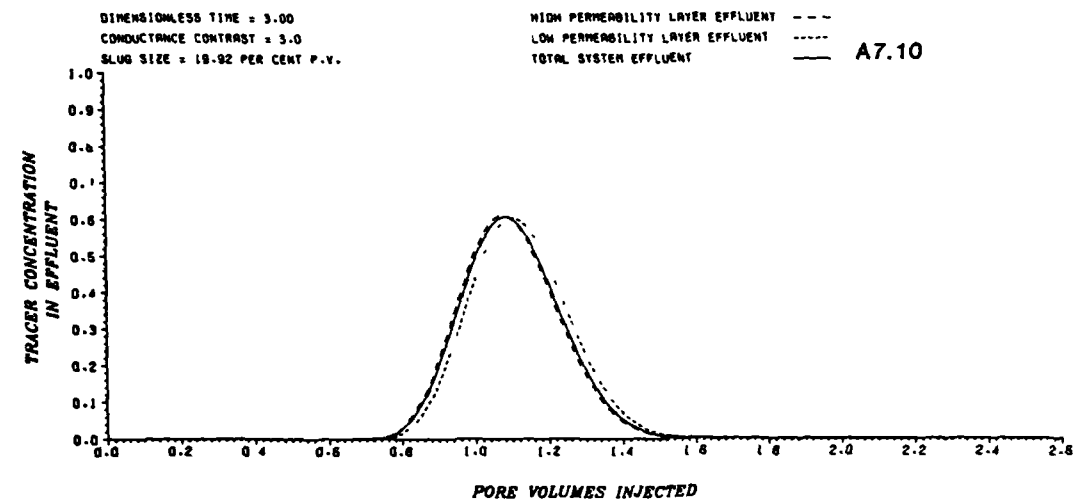
DIMENSIONLESS TIME = 3.00
CONDUCTANCE CONTRAST = 3.0
SLUG SIZE = 19.92 PER CENT P.V.
HIGH PERMEABILITY LAYER EFFLUENT
LOW PERMEABILITY LAYER EFFLUENT
TOTAL SYSTEM EFFLUENT
A7.10
TRACER CONCENTRATION IN EFFLUENT
PORE VOLUMES INJECTED

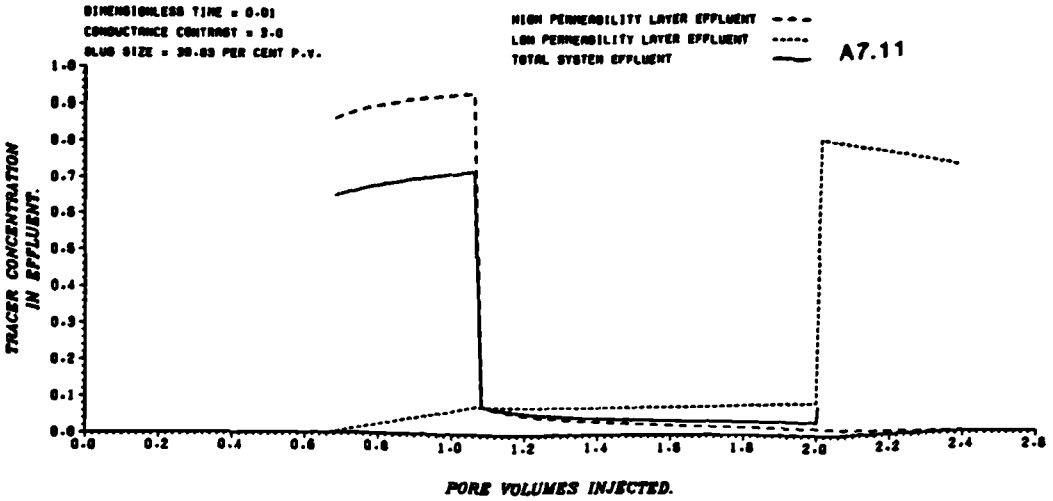
DIMENSIONLESS TIME = 0.01
CONDUCTANCE CONTRAST = 3.0
SLUG SIZE = 30.03 PER CENT P.V.
HIGH PERMEABILITY LAYER EFFLUENT
LOW PERMEABILITY LAYER EFFLUENT
TOTAL SYSTEM EFFLUENT
A7.11
TRACER CONCENTRATION IN EFFLUENT.
PORE VOLUMES INJECTED.

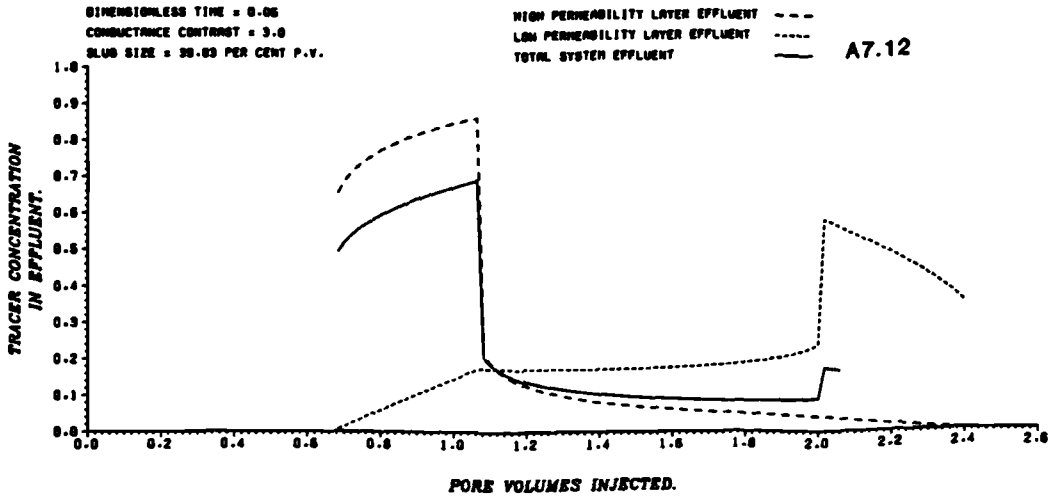
DIMENSIONLESS TIME = 0.05
CONDUCTANCE CONTRAST = 3.0
SLUG SIZE = 30.03 PER CENT P.V.
HIGH PERMEABILITY LAYER EFFLUENT
LOW PERMEABILITY LAYER EFFLUENT
TOTAL SYSTEM EFFLUENT
A7.12
TRACER CONCENTRATION IN EFFLUENT.
PORE VOLUMES INJECTED.

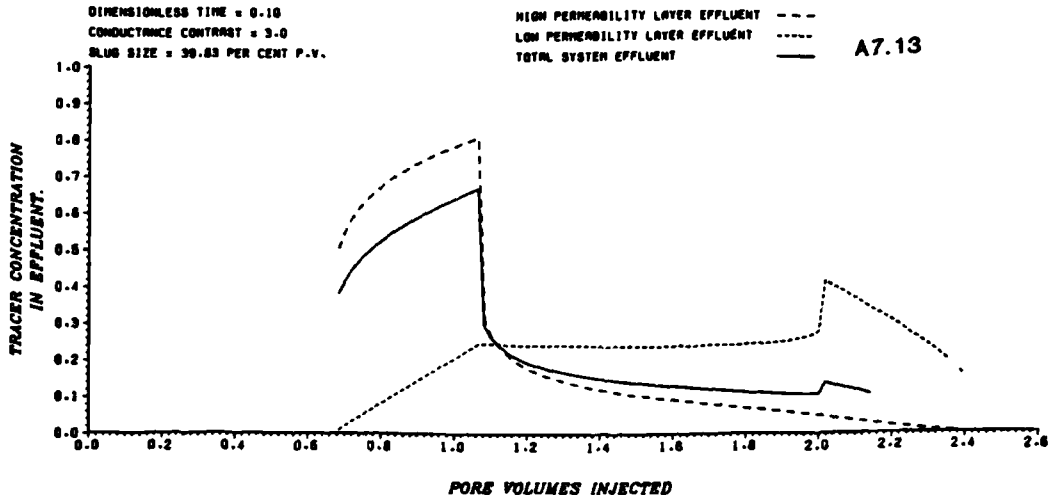
DIMENSIONLESS TIME = 0.10
CONDUCTANCE CONTRAST = 3.0
SLUG SIZE = 30.03 PER CENT P.V.
HIGH PERMEABILITY LAYER EFFLUENT
LOW PERMEABILITY LAYER EFFLUENT
TOTAL SYSTEM EFFLUENT
A7.13
TRACER CONCENTRATION IN EFFLUENT.
PORE VOLUMES INJECTED

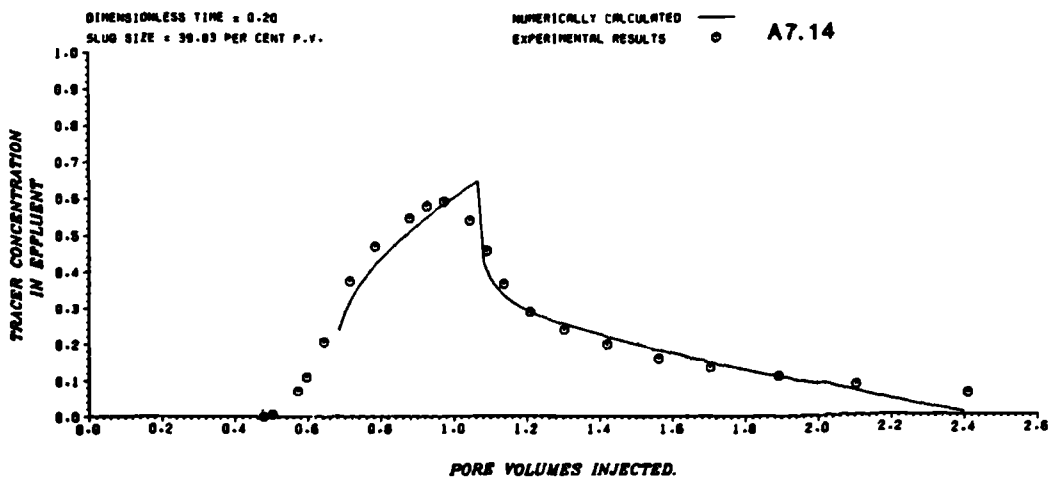
DIMENSIONLESS TIME = 0.20
SLUG SIZE = 30.03 PER CENT P.V.
NUMERICALLY CALCULATED
EXPERIMENTAL RESULTS
A7.14
TRACER CONCENTRATION IN EFFLUENT.
PORE VOLUMES INJECTED.

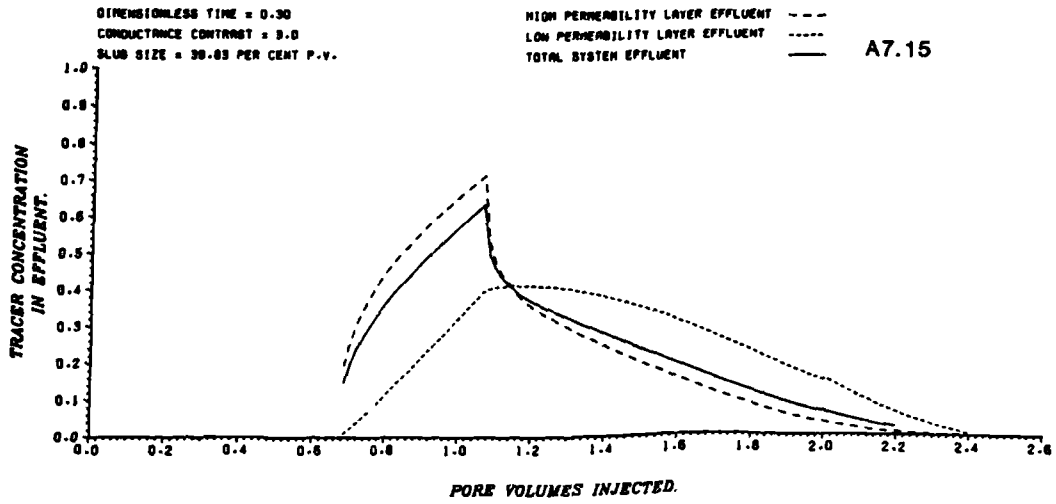

A7.15

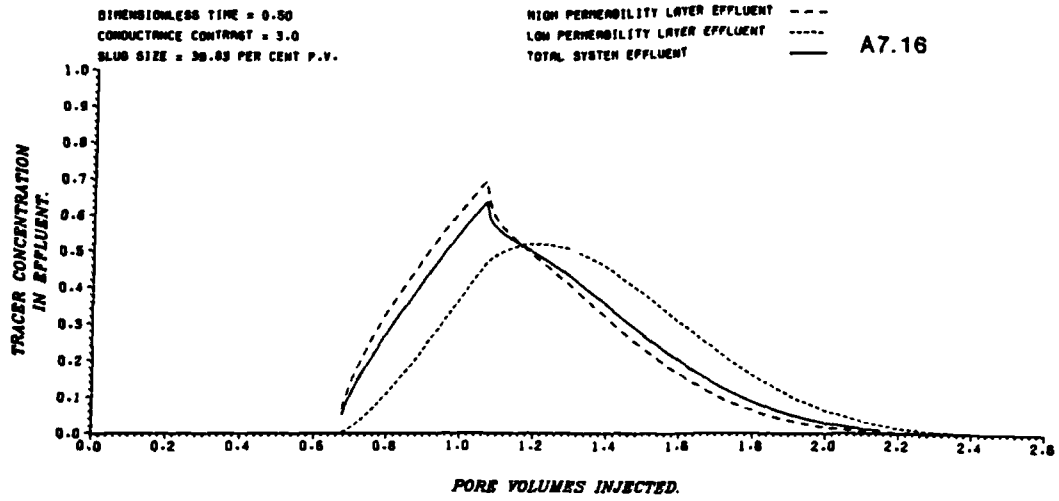

A7.16

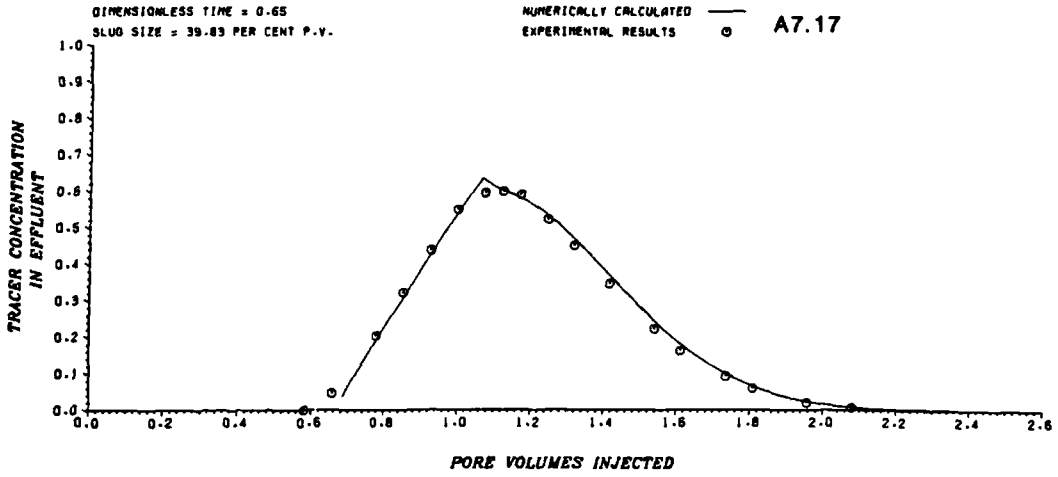

A7.17

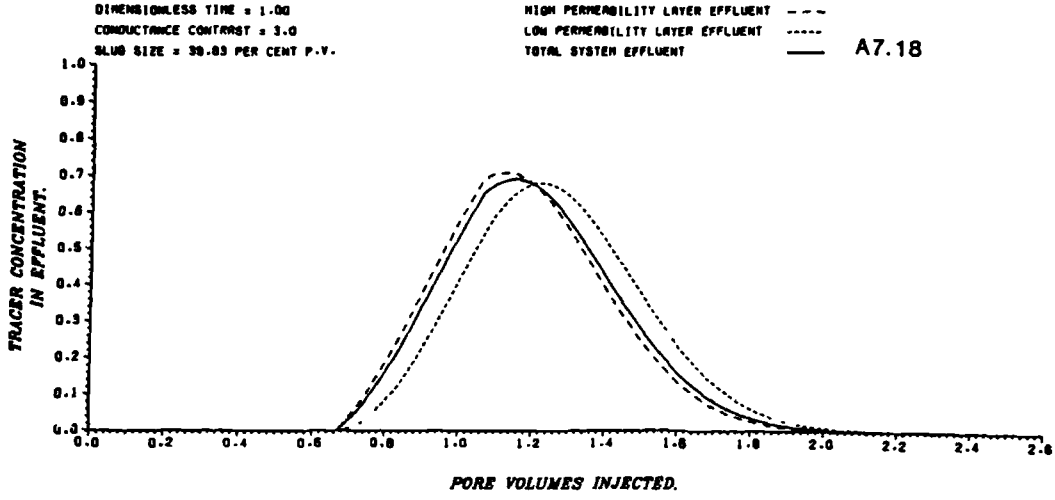

A7.18

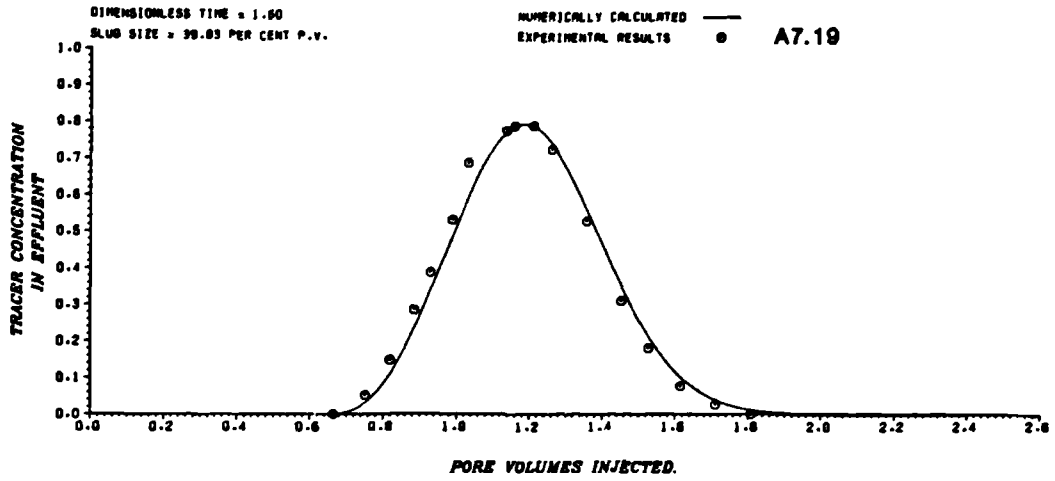
DIMENSIONLESS TIME = 1.00
SLUG SIZE = 30.03 PER CENT P.V.
NUMERICALLY CALCULATED
EXPERIMENTAL RESULTS
A7.19
TRACER CONCENTRATION IN EFFLUENT
PORE VOLUMES INJECTED.

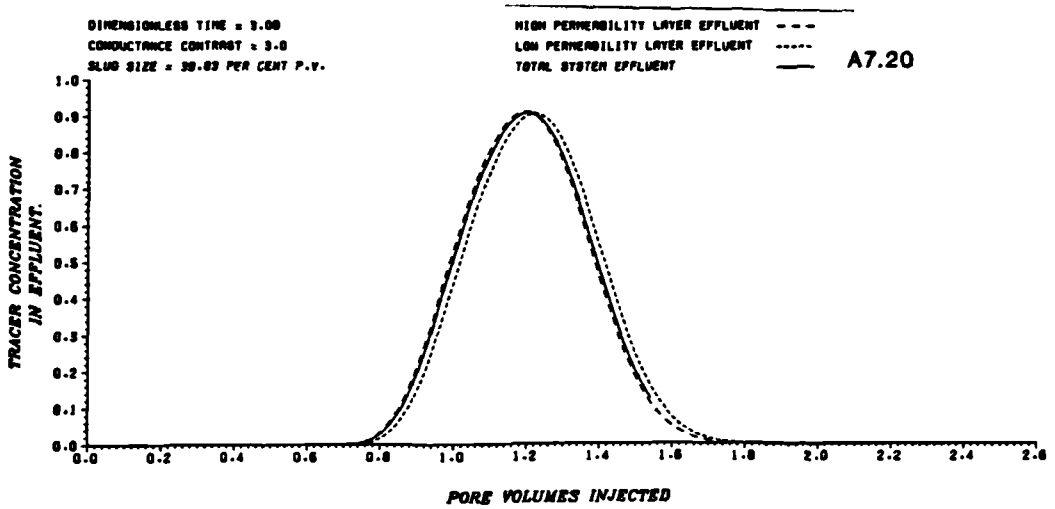
DIMENSIONLESS TIME = 3.00
CONDUCTANCE CONTRAST = 3.0
SLUG SIZE = 30.03 PER CENT P.V.
HIGH PERMEABILITY LAYER EFFLUENT
LOW PERMEABILITY LAYER EFFLUENT
TOTAL SYSTEM EFFLUENT
A7.20
TRACER CONCENTRATION IN EFFLUENT.
PORE VOLUMES INJECTED

A7.2 Prediction of the Volume of the System Swept in Slug Mode Processes

Calculations of the volume of the system swept by slug chemical above the critical concentration are presented graphically in this section.

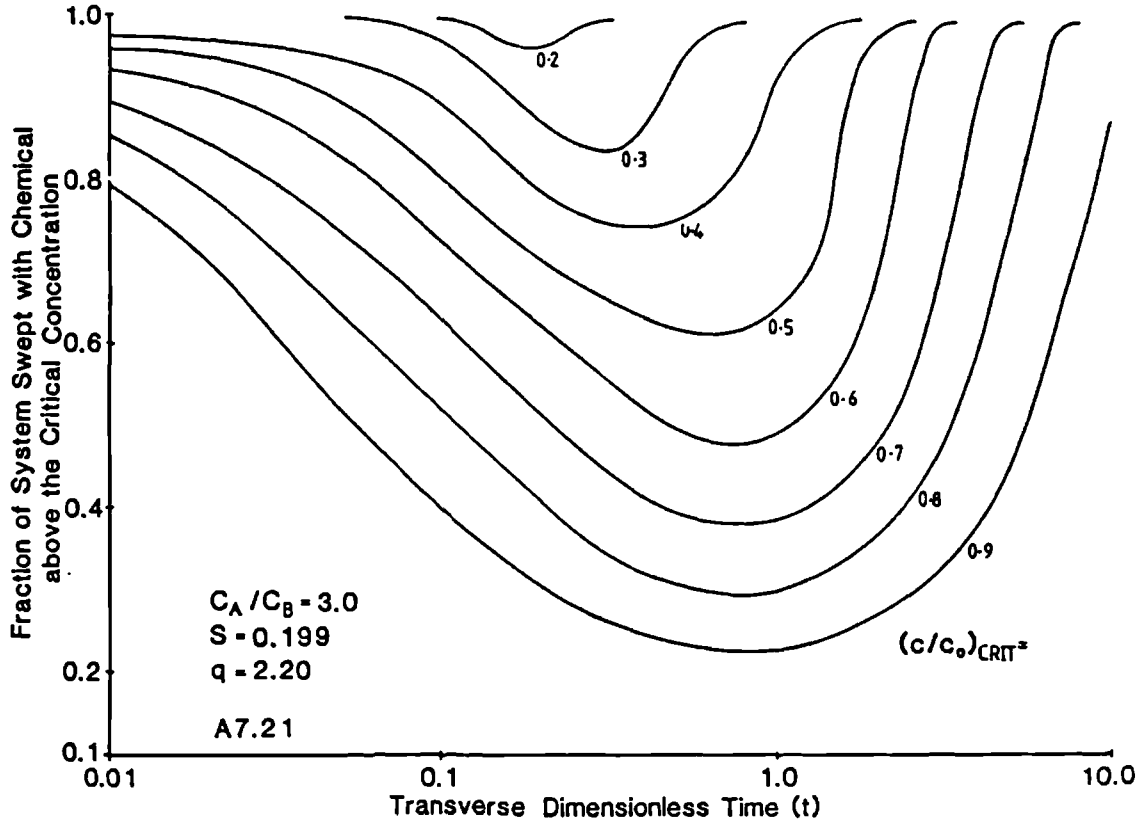

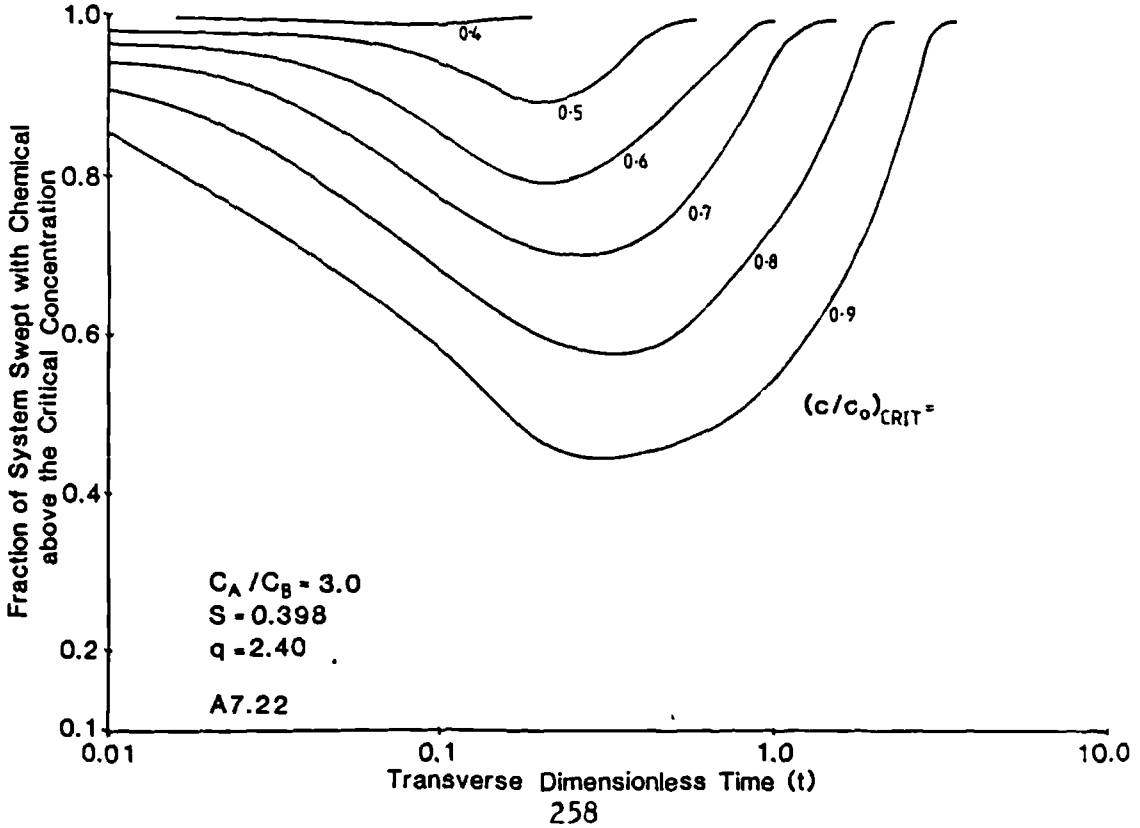

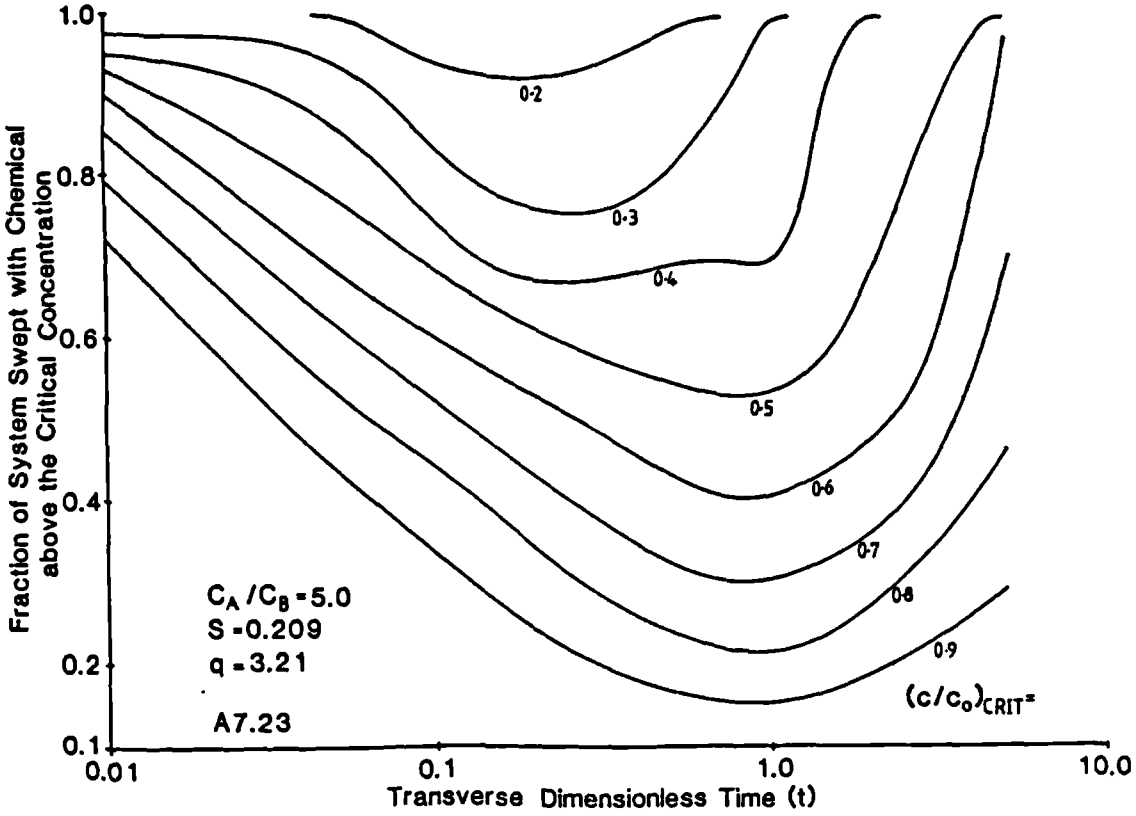
Fraction of System Swept with Chemical above the Critical Concentration
1.0
0.8
0.6
0.4
0.2
0.1
0.01
0.1
1.0
10.0
Transverse Dimensionless Time (t)
0·2
0·3
0·4
0·5
0·6
0·7
0·8
0·9
$(c/c_o)_{CRIT}$=
C_A/C_B = 5.0
S = 0.209
q = 3.21
A7.23

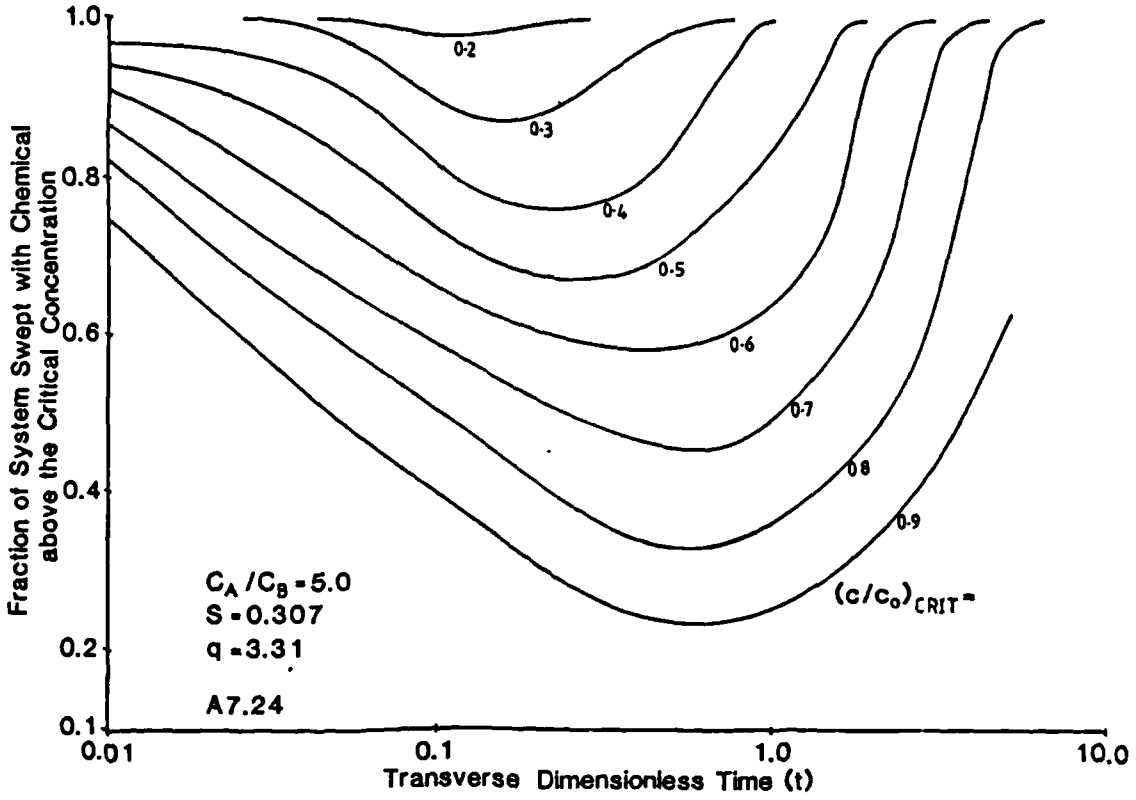
Fraction of System Swept with Chemical above the Critical Concentration
1.0
0.8
0.6
0.4
0.2
0.1
0.01
0.1
1.0
10.0
Transverse Dimensionless Time (t)
0·2
0·3
0·4
0·5
0·6
0·7
0·8
0·9
$(c/c_o)_{CRIT}$=
C_A/C_B = 5.0
S = 0.307
q = 3.31
A7.24

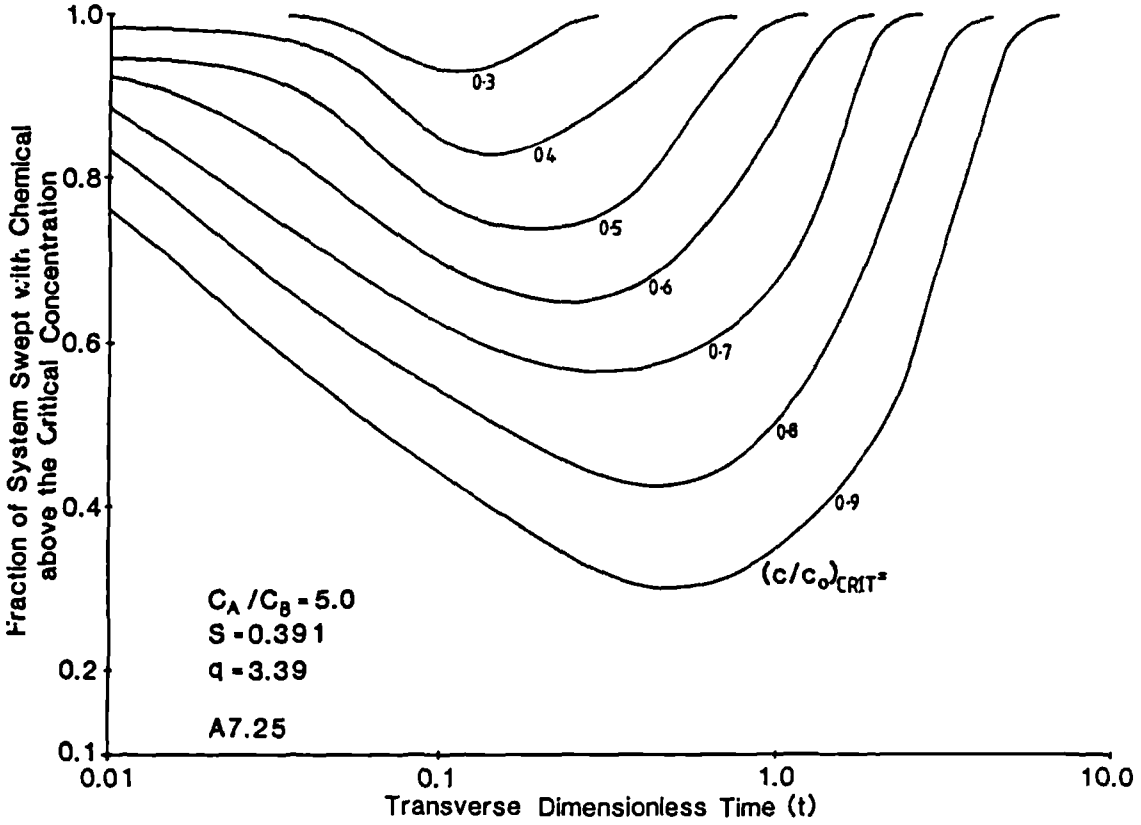
Fraction of System Swept with Chemical above the Critical Concentration
1.0
0.8
0.6
0.4
0.2
0.1
0.01
0.1
1.0
10.0
Transverse Dimensionless Time (t)
0·3
0·4
0·5
0·6
0·7
0·8
0·9
(c/c₀)CRIT=
CA/CB=5.0
S=0.391
q=3.39
A7.25

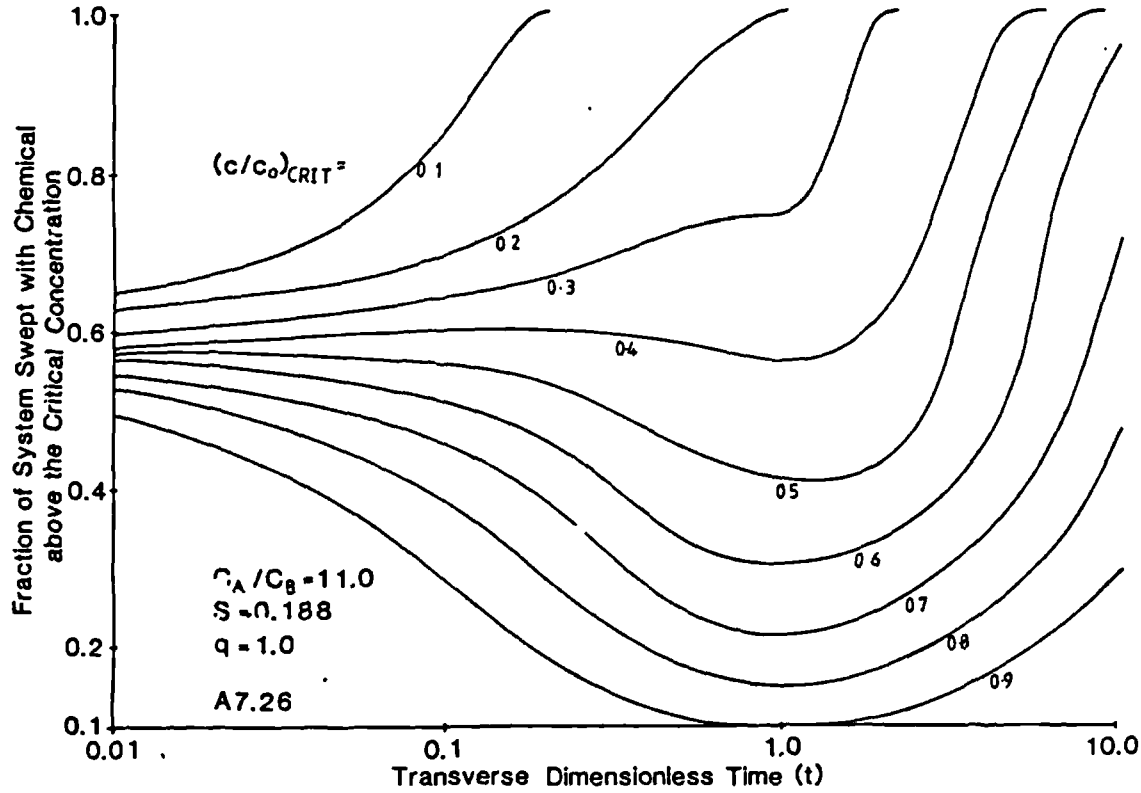
Fraction of System Swept with Chemical above the Critical Concentration
1.0
0.8
0.6
0.4
0.2
0.1
0.01
0.1
1.0
10.0
Transverse Dimensionless Time (t)
(c/c₀)CRIT=
0·1
0·2
0·3
0·4
0·5
0·6
0·7
0·8
0·9
CA/CB=11.0
S=0.188
q=1.0
A7.26

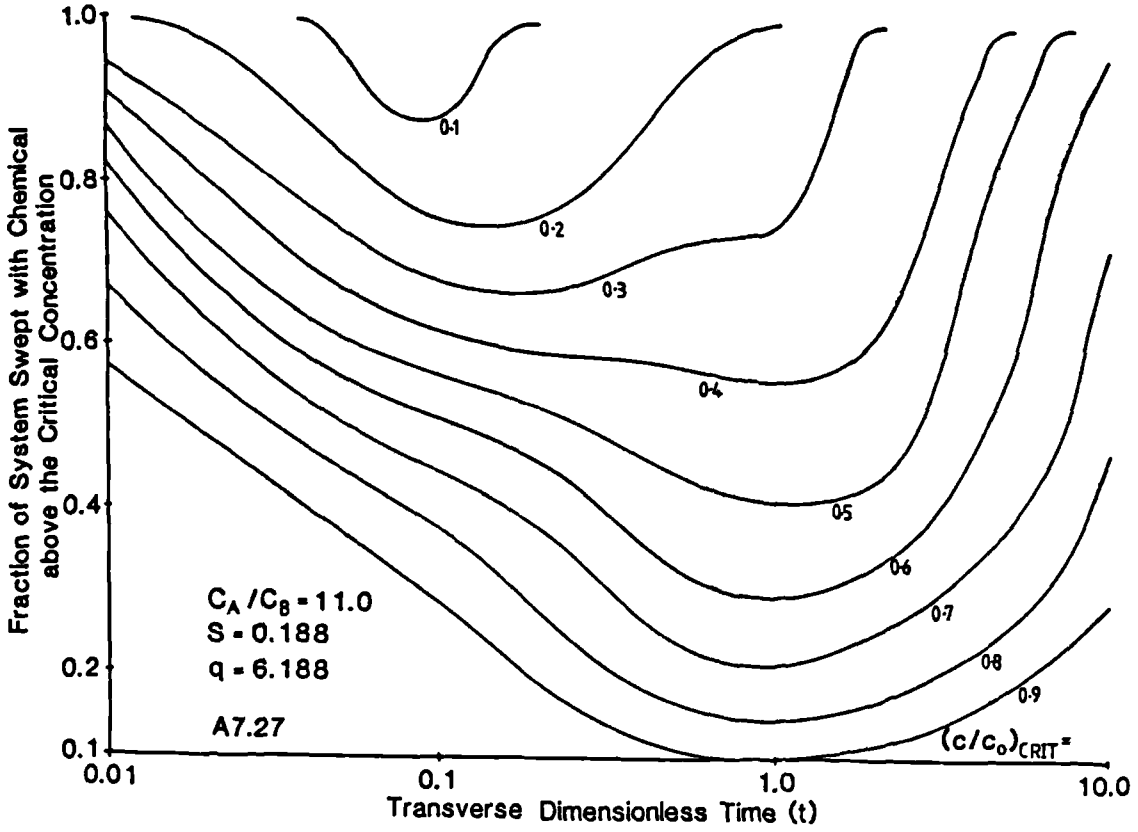
Fraction of System Swept with Chemical above the Critical Concentration
1.0
0.8
0.6
0.4
0.2
0.1
0.01
0.1
1.0
10.0
Transverse Dimensionless Time (t)
0·1
0·2
0·3
0·4
0·5
0·6
0·7
0·8
0·9
$(c/c_o)_{CRIT}$ =
C_A/C_B = 11.0
S = 0.188
q = 6.188
A7.27

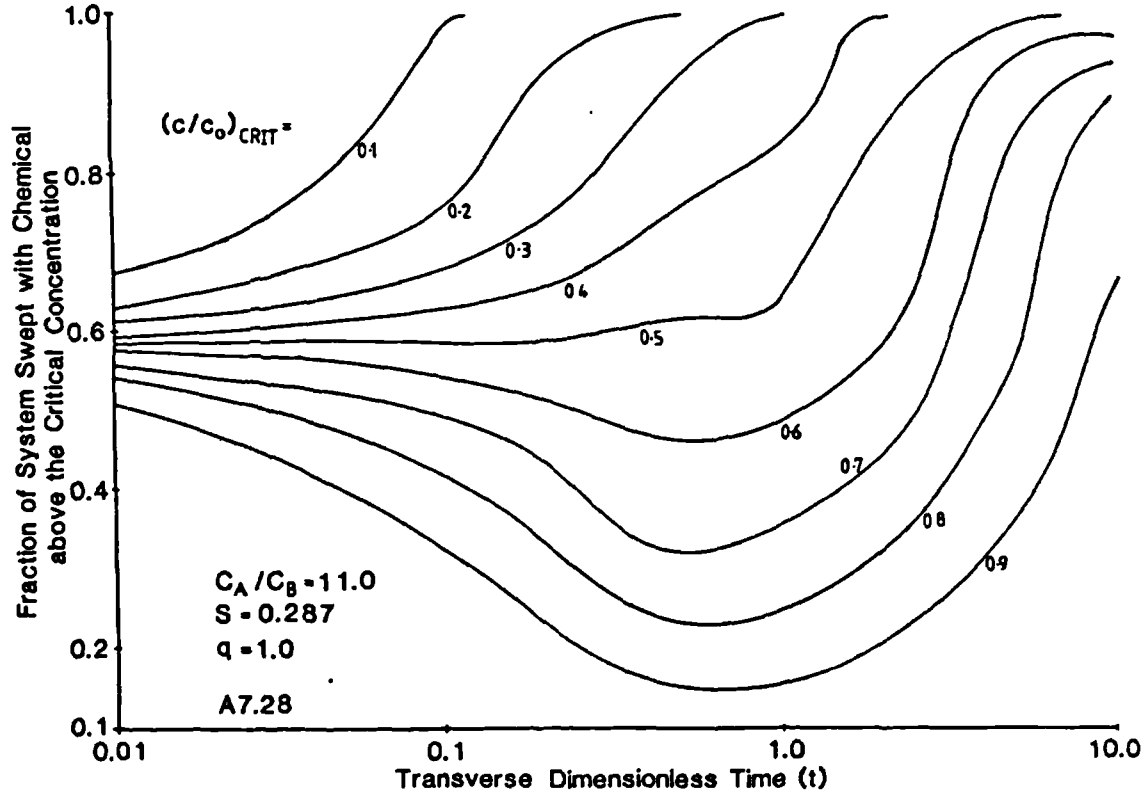
Fraction of System Swept with Chemical above the Critical Concentration
1.0
0.8
0.6
0.4
0.2
0.1
0.01
0.1
1.0
10.0
Transverse Dimensionless Time (t)
$(c/c_o)_{CRIT}$ =
0·1
0·2
0·3
0·4
0·5
0·6
0·7
0·8
0·9
C_A/C_B = 11.0
S = 0.287
q = 1.0
A7.28

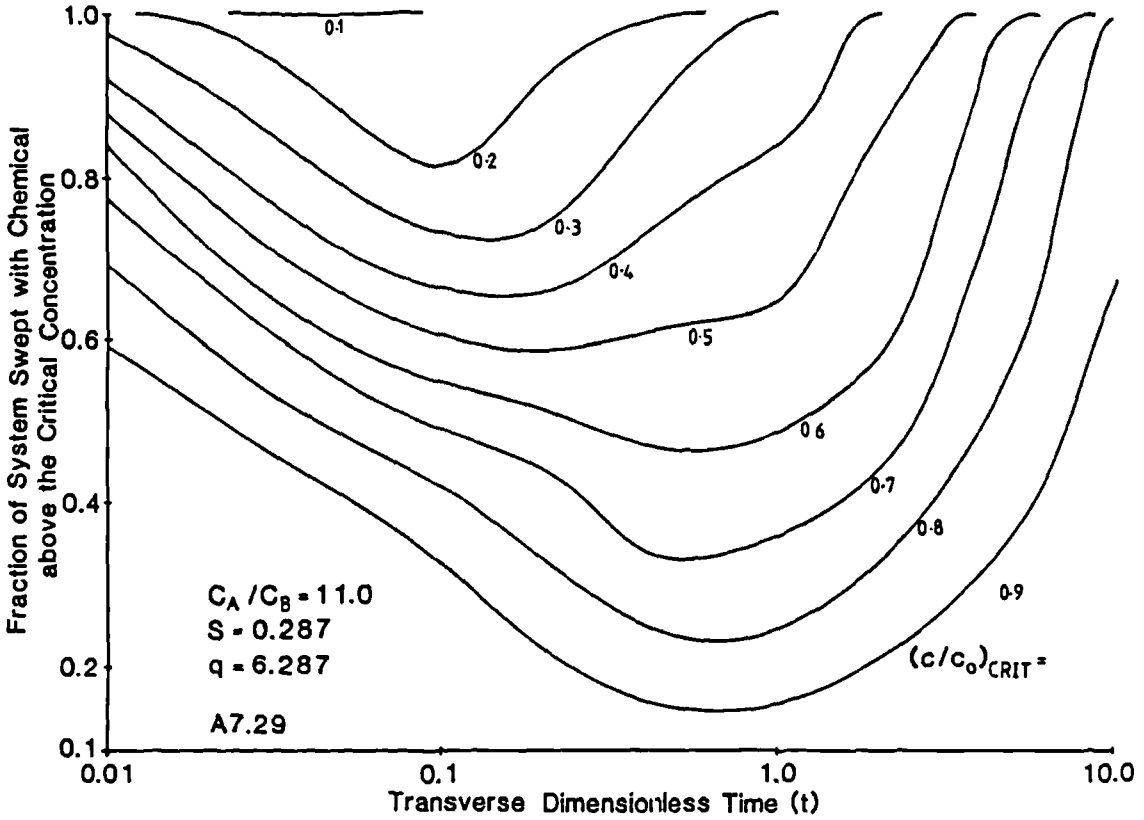
Fraction of System Swept with Chemical above the Critical Concentration
1.0
0.8
0.6
0.4
0.2
0.1
0.01
0.1
1.0
10.0
Transverse Dimensionless Time (t)
0·1
0·2
0·3
0·4
0·5
0·6
0·7
0·8
0·9
$(c/c_o)_{CRIT}$ =
C_A/C_B = 11.0
S = 0.287
q = 6.287
A7.29

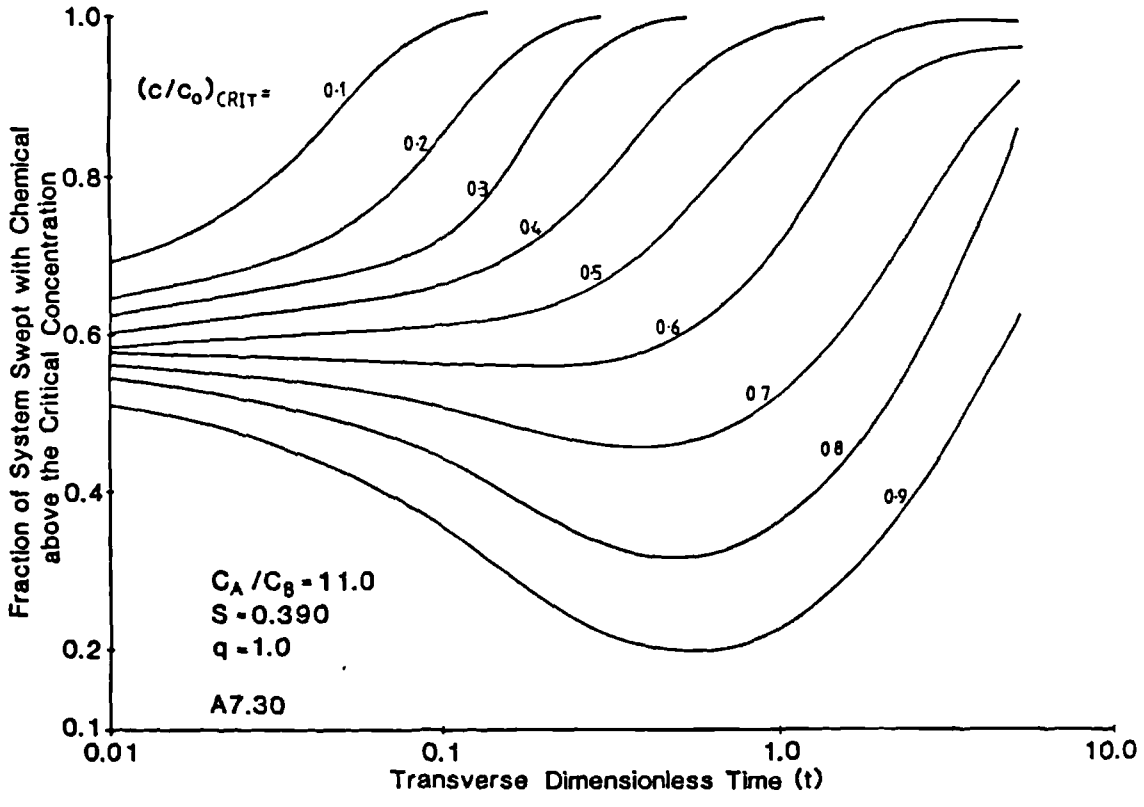
Fraction of System Swept with Chemical above the Critical Concentration
1.0
0.8
0.6
0.4
0.2
0.1
0.01
0.1
1.0
10.0
Transverse Dimensionless Time (t)
$(c/c_o)_{CRIT}$ =
0·1
0·2
0·3
0·4
0·5
0·6
0·7
0·8
0·9
C_A/C_B = 11.0
S = 0.390
q = 1.0
A7.30

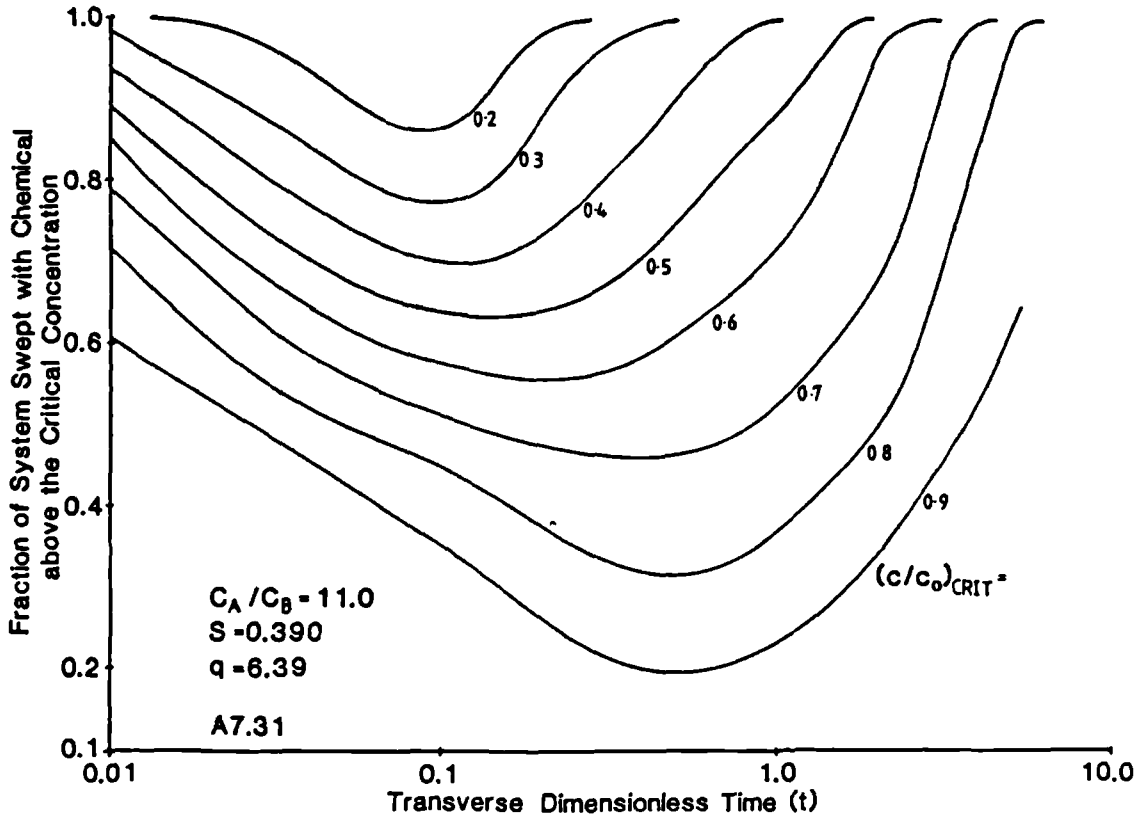
Fraction of System Swept with Chemical above the Critical Concentration
1.0
0.8
0.6
0.4
0.2
0.1
0.01
0.1
1.0
10.0
Transverse Dimensionless Time (t)
0·2
0·3
0·4
0·5
0·6
0·7
0·8
0·9
(c/c₀)CRIT =
CA /CB = 11.0
S = 0.390
q = 6.39
A7.31

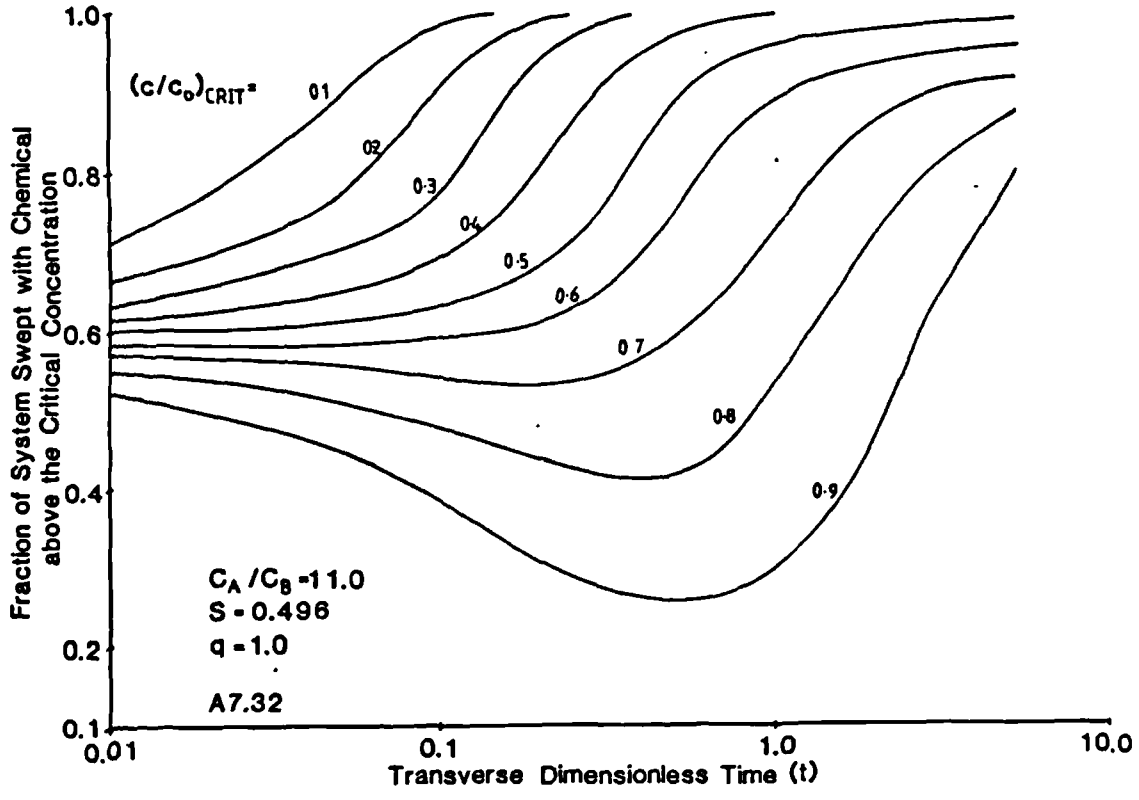
Fraction of System Swept with Chemical above the Critical Concentration
1.0
0.8
0.6
0.4
0.2
0.1
0.01
0.1
1.0
10.0
Transverse Dimensionless Time (t)
(c/c₀)CRIT =
01
02
0·3
04
0·5
0·6
0 7
0·8
0·9
CA /CB = 11.0
S = 0.496
q = 1.0
A7.32

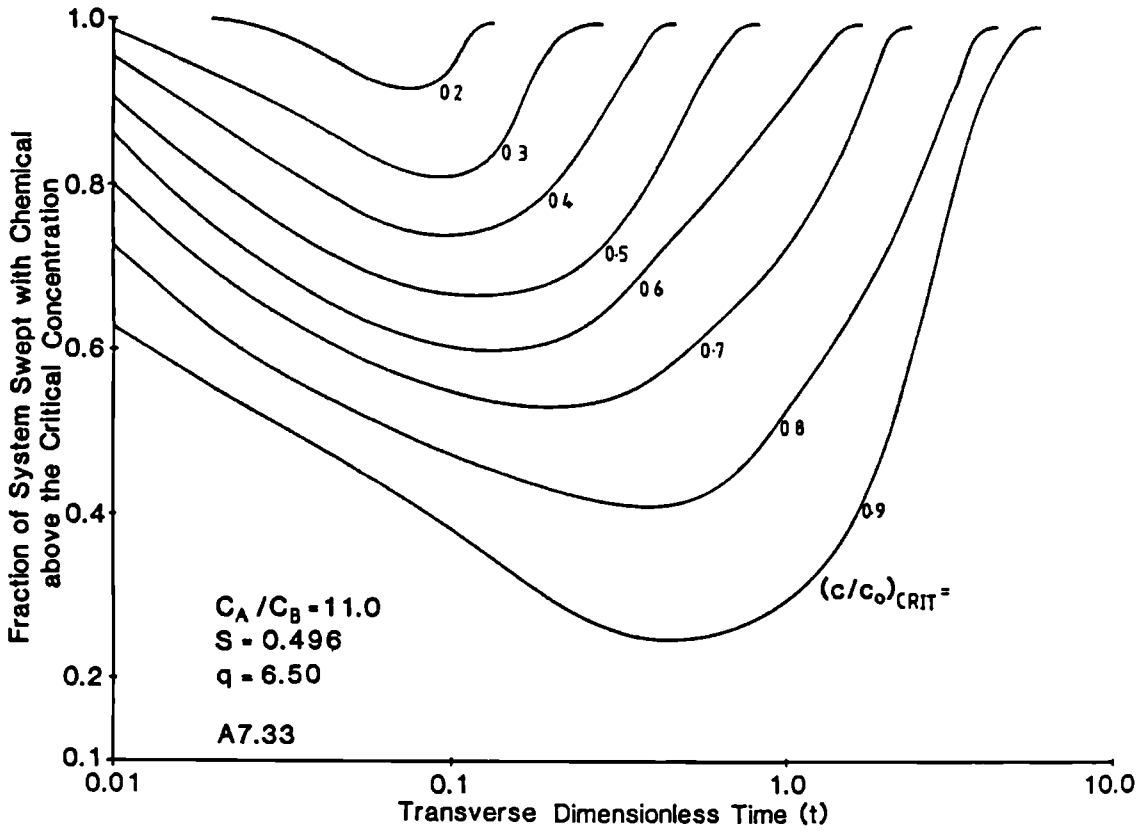
1.0
0.8
0.6
0.4
0.2
0.1
0.01
0.1
1.0
10.0
Fraction of System Swept with Chemical above the Critical Concentration
Transverse Dimensionless Time (t)
0.2
0.3
0.4
0.5
0.6
0.7
0.8
0.9
$(c/c_o)_{CRIT}$ =
C_A/C_B = 11.0
S = 0.496
q = 6.50
A7.33

APPENDIX EIGHT

DATA FROM NON-UNIT MOBILITY RATIO DISPERSION SENSITIVE EXPERIMENTS

Numerical and experimental effluent profiles used to study the coupling of viscous forces and transverse microscopic dispersion are presented in this appendix. These data are discussed in chapter seven.

A8.1 Continuous Injection Data

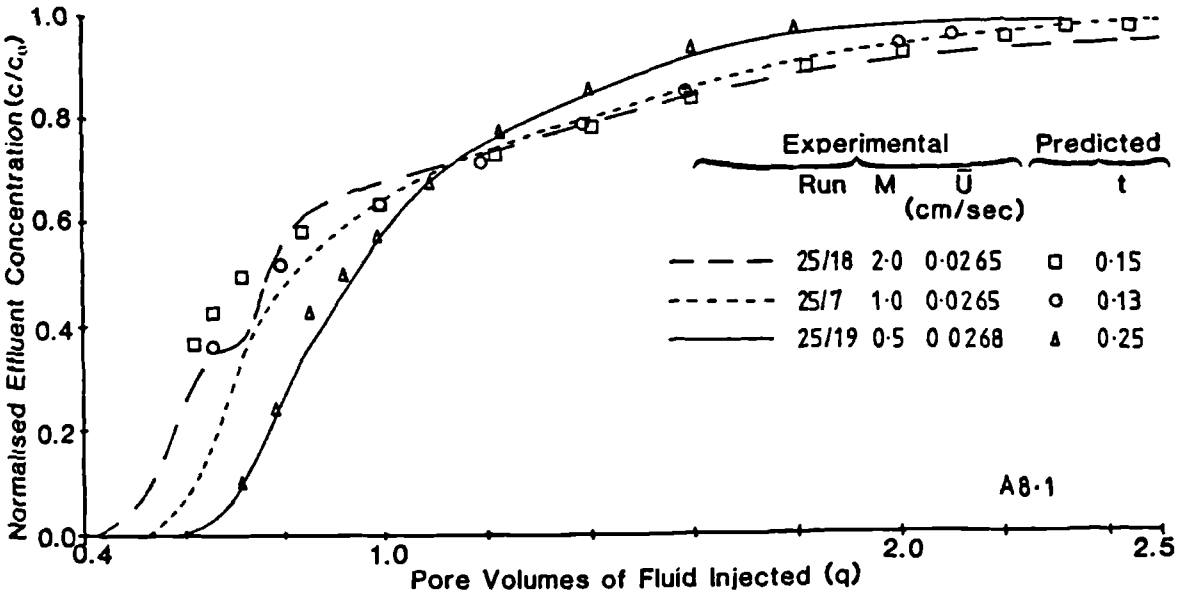

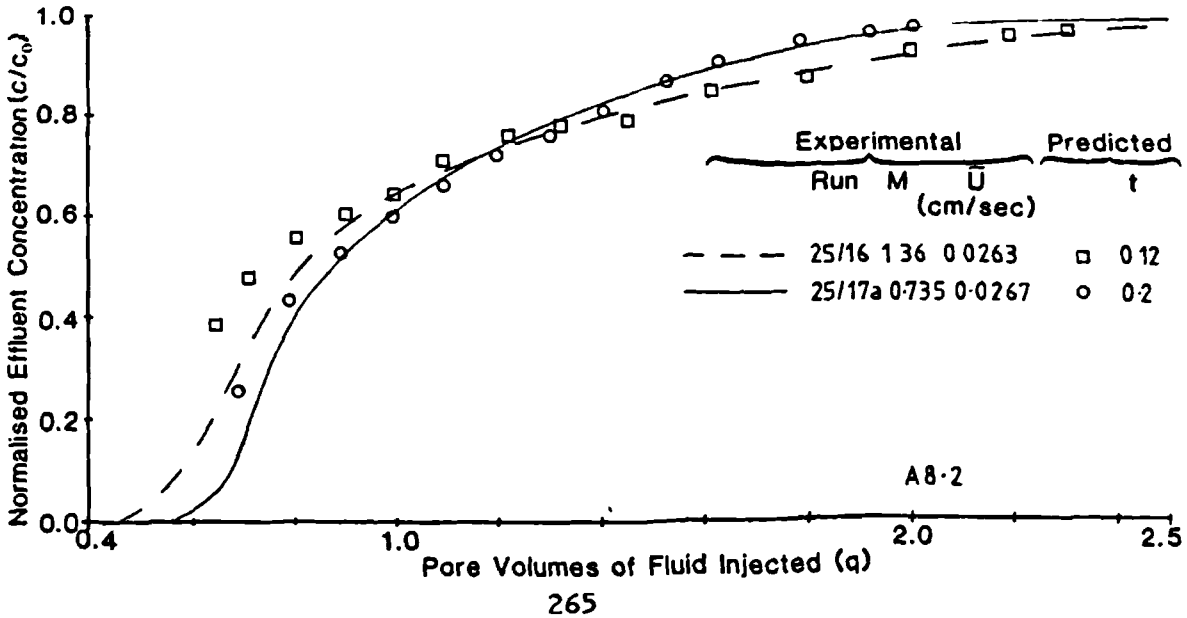

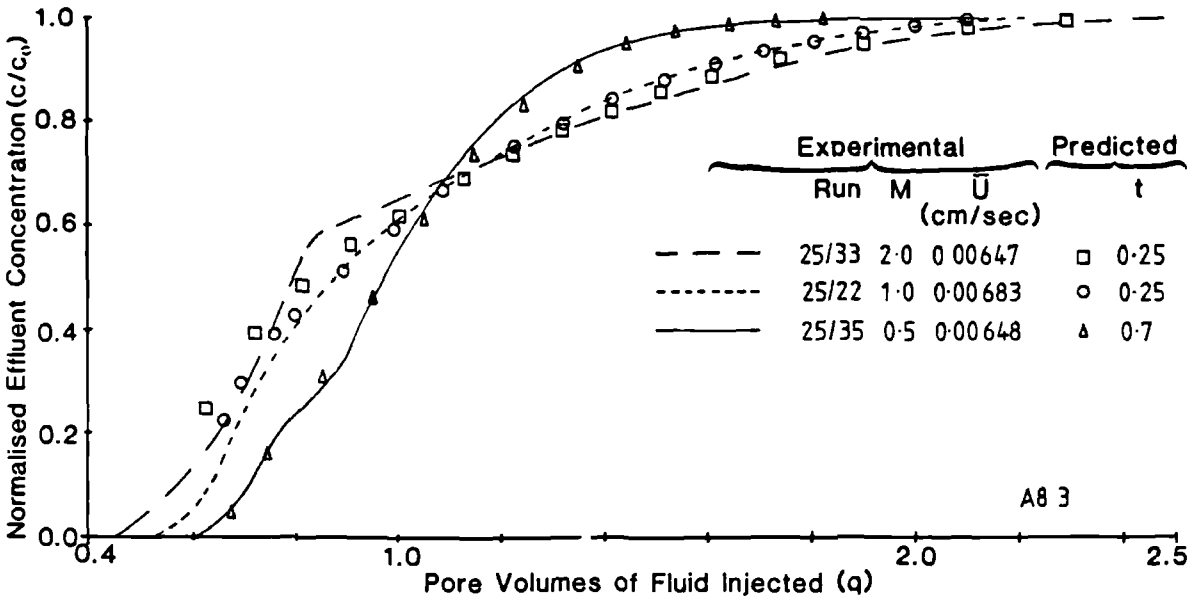
Normalised Effluent Concentration (c/c0)
1.0
0.8
0.6
0.4
0.2
0.0
0.4
1.0
2.0
2.5
Pore Volumes of Fluid Injected (q)
Experimental
Predicted
Run M Ū (cm/sec) t
25/33 2·0 0 00647 0·25
25/22 1·0 0·00683 0·25
25/35 0·5 0·00648 0·7
A8 3

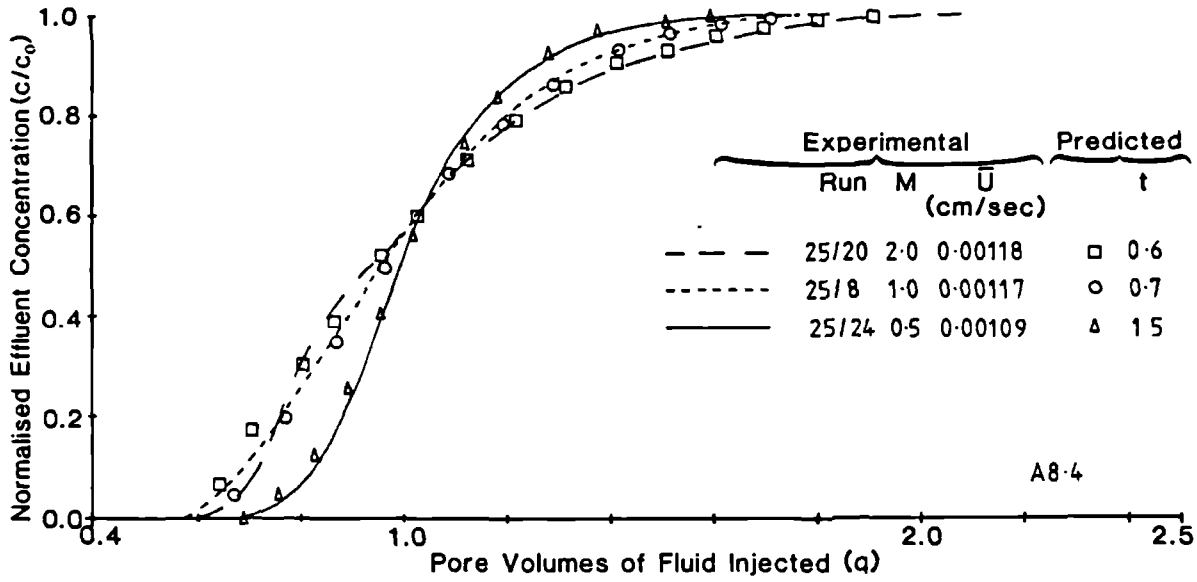
Normalised Effluent Concentration (c/c0)
1.0
0.8
0.6
0.4
0.2
0.0
0.4
1.0
2.0
2.5
Pore Volumes of Fluid Injected (q)
Experimental
Predicted
Run M Ū (cm/sec) t
25/20 2·0 0·00118 0·6
25/8 1·0 0·00117 0·7
25/24 0·5 0·00109 1 5
A8·4

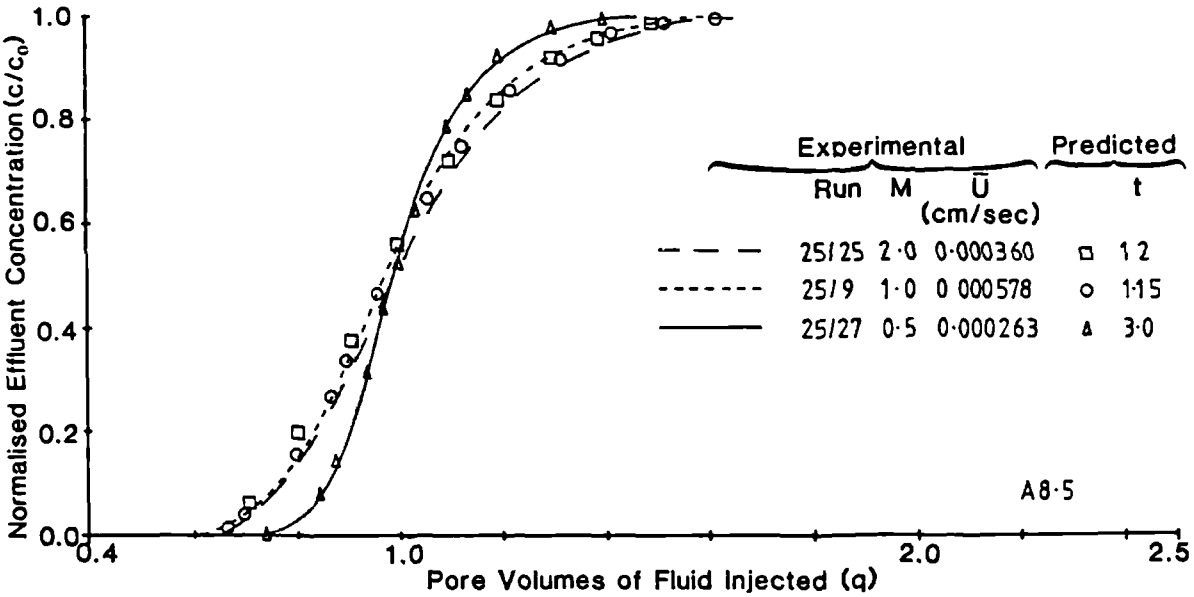
Normalised Effluent Concentration (c/c0)
1.0
0.8
0.6
0.4
0.2
0.0
0.4
1.0
2.0
2.5
Pore Volumes of Fluid Injected (q)
Experimental
Predicted
Run M Ū (cm/sec) t
25/25 2·0 0·000360 1 2
25/9 1·0 0 000578 1·15
25/27 0·5 0·000263 3·0
A8·5

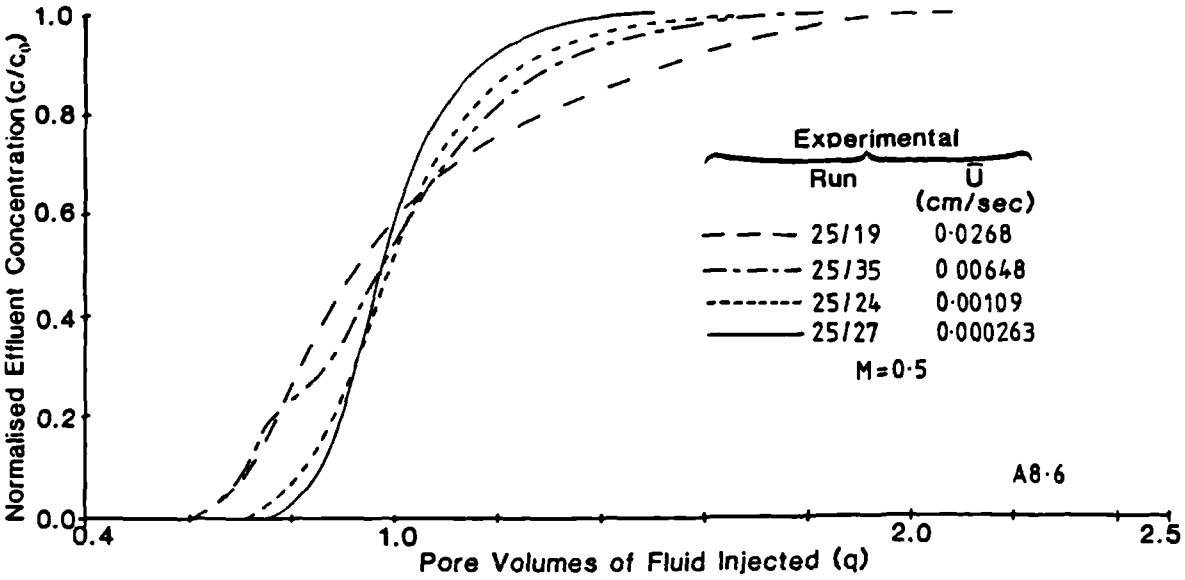
Normalised Effluent Concentration (c/c0)
1.0
0.8
0.6
0.4
0.2
0.0
0.4
1.0
2.0
2.5
Pore Volumes of Fluid Injected (q)
Experimental
Run
Ū (cm/sec)
25/19 0·0268
25/35 0 00648
25/24 0·00109
25/27 0·000263
M=0·5
A8·6

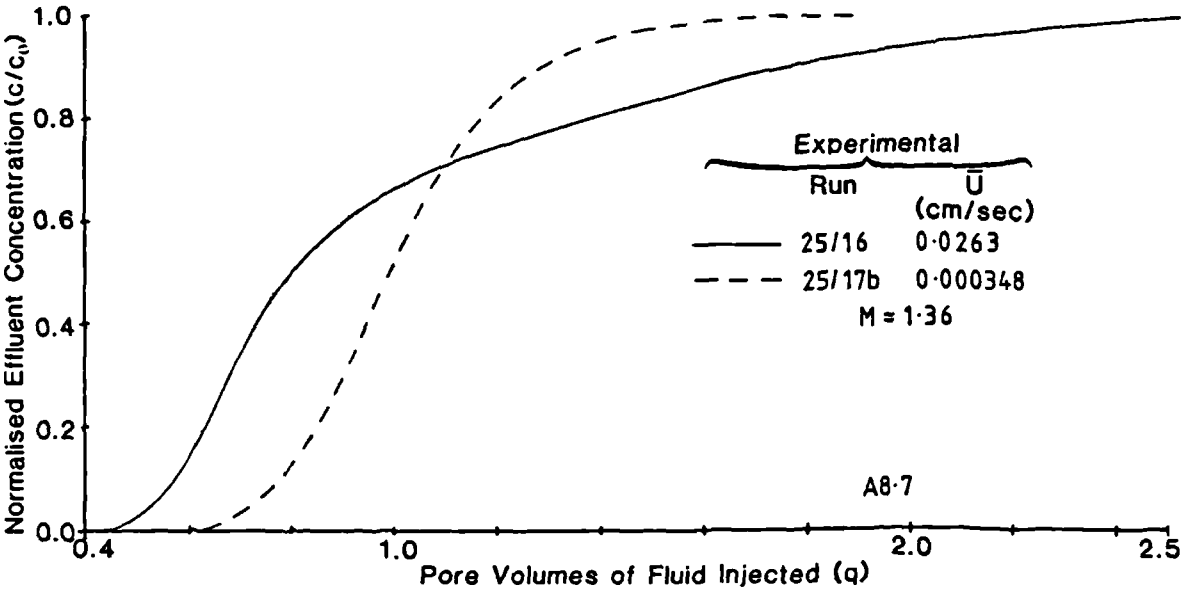
Normalised Effluent Concentration (c/c0)
1.0
0.8
0.6
0.4
0.2
0.0
0.4
1.0
2.0
2.5
Pore Volumes of Fluid Injected (q)
Experimental
Run
Ū (cm/sec)
25/16 0·0263
25/17b 0·000348
M = 1·36
A8·7

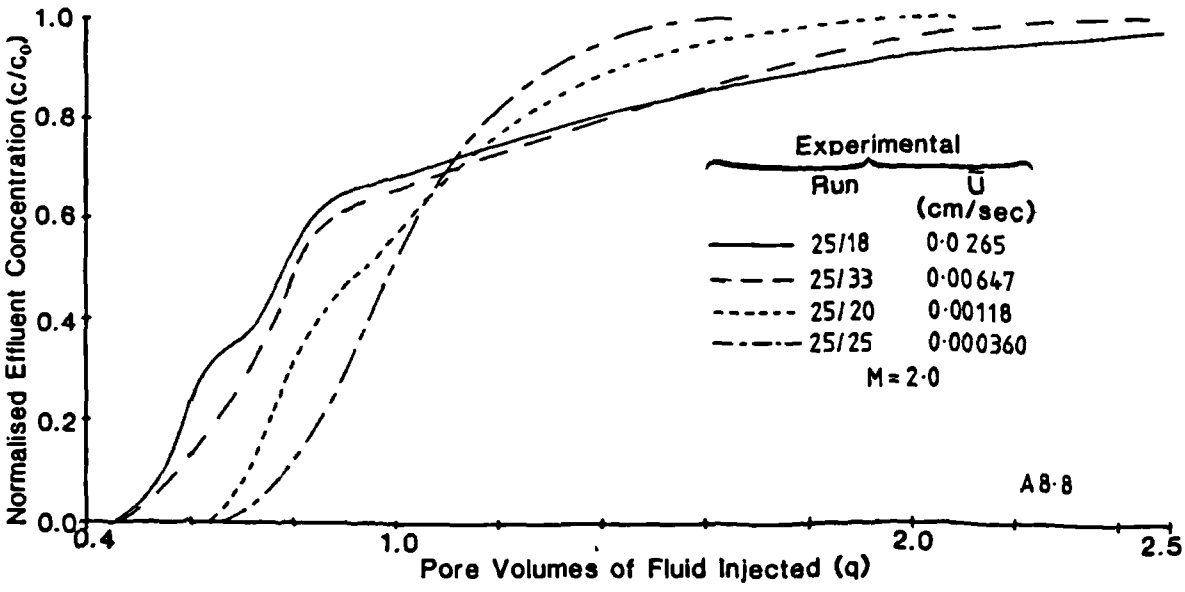
Normalised Effluent Concentration (c/c0)
1.0
0.8
0.6
0.4
0.2
0.0
0.4
1.0
2.0
2.5
Pore Volumes of Fluid Injected (q)
Experimental
Run
Ū (cm/sec)
25/18 0·0 265
25/33 0·00647
25/20 0·00118
25/25 0·000360
M = 2·0
A8·8

A8.2 Slug Mode Injection Data

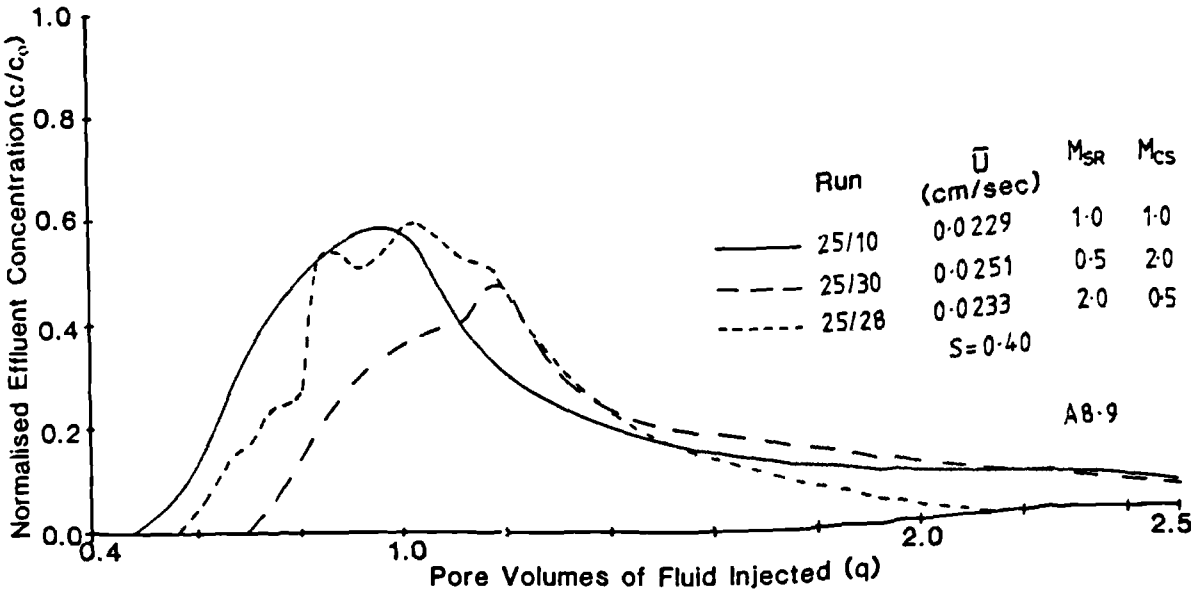

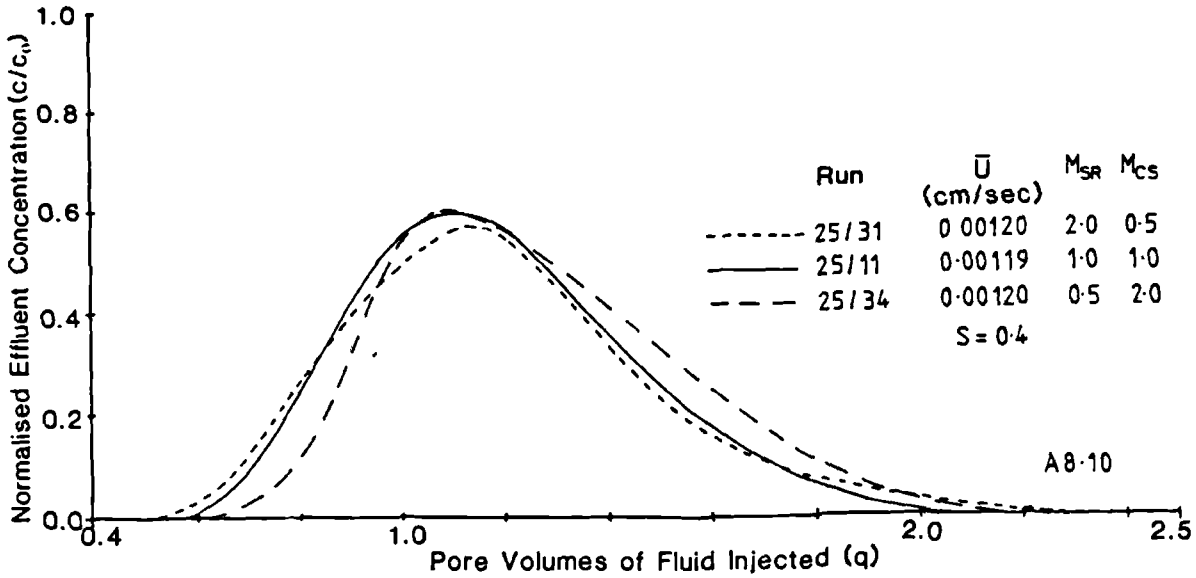

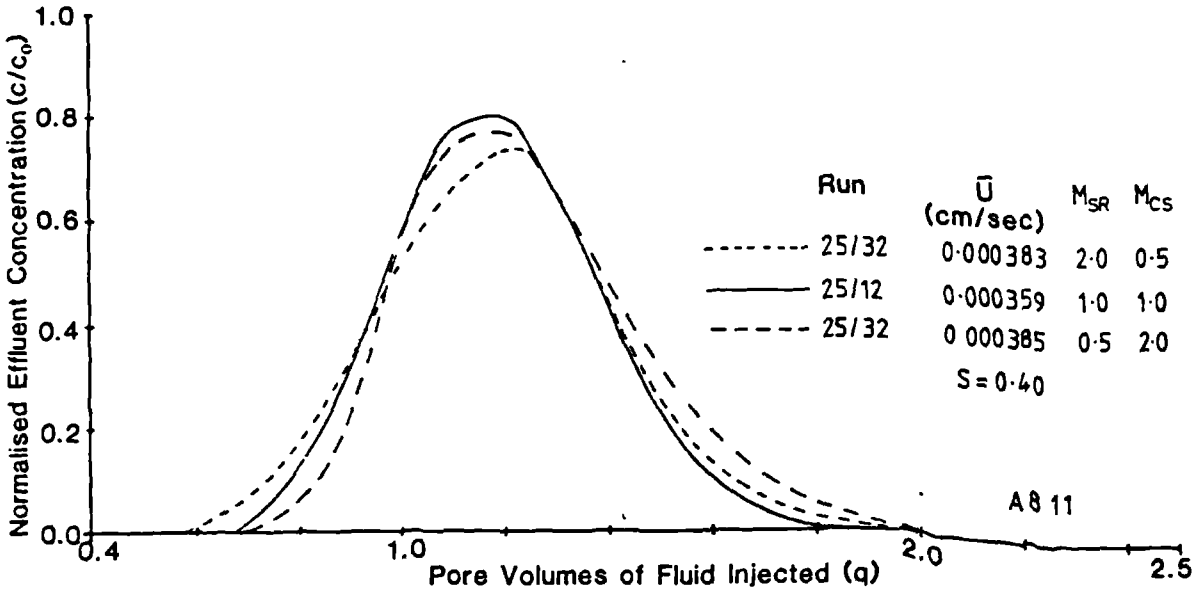

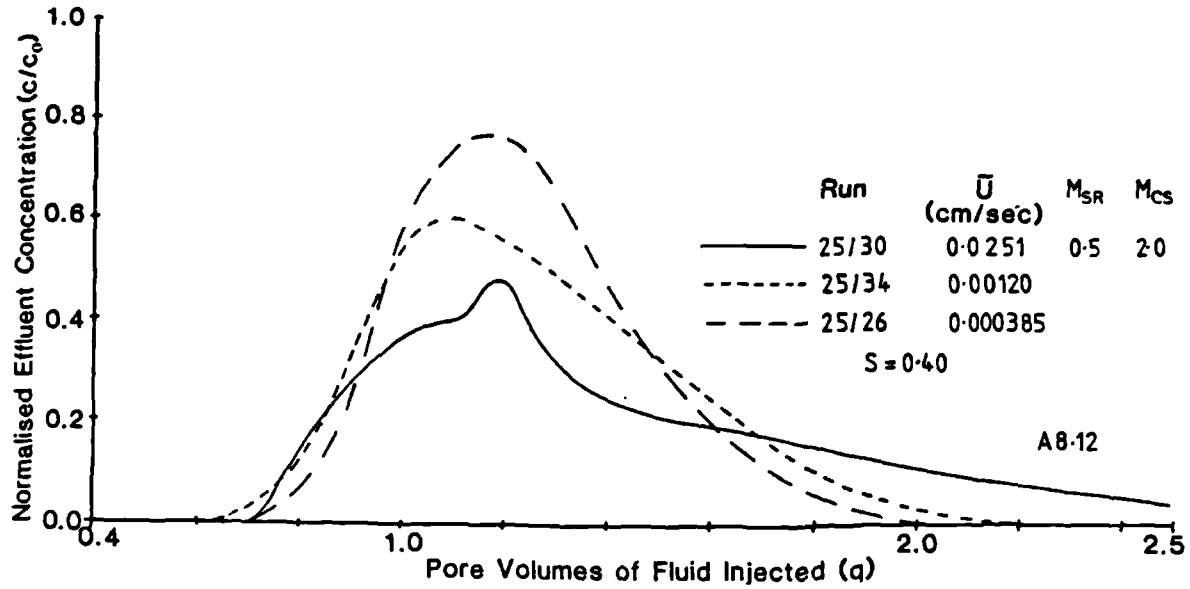
Normalised Effluent Concentration (c/c0)
1.0
0.8
0.6
0.4
0.2
0.0
0.4
1.0
2.0
2.5
Pore Volumes of Fluid Injected (q)
Run
Ū (cm/sec)
MSR
MCS
25/30 0·0251 0·5 2·0
25/34 0·00120
25/26 0·000385
S = 0·40
A8·12

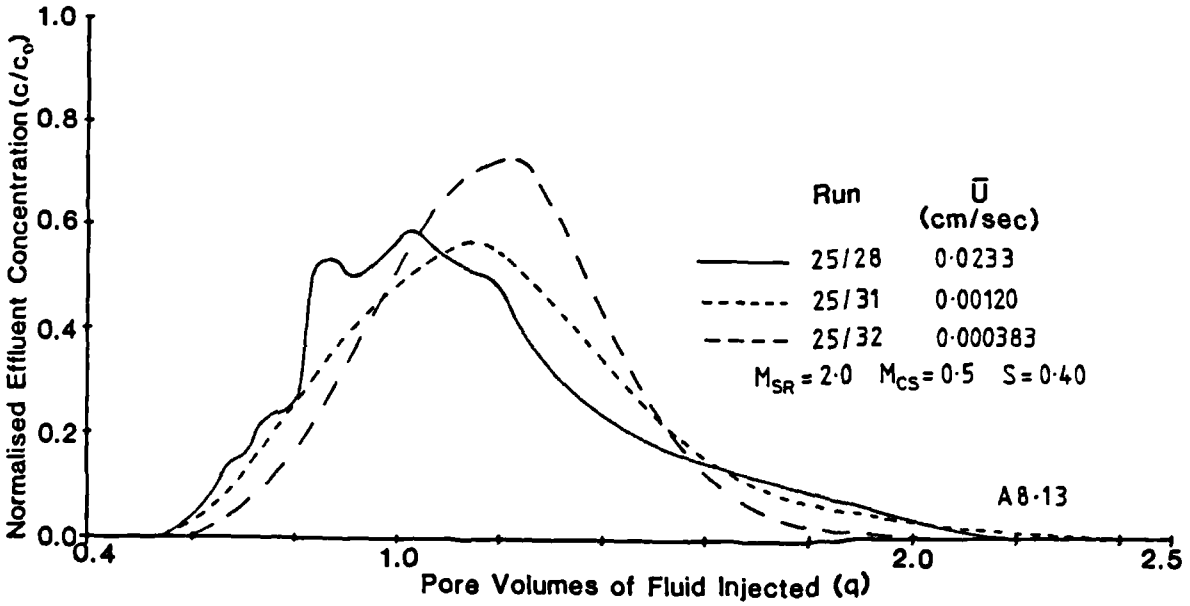
Normalised Effluent Concentration (c/c0)
1.0
0.8
0.6
0.4
0.2
0.0
0.4
1.0
2.0
2.5
Pore Volumes of Fluid Injected (q)
Run
Ū (cm/sec)
25/28 0·0233
25/31 0·00120
25/32 0·000383
MSR = 2·0 MCS = 0·5 S = 0·40
A8·13

APPENDIX NINE

DATA FROM DISPLACEMENTS IN LENSED SYSTEMS

This appendix contains characteristic curves for continuous injection experiments conducted to study fluid flow in lensed systems. Analytical predictions are compared to the experimental data in eacn case. These results are discussed in chapter eight.

A9.1 Unit Mobility Ratio Displacements

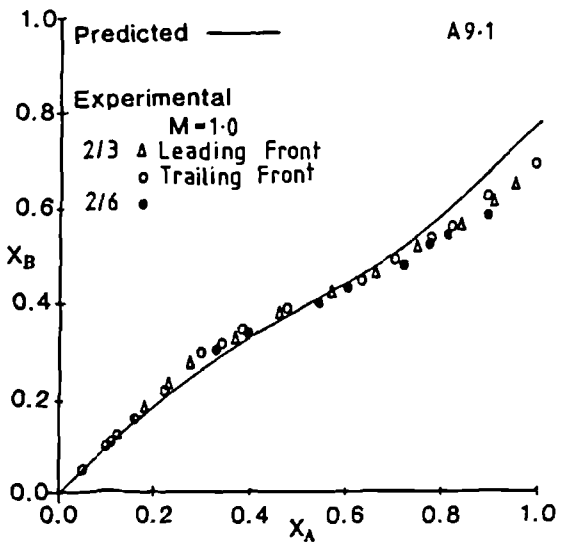

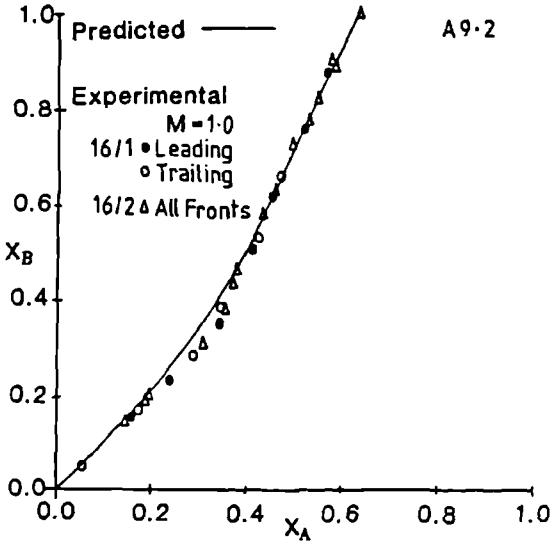

A9.2 Non-Unit Mobility Ratio Displacements

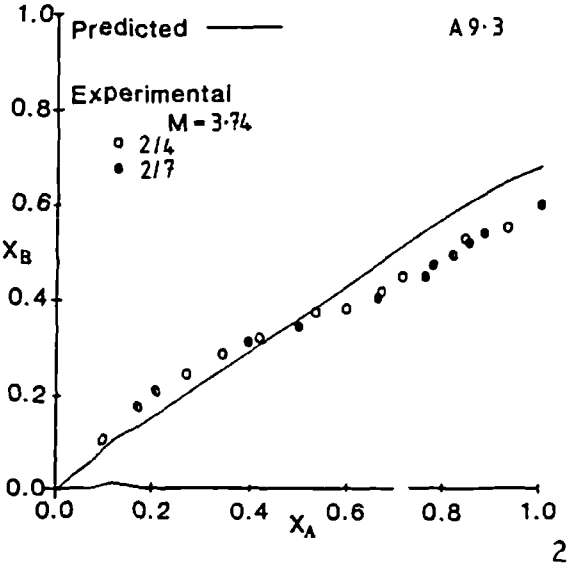

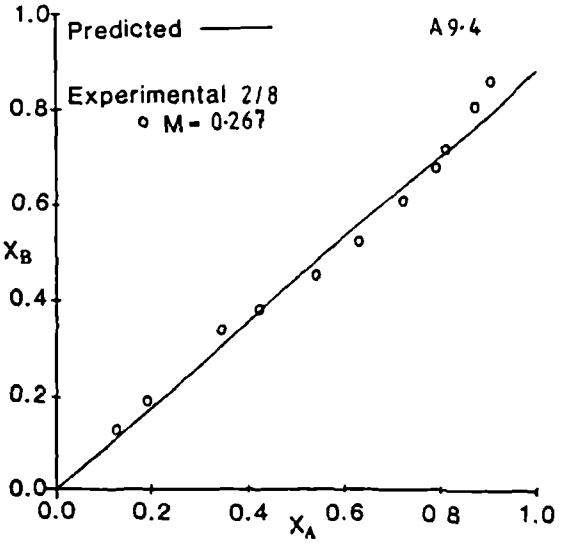

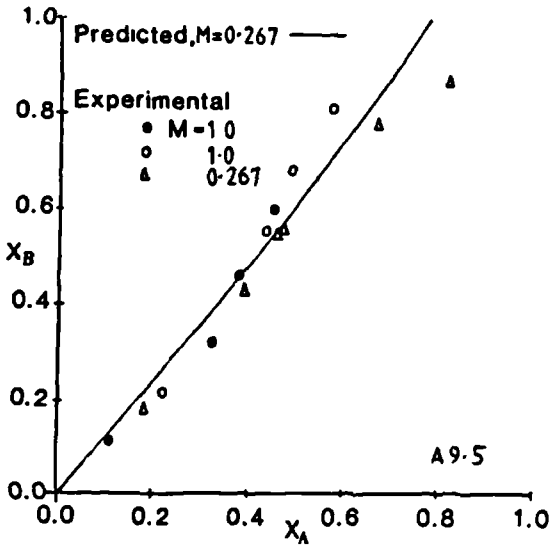
Predicted, M=0·267
Experimental
M=1·0
1·0
0·267
A9·5
X_B
X_A
0.0
0.2
0.4
0.6
0.8
1.0

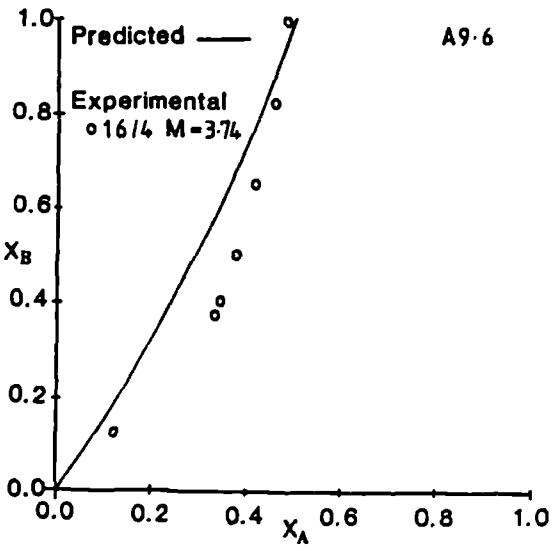
Predicted
A9·6
Experimental
1614 M=3·74
X_B
X_A
0.0
0.2
0.4
0.6
0.8
1.0

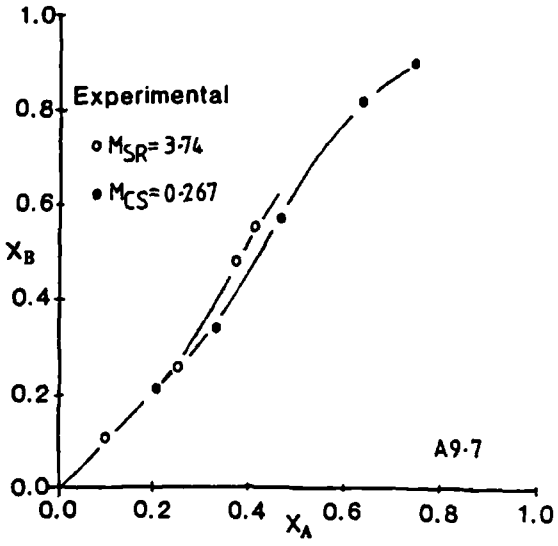
Experimental
M_{SR}=3·74
M_{CS}=0·267
A9·7
X_B
X_A
0.0
0.2
0.4
0.6
0.8
1.0

APPENDIX TEN

DERIVATION OF EQUATIONS TO CALCULATE THE FINITE CROSSFLOW OF FLUID IN A LENSED SYSTEM DURING AN EQUIVISCOUS DISPLACEMENT

Consider the system, figure 8.3, where layer A contains a lens. A differential material balance over a small element of layer A (figure 4.14) gives:

$$\frac{\partial^2 P_A}{\partial X^2} = \alpha(P_A - P_B) \qquad \text{(A10.1)}$$

where $$\alpha = \frac{4}{h_D^2 \left(1 + \frac{C_A}{C_B} M\right)} \quad .$$

As there are no mobility changes in the system it is reasonable to assume that there is steady-state flow in layer B . Under these circumstances $P_B = 1 - X$. Thus equation A10.1 becomes:

$$\frac{\partial^2 P_A}{\partial X^2} - \alpha P_A = \alpha(X-1) \qquad \text{(A10.2)}$$

for which the general solution is:

$$P_A = A \exp(X\sqrt{\alpha}) + B \exp(-X\sqrt{\alpha}) + 1 - X \quad . \qquad \text{(A10.3)}$$

Using the appropriate boundary conditions in equation A10.3 the axial pressure profile within layer A can be calculated.

BC1 - $P_A = 1.0$ at $X = 0.0$ for $0.0 \leq X \leq X_1$, here

$$\sqrt{\alpha} = \beta = \frac{\sqrt{2}}{h_D}$$

$$P_A = A_1[\exp(X\beta)-\exp(-X\beta)] + 1 - X \qquad \text{(A10.4)}$$

$$\frac{dP_A}{dX} = A_1\beta[\exp(X\beta)+\exp(-X\beta)] - 1 \quad . \qquad \text{(A10.5)}$$

BC2 - $P_A = 0.0$ at $X = 1.0$ for $X_2 \leq X \leq 1.0$, here

$$\sqrt{\alpha} = \omega = \frac{\sqrt{2}}{h_D}$$

$$P_A = A_3[\exp(X\omega)-\exp(\omega(2-X))] + 1 - X \qquad \text{(A10.6)}$$

$$\frac{dP_A}{dX} = A_3\omega[\exp(X\omega)+\exp(\omega(2-X))] - 1 \quad . \qquad \text{(A10.7)}$$

For the region $X_1 \leq X \leq X_2$:

$$\sqrt{\alpha} = \gamma = \frac{2}{h_D\left\{1 + \frac{C_1}{C_2}\right\}^{\frac{1}{2}}}$$

and $$P_A = A_2 \exp(X\gamma) + B_2 \exp(-X\gamma) + 1 - X \qquad \text{(A10.8)}$$

$$\frac{dP_A}{dX} = \gamma[A_2 \exp(X\gamma) - B_2 \exp(-X\gamma)] - 1 \quad . \qquad \text{(A10.9)}$$

BC3 and BC4

$$\left.\begin{aligned} P_{A,UPSTREAM} &= P_{A,DOWNSTREAM} \\ \left(\frac{dP_A}{dX}\right)_{UPSTREAM} &= \frac{C_1}{C_2}\left(\frac{dP_A}{dX}\right)_{DOWNSTREAM} \end{aligned}\right\} X = X_1$$

BC3 gives

$$A_1 = \frac{A_2H + B_2I}{F} \qquad \text{(A10.10)}$$

and BC4 gives

$$A_1 = \frac{\frac{C_1\gamma(A_2H-B_2I)}{C_2} - \frac{C_1}{C_2} + 1}{\beta G} \qquad \text{(A10.11)}$$

where $F = \exp(X_1\beta) - \exp(-X_1\beta)$

$G = \exp(X_1\beta) + \exp(-X_1\beta)$

$H = \exp(X_1\gamma)$

$I = \exp(-X_1\gamma)$.

Combining equations A10.10 and A10.11 gives

$$A_2 = \frac{F(1 - \frac{C_1}{C_2}) - B_2I(\beta G + \frac{C_1\gamma F}{C_2})}{H(\beta G - \frac{C_1\gamma F}{C_2})} \qquad \text{(A10.12)}$$

BC5 and BC6

$$\left.\begin{aligned} P_{A,UPSTREAM} &= P_{A,DOWNSTREAM} \\ \left(\frac{dP_A}{dX}\right)_{UPSTREAM} &= \frac{C_2}{C_1}\left(\frac{dP_A}{dX}\right)_{DOWNSTREAM} \end{aligned}\right\} \quad X = X_2$$

BC5 gives

$$A_3 = \frac{(A_2L+B_2N)}{J} \tag{A10.13}$$

and BC6 gives

$$A_3 = \frac{\frac{C_1\gamma(A_2L-B_2N)}{C_2} - \frac{C_1}{C_2} + 1}{\omega k} \tag{A10.14}$$

where $J = \exp(X_2\omega) - \exp(\omega(2-X_2))$

$K = \exp(X_2\omega) + \exp(\omega(2-X_2))$

$L = \exp(X_2\gamma)$

$N = \exp(-X_2\gamma)$.

Combined equations A10.13 and A10.14 gives:

$$A_2 = \frac{J(1 - \frac{C_1}{C_2}) - B_2N(\frac{C_1\gamma J}{C_2} + \omega K)}{L(\omega K + \frac{C_1\gamma J}{C_2})} \tag{A10.15}$$

Combined equations A10.12 and A10.15 gives:

$$B_2 = \frac{(1-C_1/C_2)(JHQ-FLS)}{(NHPQ-ILRS)} \qquad (A10.16)$$

where $S = \omega k - (C_1\gamma J)/C_2$

$P = \omega k - (C_1\gamma J)/C_2$

$Q = \beta G - (C_1\gamma F)/C_2$

$R = \beta G - (C_1\gamma F)/C_2$

The axial pressure profiles discussed in section 8.1 for unit mobility ratio displacement were calculated from equations A10.4, A10.6 and A10.8.

APPENDIX ELEVEN

DERIVATION OF EQUATIONS FOR NON-UNIT MOBILITY RATIO DISPLACEMENTS IN A NON-COMMUNICATING LENSED SYSTEM

Consider the non-communicating lens system (figure 8.3a). If the two layers are joined at the injection (X = 0.0) and production (X = 1.0) ends of the system , the relative propagation of the fronts through the system are given by:

$$\frac{U_A}{U_B} = \frac{\lambda_A}{\lambda_B}\,\frac{\phi_B}{\phi_A} = \frac{dX_A}{dX_B} \quad . \tag{A11.1}$$

Thus the frontal positions can be calculated from:

$$\int_0^{X_B} \frac{\phi_B}{\lambda_B}\, dX_B = \int_0^{X_A} \frac{\phi_A}{\lambda_A}\, dX_A \quad . \tag{A11.2}$$

For layer B :

$$\lambda_B = \frac{k_1}{\mu_R(X_B(1-M)+M)} \quad . \tag{A11.3}$$

But for layer A , λ_A is different when X_A is in each section of the media. Thus:

$$\lambda_A = \frac{k_1}{\mu_R \left(\frac{C_1 X_A}{C_2} \right) + \frac{MC_1(X_1 - X_A)}{C_2} + M(X_2 - X_1) + \frac{MC_1(1 - X_2)}{C_2}} \quad .$$

$$0.0 \leq X_A \leq X_1 \qquad \text{(A11.4)}$$

$$\lambda_A = \frac{k_1}{\mu_R \left(\frac{C_1 X_1}{C_2} \right) + (X_A - X_1) + M(X_2 - X_1) + \frac{MC_1(1 - X_2)}{C_2}} \quad ,$$

$$X_1 \leq X_A \leq X_2 \qquad \text{(A11.5)}$$

$$\lambda_A = \frac{k_1}{\mu_R \left(\frac{C_1 X_1}{C_2} \right) + (X_2 - X_1) + \frac{C_1(X_A - X_2)}{C_2} + \frac{MC_1(1 - X_A)}{C_2}} \quad ,$$

$$X_2 \leq X_A \leq 1.0 \quad . \qquad \text{(A11.6)}$$

NOMENCLATURE

A - Cross-sectional area available to flow

a - Radius of capillary tube

b - Fraction of system that is high conductance media

C - Conductance of media (k/ϕ)

c - Concentration

c_o - Injection concentration

D - Effective diffusion coefficient

D_o - Molecular diffusion coefficient

d - Dimension in Reynolds number (equation 2.1)

d_p - Particle diameter

E - Microscopic convective dispersion term

E_{BT} - Fraction of the system swept at breakthrough

E_V - Vertical Sweep

$E_{1.0}$ - Fraction of system swept after one pore volume has been injected

F - Electrical formation factor

F_D - Fraction of the displacing fluid in effluent stream

f - Fanning friction factor

G - Quantity of diffusing material (moles)

g - Gravitational acceleration

H - System Width

h - Layer Width

h_D - Layer aspect ratio (h/L)

I_A - Volume of slug fluid in layer A

I_B - Volume of slug fluid in layer B

I_{TD} - Transverse dispersion index

J - Leverett's J function

K - Microscopic dispersion coefficient

$\bar{K}_L$ - Thickness weighted average longitudinal dispersion coefficient

K_L' - Effective longitudinal dispersion coefficient for a capillary tube

K_{Leff} - Effective longitudinal dispersion coefficient for a porous media

k - Absolute permeability

k_i - Effective permeability

k_i' - End point effective permeability

k_{ri} - Relative permeability

k_{ri}' - End point relative permeability

ℓ - System length

L_c - Length of capillary tube

l - Longitudinal mixing group

M - Mobility Ratio

N_{CT} - Transverse capillary number

N_c - Capillary number $(V\mu/\gamma)$

n - Refractive index

P - Normalised pressure (dimensionless)

P - Pore volumes of chase fluid (equations 6.6 and 6.7)

p - Pressure

Q - Flow rate

q - Dimensionless pore volumes injected

q_{ULT} - Total injected fluid pore volumes required to sweep entire system

Re - Reynold's number

$R_{V/G}$ - Viscous/gravity force ratio

$R_{C/V}$ - Capillary/viscous force ratio

S - Pore volumes of slug fluid

S_{OPT} - Optimum slug volume (pore volumes)

S_W - Water saturation

T - Time

T^* - Dimensionless time

t^* - Transverse mixing group

t - Transverse dimensionless time

U - Interstitial velocity

$\overline{U}$ - Average interstitial velocity

V - Superficial velocity

$\overline{V}$ - Coefficient of variation

VOL - Volume

VR - Viscosity ratio

W - System width

X - Dimensionless axial dimension (x/L)

X_A - Frontal position within layer A

X_B - Frontal position within layer B

$\overline{X}$ - Mean

x - Axial dimension

Y - Dimensionless lateral dimension (y/h)

y - Lateral dimension

Greek

α - Crossflow index

α_t - Transverse dispersivity

α_L - Longitudinal dispersivity

β - Crossflow index

γ - Crossflow index

γ - Surface or interfacial tension

θ - Contact angle

λ - Fluid mobility

μ - Fluid viscosity

ρ - Fluid density

σ - Standard deviation (equation 2.16)

σ - Local inhomogeneity factor

Φ - Fluid potential

ψ - Pressure potential

ω - Todd and Longstaff mixing parameter

ϕ - Matrix porosity

Subscript

A - High conductance layer

B - Low conductance layer

BT - Breakthrough

c - Capillary

CR - Crossover point

C - Chase fluid

D - Displacing

eff - Effective

L - Longitudinal

m - Mixing zone

nw - Non-wetting

P - Produced

R - Residual fluid

S - Slug fluid

t - Transverse

W - Water

w - Wetting

x - Axial direction

XF - Crossflowing fluid

REFERENCES

1. MAHERS, E.G.; "Mass Transfer and Interfacial Phenomena in Oil Recovery.", PhD Thesis, Imperial College, London (1983).

2. DIETZ, D.N.; "A Theoretical Approach to the Problem of Encroaching and By-Passing Edge Water.", Proc. Koninklijke Nederlandse Akademie Van Wetenschappen Series B (Phy.Sci.) **56** (1953).

3. HAWTHORNE, R.G.; "Two-Phase Flow in Two-Dimensional Systems - Effects of Rate, Viscosity and Density on Fluid Displacement in Porous Media.", Trans AIME **219** (1960) 81-87.

4. MAHERS, E.G. and DAWE, R.A.; "Quantification of Diffusion Inside Porous Media for EOR Processes by Micromodel and Holography.", SPE/DOE 4th Symp. on EOR, Tulsa, Oklahoma, USA (1984); SPE/DOE Paper 12679.

5. BEAR, J.; "Dynamics of Fluids in Porous Media.", Wiley (1972).

6. RICHARDSON, J.G.; "Flow through Porous Media.", Section 16, Handbook of Fluid Dynamics, Ed. Streeter, McGraw-Hill (1961).

7. COLLINS, R.E.; "Flow of Fluids through Porous Materials.", Reinhold (1961).

8. MUSKAT, M.; "Physical Principles of Oil Production.", IHRDC (1981).

9. DAKE, L.P.; "Fundamentals of Reservoir Engineering.", Elsevier (1978).

10. CRAIG, F.F.Jr.; "The Reservoir Aspects of Water-flooding.", Monograph Series 3, SPE, Dallas (1971).

11. HEARN, C.L.; "Simulation of Stratified Waterflooding by Pseudo Relative Permeability Curves.", J. Pet. Tech **23** (1971) 805-813.

12. KYTE, J.R. and BERRY, D.W.; "New Pseudo Functions to Control Numerical Dispersion.", Soc. Pet. Eng. J. **15** (1975) 269-276.

13. JACKS, H.H., SMITH. O.J.E. and MATTAX, C.C.; "The Modelling of a Three-Dimensional Reservoir with a Two-Dimensional Reservoir Simulator - The Use of Dynamic Pseudo Functions.", Soc. Pet. Eng. J. **13** (1973) 175-185.

14. BUCKLEY, S.E. and LEVERETT, M.C.; "Mechanism of Fluid Displacement in Sands.", Trans. AIME **146** (1942) 107-116.

15. WELGE, H.J.; "A Simplified Method for Computing Oil Recovery by Gas or Water Drive.", Trans. AIME **195** (1952) 91-98.

16. MARLE, C.M.; "Multiphase Flow in Porous Media.", Technip (1981).

17 BENTSEN, R.G. and SAEEDI, J.; "Liquid-Liquid Immiscible Displacement in Unconsolidated Porous Media.", J. Can. Pet. Tech. (Jan-March 1981) 93-103.

18. BENTSEN, R.G.; "Conditions under which the Capillary Term may be Neglected.", J. Can. Pet. Tech. **17** (Oct-Dec 1978) 25-30.

19. HABERMANN, B.; "The Efficiency of Miscible Displacement as a Function of Mobility Ratio.", Trans. AIME **219** (1960) 264-272.

20. JACQUARD, J. and SEGUIER, P.; "Mouvement De Deux Fluids En Contact Dans Un Milieu Poreux.", J. De Mecanique **1** (Dec 1962) 367-394.

21. PERKINS, T.K. and JOHNSON, O.C.; "A Study of Immiscible Fingering in Linear Models.", Soc. Pet. Eng. J. **9** (1969) 39-46.

22 PERRINE, R.L.; "Stability Theory and its Use to Optimize Solvent Recovery of Oil.", Soc. Pet. Eng. J **1** (1961) 9-16.

23. PERRINE, R.L.; "The Development of Stability Theory for Miscible Liquid-Liquid Displacement.", Soc. Pet. Eng. J. **1** (1961) 17-25.

24. GARDNER, J.W. and YPMA, J.G.J.; "An Investigation of Phase Behaviour - Macroscopic Bypassing Interaction in CO2 Flooding.", SPE/DOE 3rd Symp. on EOR, Tulsa, Oklahoma, USA (1982); SPE/DOE 10686.

25 PERKINS, T.K., JOHNSON, O.C. and HOFFMAN, R.N.; "Mechanics of Viscous Fingering in Miscible Systems.", Soc. Pet. Eng. J. **5** (1965) 301-317.

26. DOUGHERTY, E.L.; "Mathematical Model of an Unstable Miscible Displacement.", Soc. Pet. Eng. J. **3** (1963) 155-163.

27. SLOBOD, R.L. and THOMAS, R.A.; "Effect of Transverse Diffusion on Fingering in Multiphase Displacements.", Soc. Pet. Eng. J. **3** (1963) 9-13.

28. VAN MEARS, P. and VAN DER POEL, C.; "A Theoretical Description of Water-Drive Processes Involving Viscous Fingering.", Trans. AIME **213** (1958) 103-112.

29. KOVAL, E.J.; "A Method of Predicting the Performance of Unstable Miscible Displacement in Heterogeneous Media.", Soc. Pet. Eng. J. **3** (1963) 145-154.

30. BENHAM, A.L. and OLSON, R.W.; "A Model Study of Viscous Fingering.", Soc. Pet. Eng. J. **3** (1963) 138-144.

31. TODD, M.R. and LONGSTAFF, W.J.; "The Development, Testing and Application of a Numerical Simulator for Predicting Miscible Flood Performance.", J. Pet. Tech. **24** (1972) 875-882.

32. STILES, W.E.; "Use of Permeability Distrbution in Waterflood Calculations.", Trans. AIME **186** (1949) 9-13.

33. DYKSTRA, H. and PARSONS, R.L.; "The Prediction of Oil Recovery by Waterflood.", Secondary Recovery of Oil in the US, Sec. Ed. API (1950) 160-174.

34. HIATT, W.N.; "Injected-Fluid Coverage of Multi-Well Reservoirs with Permeability Stratification.", Drilling and Prod. Prac. (1958) 165-194.

35. WARREN, J.E. and COSGROVE, J.J.; "Prediction of Waterflood Behaviour in a Stratified System.", Soc. Pet. Eng. J. **4** (1964) 149-157.

36. ZAPATA, V.J. and LAKE, L.W.; "A Theoretical Analysis of Viscous Crossflow.", 56th SPE Ann. Fall. Conf. San Antonio, Texas (1981); SPE paper 10111.

37. WRIGHT, R.J. and DAWE, R.A.; "Fluid Displacement Efficiency in Layered Porous Media - Mobility Ratio Influence.", Revue de L'Institut Francais du Petrole **38** No.2 (1983) 455-474.

38. DOSCHER, T.M. and EL-ARABI, M.A.; "A Controversial Laboratory Study of the Mechanism of Crude Oil Displacement by Carbon Dioxide. Part III - Nitrogen vs. Carbon Dioxide in Dipping Models.", 1983 California Regional Meeting, Ventura; SPE paper 11678.

39. CRANK, J.; "The Mathematics of Diffusion.", 2nd Edition, Oxford University Press (1975).

40. BLACKWELL, R.J., RAYNE, J.R. and TERRY, W.M.; "Factors Influencing the Efficiency of Miscible Displacement.", Trans. AIME **216** (1959) 1-8.

41. PERKINS, T.K. and JOHNSON, O.C.; "A Review of Diffusion and Dispersion in Porous Media.", Soc. Pet. Eng. J. **3** (1963) 70-84.

42. BRIGHAM, W.E., REED, D.W. and DEW, J.N.; "Experiments on Mixing During Miscible Displacement in Porous Media.", Soc. Pet. Eng. J. **1** (1961) 1-8.

43 US Department of Energy Report; "El Dorado Micellar-Polymer Demonstration Project - Third Annual Report.", June 1976-Aug 1977, BERC/TPR-77/12.

44. SHEELY, C.Q.; "Description of Field Tests to Determine Residual Oil Saturations by Single-Well Tracer Methods." J. Pet. Tech. **30** (1978) 194-202.

45. WARREN, J.E. and SKIBA, F.F.; "Macroscopic Dispersion.", Soc. Pet. Eng. J. **4** (1964) 215-230.

46. LAKE, L.W. and HIRASAKI, G.J.; "Taylor Dispersion in Stratified Porous Media.", Soc. Pet. Eng. J. **21** (1981) 459-468.

47. TAYLOR, G.I.; "Dispersion of Soluble Matter in Solvent Flowing Slowly Through a Tube.", Proc. Royal Soc. **A219** (1953) 186-203.

48. TAYLOR, G.I.; "Conditions Under Which Dispersion of a Solute in a Stream of Solvent can be Used to Measure Molecular Diffusion.", Proc. Royal Soc. **A225** (1954) 473-477.

49. ARIS, R.; "On the Dispersion of a Solute in a Fluid Flowing Through a Tube.", Proc. Royal Soc. **A235** (1956) 67-77.

50. MARLE, C., SIMANDOUX, P., PACSIRSZKY, J. and GAULIER, C.; "Etude du Displacement de Fluides Miscibles en Milieu Poreux Stratifie.", Revue de L'Institut Francais du Petrole **22** No.2 (1967) 272-294.

51. LEVERETT, M.C.; "Capillary Behaviour in Porous Sands.", Trans. AIME **142** (1941) 152-169.

52. DOUGLAS, J., BLAIR, P.M. and WAGNER, R.J.; "Calculation of Linear Waterflood Behaviour Including the Effects of Capillary Pressure.", Trans. AIME **213** (1958) 96-102.

53. RICHARDSON, J.G. and PERKINS, F.M.; "A Laboratory Investigation of the Effect of Rate on Recovery of Oil by Waterflooding.", Trans. AIME **210** (1957) 114-121.

54. YOKOYAMA, Y. and LAKE, L.W.; "The Effect of Capillary Pressure on Immiscible Displacements in Statified Porous Media.", 56th Ann. Fall Conf. San Antonio, Texas (1981); SPE paper 10109.

55. CRANE, F.E., KENDALL, H.A. and GARDNER, G.H.F.; "Some Experiments on the Flow of Miscible Fluids of Unequal Density Through Porous Media.", Soc. Pet. Eng. J. **3** (1963) 277-230.

56. CRAIG, F.F., SANDERLIN, J.L., MOORE, D.W. and GEFFEN, T.M.; "A Laboratory Study of Gravity Segregation in Frontal Drives.", Trans. AIME **210** (1957) 275-282.

57. DUMORE, J.M.; "Stability Considerations in Downward Miscible Displacements.", Soc. Pet. Eng. J. **4** (1964) 356-362.

58. POZZI, A.L. and BLACKWELL, R.J.; "Design of Laboratory Models for Study of Miscible Displacement.", Soc. Pet. Eng. J. **3** (1963) 28-40.

59. GEERTSMA, J., CROES, G.A. and SCHWARZ, N.; "Theory of Dimensionally Scaled Models of Petroleum Reservoirs.", Trans. AIME **207** (1956) 118-127.

60. RAPOPORT, L.A.; "Scaling Laws for Use in Design and Operation of Water-Oil Flow Models.", Trans. AIME **204** (1955) 143-150.

61. BENTSEN, R.G.; "Scaled Fluid-Flow Models with Permeabilities Differing from that of the Prototype.", J. Can. Pet. Tech. **15** (July-Sept. 1976) 46-52.

62. PERKINS, F.M. and COLLINS, R.E.; "Scaling Laws for Laboratory Flow Models of Oil Reservoirs.", Trans. AIME **219** (1960) 383-385.

63. VAN DAALEN, F. and VAN DOMSELAAR, H.R.; "Scaled Fluid-Flow Models with Geometry Differing from that of Prototype.", Soc. Pet. Eng. J. **12** (1972) 220-228.

64. CARPENTER, C.W.; "A Verification of Waterflood Scaling in Heterogeneous Communicating Flow Models.", Soc. Pet. Eng. J. **2** (1962) 9-12.

65. TAN, T.C.; "Techniques for Control of Numerical Dispersion in Black-Oil and Compositional Reservoir Simulation.", PhD Thesis, Imperial College (1982).

66. YOUNG, M.S., CASINADER, P.C. and WILSON, D.C.; "The Use of Higher Order Finite Difference Methods in Reservoir Simulation.", Proc. Europec London (1980); EUR 180.

67. LANTZ, R.B.; "Quantitative Evaluation of Numerical Diffusion (Truncation Error).", Soc. Pet. Eng. J. **11** (1971) 315-320.

68. STALKUP, F.I.Jr.; "Miscible Displacement.", Monograph Series **8**, SPE, Dallas (1983).

69. PADDAY, J.F.; "Surface Tension Part II. The Measurement of Surface Tension.", Surface and Colloid Science Volume One, Ed. E. Matijevia, Wiley Interscience (1969) 101-149.

70. SORBIE, K.S., AEE Winfrith, Dorset. - Personal Communication (1984).

71. JONES, S.C. and ROSZELLE, W.O.; "Graphical Te
for Determining Relative Permeability from Displace...
Experiments.", J. Pet. Tech. **30** (1978) 807-817.

72. JENNINGS, R.R., ROGERS, J.H. and WEST, T.J.; "Factors Influencing Mobility Control by Polymer Solutions.", J. Pet. Tech. **23** (1971) 391-401.

73. KOONCE, K.T. and BLACKWELL, R.J.; "Idealised Behaviour of Solvent Banks in Stratified Reservoirs.", Soc. Pet. Eng. J. **5** (1965) 318-328.

74. GARDER, A.O., PEACEMAN, D.W. and POZZI, A.L.; "Numerical Calculation of Multidimensional Miscible Displacement by the Method of Characteritics.", Soc. Pet. Eng. J. **4** (1964) 26-36.

75. ABBASZADEH-DEHGHANI, M. and BRIGHAM, W.E.; "Analysis of Well-to-Well Tracer Flow to Determine Reservoir Heterogeneity.", California Regional Meeting, San Francisco (1982); SPE paper 10760.

76. Department of Energy Project OT/F/790; Pet. Eng. Dept., Imperial College, London.

77. HUPPLER, J.D.; "Numerical Investigation of the Effects of Core Heterogeneities on Waterflood Relative Permeabilities.", Soc. Pet. Eng. J. **10** (1970) 381-392.

78. JOHNSON, E.F., BOSSLER, D.P. and NAUMANN, V.O.; "Calculation of Relative Permeability from Displacement Experiments.", Trans. AIME **216** (1959) 370-372.

79. SCHWARTZ, F.W.; "Macroscopic Dispersion in Porous Media: The Controlling Factors.", Water Resources Research **13** No.4 (1977) 743-752.

80. MOULU, J.C.; "Etude Experimentale Du Displacement Miscible Dans Un Milieu Heterogene A Nodule.", Communication No. 30, IFP 16020 (Juin 1968).

81. ROSMAN, A. and SIMON, R.; "Flow Heterogeneity in Reservoir Rocks.", J. Pet. Tech. **28** (1976) 1427-1429.

82. PARSONS, R.W.; "Microwave Attenuation - A New Tool for Monitoring Saturations in Laboratory Flowing Experiments", Soc. Pet. Eng. J. **15** (1975) 302-310.

83. GREENKORN, R.A.; "Experimental Study of Waterflood Tracers.". J. Pet. Tech. (1962) 87-92.